

VORTEX-INDUCED MOTIONS OF MULTIPLE CYLINDRICAL OFFSHORE STRUCTURES

by

Yibo Liang

This thesis is presented

for

The Degree of Doctor of Philosophy

of

Newcastle University

School of Marine Science and Technology

Newcastle University

August, 2017

Abstract

VORTEX-INDUCED MOTIONS OF MULTIPLE CYLINDRICAL OFFSHORE STRUCTURES

Yibo Liang

Vortex-induced motions (VIM) has been receiving continuous attention in the field of offshore exploration and exploitation as an increasing number of deep-draft floating structures have been operating in different regions around world. Deep-draft floating structures are well known for their favourable vertical motions behaviour compared with other types of floating offshore structures. However, the increases in the structure's draft can also lead to more severe VIM, which may lead to potential damage particularly causing fatigue to the mooring and riser systems. This research is to carry out an in-depth study on the fundamental fluid physics and the associated hydrodynamic characteristics of a multi-column structure, i.e. the deep-draft semi-submersible (DDS).

A comprehensive set of numerical simulations has been conducted and experimentally validated in physical models. Good correlation has been demonstrated among the vortex shedding patterns, the fluctuation forces on the structures, and the VIM trajectory in the present work. The “lock-in” phenomenon was found to have the most striking effect on the vortex shedding processes, the force and the VIM trajectories. Analysis of the drag and lift force coefficients on and the work done by different members of the DDS revealed that the portside and starboard side columns are the key structure members responsible for amplifying the VIM responses while the pontoons are acting to restrain VIM responses. Additionally, based on the analysis of flow over a stationary structure, it is revealed that adding the pontoons into the structures can significantly alter the flow patterns around the structure. The vortex street tends to be more tidy and structured. Hence, the vortex shedding period and the lift force coefficient for the overall structure are increased.

Acknowledgements

I would like to express my great thanks and gratitude to my supervisor Prof. Longbin Tao at Newcastle University, for his quality and kindly academic supervision, guidance as well as endless support throughout the years of this research. I thank him for the enormous concern for my work at Newcastle University. During my PhD time, his kindly encouragement of my current and future research development inspired me in what I do, especially for building a decent foundation of my academic career.

I also would like to thank my co-supervisor, Dr. Yongchang Pu at Newcastle University who has always been accessible to advise me, for his valuable advice and helpful suggestions during my study.

My sincere appreciation goes to Prof. Longfei Xiao at Shanghai Jiao Tong University for his support and advise throughout the experimental work.

I want to extend my great appreciation to Mr. John Garside who has helped me with his experience on fluid dynamics from the beginning of my research. His valuable comments always extend and inspire my understanding of the research.

I also wish to great thank three of my friends and schoolmates, Martin Nuernberg, Weichao Shi and Arriya Leelachai at Newcastle University, for their endless help throughout my PhD programme.

Many thanks as well to Dr. Xinliang Tian at Shanghai Jiao Tong University and Dr. Carlos Ariel Garrido Mendoza for guiding me in patience on the early stage for understanding the CFD theory.

I would like to thank Dr. Mingyue Liu, Mr. Yufeng Kou, Dr. Wenyue Lu, Mr. Hong Xiong, Mr. Zhichao Fang and Mr. Yi Dai at Shanghai Jiao Tong University for their kind support and sharing their experience about experimental model tests. Special thanks are due to the staffs at Shanghai Jiao Tong University who have helped and supported me during my exchange in China.

I am grateful to the School of Marine Science and Technology and all my colleagues, who proceed a wonderful and enjoyable place of study, especially Serena Lim, Jaime Torres,

Maria Syrigou, Batuhan Aktas, Ralitsa Mihaylova, Lynna Rosli, Pierre-Adrien Opinel, Bowen Ma, De Wang Chia, Ikenna Okaro and Zhenhua Zhang as well as my office mates Christopher Lyons, I Putu Arta Wibawa, Sudheesh Ramadasan and Vita Kurniawati.

Abundant appreciation to the support staff in the university especially Carol Andrew for her patient and enthusiastic help through the applications for my MPhil and PhD programmes and Brenden Ward for his kindly help for all my IT issues, as well as Mr. Richard Carter and Dr. Simon Benson for their advice in my academic development.

Great appreciation to the support from CD-adapco and N8 HPC, especially Dr. Konstantinos Karantonis who support the Star-CCM+ package student licence during my PhD time.

Thank you also for Dr. Xiangyin Meng and Dr. Dawei Wu at Newcastle University, for their valuable advice and suggestions in both academic and career development.

It is an enormous pleasure to thank all the people who contributed but not mentioned above, in many different ways to the research.

Finally, I would like to thank my parents, Lin Li and Hongqiang Liang for believing, encouraging and funding me throughout my PhD study and my life. Their love and hearts have been always with me through the distance of thousands of miles, from Tianjin to Newcastle. They always encourage and believe in me and my goals. I do not know how much thanks I should say to them. Mom and Dad, I actually love you all.

Table of Contents

Abstract.....	i
Acknowledgements	iii
Table of Contents	vii
List of Tables.....	xi
List of Figures.....	xiii
List of Symbols.....	xxiii
List of Publications.....	xxix
Chapter 1. Introduction.....	1
1.1 Background.....	1
1.2 Aims & Objectives	9
1.3 Thesis Outline.....	9
1.4 Key Parameters.....	11
1.4.1 Reduced velocity	12
1.4.2 Reynolds number.....	12
1.4.3 Froude number.....	12
1.4.4 Force coefficients	13
1.4.5 Strouhal number	14
1.4.6 Non-dimensional characteristic amplitude	14
Chapter 2. Literature Review.....	15
2.1.1 Flow around a single cylinder	15
2.1.2 Flow around a multiple cylinder group	19
2.1.3 Vortex-induced vibrations	21
2.1.4 Vortex-induced motions on single and multiple cylindrical offshore structures.....	21
Chapter 3. Experimental Study.....	31
3.1 Towing Tank Tests	31
3.1.1 Experimental set-up.....	31

3.1.2 Model characteristics	33
3.1.3 Test arrangement of mooring system.....	34
3.1.4 Test programme	35
3.1.5 Natural periods of the motions in calm water	35
3.2 Circulating Water Channel Tests	38
3.2.1 Model characteristics	38
3.2.2 Experimental set-up	40
3.2.3 Vacuum water channel PIV tests	44
3.3 Summary	47
Chapter 4. Numerical Simulation.....	49
4.1 Computational Overview	49
4.1.1 Governing equations	50
4.1.2 IDDES approach	50
4.1.3 Computational domain.....	50
4.2 Sensitivity Study	54
4.2.1 Sensitivity studies for the DDS model	54
4.2.2 Sensitivity studies for the four columns model.....	60
4.3 Model Validation	62
4.3.1 Validation against MARIN experiments.....	63
4.3.2 Validation against the present model tests	63
4.4 Summary	66
Chapter 5. Results and Discussions	67
5.1 Experimental and numerical study on VIM of a DDS	67
5.1.1 Motion characteristics	67
5.1.2 Force analysis.....	77
5.1.3 Vortex shedding characteristics	79
5.1.4 Correlation of vortex shedding, force and VIM.....	81
5.2 Interaction of vortex shedding processes at 45° angle of incidence	88

5.2.1 Motion characteristics.....	89
5.2.2 Drag and lift force analysis.....	91
5.2.3 Flow pattern.....	100
5.3 Interaction of vortex shedding processes on the flow around four columns with and without pontoons connected	117
5.3.1 Flow characteristics in the horizontal plane	117
5.3.2 Flow characteristics in the vertical plane	125
5.3.3 Overall drag and lift forces	131
5.3.4 Drag and lift force on each member	135
Chapter 6. Conclusions and Future Works	139
6.1 Conclusions	139
6.2 Suggestions for future work	140
Appendix A	143
Appendix B.....	145
Appendix C.....	147
References	149

List of Tables

Table 2.1 Summary of the various studies on VIM of the multiple square-section columns structures.....	29
Table 3.1 Main characteristics of the DDS unit.	33
Table 3.2 Natural periods of the motions in calm water.	36
Table 3.3 Damping ratio of the DDS for two incidences.	37
Table 3.4 Main characteristics of the four columns configuration model (model I).....	38
Table 3.5 Main characteristics of the four columns with pontoons connected configuration model/DDS model (model II).....	38
Table 3.6 Characteristics of the three component force transducer (KYOWA LSM-B-SA1).	40
Table 3.7 PIV Laser and CCD Cameras settings.....	41
Table 3.8 DaVis Image processing settings.....	42
Table 4.1 The regional refinement level.....	53
Table 4.2 Numerical set-up information.....	54
Table 4.3 Calculations of discretization error (Celik <i>et al.</i> , 2008) for the DDS model; the grid convergence index (<i>GCI</i>) represents the numerical uncertainty.	57
Table 4.4 The mesh refinement tests.	58
Table 4.5 The time step sensitivity study.	59
Table 4.6 Mesh sensitivity study for the four columns model.	60
Table 4.7 Calculations of discretization error (Celik <i>et al.</i> , 2008) for the four columns model; the grid convergence index (<i>GCI</i>) represents the numerical uncertainty.	60
Table 4.8 The main characteristics of the MARIN DDS.	63
Table 4.9 Comparison of \bar{C}_D from the present numerical calculation and the MARIN experimental measurements.	63
Table 4.10 Comparison of the results from the present numerical calculations and experimental measurements for the stationary DDS model at 45° incidence.	64
Table 4.11 Comparison of the results from the present numerical calculations and experimental measurements for the four columns configuration model at 45° incidence.	64
Table 4.12 Comparison of the results from the present numerical calculations and experimental measurements for 45° incidence.....	66
Table 5.1 Comparison of the mooring line mean forces for 0° incidence at $Ur = 3.9, 6.4$ (The mooring lines arrangement is shown in Figure 3.3).	79
Table 5.2 The chronological order of vortices genesis for each column.....	105

Table 5.3 The resulting non-dimensional coefficients \bar{C}_D , C_{Lrms} and St for the four columns configuration (“num.” represents “numerical”; “exp.” represents “experimental”).. 132

Table 5.4 The resulting non-dimensional coefficients \bar{C}_D , C_{Lrms} and St for the four columns with pontoons connected configuration (“num.” represents “numerical”; “exp.” represents “experimental”)..... 132

List of Figures

Figure 1.1 The global primary energy consumption in 2011, together with the percentage share for each energy source. For oil, the primary energy consumption is shown in millions of tonnes. For the other energy sources, they are shown in millions of tonnes equivalent (Maribus, 2014).	1
Figure 1.2 Global offshore production by water depth (Manning, 2016). Source: U.S. Energy Information Administration, based on Rystad Energy. Note: Includes lease condensate and hydrocarbon gas liquids.	3
Figure 1.3 Offshore crude oil production by water depth (Manning, 2016). Source: U.S. Energy Information Administration, based on Rystad Energy. Note: Includes lease condensate and hydrocarbon gas liquids.	3
Figure 1.4 Deepwater system types (Christopher <i>et al.</i> , 2012).	4
Figure 1.5 Examples of installed worldwide deepwater structures (Christopher <i>et al.</i> , 2012). (DDCV – Deep Draft Caisson Vessel; DDF – Deep Draft Floater; DDS – Deep Draft Semi-Submersible; FDPSO – Floating Drilling, Production, Storage and Offloading System; FPSO – Floating Production, Storage and Offloading System; MiniDOC – Cross between a semisubmersible and a truss Spar; MODU – Mobile Offshore Drilling Unit; Semi-FPU – Semi-Submersible Floating Production Unit; TLP – Tension Leg Platform).	5
Figure 1.6 Gulf of Mexico surface water conditions during 27 th – 28 th , March, 2017, derived from a variety of infrared sensors to obtain sea surface temperatures (SST) from NASA, NOAA and JPSS satellites. Main features and surface currents are labelled (Upton. <i>et al.</i> , 2017).	6
Figure 1.7 Comparison between geometries able to present VIM: (a) semi-submersible, tension-leg platform; (b) mono-column; (c) classic Spar; (d) truss Spar and (e) cell Spar platforms (Fujarra <i>et al.</i> , 2012).	7
Figure 1.8 The Genesis Spar under tow to location (Smith <i>et al.</i> , 2004b).	8
Figure 1.9 Deep Draft Semi® platform (Rijken and Leverette, 2008).	8
Figure 1.10 Thesis Outline.	10
Figure 1.11 Regimes of flow around a smooth, circular cylinder in steady current (Sumer and Fredsøe, 1997).	13
Figure 2.1 Progression of Spar deepwater development systems (Christopher and Chad, 2012).	24
Figure 3.1 Zhejiang Ocean University towing tank.	32

Figure 3.2 Experimental set-up in the towing tank.....	32
Figure 3.3 Schematic of the experimental set-up.....	33
Figure 3.4 Characteristic dimensions of the DDS.....	34
Figure 3.5 The top deck of the model.	35
Figure 3.6 Decay curves for the DDS for the transverse motion.....	36
Figure 3.7 Decay curves for the DDS for the in-line motion.....	36
Figure 3.8 Decay curves for the DDS for the yaw motion.	37
Figure 3.9 Four columns configuration model (model I).....	39
Figure 3.10 Four columns with pontoons connected configuration model/DDS model (model II).....	39
Figure 3.11 The test section of the circulating water channel.	40
Figure 3.12 KYOWA LSM-B-SA1 three component transducer.....	41
Figure 3.13 Columns arrangement and flow direction.	42
Figure 3.14 Experimental set-up in the circulating water channel.	43
Figure 3.15 Laser head and translation unit.....	44
Figure 3.16 PIV measurements during the test.	44
Figure 3.17 The measured plan of the vacuum water channel PIV test, where “A – A” is the vertical plane and “B – B” is the horizontal plane at the middle draft level of the DDS (the model presented in the figure is only for showing the position. During the vacuum water channel PIV test, there is no model in the water channel).	45
Figure 3.18 Current velocity profile at “A – A” plane.....	46
Figure 3.19 Current velocity profile at “B – B” plane.....	46
Figure 4.1 Computational domain.	51
Figure 4.2 Visualization of the mesh at the middle draft level of the DDS (XY plane at the middle draft of the DDS).	52
Figure 4.3 Mesh around the column at the middle draft level of the DDS (XY plane at the middle draft of the DDS) showing the “Prims Layer Mesher”.	52
Figure 4.4 The outlines of five regional refinements.....	53
Figure 4.5 Convergence line for the mean drag force coefficient (\bar{C}_D) for the DDS model. ..	55
Figure 4.6 Convergence line for the root-mean-square lift force coefficient (C_{Lrms}) for the DDS model.....	56
Figure 4.7 Convergence line for the Strouhal number (St) for the DDS model.	56
Figure 4.8 Convergence line for the mean drag force coefficient (\bar{C}_D) for the four columns model.....	61

Figure 4.9 Convergence line for the root-mean-square lift force coefficient (C_{Lrms}) for the four columns model.....	61
Figure 4.10 Convergence line for the Strouhal number (St) for the four columns model.....	62
Figure 5.1 Non-dimensional in-line and transverse characteristics amplitudes (A_x/L , A_y/L), the Ur is defined based on $T_{0transverse}$).	69
Figure 5.2 FFT of the motions in the transverse direction as a function of Ur and f_y for 0° incidence (the Ur is defined based on $T_{0transverse}$).	69
Figure 5.3 FFT of the motions in the transverse direction as a function of Ur and f_y for 45° incidence (the Ur is defined based on $T_{0transverse}$).	70
Figure 5.4 FFT of lift force coefficient as a function of Ur and f_s for 0° incidence (the Ur is defined based on $T_{0transverse}$).	70
Figure 5.5 FFT of lift force coefficient as a function of Ur and f_s for 45° incidence (the Ur is defined based on $T_{0transverse}$).	71
Figure 5.6 FFT of the transverse motions and the lift force coefficients at $Ur = 6.4$ for 0° incidence, (a) transverse motion (y/L); (b) lift force coefficient (C_L).	71
Figure 5.7 FFT of the transverse motions and the lift force coefficients at $Ur = 6.6$ for 45° incidence, (a) transverse motion (y/L); (b) lift force coefficient (C_L).	72
Figure 5.8 FFT of the transverse motions and the lift force coefficients at $Ur = 15.7$ for 0° incidence, (a) transverse motion (y/L); (b) lift force coefficient (C_L).	72
Figure 5.9 Significant values of the transverse peaks ($H_{1/3}/L$). The Ur is defined based on $T_{0transverse}$	73
Figure 5.10 Maximum characteristic amplitude (H_{max}/L) of the transverse motion (the Ur is defined based on $T_{0transverse}$).	74
Figure 5.11 Non-dimensional yaw characteristics amplitude (the Ur is defined based on T_{0yaw}).	76
Figure 5.12 FFT of the yaw motion as a function of Ur and f_{yaw} for 0° incidence (the Ur is defined based on T_{0yaw}).	76
Figure 5.13 FFT of the yaw motion as a function of Ur and f_{yaw} for 45° incidence (the Ur is defined based on T_{0yaw}).	77
Figure 5.14 Mean drag coefficient (\bar{C}_D), where A is the projected area at 0° incidence.....	79
Figure 5.15 Non-dimensional vorticity magnitude ($\omega D/U$) contours of the DDS model for “pre lock-in”, “lock-in” and “post lock-in” regions for 0° and 45° incidence, XY plane at middle draft location of the DDS.	80

Figure 5.16 Time history of the motion in the transverse direction (y/L), lift force coefficient (C_L) for 0° incidence at $Ur = 3.9$ (pre lock-in), the vorticity contours in the XY plane at middle draft of the DDS (A and C refer to the point close to the transverse motion peak value within one oscillation period, B is the vortex shedding process between A and C, D is the vortex shedding process after C, corresponded simulation time are shown in the figure), and the motion trajectory in the XY plane.	84
Figure 5.17 Time history of the motion in the transverse direction (y/L), lift force coefficient (C_L) for 0° incidence at $Ur = 6.4$ (lock-in), the vorticity contours in the XY plane at middle draft of the DDS (A and C refer to the point close to the transverse motion peak value within one oscillation period, B is the vortex shedding process between A and C, D is the vortex shedding process after C, corresponded simulation time are shown in the figure), and the motion trajectory in the XY plane.	85
Figure 5.18 Time history of the motion in the transverse direction (y/L), lift force coefficient (C_L) for 0° incidence at $Ur = 11.8$ (post lock-in), the vorticity contours in the XY plane at middle draft of the DDS (A and C refer to the point close to the transverse motion peak value within one oscillation period, B is the vortex shedding process between A and C, D is the vortex shedding process after C, corresponded simulation time are shown in the figure), and the motion trajectory in the XY plane.	86
Figure 5.19 Time history of the motion in the transverse direction (y/L), lift force coefficient (C_L) for 45° incidence at $Ur = 6.6$ (lock-in), the vorticity contours in the XY plane at middle draft of the DDS (A and C refer to the point close to the transverse motion peak value within one oscillation period, B is the vortex shedding process between A and C, D is the vortex shedding process after C, corresponded simulation time are shown in the figure), and the motion trajectory in the XY plane.	87
Figure 5.20 Non-dimensional transverse characteristic amplitudes (A_y/L), the Ur is defined based on the natural period of the transverse motion.....	89
Figure 5.21 Non-dimensional in-line characteristic amplitudes (A_x/L), the Ur is defined based on the natural period of the transverse motion.....	90
Figure 5.22 Non-dimensional yaw characteristic amplitudes, the Ur is defined based on the natural period of the yaw motion.	90
Figure 5.23 Mean drag coefficient (\bar{C}_D) from the numerical and experimental results on the VIM model, the Ur is defined based on the natural period of the transverse motion..	91

Figure 5.24 Root-mean-square lift coefficient (C_{Lrms}) from the numerical and experimental results on the VIM model, the Ur is defined based on the natural period of the transverse motion.....	92
Figure 5.25 Added mass coefficient (C_a) of the VIM model from the numerical predictions and the experiments, the Ur is defined based on the natural period of the transverse motion. (*To better compare the general trend with present results, the results from Zhang <i>et al.</i> (2014) is scaled 20% from their original data).	93
Figure 5.26 FFT of the transverse motions and the lift force coefficients at $Ur = 3.9$, (a) transverse motion; (b) lift force coefficient.	95
Figure 5.27 FFT of the transverse motions and the lift force coefficients at $Ur = 5.1$, (a) transverse motion; (b) lift force coefficient.	95
Figure 5.28 FFT of the transverse motions and the lift force coefficients at $Ur = 6.6$, (a) transverse motion; (b) lift force coefficient.	95
Figure 5.29 FFT of the transverse motions and the lift force coefficients at $Ur = 8.9$, (a) transverse motion; (b) lift force coefficient.	96
Figure 5.30 FFT of the transverse motions and the lift force coefficients at $Ur = 12.1$, (a) transverse motion; (b) lift force coefficient.	96
Figure 5.31 The DDS model (A is the entire model and B is the decomposed model which show the definition of the individual members).	97
Figure 5.32 Mean drag coefficients (\bar{C}_D) on each member of the DDS from the VIM model.	98
Figure 5.33 Root-mean-square lift coefficients (C_{Lrms}) on each member of the DDS from the VIM model.	98
Figure 5.34 Work done by each member of the DDS on VIM model.	99
Figure 5.35 Lift force coefficient time history on different members of the stationary DDS at $Re = 4.3 \times 10^4$, including locally zoomed in the last 6s.....	100
Figure 5.36 A time series of the pressure distribution around the DDS at middle draft showing the instantaneous flow fields around the stationary DDS at $Re = 4.3 \times 10^4$ corresponding to the lift force coefficient time history (A: 120.6 s; B: 122.4 s; C: 124.2 s; D: 126.0 s).....	101
Figure 5.37 A time series of non-dimensional spanwise vorticity ($\vec{\omega}_z D/U$) contours around the DDS at the middle draft level showing the instantaneous flow fields around the stationary DDS at $Re = 4.3 \times 10^4$ corresponding to the lift force coefficient time history (A: 120.6 s; B: 122.4 s; C: 124.2 s; D: 126.0 s).	102

Figure 5.38 Lift force coefficient time history on different members of the DDS during VIM at $Ur = 3.9, 5.1, 6.6, 8.9$ and 12.1	104
Figure 5.39 Definition of the regions around an individual column.....	105
Figure 5.40 A time series of the non-dimensional spanwise vorticity ($\vec{\omega}_z D/U$) contours around the DDS at middle draft showing the instantaneous flow fields around the DDS at $Ur = 3.9$ (A, B, C, D, E) and the non-dimensional transverse motion (y/L) time history (F); the red arrow is the DDS transverse velocity direction.	107
Figure 5.41 A time series of the non-dimensional vorticity ($\omega D/U$) contours around the DDS at middle draft showing the instantaneous flow fields around the DDS at $Ur = 3.9$ (A, B, C, D, E) and the non-dimensional motion trajectory (F); the red arrow is the DDS transverse velocity direction.	108
Figure 5.42 A time series of the non-dimensional spanwise vorticity ($\vec{\omega}_z D/U$) contours around the DDS at middle draft showing the instantaneous flow fields around the DDS at $Ur = 5.1$ (A, B, C, D, E) and the non-dimensional transverse motion (y/L) time history(F); the red arrow is the DDS transverse velocity direction.	109
Figure 5.43 A time series of the non-dimensional vorticity ($\omega D/U$) contours around the DDS at middle draft showing the instantaneous flow fields around the DDS at $Ur = 5.1$ (A, B, C, D, E) and the non-dimensional motion trajectory (F); the red arrow is the DDS transverse velocity direction.	110
Figure 5.44 A time series of the non-dimensional spanwise vorticity ($\vec{\omega}_z D/U$) contours around the DDS at middle draft showing the instantaneous flow fields around the DDS at $Ur = 6.6$ (A, B, C, D, E) and the non-dimensional transverse motion (y/L) time history (F); the red arrow is the DDS transverse velocity direction.	111
Figure 5.45 A time series of the non-dimensional vorticity ($\omega D/U$) contours around the DDS at middle draft showing the instantaneous flow fields around the DDS at $Ur = 6.6$ (A, B, C, D, E) and the non-dimensional motion trajectory (F); the red arrow is the DDS transverse velocity direction.	112
Figure 5.46 A time series of the non-dimensional spanwise vorticity ($\vec{\omega}_z D/U$) contours around the DDS at middle draft showing the instantaneous flow fields around the DDS at $Ur = 8.9$ (A, B, C, D, E) and the non-dimensional transverse motion (y/L) time history (F); the red arrow is the DDS transverse velocity direction.	113
Figure 5.47 A time series of the non-dimensional vorticity ($\omega D/U$) contours around the DDS at middle draft showing the instantaneous flow fields around the DDS at $Ur = 8.9$ (A, B,	

C, D, E) and the non-dimensional motion trajectory (F); the red arrow is the DDS transverse velocity direction.	114
Figure 5.48 A time series of the non-dimensional spanwise vorticity ($\vec{\omega}_z D/U$) contours around the DDS at middle draft showing the instantaneous flow fields around the DDS at $Ur = 12.1$ (A, B, C, D, E) and the non-dimensional transverse motion (y/L) time history (F); the red arrow is the DDS transverse velocity direction.	115
Figure 5.49 A time series of the non-dimensional vorticity ($\omega D/U$) contours around the DDS at middle draft showing the instantaneous flow fields around the DDS at $Ur = 12.1$ (A, B, C, D, E) and the non-dimensional motion trajectory (F); the red arrow is the DDS transverse velocity direction.	116
Figure 5.50 Time-averaged velocity distribution after column 3 at the middle draft level of the four columns configuration in XY plane.	118
Figure 5.51 Time-averaged velocity distribution after column 3 at the middle draft level of the four columns with pontoons connected configuration in XY plane.	118
Figure 5.52 Time-averaged flow properties of the U_{mean}/U_C in XY plane (middle draft level of the structure) for column 3, at $x/D = 0.75$ $Re = 4.3 \times 10^4$, “FC” is the four columns configuration and “FCP” is the four columns with pontoons connected configuration.	119
Figure 5.53 Time-averaged flow properties of the \overline{U}_i/U_C (velocity component i) in XY plane (middle draft level of the structure) for column 3 at $x/D = 0.75$, $Re = 4.3 \times 10^4$. “FC” is the four columns configuration and “FCP” is the four columns with pontoons connected configuration.	119
Figure 5.54 Numerical predicted time-averaged flow properties of the \overline{U}_i/U_C (velocity component i) in XY plane (middle draft level of the structure) for each column at $x/D = 0.75$, $Re = 4.3 \times 10^4$. “FC” is the four columns configuration and “FCP” is the four columns with pontoons connected configuration.	120
Figure 5.55 Instantaneous flow fields around column 3 for the four columns configuration at XY plane (middle draft level of the structure), where $\vec{\omega}_z D/U$ is the non-dimensional spanwise vorticity.	121
Figure 5.56 Instantaneous flow fields around column 3 for the four columns with pontoons connected configuration at XY plane (middle draft level of the structure), where $\vec{\omega}_z D/U$ is the non-dimensional spanwise vorticity.	122

Figure 5.57 A time series of the non-dimensional spanwise vorticity ($\vec{\omega}_z D/U$) contours around the four columns configuration model at the middle draft level showing the instantaneous flow fields in XY plane at $Re = 4.3 \times 10^4$	123
Figure 5.58 A time series of the non-dimensional spanwise vorticity ($\vec{\omega}_z D/U$) contours around the four columns with pontoons connected configuration model at the middle draft level showing the instantaneous flow fields in XY plane at $Re = 4.3 \times 10^4$	124
Figure 5.59 Numerically predicted time-averaged flow properties of the \overline{U}_k/U_C (velocity component k) in XZ plane for column 1 with certain distances ($x/D= 0.25$, $x/D = 0.75$ and $x/D = 1.5$) at $y/D = 0$ (the central line of column), $Re = 4.3 \times 10^4$. “FC” is the four columns configuration and “FCP” is the four columns with pontoons connected configuration. “ $z/D = 0$ ” is the bottom of the column and “ $z/D = 0.36$ ” is the pontoon upper face level.	125
Figure 5.60 Numerically predicted time-averaged flow properties of the \overline{U}_k/U_C (velocity component k) in XZ plane for column 2 with certain distances ($x/D= 0.25$, $x/D = 0.75$ and $x/D = 1.5$) at $y/D = 0$ (the central line of column), $Re = 4.3 \times 10^4$. “FC” is the four columns configuration and “FCP” is the four columns with pontoons connected configuration. “ $z/D = 0$ ” is the bottom of the column and “ $z/D = 0.36$ ” is the pontoon upper face level.	126
Figure 5.61 Numerically predicted time-averaged flow properties of the \overline{U}_k/U_C (velocity component k) in XZ plane for column 3 with certain distances ($x/D= 0.25$, $x/D = 0.75$ and $x/D = 1.5$) at $y/D = 0$ (the central line of column), $Re = 4.3 \times 10^4$. “FC” is the four columns configuration and “FCP” is the four columns with pontoons connected configuration. “ $z/D = 0$ ” is the bottom of the column and “ $z/D = 0.36$ ” is the pontoon upper face level.	127
Figure 5.62 A time series of the non-dimensional transverse vorticity ($\vec{\omega}_y D/U$) contours around the four columns configuration model at the central line of column 1 and 3 showing the instantaneous flow fields in XZ plane at $Re = 4.3 \times 10^4$	128
Figure 5.63 A time series of the non-dimensional transverse vorticity ($\vec{\omega}_y D/U$) contours around the four columns configuration model at the central line of column 2 showing the instantaneous flow fields in XZ plane at $Re = 4.3 \times 10^4$	129
Figure 5.64 A time series of the non-dimensional transverse vorticity ($\vec{\omega}_y D/U$) contours around the four columns with pontoons connected configuration model at the central line of column 1 and 3 showing the instantaneous flow fields in XZ plane at $Re = 4.3 \times 10^4$	130

Figure 5.65 A time series of the non-dimensional transverse vorticity ($\vec{\omega}_y D/U$) contours around the four columns with pontoons connected configuration model at the central line of column 2 showing the instantaneous flow fields in XZ plane at $Re = 4.3 \times 10^4$	131
Figure 5.66 Mean drag coefficient (\bar{C}_D) from the numerical (num.) and experimental (exp.) results for the four columns configuration (FC) and the four columns with pontoons connected configuration (FCP).....	133
Figure 5.67 Root-mean-square lift coefficient (C_{Lrms}) from the numerical (num.) and experimental (exp.) results for the four columns configuration (FC) and the four columns with pontoons connected configuration (FCP).	134
Figure 5.68 Strouhal number (St) from the numerical (num.) and experimental (exp.) results for the four columns configuration (FC) and the four columns with pontoons connected configuration (FCP).....	134
Figure 5.69 Mean drag coefficients (\bar{C}_D) on each member of the models (FC represents the four columns configuration; FCP represents the four columns with pontoons connected configuration).	136
Figure 5.70 Root-mean-square lift coefficients (C_{Lrms}) on each member of the models (FC represents the four columns configuration; FCP represents the four columns with pontoons connected configuration).	136
Figure 5.71 Mean lift coefficient (\bar{C}_L) on each member of the models (FC represents the four columns configuration; FCP represents the four columns with pontoons connected configuration).	137

List of Symbols

A	Projected area
A_x/L	Non-dimensional characteristics amplitude of in-line motion
A_y/L	Non-dimensional characteristics amplitude of transverse motion
B_L	Platform width
B_T	Platform draft
C	Structural damping
c	Damping coefficient
C_a	Added mass coefficient
C_D	Drag force coefficient
C_L	Lift force coefficient
CFD	Computational fluid dynamics
CFL	Courant–Friedrichs–Lewy
D	Column projected width
DDS	Deep-draft semi-submersilbe
exp.	Experimental results
f_s	Vortex shedding frequency
f_0	Natural frequency in clam water

Fr	Froude number
FC	Four columns configuration
FCP	Four columns with pontoons connected configuration
F_D, F_x	Hydrodynamic drag force acting on the structure
F_L, F_y	Hydrodynamic lift force acting on the structure
g	Acceleration of gravity
GCI	Grid convergence index
GoM	Gulf of Mexico
H	Immersed column height above the pontoon
h	Grid size
H_I	Immersed column height
H_{bottom}	Bottom points when $dy/dt = 0$ within one oscillation period
H_m	Individual oscillation height
H_{peak}	Peak points when $dy/dt = 0$ within one oscillation period
H/L	Aspect ratio
$H_{1/3}/L$	Non-dimensional significant values of the transverse peaks
I	Moment of inertia / Kronecker delta
K_x	Linear spring constant in the in-line direction
K_y	Linear spring constant in the transverse direction

k	Turbulent kinetic energy
L	Column width
m	Platform mass
m_a	Added mass
N	Total number
NaN	Not a number
num.	Numerical results
P	Pontoon height
p	Apparent order / Pressure
Re	Reynolds number
r	Grid refinement factor
rms	Root-mean-square
S	Distance between centre columns / Mean strain rate tensor
S/L	Spacing ratio
St	Strouhal number
T_0	Natural periods in calmwater
t	Time
Δt	Numerical simulation time step
TLP	Tension leg platform.

U, U_c	Current speed
u	Velocity vector
u'	Fluctuating velocity
u_t	Turbulent eddy viscosity
u_*	Friction velocity at the nearest wall
U_i	Streamwise flow velocity (velocity component i)
U_j	Transverse flow velocity (velocity component j)
U_k	Spanwise flow velocity (velocity component k)
U_{mean}	Mean flow velocity of streamwise and transverse flow velocities
Ur	Reduced velocity
VIM	Vortex-induced motions
VIV	Vortex-induced vibrations
Yaw	Non-dimensional characteristics amplitude of yaw motion
ρ	Fresh water density
Δ	Displacement
Δy_l	First layer thickness
∇	Hamiltonian operator
λ	Scale ratio
θ	Attack angle; Flow incidence

ν	Kinematic viscosity of the fresh water
\emptyset	Calculation results for different grid refinements
ζ	Damping ratio
τ	Reynold stress tensor
ω	Vorticity magnitude
$\vec{\omega}_x$	Streamwise vorticity
$\vec{\omega}_y$	Transverse vorticity
$\vec{\omega}_z$	Spanwise vorticity
x, X	In-line motion/distance
y, Y	Transverse motion/distance
y^+	Y plus value
z, Z	Vertical motion/distance

List of Publications

- Liang, Y., Tao, L., Xiao, L. and Liu, M. (2017) 'Experimental and numerical study on vortex-induced motions of a deep-draft semi-submersible', *Applied Ocean Research*, 67, pp. 169-187.
- Liang, Y. and Tao, L. (2017) 'Interaction of vortex shedding processes on flow over a deep-draft semi-submersible', *Ocean Engineering*, 141, pp. 427-449.
- Liu, M., Xiao, L., Liang, Y. and Tao, L. (2017) 'Experimental and numerical studies of the pontoon effect on vortex-induced motions of deep-draft semi-submersibles', *Journal of Fluids and Structures*, 72, pp. 59-79.
- Liang, Y., Tao, L., Xiao, L. and Liu, M. (2016) 'Experimental and Numerical Study on Flow Past Four Rectangular Columns in Diamond Configuration', *ASME 2016 35th International Conference on Ocean, Offshore and Arctic Engineering*. American Society of Mechanical Engineers, pp. V001T01A044-V001T01A044.

Chapter 1. Introduction

1.1 Background

In the modern world, oil is the most important fossil fuel for most societies (affecting such as economy, politics and technology), closely followed by coal and natural gas. In 2011, oil provided around 33% of the global primary energy consumption (Maribus, 2014). Additionally, gas accounted for about a quarter of the consumption (see Figure 1.1). Thus, more than half of the world's energy demand is met by the oil and gas production. The usage of coal is expected to reduce owing to the demand for clean air requirements.

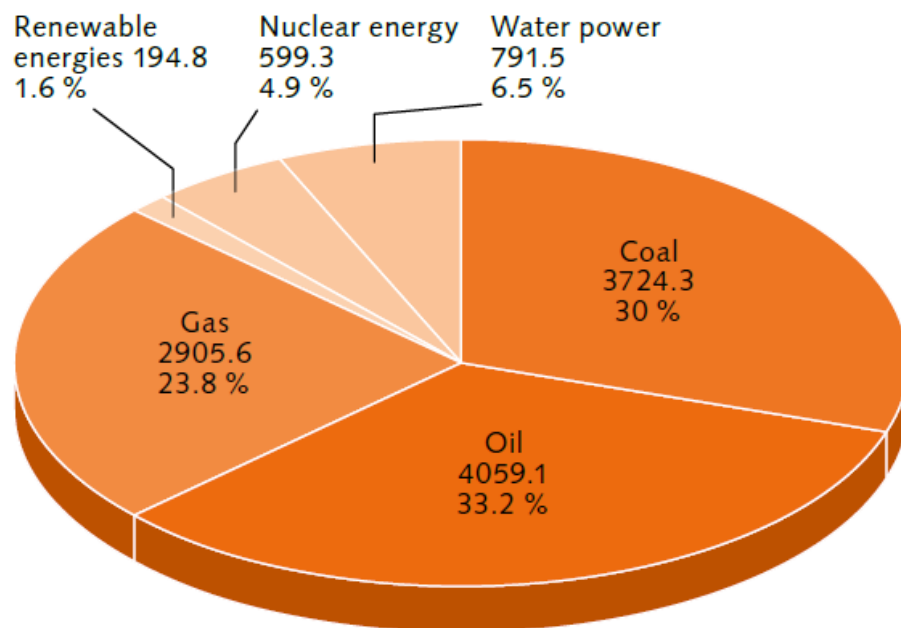


Figure 1.1 The global primary energy consumption in 2011, together with the percentage share for each energy source. For oil, the primary energy consumption is shown in millions of tonnes. For the other energy sources, they are shown in millions of tonnes equivalent (Maribus, 2014).

Most of the oil and gas which is pumped from deep below the ground is taking place on-shore. Nonetheless, an increasing volume of oil and gas has already been extracted from sites that are located offshore. Approximately a hundred years ago (in the late 19th century), the first oil well was extended to the coastline in United States (National Academies of Sciences and Medicine, 2016). Henry L. Williams, who ventured offshore as one of the pioneers in the Californian coast region, constructed oil wells on the sea floor that were connected by a 100 m long wooden pier to the shore (Maribus, 2014; National Academies of Sciences and Medicine, 2016). As the

subsequent exploitation of the offshore oil and gas fields moved further out from the shoreline, drilling wells based on the use of simple wooden piers became more and more difficult to construct. At that time, moveable barges started to be used for the offshore drilling activities. The first free-standing structure had been installed in the Gulf of Mexico 1.5 miles offshore with the aim to drill for oil through the seabed (Pratt *et al.*, 1997). Later, developed technology was taking wells far into this region and with deeper waters for the offshore drilling and exploitation activities. With the developments in the safe and reliable technology of offshore operations, many of the challenges of working in the offshore environment were overcome. The offshore exploration and exploitation work were gaining an increasing popularity in the oil and gas community. In 2011, 37% of global oil production was from offshore extraction and 28% of global gas production took place offshore (Maribus, 2014). Eventually 30% of total global oil production was contributed by the offshore oil production over the last decade (Manning, 2016).

For many years, offshore production was limited to the relatively shallow water regions such as in the coastal areas. However, due to many of the oil and gas deposits in the shallow water region becoming either exhausted or uneconomic. The oil and gas industry started to move further into the deepwater regions. The definition of three separate depth categories are listed below (Maribus, 2014; Manning, 2016):

- Shallow water production at a water depth of less than 400 m (it is less than 125 m in the definition made by Manning (2016)).
- Deepwater production at depths up to around 1500 m.
- Ultra-deepwater production at depths greater than 1500 m.

As can be seen in Figure 1.2, in 2015 the percentage of offshore oil production from shallow water fields was 64%, the lowest on recent records by 2015 (Manning, 2016). With the latest geophysical technology, potential oil and gas deposits located to a depth below the seabed of up to 12 km can be detected (Maribus, 2014). As a consequence, many new oil and gas fields in deepwater regions have been discovered recently. It also can be clearly seen in Figure 1.3, in most of the world, the share of offshore production from deepwater locations increased between 2005 and 2015.

Global offshore production by water depth (2005-15)

million barrels per day

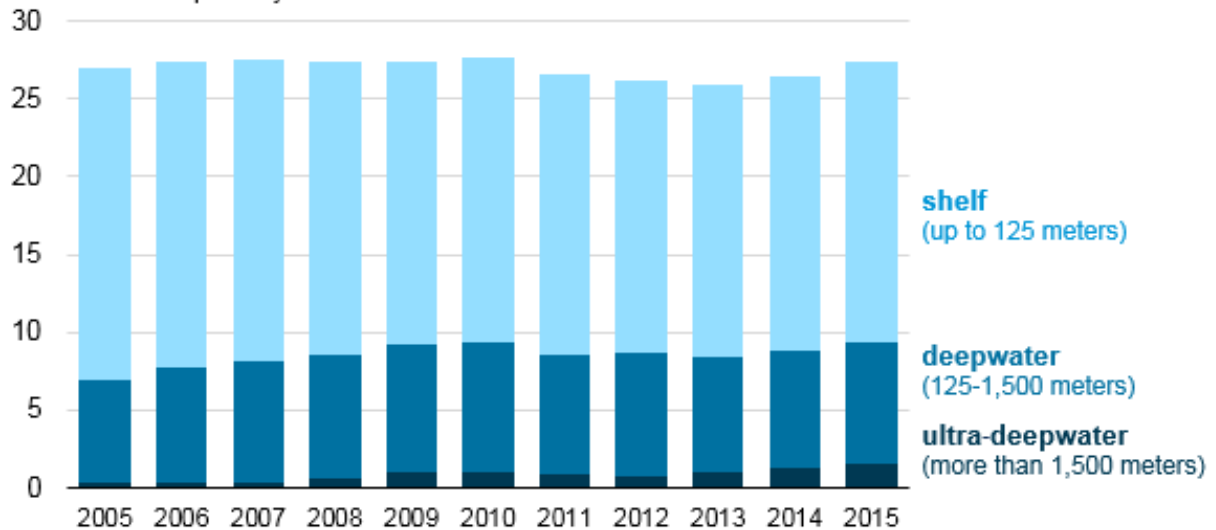


Figure 1.2 Global offshore production by water depth (Manning, 2016). Source: U.S. Energy Information Administration, based on Rystad Energy. Note: Includes lease condensate and hydrocarbon gas liquids.

Offshore crude oil production by water depth (2005-15)

million barrels per day

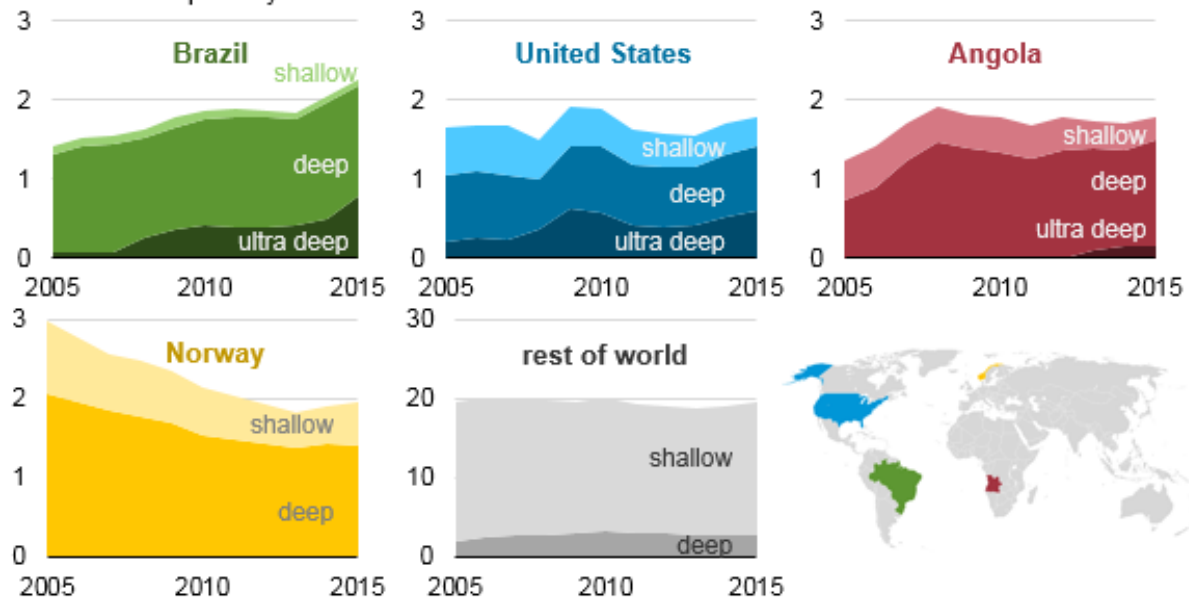


Figure 1.3 Offshore crude oil production by water depth (Manning, 2016). Source: U.S. Energy Information Administration, based on Rystad Energy. Note: Includes lease condensate and hydrocarbon gas liquids.

Due to the drilling activities slowly moving further out into the deepwater regions, the traditional fixed platforms (e.g. jackup platforms) were considered to be no longer suitable for

the deepwater exploitation work. Driven by the demands for fuel and the potential oil and gas profits, different types of offshore exploration drilling and exploitation facilities (e.g. floating production storage and offloading vessels, Spar platforms, semi-submersibles and tension-leg platforms, illustrated in Figure 1.4) were developed and started to appear with the more advanced state-of-the-art technologies and which offered increasing drilling ability to operate in deepwater regions. Thus, a considerable number of large size floating structures have been fabricated and installed in different deepwater regions around the world (see Figure 1.5), such as Gulf of Mexico (GoM).

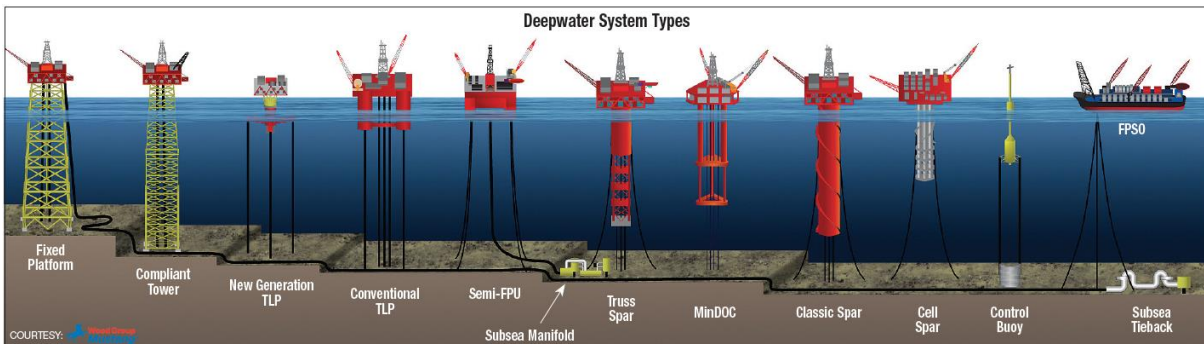


Figure 1.4 Deepwater system types (Christopher *et al.*, 2012).

However, in Gulf of Mexico, a relatively unique problem is that a long term loop current can be observed as the water enters into the gulf through the Yucatan Strait and subsequently exits through the Florida Strait. Parts of the loop current sometimes break away forming loop current eddies, which frequently affect the regional current patterns as shown in Figure 1.6.

These currents can be very strong, which may cause some operational safety issues for the floating structures. One of the serious issues is the vortex-induced motions (VIM). VIM is a cyclic rigid body motion that is induced by vortex shedding from a large sized floating structure. When the current flows over a cylindrical structure, the structure which is affected by the vortices that are generated and then systematically shed in the downstream region, may begin oscillating either in a side to side or in a fore and aft manner. If the vortex shedding frequency is close to the natural frequency of the structure, a so-called “lock-in” phenomenon can occur, which could amplify the cyclic motions of the structure dramatically. This resonance phenomenon may lead to potential damages to offshore systems, especially causing fatigue of the mooring and riser systems.

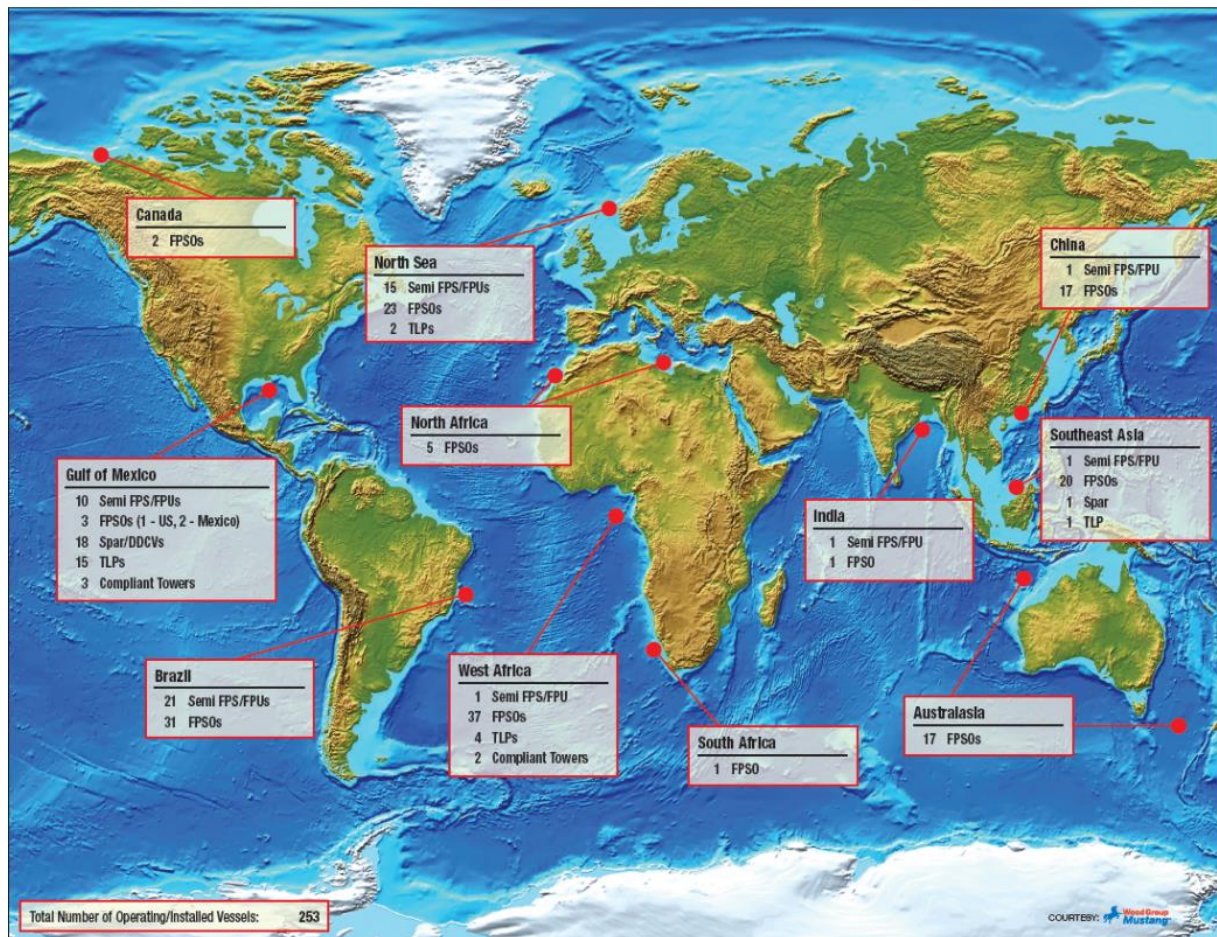


Figure 1.5 Examples of installed worldwide deepwater structures (Christopher *et al.*, 2012). (DDCV – Deep Draft Caisson Vessel; DDF – Deep Draft Floater; DDS – Deep Draft Semi-Submersible; FDPSPSO – Floating Drilling, Production, Storage and Offloading System; FPSO – Floating Production, Storage and Offloading System; MiniDOC – Cross between a semisubmersible and a truss Spar; MODU – Mobile Offshore Drilling Unit; Semi-FPU – Semi-Submersible Floating Production Unit; TLP – Tension Leg Platform).

In deepwater region developments, a favourable motion response of the floater is critical to the safe operations of top-tensioned facilities, as well as being able to ensure an adequate fatigue life of the mooring system and the risers. As most of the deep draft floaters are either single or multiple columns structures (see Figure 1.7), it is common practice to increase the draft of the columns in order to achieve the desired hydrodynamic characteristics in the vertical plane motions. However, an increase in the columns' draft can also potentially lead to more severe VIM developing. Therefore, VIM have been receiving continuous attention since the Genesis Spar was commissioned in 1997 (Kokkinis *et al.*, 2004; Fajarra *et al.*, 2012).

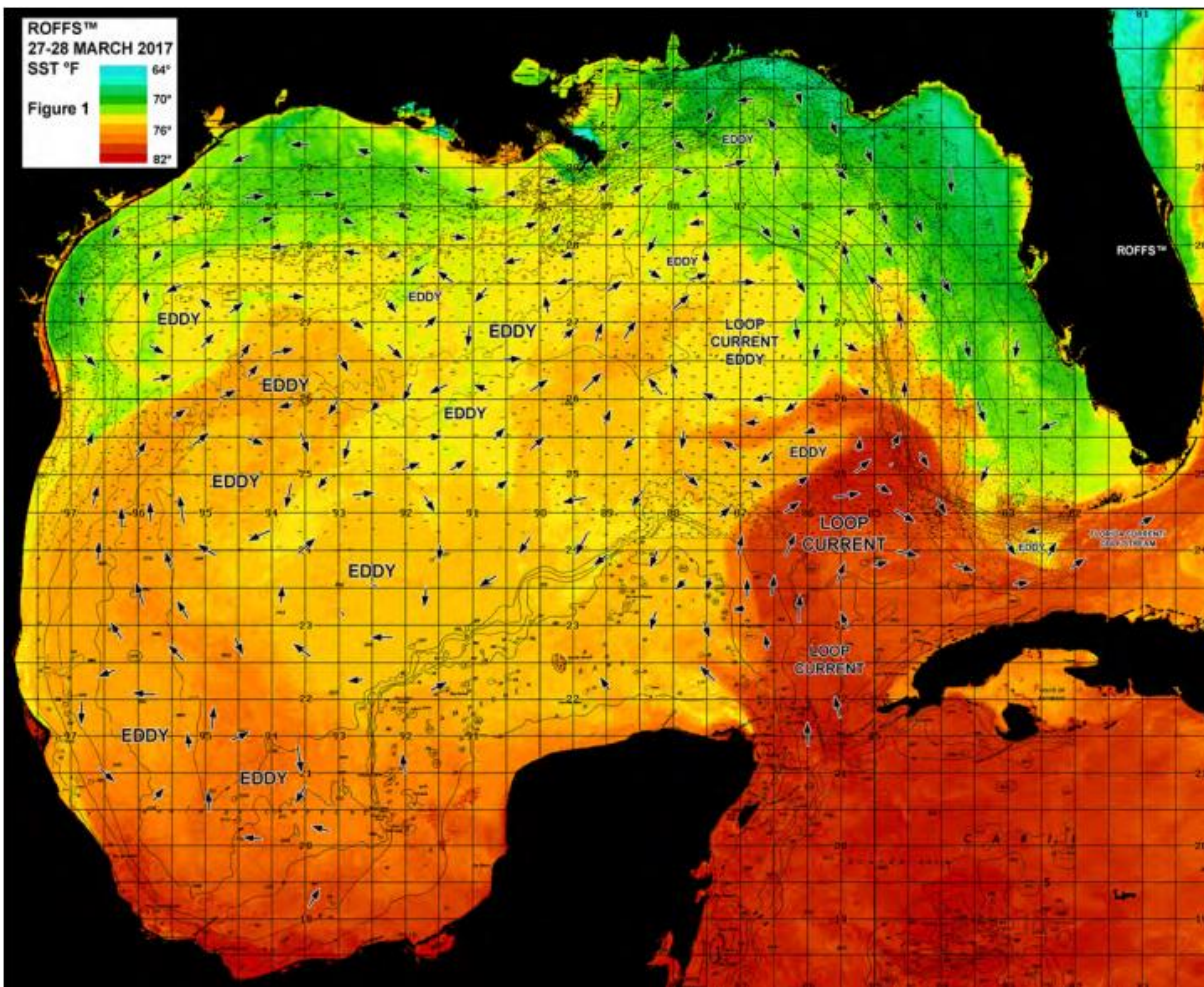


Figure 1.6 Gulf of Mexico surface water conditions during 27th – 28th, March, 2017, derived from a variety of infrared sensors to obtain sea surface temperatures (SST) from NASA, NOAA and JPSS satellites. Main features and surface currents are labelled (Upton. *et al.*, 2017).

In addition to traditional offshore oil & gas industry, VIM is also an important issue needing consideration for the development of many offshore renewable energy concepts (e.g. offshore floating wind turbines) as these devices are normally deployed in harsh environments typically those having strong currents.

Thus, restraining VIM has become one of the key research topic for operating the deep-draft floating structures in deepwater region. By limiting the VIM amplitude, the mooring system and risers can have a sustainably longer serving life. Some of the methods to restrain VIM have been developed in the last two decades. A typical method is adding on the strakes around the column especially for the Spar platform (see Figure 1.8). The strakes can break the strong vortices shed from the column in pieces. Thus, VIM amplitude can be limited to a relative small range. However, the manufacture and installation processes of the Spar platform become more

complicated due to the procedure of attaching strakes. For example, some of the Spar platforms were built far away from their operation zone. There is always a long distance between the building shipyard and the platform operated region. Thus, the platforms need to be transported by vessels (see Figure 1.8). In this case, compared with transporting a pure cylindrical column, the transportation becomes more sophisticated with the strakes attached around. The contact surface between the platform and the operation vessel was significantly reduced by adding on the strakes. To solve this problem, there is no strake on the contact area between the Spar column and the transportation vessel. These strakes will be added on the Spar platform during the installation process after arriving at the operation area. Thus, the installation time is significantly increased due to the strakes. If VIM can be limited without adding the strakes around the platform, the transportation and installation time can be significantly reduced. This is one of the motivation which driven the present research – to reveal the insights of the fundamental fluid physics in order to better understand VIM. Thus, some benchmarks can be offered to improve the engineering design.

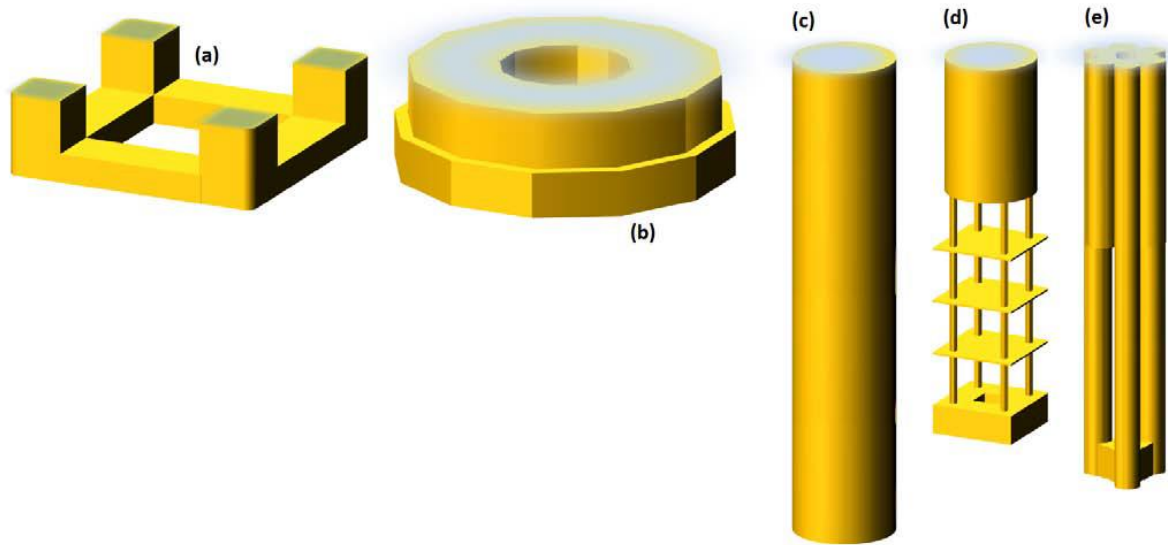


Figure 1.7 Comparison between geometries able to present VIM: (a) semi-submersible, tension-leg platform; (b) mono-column; (c) classic Spar; (d) truss Spar and (e) cell Spar platforms (Fujarra *et al.*, 2012).

Although the concept of Spar platform gives a relatively good solution for the deepwater region development, the small deck area of the Spar platform still limits its operation. In 2002, the concept of deep-draft semi-submersible (DDS) was early introduced by Bindingsbø and Bjørset (2002). This new concept offers a large deck area along with a favourable vertical motion response. Thus, the feasibility of DDS starts to draw a strong attentions among the offshore

technology community. However, the vortex shedding phenomenon becomes more complicated due to the multi-column arrangement, and the VIM responses turn out to be more complex. Thus, there is a strong motivation to understand VIM of a DDS which can offer a benchmark for the practical new engineering design in the demonstration stage, especially for predicting the fatigue life of the mooring system and risers.



Figure 1.8 The Genesis Spar under tow to location (Smith *et al.*, 2004b).

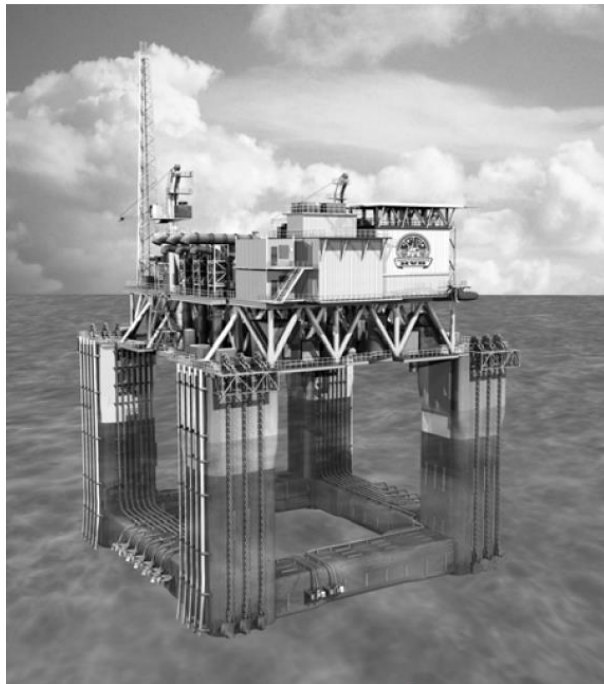


Figure 1.9 Deep Draft Semi® platform (Rijken and Leverette, 2008).

Despite considerable research and development efforts that have been made to date, many issues related to the mechanisms of VIM such as the complex flow patterns of the vortex shedding, the fluctuation forces on the structure and the correlation between the flow patterns

and the fluctuation forces are not fully understood, particularly for the multi-column structures. The present research is aimed to undertake an in-depth study on the fundamental fluid physics and the associated hydrodynamic characteristics on a DDS model in order to better understand VIM.

1.2 Aims & Objectives

As indicated in the above introduction and review of some earlier studies, many important issues on the mechanisms of VIM, particularly for the deep-draft semi-submersible, have to be clarified for consideration in practical design. A better understanding is needed of the complex flow patterns of the vortex shedding, the fluctuation forces on the structure, the VIM trajectory and the correlation among the flow patterns, the fluctuation forces and the VIM trajectory, in particular with regards to the flow interactions with multiple columns arrangements. The present study is intended to reveal some of the fluid physics behind the VIM behaviour by using both experimental and numerical methods. Accordingly, the main objectives of the current research are:

- To develop an advanced CFD model to predict VIM of a typical multiple columns structure.
- To conduct high quality physical experiments to validate the numerical model and provide benchmarks for future studies on VIM.
- To investigate the fluid physics that are related to the development of the VIM phenomenon, e.g. vortex shedding characteristics and the interaction of vortex shedding patterns within and from multiple columns arrangements.
- To predict the dynamics of multi-column structures related to VIM, such as the fluctuations of the hydrodynamic forces and the overall rigid body motion characteristics.
- To demonstrate the correlations among the flow patterns, the fluctuation forces and the VIM trajectory.
- To determine the key members responsible for amplifying and restraining VIM.

1.3 Thesis Outline

Apart from Chapter 1, which is an introduction to the research topic and a statement of the objectives of the present study following with the outlines; Chapter 2 summarises a literature

review of this research area. Chapter 6 presents the conclusions drawn from the current work and suggestions for future studies. The thesis is divided into following three major parts, as shown in Figure 1.10. A list of references is presented at the end of the thesis.

Chapter 3 and Chapter 4 introduce the experimental and numerical methods which were employed in the present study. In Chapter 3, details of the experimental set-up and the test programme are presented. Two series of experiments were performed, one in a towing tank and the other in a circulating water channel in order to investigate the characteristics of both VIM and the vortex shedding processes. In Chapter 4, the numerical models that were developed and employed in the present research are introduced, including the numerical scheme and the computational domain settings. The issues related to the sensitivity study, e.g. mesh sensitivity study (grid dependence) and the time-step study, are examined and followed by a brief pilot validation study.

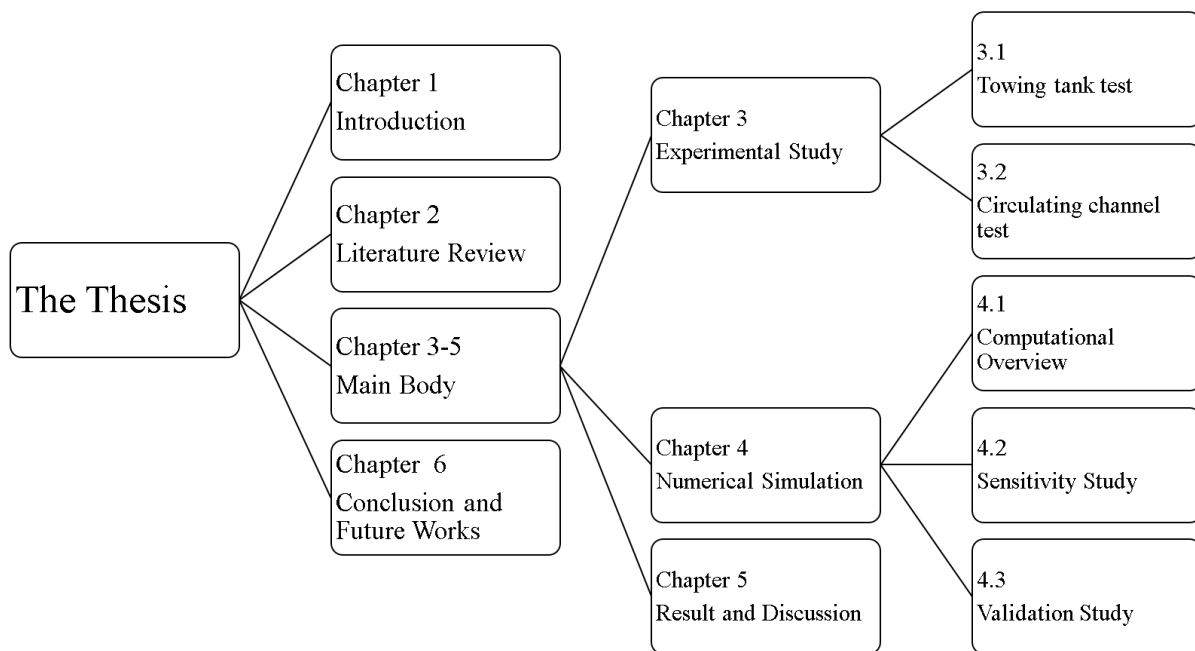


Figure 1.10 Thesis Outline.

Based on the experimental and numerical methods described in Chapter 2 and Chapter 4, Chapter 5 presents the results obtained from both the experimental study and the numerical simulation. The differences between the numerical simulations and the experimental measurements are analysed in detail. This chapter mainly consists of three sub-sections. Each of the sub-sections is focused on one of significant technical aspects of the present research topic:

- 5.1 Experimental and numerical study on VIM of a DDS

In this section, the results of the experimental study of a DDS, which was carried out in the towing tank, are presented with the aim to investigate the VIM effects on the overall hydrodynamics of the structure. In order to study the fluid physics associated with the development of VIM of the DDS, a related numerical simulation was undertaken to examine the characteristics of the vortex shedding processes and their interactions due to the multiple cylindrical columns (Liang *et al.*, 2017; Liu *et al.*, 2017a).

- 5.2 Interaction of vortex shedding processes at 45° angle of incidence

As a continuation to the earlier section, a numerical study on the flow over a DDS for both stationary and VIM conditions was carried out with the aim to investigate the key factors and members responsible for amplifying VIM and the key members conversely for restraining VIM when the most significant VIM occurred (in the present study, the most severe VIM developed at 45° incidence). In addition, the hysteresis phenomenon between the force and motion domains is discussed and explained in the section (Liang and Tao, 2017).

- 5.3 Interaction of vortex shedding processes on the flow around four columns with and without pontoons connected

Following from the outcomes obtained from the earlier section 5.2, the results from both experimental and numerical studies of the flow around four square shaped columns, both with and without pontoons connected, and at a 45° incidence are presented in this section. The effects of adding the pontoons onto the structure are discussed in detail, including discussions of the drag and lift forces on each individual member of the structure as well as on the whole structure and the flow characteristics around the whole structure (Liang *et al.*, 2016).

1.4 Key Parameters

To better understand the phenomenon of VIM, some non-dimensional parameters have been introduced into the present work. In this section, all the key non-dimensional parameters following with the equations are presented to give a general information before starting the main contents of the thesis.

1.4.1 Reduced velocity

When discussing VIM, the so-called reduced velocity (Ur) is normally used as the reference value and is defined as:

$$Ur = \frac{UT_0}{D}, \quad (1.1)$$

where U is the current speed, T_0 is the natural period of the motions in calm water and D is the projected length of the column.

The “lock-in” phenomenon (a resonance phenomenon for oscillation problems) always occurs around $Ur = 7$.

1.4.2 Reynolds number

The Reynolds number (Re) is a key parameter to describe the flow separations. The Reynolds number is defined as:

$$Re = UD/\nu, \quad (1.2)$$

where U is the current velocity, D is the projected width of the column and ν is the kinematic viscosity of the fresh water.

With Reynolds number increasing, the flow characteristics around a cylinder will have different separation phenomena due to the viscous effects. The vortex street behind the cylinder can vary hugely by increasing the Reynolds number. Details of the flow regimes are shown in Figure 1.11.

1.4.3 Froude number

Froude number (Fr) is a dimensionless number defined as the ratio of the flow inertia to the gravity field, which defined as:

$$Fr = U/\sqrt{gD}, \quad (1.3)$$

where U is the current velocity, g is the acceleration of gravity and D is the projected width of the column.





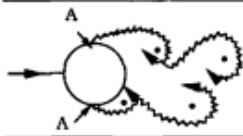
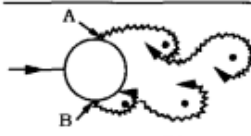
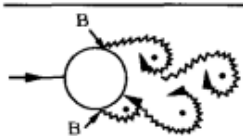


a)		No separation. Creeping flow	$Re < 5$
b)		A fixed pair of symmetric vortices	$5 < Re < 40$
c)		Laminar vortex street	$40 < Re < 200$
d)		Transition to turbulence in the wake	$200 < Re < 300$
e)		Wake completely turbulent. A: Laminar boundary layer separation	$300 < Re < 3 \times 10^5$ Subcritical
f)		A: Laminar boundary layer separation B: Turbulent boundary layer separation; but boundary layer laminar	$3 \times 10^5 < Re < 3.5 \times 10^5$ Critical (Lower transition)
g)		B: Turbulent boundary layer separation; the boundary layer partly laminar partly turbulent	$3.5 \times 10^5 < Re < 1.5 \times 10^6$ Supercritical
h)		C: Boundary layer com- pletely turbulent at one side	$1.5 \times 10^6 < Re < 4 \times 10^6$ Upper transition
i)		C: Boundary layer comple- tely turbulent at two sides	$4 \times 10^6 < Re$ Transcritical

Figure 1.11 Regimes of flow around a smooth, circular cylinder in steady current (Sumer and Fredsøe, 1997).

1.4.4 Force coefficients

The force coefficients (C_D , C_L) are the nominal coefficients describing the drag and lift force on the structure, which are defined as:

$$C_D = \frac{F_D}{\frac{1}{2}\rho U_C^2 A}, \quad (1.4)$$

$$C_L = \frac{F_L}{\frac{1}{2}\rho U_C^2 A}, \quad (1.5)$$

where, F_D is the drag force on the structure, F_L is the lift force on the structure, ρ is the fresh water density, U_C is the free stream velocity, A is the projected area of the immersed structure.

1.4.5 Strouhal number

The Strouhal number (St) is a dimensionless number describing vortex shedding phenomenon, which is given by:

$$St = \frac{fL}{U_c}, \quad (1.6)$$

where f is the vortex shedding frequency that is obtained from the power spectra of lift force coefficient fluctuations as followed by Schewe (1983) and L is the width of the column.

1.4.6 Non-dimensional characteristic amplitude

To describe VIV or VIM oscillation characteristics, the non-dimensional characteristic amplitude (A/L) is chosen as the common variable, which is defined as:

$$A/L = \sqrt{2} \times \sigma \left(\frac{y(t)}{L} \right), \quad (1.7)$$

where σ is the standard deviation of the time series $y(t)/L$, and $y(t)$ represents the time series of in-line, transverse and yaw motions. For yaw motions, the non-dimensional amplitude is defined as $\sqrt{2} \times \sigma(y(t))$.

Chapter 2. Literature Review

Following with the introduction in Chapter 1, Chapter 2 summarizes the previous research related to flow around cylindrical structures and further to the cases of VIV/VIM. Thus, the current research gaps can be identified which drives the present study. The literature review contains summarizations of single cylinder cases, multi-cylinder group cases along with VIV and VIM studies.

2.1.1 *Flow around a single cylinder*

Most of the current floating structures such as Spar platforms, semi-submersibles and tension-leg platforms are single or multiple columns structures. Thus, study of the steady state flow around the columns, is a classical case in the area of offshore engineering. In this research area, the flow around a circular cylinder has been a common predominant benchmark for investigating flow separation.

Thom (1933) performed an early study on the flow past cylinders at low Reynolds numbers. Both numerical simulations and experimental measurements had been undertaken in his work. In the numerical method that was developed by Thom (1933), the hydrodynamics around a cylinder at a Reynolds number equal to 20 were presented, e.g. the streamlines around the cylinder, the pressure distribution and the drag force on the cylinder. A fixed pair of symmetric vortices has been overserved. But this research was still limited at a small Reynolds number within the laminar flow regime which means the vortex shedding phenomenon is dominated by the laminar theory. Additionally, a series of experiments with the Reynolds number varying from 3.5 to 174 was carried out and compared to the numerical predictions. It was noted that the channel walls in the experimental test facility delayed the evolution of eddies to a higher flow speed. The steady wake characteristics as well as the pressure distributions were experimentally measured by Grove *et al.* (1964). Clear pictures which were taken during the experiments showed the wake region behind the cylinder with Reynolds numbers from 25 to 177, which is a considerably larger range than the previous research. Due to the limitations of technology at that time in both measurements and flow pattern observations, most of the research published before 1960s was focused on a relative low Reynolds numbers range. Thus, the flow separation phenomena investigated in those studies were still a laminar state. Bishop and Hassan (1964a) experimentally investigated the drag and lift forces on a stationary cylinder in a water channel for the range of Reynolds numbers 0.36×10^4 to 1.10×10^4 . Based on the

results and observations from the experiments, Bishop and Hassan (1964b) subsequently studied the fluctuating lift and drag forces on an oscillating cylinder in a flowing fluid with the same Reynolds number range as in their earlier study (Bishop and Hassan, 1964a). Different forced oscillation amplitudes and frequencies with various flow velocities were contained in their experiments. This was a very early example of experimental research for an oscillating cylinder condition. It was noted that the cylinder should always be oscillated at the Strouhal frequency. In addition, Bishop and Hassan (1964a) carried out an early study on the three-dimensional, the free surface and the flow channel blockage effects in their work. For the free surface effect, the depth and velocity range of the fluid were chosen to keep the wave resistance negligibly small when the Froude number was less than 0.375. For the blockage ratio effect, it was set at a value of 0.23 in their work. It was found to be fairly applicable for determining the drag coefficient. Bearman (1969) experimentally examined the vortex shedding behaviour from a cylinder over the Reynolds numbers range 10^5 to 7.5×10^5 which had already reached into the critical regime. Narrow-band vortex shedding was observed in their study. The drag coefficient on the cylinder was not directly measured but calculated from the pressure distribution. In the same year, Son and Hanratty (1969) employed electrochemical techniques to measure the velocity gradients adjacent to the surface of a cylinder within the subcritical regime. A sketch of flow patterns was proposed to show the formation and shedding of the vortices (Son and Hanratty, 1969).

In the early 1970s, Dennis and Chang (1970) developed and presented a finite-difference numerical solution for the steady flow around a fixed cylinder. The results obtained from their numerical predictions such as the drag force coefficient and the locations of flow separation points were seen to be generally agreed with previous outcomes as well as with the pressure distributions. However, this finite-difference method can be only applied for calculating laminar phenomena with steady flow in their study. As severe turbulence may disrupt the vortex shedding behaviour, Surry (1972) carried out research about the effects of intense turbulence on the flow over a cylinder. It was revealed that at subcritical Reynolds numbers, intense turbulence does not significantly disrupt the vortex shedding. Subsequently, Szechenyi (1975) performed an experimental study which indicated that increasing the roughness of the cylinder's surface can alter the flow regime to transcritical. Kiya *et al.* (1980) implemented a series of experiments to investigate the effects of shear flow. In the Reynolds numbers range from 43 to 220, they found that the vortex shedding disappeared for sufficiently large shear parameters (describing the level of shear flow). However, when the Reynolds number increased to a range

of 100 to 1000, the Strouhal number of the vortex shedding was increased by increasing the shear parameter to a value beyond about 0.1.

After numerous studies concerning the flow past a cylinder, Cantwell and Coles (1983) summarized the earlier results on the flow past a single smooth cylinder in their study and further performed a test in a wind tunnel at a Reynolds number 1.4×10^5 . By employing the X-array hot-probes into the experimental measurement, the velocity field and global mean Reynolds shear stress were detailed and presented to show the near wake flow characteristics. The understanding of the downstream wake region was significantly improved. However, the relationship between the fluid induced forces and the flow patterns was still lack of understanding due to the limitation of technology. At this stage, Williamson (1988) defined the Strouhal-Reynolds number relationship within the Reynolds number range $49 \sim 178$. Since the late 1980s, Norberg (1987) has carried out several studies on the flow past a cylinder, including such as the influences of Reynolds number and freestream turbulence (Norberg, 1987) and the effects of aspect ratio (Norberg, 1994). Norberg (2003) subsequently made an extensive review about the classical problem of a cylinder in cross flow.

During this time period, Williamson (1996) also published a detailed review focusing on the vortex dynamics in the wake region, including the results from the last 20 years of studies of flow past circular section cylinders. The very near wake region velocity field has been demonstrated by Ong and Wallace (1996) at a Reynolds number of 3,900 in a wind tunnel. In the same year, the instabilities developing in the three-dimensional flow around an infinite cylinder have been numerically investigated by Thompson *et al.* (1996), indicated that fully resolved two-dimensional simulations do not produce accurate pressure distributions for flows once they become three-dimensional. Before that time, most of the numerical studies were based on the two-dimensional calculation as the two-dimensional simulation can save numerous calculation resources. However, the three-dimensional simulation is considered to be more accurate when the turbulence appeared. After the 1990s, large eddy simulation (LES) and direct numerical simulation (DNS) methods were being more and more employed by the researchers as an ever-increasing computational capability became available. The influences of large eddy simulation have been studied by Breuer (1998). Compared with earlier two-dimensional and three-dimensional simulations, the spanwise resolution had an important role in this work which was usually ignored in the earlier studies. Tutar and Holdo (2000) used the large eddy simulation method to investigate a forced oscillating cylinder in a uniform flow. In their work, the three-dimensional simulation revealed that the root-mean-square pressures and the drag

coefficient are seen to be smaller than those given by the two-dimensional simulation results. Conversely, the Strouhal number as computed by three-dimensional simulation was seen to be larger than those given by the two-dimensional results indicating the importance of the three-dimensional simulation.

In 2005, Dong and Karniadakis (2005) numerically studied both stationary and oscillating cylinders at a Reynolds number of 1×10^4 . Direct numerical simulation method was used in their study. The Navier-Stokes equations are solved without any turbulence models in the direct numerical simulation. The results from the direct numerical simulation can produce the flow characteristics in detail offering a benchmark to other numerical simulations with turbulence models added in. However, the DNS method is extremely time-consuming. In their study, the stationary cylinder results well matched those from the previous experimental investigations. For the forced oscillating simulations, different oscillating frequencies were studied in their work with the aim to investigate the overall hydrodynamics around the cylinder. While investigating the stationary cylinder in a cross flow, many researchers tended to also keep studying the problem of an oscillating cylinder in a cross flow. According to some of the outcomes as mentioned above, Sarpkaya (2004) presented an extensive review which summarized the various studies about the forced vibrations of a cylinder in a cross flow as well as cases of vortex-induced vibrations.

After approximately a hundred years of study on this classical case, the flow over a single cylinder is now much better understood. It is noted that the majority of studies of flow separation around cylinders are based on an infinite length cylinder assumption. It has also attracted considerable attention for the study of cross-flow past a cylinder with a free end, which is more close to many real world applications such as offshore structures (e.g. Spar platform, semi-submersible platform and tension-leg platform) and towers. Sumner (2013) well documented the available literature about the flow above the free end cylinder. In his review, a great deal of research work including 52 papers was summarized.

In the field of offshore engineering, many columns are made as a square-section with rounded corners instead of a circular-section, especially for the multi-column platform concept. Thus, due to their importance in offshore engineering applications, flow around a square-section column has been widely studied in recent years. As a sharp corner cylinder, the flow separation point is fixed at the leading corner of the cross-section (Sumer and Fredsøe, 1997; Tian *et al.*, 2013). However, when the corner was rounded, the separation point is varying in its position

within the rounded area region. Delany and Sorensen (1953) experimentally studied the effects of different corner shapes on the drag force of cylinder based on a Reynolds number range of $1 \times 10^5 \sim 2 \times 10^5$ as an early stage study. The drag coefficient of a square-section cylinder can be significantly reduced by rounding the corners of the cylinder (Delany and Sorensen, 1953; Bearman *et al.*, 1984). Bearman *et al.* (1984) extended the work of Delany and Sorensen (1953). Their experiments were carried out in a U-tube water tunnel and with different corner ratio effects on both square and diamond section cylinders. However, only drag and inertia coefficients were measured respectively, the lift coefficient was not shown in their study.

Rigorous studies into the corner shapes of a basically square cylinder were numerically and experimentally demonstrated by Tamura *et al.* (1998) and Tamura and Miyagi (1999). Tamura *et al.* (1998) numerically computed the unsteady pressure on a square cylinder with different corner shapes at a Reynolds number of 10^4 . It was observed that the drag force may decrease to around 60% of the original sharp corner drag value with an appropriate corner shape. Tamura and Miyagi (1999) then continued their research about the corner shape effects in a wind tunnel. In their work, it was found that either chamfered or rounded corners designs can decrease the drag force on the cylinder as a result of changing wake width. However, their studies only covered the flow incidences from -5 degree to 30 degree. Recently, Zhao *et al.* (2014) carried out an experimental study to illustrate the fluid-structure interactions of an elastically mounted square cylinder in a free stream at different angles of incidence. The related vorticity fields together with the corresponded fluctuation forces as well as the motion trajectories are presented. The correlations among the flow patterns, the fluctuating hydrodynamic forces and the motion trajectories are well demonstrated, which has thus served as a good benchmark of the flow-induced vibrations study on a single square cylinder as well as the studies on a multiple cylinder group.

2.1.2 Flow around a multiple cylinder group

By adding on a neighbouring cylinder, the wake region of the cylinders can be significantly altered. Two cylinders in various arrangements, e.g. side-by-side, tandem, staggered and so on, have received considerable research attention over the last 20 years as being the first attempt for investigating the flow around multiple cylinder combinations. As reviewed by Sumner *et al.* (2000), in which about 150 papers were documented, this topic has become much better understood. The work by Inoue *et al.* (2006) illustrated five different flow patterns

corresponding to the space ratios by numerically simulating flow over two square cylinders in a tandem arrangement at a Reynolds number of 150.

It is noted that an arrangement of a larger number of cylinders at a relatively high Reynolds number still has not been studied in detail. By adding on more cylinders into the configuration, more complicated flow interactions will be generated and observed. In a recent review made by Khalifa *et al.* (2012), the research progresses on this topic are quite limited, especially for four cylinders in a square configuration which is considered as being a benchmark study in offshore floating structures. The first investigation on the flow around four cylinders in a square arrangement was carried out by Sayers (1988). The force coefficients and vortex shedding frequency were measured with different pitch ratios and flow incidences (Sayers, 1988; Sayers, 1990). Most of the research work on the flow interactions among the four cylinders was done by Lam and his co-authors over the last two decades (Lam and Lo, 1992; Lam and Fang, 1995; Lam *et al.*, 2003a; Lam *et al.*, 2003b; Lam *et al.*, 2008; Lam and Zou, 2010). The present understanding of the fluid mechanism on the multiple cylinder interactions is mainly based on their long-term investigation efforts. Lam and Lo (1992) performed initial experiments to investigate the flow patterns and the corresponding Strouhal number of a four cylinders group firstly. Then Lam and Fang (1995) carried out an experiment in an open circuit wind tunnel. In their work, the pressure distributions and force coefficients on each of the cylinders were measured to then discuss the effects of four incidences and on 15 spacing ratios. Following these studies, a water tunnel experiment at a Reynolds number of 200 was conducted by Lam *et al.* (2003a). The particle image velocimetry (PIV) technique was employed in their study, which can measure the velocity profiles as well as the flow patterns during the experiments. The force coefficients and vortex shedding frequencies were measured in a wind tunnel experiment that was performed by Lam *et al.* (2003b). The downstream cylinders were observed to be always subjected to a more serious lift force problem and experienced less drag forces than for the upstream cylinders (Lam *et al.*, 2003b). Lam *et al.* (2008) also used a numerical routine to simulate the cross-flow around four cylinders oriented in an in-line arrangement. The spacing ratio effects were further studied in detail by Lam and Zou (2010) at a Reynolds number of 200. Other researchers, such as Zou *et al.* (2008), Zhao and Cheng (2012) and Wang *et al.* (2013) also made their own contributions on the study of a cross-flow around four cylinders. Especially, Wang *et al.* (2013) carried out an experiment in an open water tunnel focusing on the vortex shedding patterns in the wake region of four cylinders. The spacing ratio and flow incidence effects on the vortex shedding patterns were illustrated. Good correlation between the flow patterns and the fluctuation forces was demonstrated in their study. It is noted

that all the studies listed above are focused on the multiple circular cylinders. For studying flow around multiple square-section shape cylinders similar as the present work, there is still lack of understanding on the fluid dynamics and fluid physics behind it.

2.1.3 *Vortex-induced vibrations*

Vortex-induced vibrations (VIV) have been investigated along with the research of flow around stationary cylinders as mentioned in the sections above. When a flow past a bluff body, such as a circular cylinder, it will result in the periodic shedding of vortices into the body's wake region. This process gives rise to fluctuating lift and drag forces which can result in vortex-induced vibrations (VIV). VIV occur in many engineering disciplines such as oil & gas (mooring and riser system, drilling facilities, pipeline laying and platforms), mechanical engineering (heat exchangers), wind energy (wind turbine piles and harvesting wind via VIV), civil engineering (bridges and towers), and nuclear energy (control rods).

Many progresses on the investigations of VIV have been made in the past decades, both experimentally and numerically, towards the understating of VIV. Most of the VIV research focuses on the rigid body motions, especially in the low-Reynolds number regimes. Thus, there is a strong motivation to increase the investigation Reynolds number region to present unsteady flow characteristics closed to the real engineering application. Based on the extensive review which summarized by Sarpkaya (2004), the critical elements of the evolution of the ideas, theoretical insights, experimental methods, and numerical models are traced systematically; the strengths and weaknesses of the current state of the understanding of the complex fluid-structure interaction are discussed in some details. The current challenges of studying VIV are mainly multiple cylinders interactions and high Reynolds number effects.

2.1.4 *Vortex-induced motions on single and multiple cylindrical offshore structures*

VIM is a specific VIV phenomenon happening on a large floating rigid structure without self-deformation. VIM have often been observed since the Genesis Spar platform (see Figure 1.8) was commissioned in 1997 (Kokkinis *et al.*, 2004; Fajarra *et al.*, 2012). Rijken and Leverette (2009) reported the VIM phenomenon on a deep-draft semi-submersible as well in field measurements. Ma *et al.* (2013) also observed the presence of VIM on a column stabilized floater with a chain-polyester-chain mooring system in deepwater from recent field measurements. VIM is a low frequency motion which significantly affects the fatigue life of

the mooring and riser system. There is no observation about the operation failure due to VIM. However, understanding VIM is very important for designing the practical platform especially for estimating the fatigue life of the mooring and riser system. In this aspect, a number of researches on the VIM behaviour have been carried out, including both experimental and numerical studies. As pointed out by Fajarra *et al.* (2012) in their comprehensive review, the VIM behaviour is now much better understood in engineering aspect.

After the Genesis Spar platform operated in the Gulf of Mexico, the existence of VIM on Spar platforms has been confirmed from field measurements. Thus, an increasing number of VIM studies on single column structures, such as the Spar platform (different kinds of Spar platforms are shown in Figure 2.1) or the mono-column platform, have been carried out. Finn *et al.* (2003) and van Dijk *et al.* (2003b) investigated VIM effects on the cell and truss Spar platforms. To reduce the VIM amplitude of the platform, helical strakes attached to the hull were examined as an acceptable design approach in order to minimize the VIM phenomenon. However, the helical strakes make the installation process of the Spar platform becomes very complicated. In 2003, a new concept of a Spar platform named the Holstein Truss Spar (as shown in Figure 2.1) was constructed for installation in the Gulf of Mexico. A model test for possible VIM on this new concept was demonstrated in MARIN by van Dijk *et al.* (2003a). The VIM response under different current velocities and incidences was experimentally investigated. It demonstrated that the strakes added on the Spar can significantly reduce the VIM amplitude. The results also revealed that the reliability of the model test on predicting the VIM response of the prototype was adequate. In the same year, Magee *et al.* (2003) performed a study on the prediction of the loads on the mooring system during the VIM development process. Thereafter, Perryman *et al.* (2005) elaborated on the Holstein Truss Spar project and provided insight of the challenges to be faced in order to avoid those problems in the future, such as to provide a guideline on how to control and reduce the platform's VIM. At this stage, the research on VIM was limited on the analysis of motion amplitude and trajectory. The hydrodynamic loads on the platform were rarely studied in the early stage of investigating VIM.

After several Spar platforms commissioned, Kokkinis *et al.* (2004) and Smith *et al.* (2004a) investigated the VIM effects based on the Genesis Spar platform experience and the associated field measurements. In the same year, Yung *et al.* (2004) documented the research that had been undertaken about VIM on the Hoover Spar platform. The hydrodynamics, the so-called “lock-in” phenomenon, turbulence and both single and multiple degrees of freedom were each presented in detail in their research. The drag force coefficients obtained from the model test

were compared with the field data in detail. In addition, the lift coefficient was demonstrated in their study. This is a very early study about the hydrodynamics on the platform related to VIM. However, due to the limitation of technology, the flow characteristics around the platforms during VIM were rarely investigated at that time. Based on field data obtained from three operational Spar platforms (Genesis, Hoover and Holstein), VIM on the Spar platform are now much better understood in engineering aspect, especially for the prediction of the VIM amplitude. During the last 15 years, several experiments on the Spar VIM have been carried out to mitigate the occurrence of VIM, such as Irani and Finn (2004), Halkyard *et al.* (2005) and Wang *et al.* (2009). Irani and Finn (2004) produced a guideline for obtaining VIM predictions by the experimental method. Based on model tests on three different types of Spar platforms, the advantages and disadvantages of employing different tanks or basins were compared in detail. The field measurements on VIM of the Horn Mountain Truss Spar contributed to improve the confidence in the model test predictions. It was demonstrated that model test results were quite similar to the field measurements (Irani *et al.*, 2008). Thus, the model test results can serve some benchmarks to the practical design even there is a significant Reynolds number gap between the prototype (in the order of 10^7) and the model (in the order of 10^4 to 10^5). In the meantime, another single column floating concept has been developed named as mono-column platform. Compared with the Spar platform, the mono-column platform has a relatively shallow draft and a large deck area. Based on the work carried out by Gonçalves *et al.* (2009), the presence of VIM on the mono-column design was observed in towing tank model tests. Thus, the presence of VIM was confirmed on a floating structure with a relatively shallow draft. After studying VIM on a single column structure, Gonçalves *et al.* (2011) summarised the experimental comparisons about the similarity between VIM and VIV, the oscillation curves were seen to show a good agreement in both trends and values. Thus, some of the analysis methods which have been used for predicting VIV can be partly adopted in a study of VIM now, such as the “lock-in”, fluid forces and added mass analysis etc.

Although predicting the VIM amplitude and trajectory by experiments is a kind of successful technique, the fluid physics behind VIM are still lack of understanding. During the experiments, the flow patterns around the structure are extremely hard to record in detail due to the limitation of technology (disturbances from the devices, measurement area etc.). However, the computational fluid dynamics (CFD) offers a good solution for showing the clearly flow patterns around the structure.

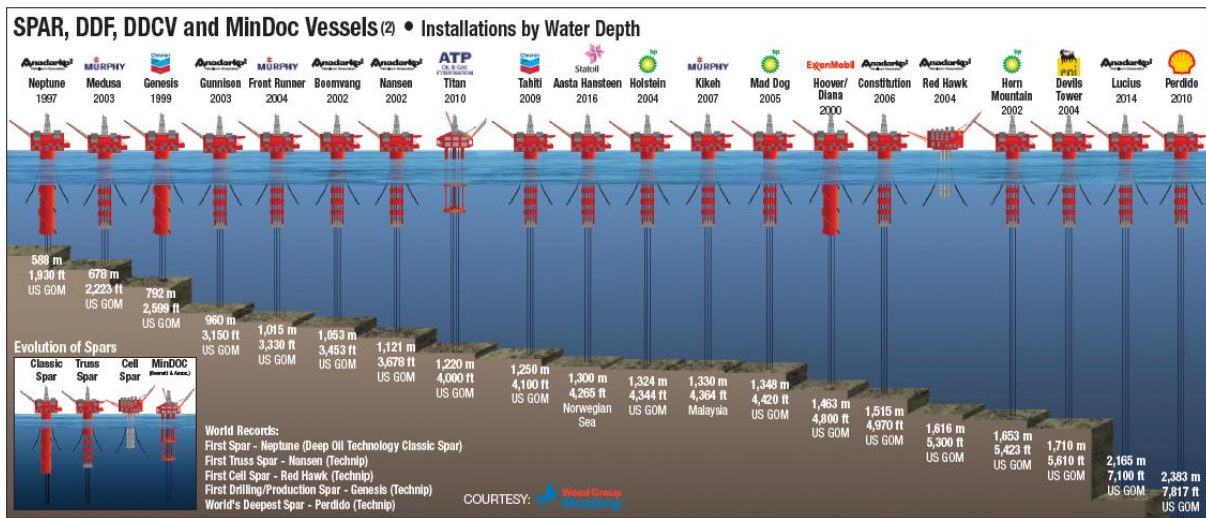


Figure 2.1 Progression of Spar deepwater development systems (Christopher and Chad, 2012).

Thus, the CFD prediction methodology for use in forecasting VIM has drawn a considerable attention since 2005. Oakley *et al.* (2005) using the method numerically studied the Genesis Spar under both uniform and shear current profiles and proposed a few suggestions on both the model tests and the corresponding numerical predictions. Additionally, they used the detached eddy simulation (DES) method to predict the prototype VIM behaviour. Halkyard *et al.* (2005) combined the results from the experimental and numerical studies to compare the VIM effects on a Spar from both the experimental measurements and CFD predictions. These studies served as an early benchmark case for the VIM predictions on a Spar platform, especially confirmed the feasibility of using CFD on the VIM prediction. Thiagarajan *et al.* (2005) further investigated both a bare cylinder and a cylinder with strakes to study comparative aspects of the VIM phenomenon. Holmes (2008) also made some suggestions on predicting VIM by using a CFD package. CFD simulations can now capture many of the important Spar VIM features as well as the experiments do. However, challenges still exist, such as running simulation at an extreme high Reynolds number range indicated the real operational conditions, predicting details of the flow characteristics during VIM as well as the correlations among the flow patterns, the hydrodynamic loads and the VIM trajectory. Recently, Lefevre *et al.* (2013) proposed a guideline for the numerical simulation of VIM on the Spar platform including its mooring systems, convergence studies and turbulence models which served as a good benchmark for the VIM prediction of a single cylindrical column by CFD.

Although VIM on Spar platforms are now much better understood and well documented, there is still lack of understanding about the VIM mechanisms on multiple cylindrical structures such

as the semi-submersible and tension-leg platform (TLP). The vortex shedding processes and subsequent VIM are much more complex due to these complex multi-body structural configurations than those of single cylindrical structures, such as the multi-column, pontoons and their complex interactions of the vortex shedding processes. Thus, the present study is aiming to focus on investigating these aspects of VIM on multiple cylindrical structures.

The concept of the deep-draft semi-submersible (DDS) configuration (also can be seen in Figure 1.9) was early introduced by Bindingsbo and Bjørset (2002). Deep-draft floating structures have gained popularity as they exhibit a favourable vertical motion response owing to the gravity centre of the deep-draft floaters being lower than that of the traditional floating structures. When the draft of a platform is increased, for example from 21 m to 40 m, the structure's heave motion is reduced significantly (Bindingsbo and Bjørset, 2002). However, with the increasing immersed part of the floater, VIM can become more severe. Rijken *et al.* (2004) later discussed the VIM of a semi-submersible with four square-section columns as an early documented example of VIM on the multiple cylindrical structures.

Waals *et al.* (2007) conducted several VIM tests on conventional semi-submersibles, deep-draft semi-submersibles and TLPs to examine the influences of the mass ratio and draft effects as well as the pontoons effects. This was an experimental study on the deep-draft floating structures. It was revealed that the nominal transverse VIM response was altered significantly by increasing the draft of the structure. Additionally, an oscillation phenomenon conventionally named as galloping was observed at a higher reduced velocity in their study, and is different from VIM. It describes a low frequency response and it is not self-limiting. When galloping occurs, the vortex shedding frequency of the floating structure is much larger than that of the structural response frequency. However, due to the experiments were implemented in a towing tank, only motion responses and drag force on the platform were recorded during the tests. A series of model tests on the global motions of a DDS were carried out by Hong *et al.* (2008) in a basin. The wind and wave effects were considered in their experiments as well as the effects of the current. The outcomes showed that the VIM phenomena depend not only on the current, but also on the waves. If the waves were strong enough, VIM may not be observed in the experiment (Hong *et al.*, 2008). In addition, both drag and lift forces on the platform were recorded during the experiment. The investigations of hydrodynamic forces on the platform offered a pilot study of the fluctuation forces on a multiple cylindrical structure. At the early stage of the experimental investigations on VIM of multiple cylindrical structures, due to the limitation of the technology, the flow patterns around the platform cannot be recorded at that

time. Thus, there is still lack of understanding on the basic of fluid physics behind VIM of multiple cylindrical structures. Rijken and Leverette (2008) experimentally studied the VIM responses of a DDS, and observed that wave and external damping can affect the VIM responses. Through their tests, it was noted that relatively low sea states do not particularly influence the VIM responses within the so-called “lock-in” region. Moreover, the additional damping delayed the onset of VIM to a higher reduced velocity. In their study, by applying the dye tracing method, the wake forming behind the structure was presented. This is a very early study on the flow visualization of semi-submersibles’ VIM. Pictures of vortices forming behind the structure were taken during the tests. Thus, the flow characteristics can be brief analysed to reveal some insights of fluid physics.

In 2009, a set of well documented field measurements of VIM on DDS was published by Rijken and Leverette (2009) and this served as a benchmark for the VIM study at that time. Rijken *et al.* (2011) subsequently analysed the influences of SCR systems and appurtenances on the development of VIM for a DDS. Their work showed that the appurtenances on the vertical faces of the columns and above the pontoons can alter the VIM responses. Magee *et al.* (2011) also performed a series of towing tank tests on the development of VIM of a TLP, and their experimental results may serve as a suitable benchmark for future three-dimensional numerical studies. If numerical method such as CFD can be applied to simulate VIM on multi-column structures, more details of flow characteristics can be obtained by analysing the numerical results. Thus, the fundamental of fluid physics related to VIM can be better understood. The numerical investigations on VIM of multi-column structures will be introduced in the following paragraph. Xu *et al.* (2012) suggested a HVS (Heave and VIM Suppressed) design which features a blister that is attached to each column to reduce the VIM by breaking the vortex shedding process from each column. Gonçalves *et al.* (2012) subsequently investigated the effects of both the current angle and appendages on a conventional semi-submersible. The presence of VIM on a conventional semi-submersible has been confirmed in their works. Following on from the initial outcomes, Gonçalves *et al.* (2013) further studied other relevant factors such as the draft conditions, the external damping and the wave effects on the development of VIM by performing a series of towing tank tests. Their study indicated that the VIM amplitudes decrease by increasing level of the overall damping. However, the scale ratio in their studies was limited at a very high level where a scaled ratio of 1:100 had been applied. A larger model with a low scaled ratio (1:50 to 1:70) may produce a relatively reliable result which is more close to the field measurement. A field observation which was carried out by Ma *et al.* (2013) indicated that the VIM phenomena in the real ocean environment shows very large

differences between the field measurements and design predictions. Due to the limited field data, they suggested to combine field data with both model tests and CFD predictions to have a more general understanding of VIM. Tan *et al.* (2014) experimentally and numerically investigated the appurtenances effects on VIM of a TLP. Their studies indicated that the numerical predictions show a good agreement compared with the experimental results. However, the model which was investigated in their study is quite specific. Unlike most of the traditional design, only two corner edges in diagonal direction of each column are rounded. Additionally, Gonçalves *et al.* (2015) performed experimental tests focusing on the effects of different column designs (i.e. sectional shapes) on the VIM responses. Their results showed that the circular section shaped column design has the most severe transverse motions developing at 0 degree flow incidence and that the square-section shaped column design has the most significant transverse motions developing at 45 degree flow incidence. However, only motion amplitudes were discussed in their study. Irani *et al.* (2015) demonstrated that damping can have a significant effect on VIM. The damping differences resulting from the mooring and riser systems as observed between model tests and field observations can in many ways explain why the VIM responses as measured in the model tests are found to be varied when compared with the actual field measurement. Recently, Antony *et al.* (2016) studied the effects of damping on VIM and investigated the force distribution on each member of the structure in detail by an experimental routine. The work done by each member in influencing the overall behaviour was presented in their investigations. The investigations showed that for a 45 degree flow incidence, which is when the maximum transverse VIM response occurs, and the three upstream columns excited VIM. The horizontal members - pontoons, however, were noted to limit the VIM responses. This is a very early article focusing on the hydrodynamic loads on each member of a DDS. The hydrodynamic loads were presented as a format of work done by each member. The drag and lift forces on each member were still out of their investigations, where this is one of the key study in the present research. To date, there is still no experimental investigation on the flow patterns in detail around a DDS. The present research is trying to carry out some pilot studies on experimental investigations of the flow visualizations around a stationary DDS to offer some benchmarks to future studies.

Unlike the experimental routine, during the last decade, the continued technological advances offer an ever-increasing computational power, resulting in CFD methods rapidly gaining in popularity for VIM predictions. By employing the CFD method, more flow characteristics without the limitation of experimental set-up can be obtained. The correlations among the flow patterns, the fluctuation forces and the VIM trajectory can be observed with a relatively easy

routine. Tan *et al.* (2013) performed a series of CFD simulations for investigating VIM on a multi-column floater. Lee *et al.* (2014) studied the differences between the prototype and model VIM responses by undertaking numerical predictions. The results revealed that the difference of Reynolds numbers between the model scale and the prototype can slightly reduce the transverse VIM response in the “lock-in” region. However, their study was only focused on the inlet current with a 45 degree incidence. Antony *et al.* (2015) numerically and experimentally investigated the VIM responses of a deep-draft column stabilized floater. Their work showed that the damping effects of the riser and mooring systems are very important in CFD simulations. In addition, the CFD predictions may have larger difference between amplitude predictions in model vs. full scale, especially for some specific geometries such as a paired column semi-submersible (PC semi). The work of Vinayan *et al.* (2015) increased the level of confidence for undertaking CFD simulations on the VIM predictions of a deep-draft column stabilized floater through a series of numerical simulations on a PC semi with different drafts and arrangements. Liu *et al.* (2015) numerically investigated the effects of pontoons on the hydrodynamic forces for a stationary DDS model and revealed that the DDS with the different numbers of pontoons affects both the drag and lift forces on the stationary structures. Unlike the approaches of other researchers, Fontoura *et al.* (2015) used a wake oscillator model to predict VIM which offered an alternative numerical way to simulate VIM. However, the VIM low order model sub-estimated only in approximately 50% of the experimental results which is far away from the accuracy offered by the CFD method. Kim *et al.* (2015) conducted a rigorous numerical study on the prediction of VIM for a PC-semi for comparison with their experimental results. The turbulence model and the level of mesh refinement were both discussed in their work. Koop *et al.* (2016) carried out a series of CFD studies to illustrate the results of the scale and damping effects for VIM on a semi-submersible. Their work showed that the scale effects at 45 degree incidence were less than that at 0 degree incidence. Under 45 degree incidence, the VIM response at the prototype Reynolds number was found to be similar when compared with that at the model scale Reynolds number. Similar observation was also reported by Lee *et al.* (2014). The results from both the earlier studies and the outcomes from the present study are summarised in Table 2.1.

It is noted that after 20 years of studying about the VIM, the state-of-art research is still lack of understandings on the basic fluid physics, especially the correlations among the flow patterns, the fluctuation forces and the VIM trajectory. Thus, this is one of the key parts in the present work.

Table 2.1 Summary of the various studies on VIM of the multiple square-section columns structures.

	λ	H/L	Ur	$\max A_y/L$ at 0°	$\max A_y/L$ at 45°
Waals <i>et al.</i> (2007)	1:70	1.75	4.0~40.0	--	0.320
Rijken and Leverette (2008)	1:50	2.18	1.0~15.0	0.151	0.468
Magee <i>et al.</i> (2011)	1:70	1.50	4.0~13.0	0.269	0.319
Tahar and Finn (2011)	1:56	1.74	2.0~15.0	--	0.330
Gonalves <i>et al.</i> (2012)	1:100	1.14	2.5~20.0	0.268	0.382
Ma <i>et al.</i> (2013)	1:1	--	3.2~13.7	0.163	0.218
Lee <i>et al.</i> (2014)	1:67	1.78	4.0~20.0	--	0.393
Lee <i>et al.</i> (2014)	1:1	1.78	4.0~20.0	--	0.344
Koop <i>et al.</i> (2016)	1:54	--	3.0~10.0	--	0.470
Present work	1:64	1.90	3.4~14.1	0.279	0.742

Chapter 3. Experimental Study

To investigate the correlation among vortex shedding processes, fluid forces on the structure and the motion response of VIM, two comprehensive sets of experimental studies were conducted in a towing tank and a circulating water channel respectively. The towing tank test based on the Froude scaling law was designed to focus on the motion-coupled VIM analysis which can offer a benchmark to the practical engineering design. The circulating channel test was focused on the hydrodynamics around stationary multi-column structures based on Reynolds scaling law. The models tested in the circulating channel have a same Reynolds number range as the towing tank test. The flow patterns were recorded to reveal some insights of fluid physics behind the vortex shedding phenomenon. These two sets of experiments also serve as a benchmark validation for the present numerical study. Details of the experiments are presented in this chapter.

3.1 Towing Tank Tests

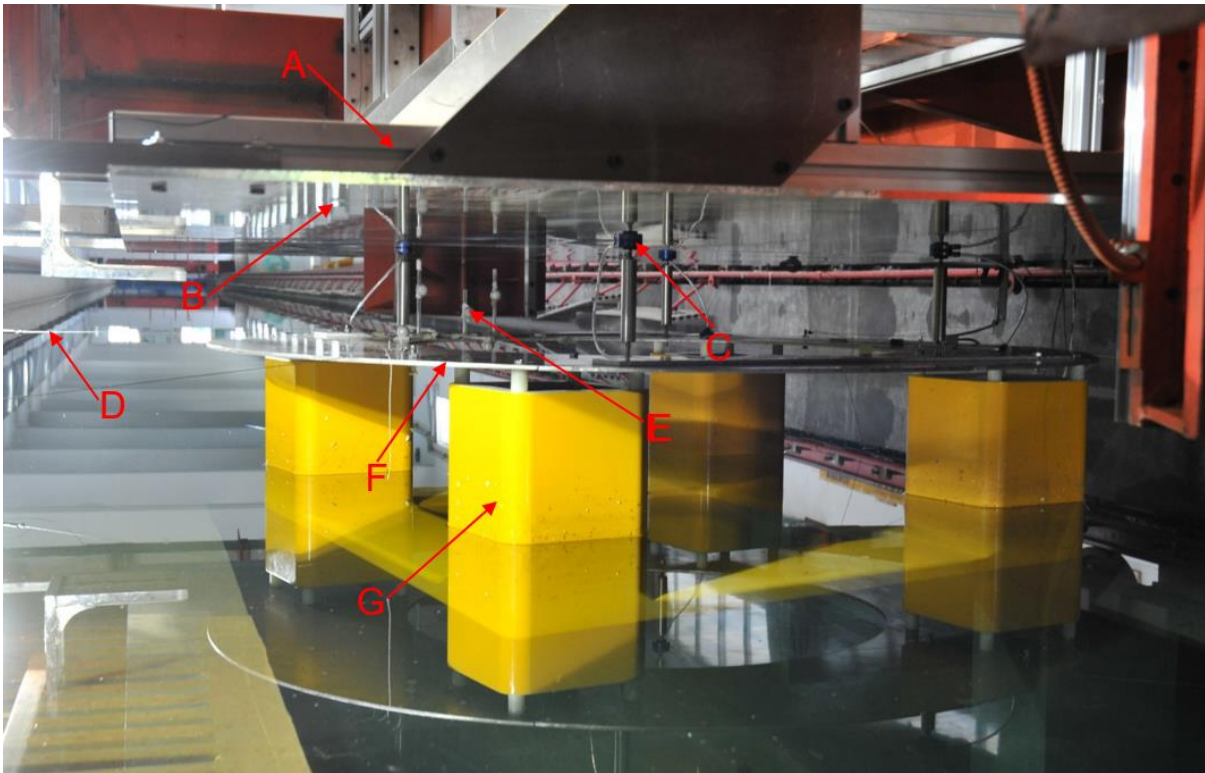
An experimental study on VIM of a representative DDS was carried out in a towing tank, with the aim to investigate the VIM effects on the overall hydrodynamics of the structure. Experimental measurements were obtained for horizontal plane motions including transverse, in-line and yaw motions as well as the drag and lift forces on the structure. Spectral analysis was further carried out based on the recorded force time history (Liang *et al.*, 2017). This section presents the experiment set-up and the model characteristics. Full Details of the test matrix are given in Appendix A.

3.1.1 Experimental set-up

The experimental set-up was characterized by the DDS model being supported above the waterline by four low friction air bearings and with a set of equivalent horizontal mooring springs in the Zhejiang Ocean University towing tank (see Figure 3.1) with dimensions of $130 \times 6 \times 3$ m (length \times width \times depth). The DDS model and the experimental set-up in the towing tank are shown in Figure 3.2 and Figure 3.3. The present towing tank test adopts a state-of-art technique – the air bearings system which can eliminate the vertical motions and allow the free horizontal plane motions.



Figure 3.1 Zhejiang Ocean University towing tank.



- A) Adjustable support structure
- B) Smooth horizontal table
- C) Low friction air bearing
- D) Horizontal spring with load cell
- E) Locomotion measure device with 6 degree of freedom
- F) Top frame
- G) DDS model in scale ratio $\lambda = 1 : 64$

Figure 3.2 Experimental set-up in the towing tank.

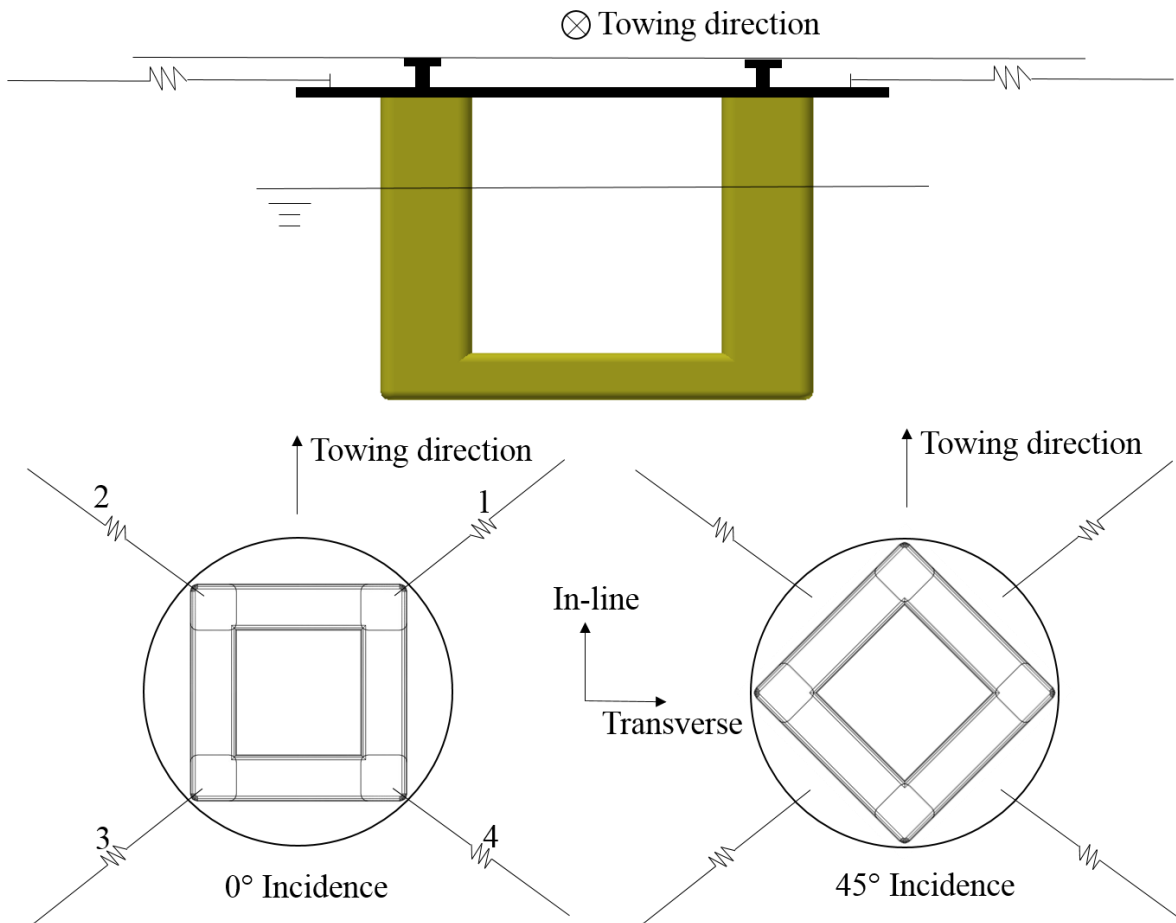


Figure 3.3 Schematic of the experimental set-up.

3.1.2 Model characteristics

Table 3.1 Main characteristics of the DDS unit.

	Unit	Prototype	Model
Distance between centre columns (S)	m	72.5	1.133
Column width (L)	m	19.5	0.305
Immersed column height above the pontoon (H)	m	37.0	0.578
Pontoon height (P)	m	10.0	0.156
Corner radius for the column	m	3.0	0.047
Corner radius for the pontoon	m	2.0	0.031
Displacement (Δ)	kg	1.03×10^8	382
Z moment of inertia (I)	kg·m ²	2.29×10^{11}	208

The model was designed based on a DDS concept. It is important to keep the similarity between the prototype and the model. Thus, the Froude scaling approach as recommended by van Dijk *et al.* (2003a) was used. It is essential to note that the Reynolds number ($Re = UD/\nu$, where U is the current velocity, D is the projected width of the column and ν is the kinematic viscosity of the fresh water) for the prototype DDS is in the order of 10^7 while the Reynolds number at model scale is significantly lower. Since the DDS model is a relatively bluff body, the flow is expected to separate at the corners of the columns. Additionally, the vortex shedding phenomenon is mostly independent of the Reynolds number from the transcritical region to the subcritical region for a square cross section column (Sumer and Fredsøe, 1997). It is also noted that the scale effects for square-section shaped structure are less than those for circular-section shaped structures (Fujarra *et al.*, 2012). The main characteristics of the DDS model are shown in Table 3.1 with the dimensions defined in Figure 3.4.

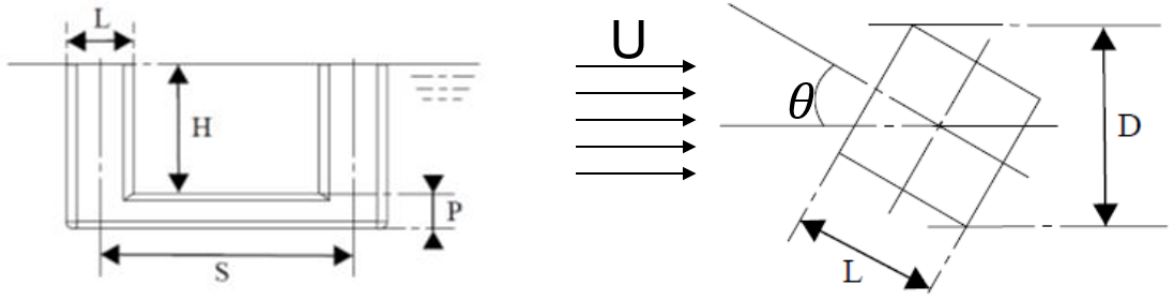


Figure 3.4 Characteristic dimensions of the DDS.

3.1.3 Test arrangement of mooring system

Four horizontal mooring lines with load cells were attached at the top frame to restrain the horizontal motions of the DDS model. An additional set of four low friction air bearings were developed in order to eliminate the vertical motions of the DDS model. Thus, only three degrees of freedom motions in the horizontal plane (namely transverse, in-line and yaw) were allowed during the test. The horizontal mooring system consists of four horizontal lines with soft springs being employed to provide the horizontal restoring force for the model and match the natural periods in the horizontal plane motions. The mooring lines were set above the water level to avoid disturbing the vortex shedding process. Each mooring line with a load cell (with a capability measurement range of 100 N) was attached to an anchor post on the carriage at one end and to the top deck of the model at the other end. The top deck featuring studs were arranged circumferentially with 15° spacing interval (see Figure 3.5). Thus, when the current incidences

need to be changed, the model with the top deck can be rotated accordingly and the horizontal lines are attached to the appropriate studs, allowing the same mooring configuration for the two different current incidence angles to be tested. Therefore, the mooring stiffness was kept the same for the two current incidences, aiming to facilitate results comparison (Liu *et al.*, 2017b). The relaxation length of each mooring line is 1.77 m and the stiffness of the mooring line is 30 N/m. A pre-tension force of 6.9 N was added on each mooring line. Thus, the horizontal stiffness at the transverse and in-line directions is 66.5 N/m.

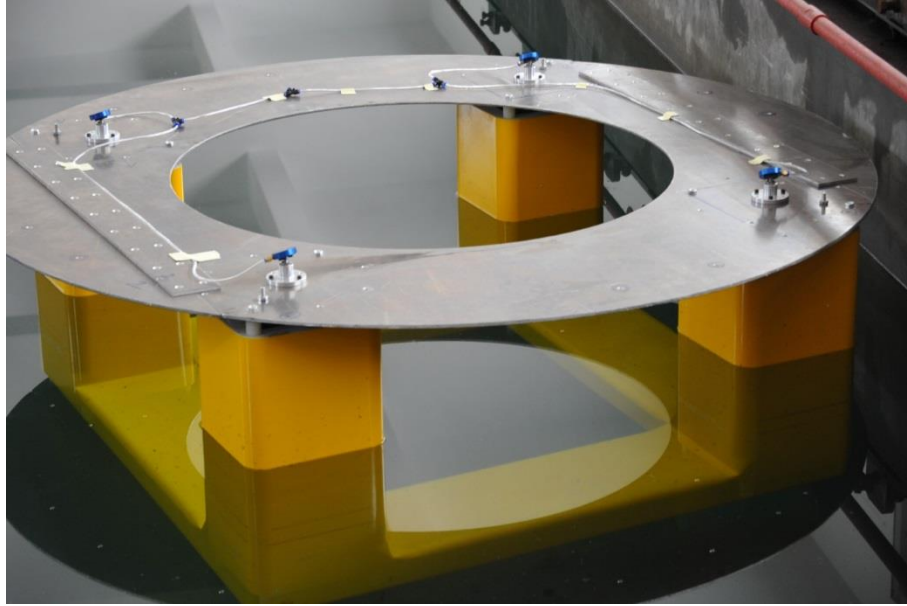


Figure 3.5 The top deck of the model.

3.1.4 Test programme

In order to investigate the effects of VIM on the DDS model under a reduced velocity ranging from 3.5 to 20.3, two incidences (0° and 45°) relative to the towing direction were tested. The definition of motions and towing directions are shown in Figure 3.3. A minimum of fifteen oscillation cycles were allowed to occur in order to reflect the quasi-steady state of the experimental VIM phenomenon.

3.1.5 Natural periods of the motions in calm water

The natural periods of the motions in calm water obtained from decay tests are presented in Table 3.2. The decay curves (time history of the motions) are shown in Figure 3.6, Figure 3.7 and Figure 3.8.

Table 3.2 Natural periods of the motions in calm water.

Incidences ($^{\circ}$)	Natural period of transverse motion, $T_{0transverse}$ (s)	Natural period of in-line motion, $T_{0in-line}$ (s)	Natural period of yaw motion, T_{0yaw} (s)
0°	19.4	19.6	17.1
45°	20.1	19.2	18.3

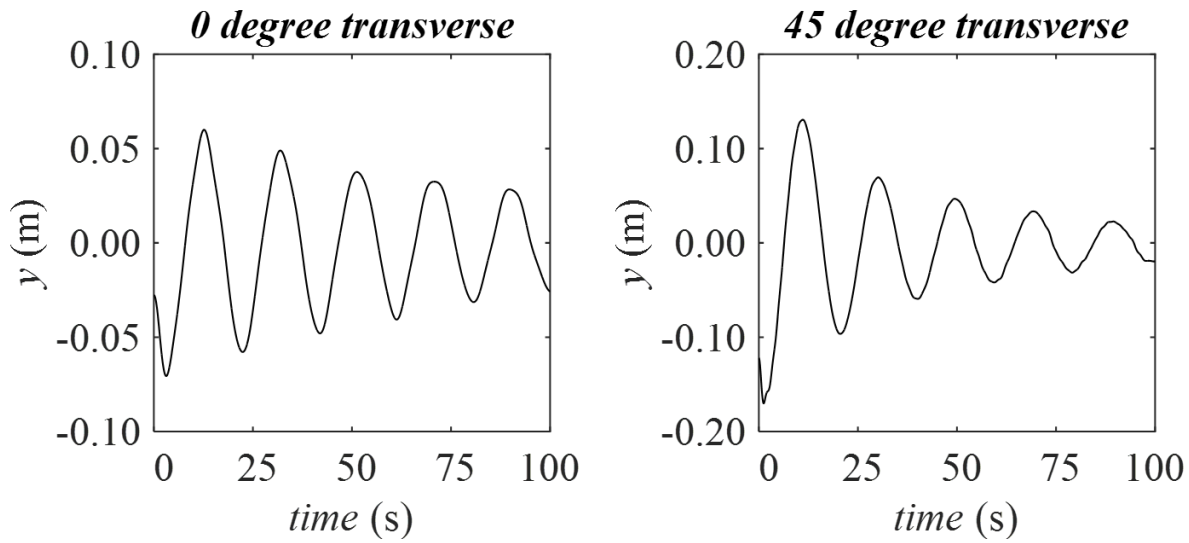


Figure 3.6 Decay curves for the DDS for the transverse motion.

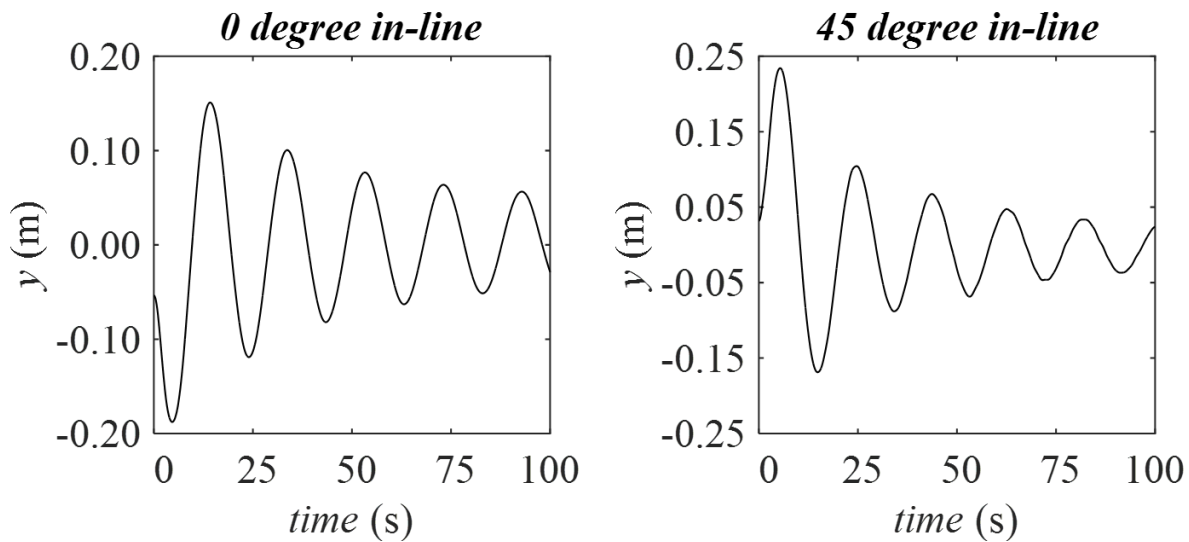


Figure 3.7 Decay curves for the DDS for the in-line motion.

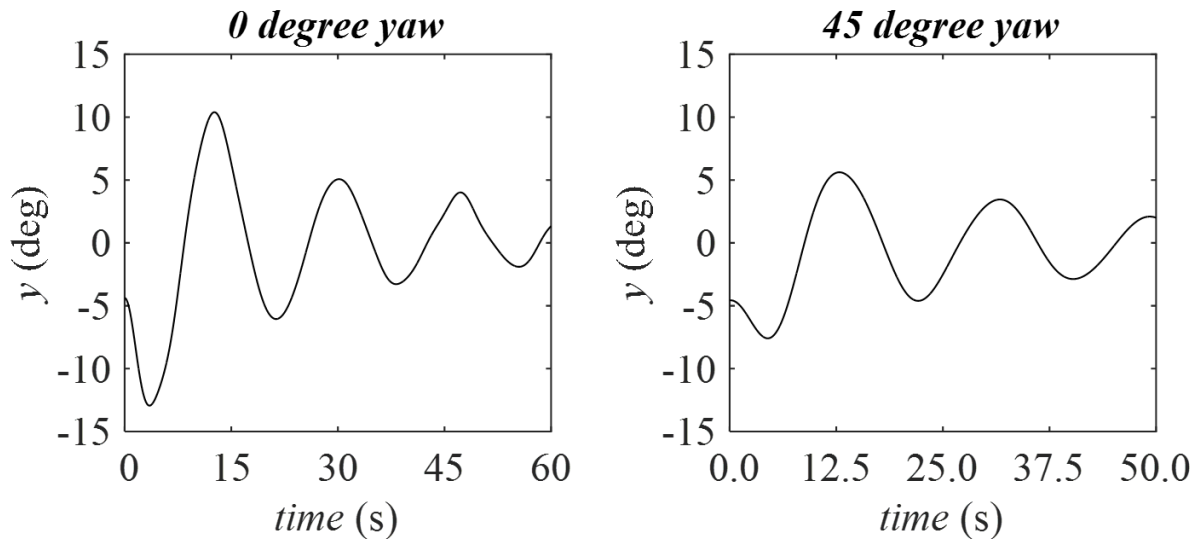


Figure 3.8 Decay curves for the DDS for the yaw motion.

The damping ratio can be calculated based on the decay curves with the following equations:

$$\zeta = \frac{1}{\pi} \ln \left| \frac{\phi_{A_n}}{\phi_{A_{n+1}}} \right|, A_n > A_{n+1}, \quad (3.1)$$

where ϕ_{A_n} and $\phi_{A_{n+1}}$ are the peak and valley value within one oscillation period.

$$\bar{\zeta} = \frac{1}{n} \sum_{n=1}^n \zeta_n, \quad (3.2)$$

and the damping coefficient is defined as:

$$c = 2\bar{\zeta}\sqrt{km}, \quad (3.3)$$

where $\bar{\zeta}$ is the damping ratio, k is the horizontal stiffness of the system and m is the mass of the structure.

Table 3.3 Damping ratio of the DDS for two incidences.

Incidences ($^{\circ}$)	$\bar{\zeta}_{transverse}$	$\bar{\zeta}_{in-line}$	$\bar{\zeta}_{yaw}$
0°	0.034	0.030	0.089
45°	0.048	0.042	0.079

Thus, the damping ratios of the system are present in Table 3.3. It is noted that the air bearing system may contribute a small friction between the four air bearings and the support panel. However, due to the friction was rather limited and can be ignored, the effect from the air bearing system was not considered in the present study.

3.2 Circulating Water Channel Tests

Flow around four square-section shaped columns both with and without pontoons connected at 45° incidence were experimentally investigated in the present study. The experiments were carried out with Reynolds numbers ranging from 3.7×10^4 to 6.0×10^4 to demonstrate the overall hydrodynamics. The total hydrodynamic forces on the two structures were directly recorded in the experiments, together with the flow field measurements that were carried out by using a digital Particle Image Velocimetry (PIV) to examine the downstream vortex shedding processes from the individual columns (Liang *et al.*, 2016). This section describes the experimental set-up and the characteristics of each model. Full details of the test matrix are given in Appendix B.

3.2.1 Model characteristics

Table 3.4 Main characteristics of the four columns configuration model (model I)

	Model I (m)
Distance between centre columns (S)	0.567
Column width (L)	0.152
Immersed column height (H)	0.367
Spacing ratio (S/L)	3.7
Aspect ratio (H/L)	2.4
Corner ratio	0.15

Table 3.5 Main characteristics of the four columns with pontoons connected configuration model/DDS model (model II).

	Model I (m)
Distance between centre columns (S)	0.567
Column width (L)	0.152
Immersed column height (H_I)	0.289
Pontoon height (P)	0.078



Figure 3.9 Four columns configuration model (model I).

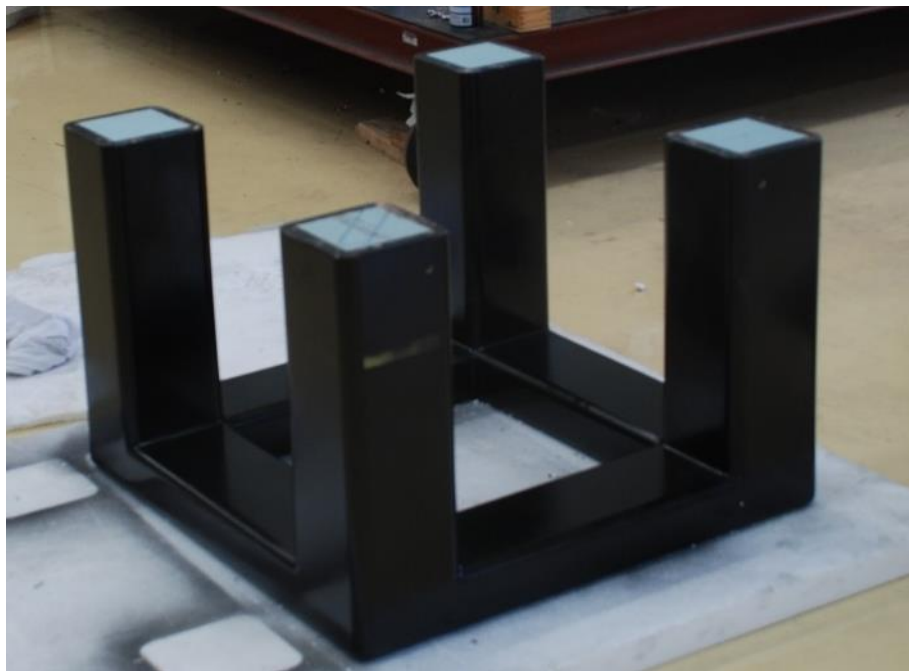


Figure 3.10 Four columns with pontoons connected configuration model/DDS model (model II).

Two sets of model test were conducted, that is one four columns configuration model and one four columns with pontoons connected configuration model (DDS model). Details are presented in Table 3.4 and Table 3.5 as well as shown in Figure 3.9 and Figure 3.10. Ballasts

have been put inside the models to balance the buoyancy of the models. Thus, the model can be upright floating in the water.

3.2.2 Experimental set-up

The experiments were conducted in the circulating water channel at Shanghai Jiao Tong University (see Figure 3.11). The circulating water channel is vertically oriented with an 8.0 m length, 3.0 m width and 1.6 m water depth measuring section. The current velocity can be varied from 0.1 m/s to 3.0 m/s, with the maximum allowable fluctuation of 0.01 m/s. The free stream ambient current velocity has very low turbulence intensity of less than 2% based on the specification and PIV measurements.

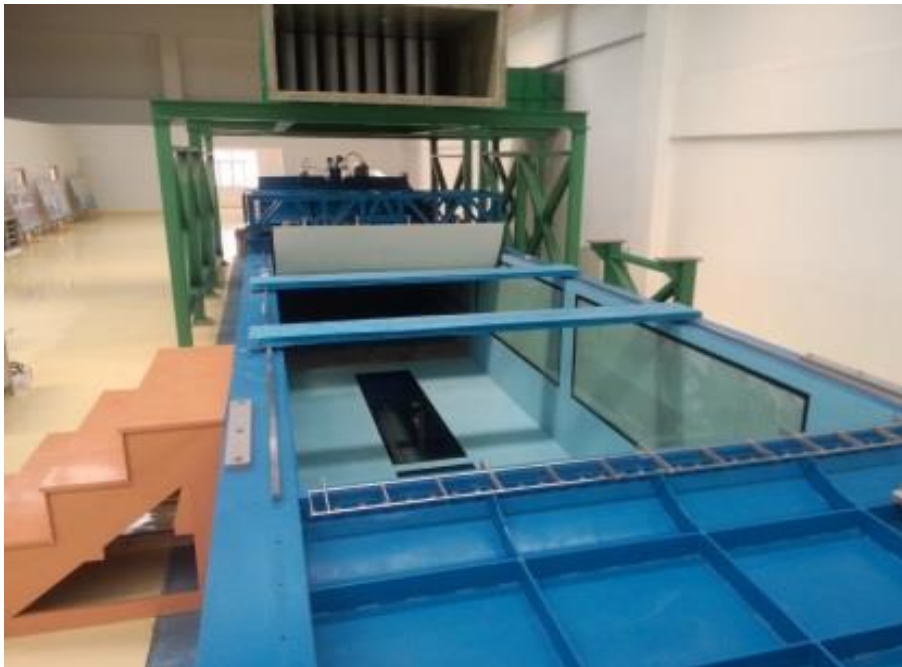


Figure 3.11 The test section of the circulating water channel.

Table 3.6 Characteristics of the three component force transducer (KYOWA LSM-B-SA1).

KYOWA LSM-B-SA1	Characteristics
Rated Capacity	500 N
Calibrated Capacity at transverse direction	44.1 N
Calibrated Capacity at in-line direction	107.8 N
Diameter	88 mm
Nonlinearity	Within $\pm 0.5\%$ RO

The models were mounted to the cross-structure at the top of the test section and connected by a three component force transducer (see Figure 3.12, details of this transducer are illustrated in Table 3.6) which can measure the transverse and in-line fluid forces on the overall model. The central line of the model was coincided with the central line of the circulating water channel at in-line direction.



Figure 3.12 KYOWA LSM-B-SA1 three component transducer.

Table 3.7 PIV Laser and CCD Cameras settings.

Laser	
Manufacturer	Litron Lasers
Laser	Nano TRL PIV
Type	Double Pulsed Nd:YAG
Output Energy @ 532nm (specified)	425mJ
Repetition Rate (Hz)	0-10
CCD Cameras	
Cameras	1 x ImagerProX11M (1GB)
Resolution	4008 x 2672
Buffer	2 x 2 (2004 x 1336)
Max. acquisition rate	4.5Hz

For each individual test case, the experiments were running at least two times (for some of the cases, they were running three times) and the final results from each individual case were averaged from the two or three experimental data sets.

Table 3.8 DaVis Image processing settings.

Image Pre-Processing	
Sliding background scale length	8 pixel
Particle Intensity normalisation	6 pixel
Vector Calculation	
Cross Correlation Mode	Cross-correlation
Interrogation Window Size	128 x 128 (1s Pass)
Shape	Square
Overlap	50%
Final Pass	48 x 48, Adaptive PIV, 1 passes
Post-Processing	
Median Filter	1 iterations
Smoothing	1x Smoothing 3x3

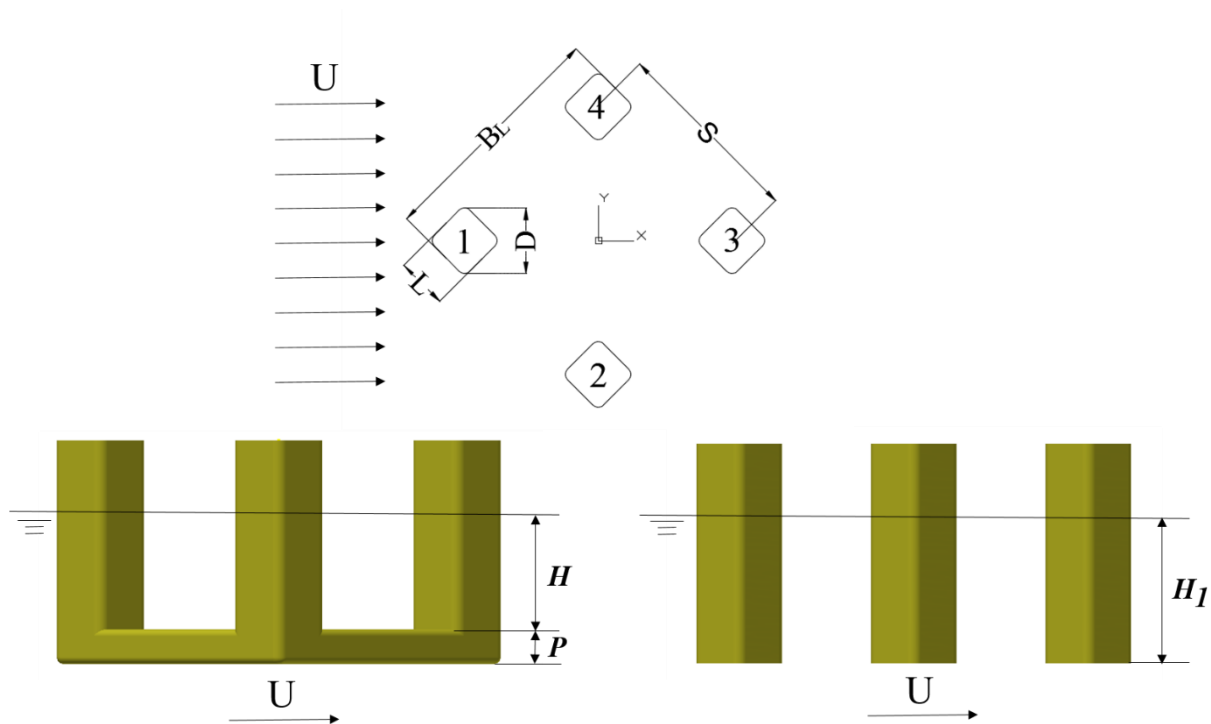
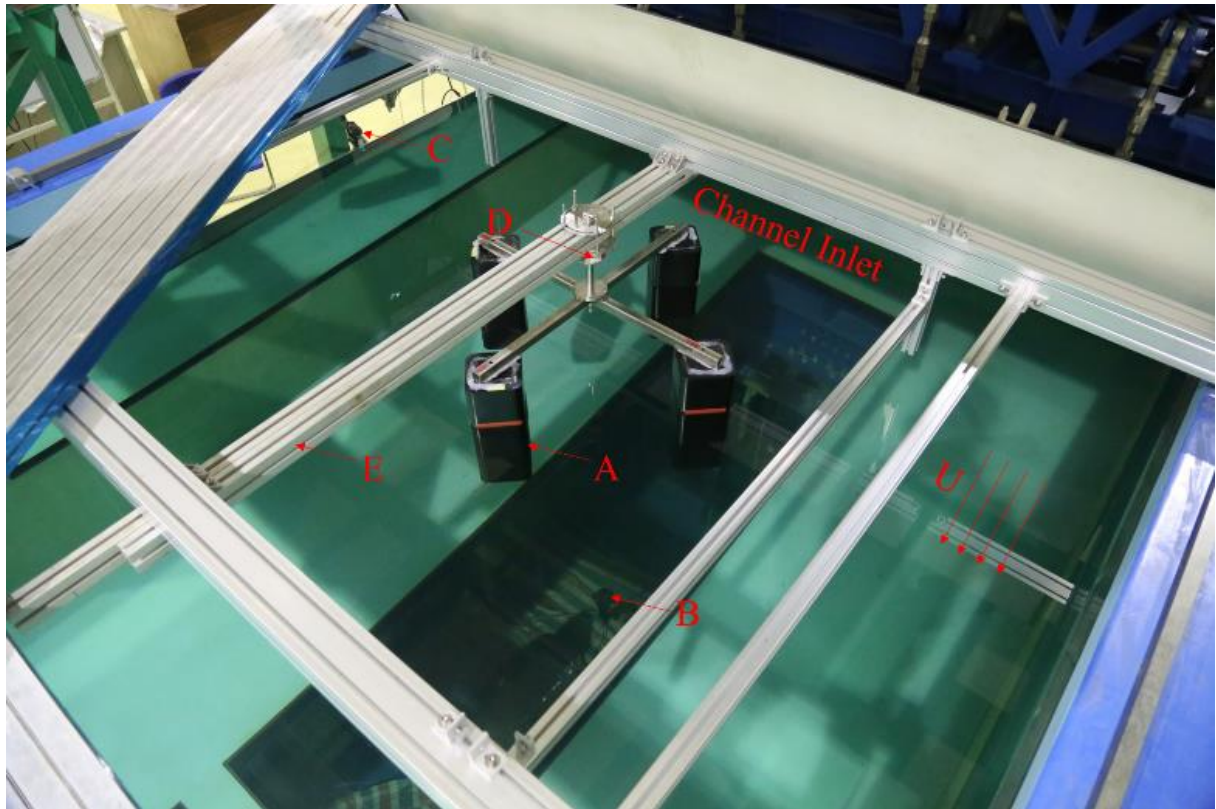


Figure 3.13 Columns arrangement and flow direction.

With the aim to record visual images of flow patterns developing around and behind column 3 (definition of the column arrangement and numbering can be found in Figure 3.13) during the experiments, the LaVision GmbH Particle imaging velocimetry (PIV) system was employed. A LaVision ImgaerProX11M CCD camera was used to record two-dimensional (2D) images of the illuminated field of view at a frequency of 4.5 Hz (see Table 3.7). Two hundred images were collected for each individual case. Images were pre-processed using a sliding background filter to remove large intensity fluctuations due to reflections in the background of the image

and particle intensity normalisation to achieve more homogeneous particle intensities, allowing smaller particles to contribute to the cross-correlation. The DaVis 8.2.2 package was then used to process and provide the velocity and vorticity contours (see Table 3.8). The experimental set-up is shown in Figure 3.14, Figure 3.15 and Figure 3.16. In the present study, the two models were each tested under 45 degree incidence with Reynolds number ranging from 3.7×10^4 to 6.0×10^4 .



- A) Model
- B) PIV recording camera
- C) PIV laser head
- D) Three component force transducer
- E) Adjustable support structure and top frame

Figure 3.14 Experimental set-up in the circulating water channel.

Figure 3.14 shows the overall experiment set-up sketch. Figure 3.15 includes the laser head and translate unit which shoots the laser light from the side of the channel. Figure 3.16 is an example of the PIV measurements during the test. Some of the seeds mixed in the water channel can be found in the picture.

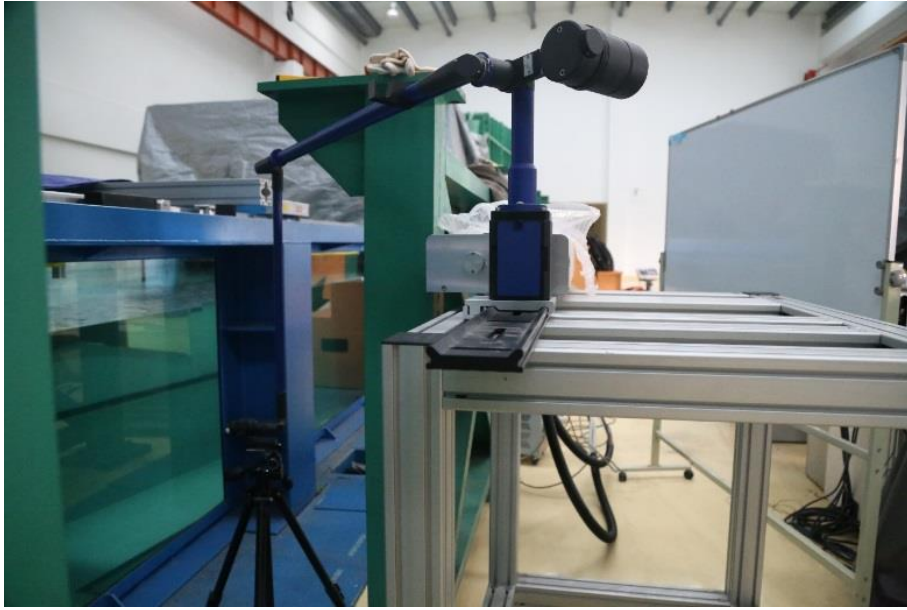


Figure 3.15 Laser head and translation unit.

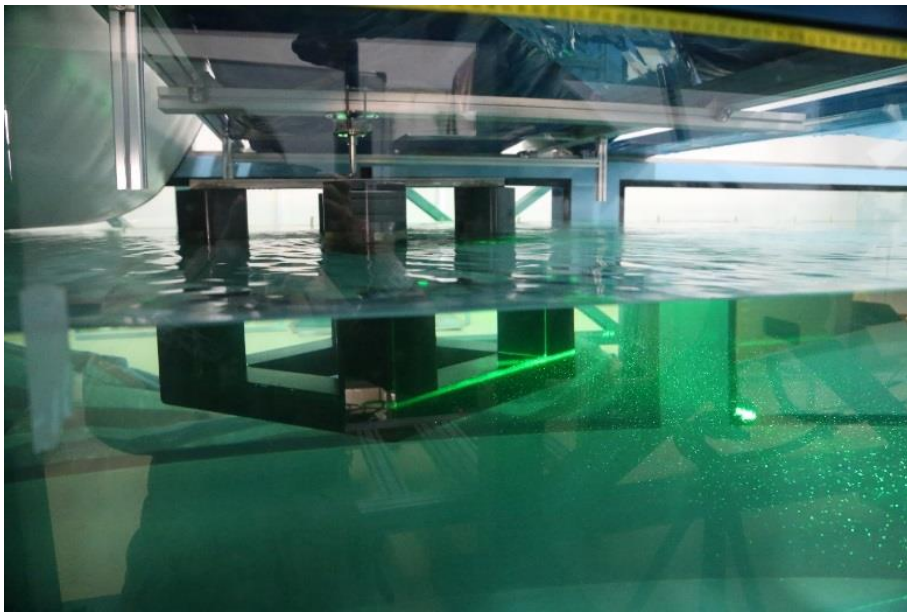


Figure 3.16 PIV measurements during the test.

3.2.3 *Vacuum water channel PIV tests*

A vacuum water channel PIV test was conducted first in the circulating water channel to measure the uniform current quality before setting the test models into the channel. Both horizontal and vertical uniform flow velocity profiles (the two measured planes are shown in Figure 3.17. It is noted that the model presented in the figure is only for showing the model

position) were recorded at a current speed of 0.2 m/s. The velocity profiles are presented in Figure 3.18 and Figure 3.19.

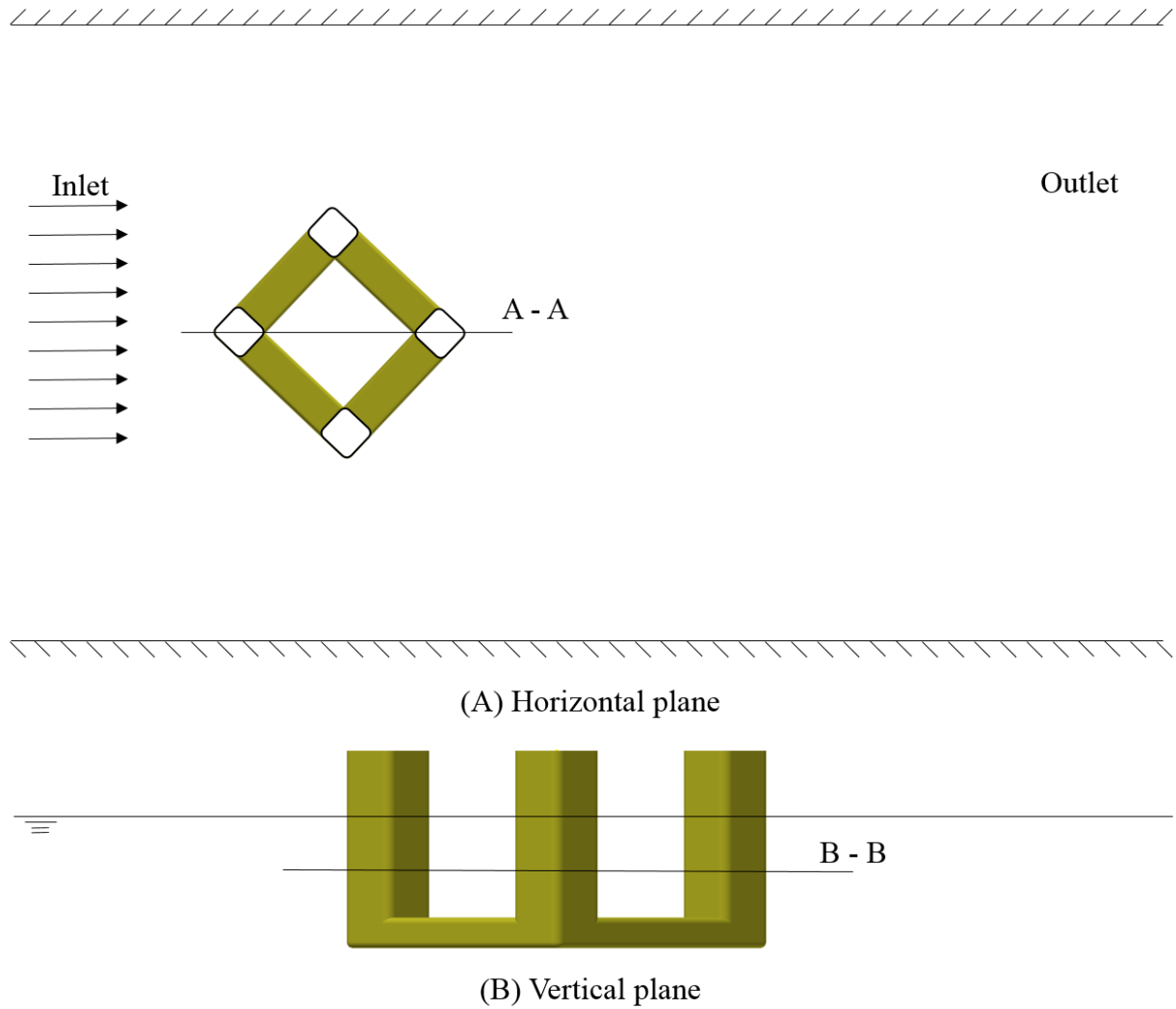


Figure 3.17 The measured plan of the vacuum water channel PIV test, where “A – A” is the vertical plane and “B – B” is the horizontal plane at the middle draft level of the DDS (the model presented in the figure is only for showing the position. During the vacuum water channel PIV test, there is no model in the water channel).

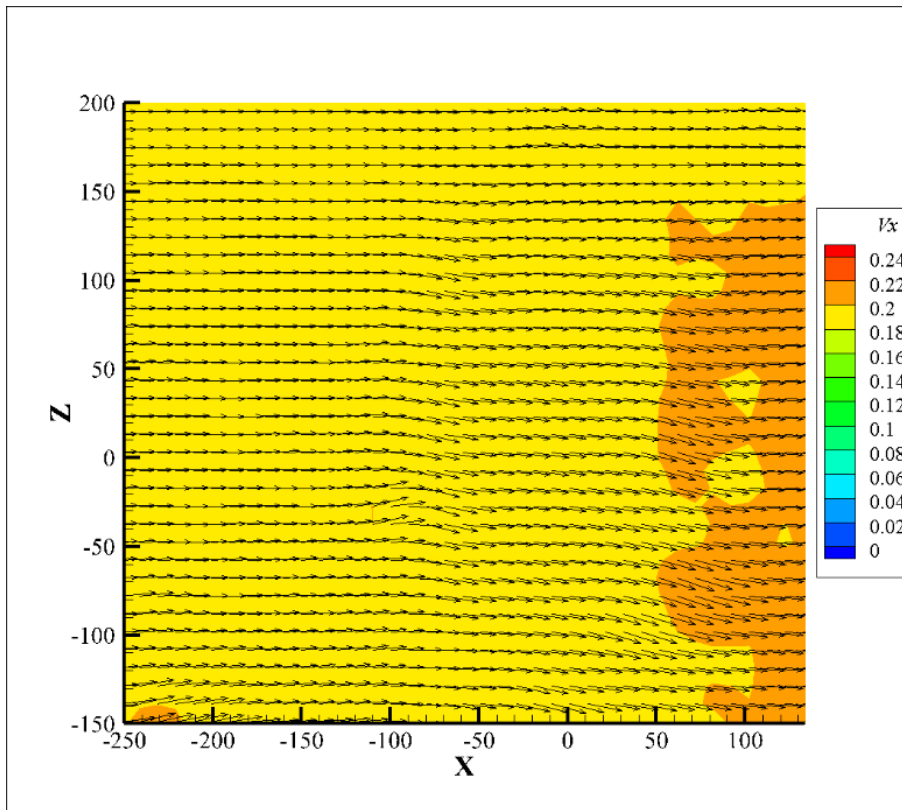


Figure 3.18 Current velocity profile at “A – A” plane.

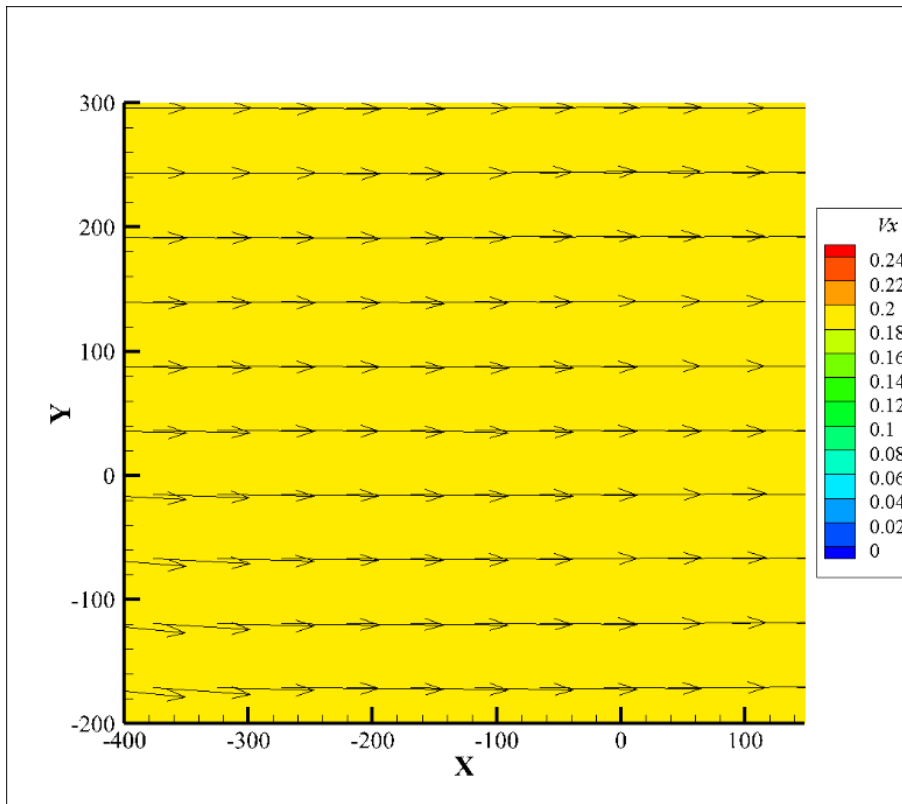


Figure 3.19 Current velocity profile at “B – B” plane.

As can be seen from Figure 3.18 and Figure 3.19, the quality of the velocity profiles was quite good in general, especially in the horizontal plane. However, in Figure 3.18, from “A – A” plane, it can be see some velocity fluctuations in terms of direction at $x = -100$ to -50 and the velocity value towards the end around $x = 100$. Due to limitation of the facility, the fairing equipment in the circulating channel may not make the flow as a pure uniform flow in vertical plane. It is noted that a small irregularity can be accepted during the experiments as long as the velocity profiles show a uniform trend in general. In addition, the resolution ratio in the vertical plane “A – A” is higher than the horizontal plane “B – B”. Thus, minor fluctuations can be found in the vertical plane velocity profile.

3.3 Summary

This chapter introduces the experiment set-up and preparation works for both the towing tank test and the circulating water channel test. All the results obtained from the experiments are presented and discussed in Chapter 5.

Chapter 4. Numerical Simulation

To further investigate the fluid physics associated with VIM, a comprehensive numerical study was conducted to examine both the vortex shedding characteristics and the overall vortex dynamics that lead to the motions of a DDS as well as the hydrodynamics around stationary structures. Due to the limitations of the experiments (e.g. test cases and time, measurement area, detail analysis etc.), the numerical simulations can supply more details (e.g. force distribution on different member of the structure, overall flow patterns etc.). In the present chapter, both mesh and iterative time step sensitivity assessments have been carried out on the numerical model in order to develop a computationally efficient process giving reliable results and followed by the actual simulations (Liang and Tao, 2017; Liang *et al.*, 2017).

4.1 Computational Overview

The detached eddy simulation (DES) was used in this study. For the DES model, the improved delayed detach eddy simulation (IDDES) model (Shur *et al.*, 2008) with the Spalart-Almaras (SA) (Spalart *et al.*, 1997) was used. The delayed detached eddy simulation (DDES) (Spalart *et al.*, 2006) is a recently developed modification of the earlier established detached eddy simulation (DES) (Spalart *et al.*, 1997). IDDES is a capable model which builds a single set of formulas both for natural (D)DES applications and for the wall-modelling in large eddy simulation (WMLES) (Shur *et al.*, 2008). In this case, the boundary layers and irrotational regions are solved using SA model. However, when the grid is fine enough, it will emulate a basic large eddy simulation (LES) subgrid scale model in the detached flow regions (CD-adapco, 2014). This approach can improve the boundary layer simulation and in the meantime, reduce the computational cost. It is noted that the SA model requires $y^+ < 1$ (where $y^+ = u_* \Delta y_l / \nu$, and where u_* denotes the friction velocity at the nearest wall, Δy_l is the first layer thickness and ν is the kinematic viscosity) indicating that the viscous sublayer is properly resolved. All the simulations were carried out using a commercial CFD code, STAR-CCM+ 9. The finite volume method (FVM) is adopted to discretize the incompressible flow field equations (Blazek, 2015). The second-order implicit three time levels (ITTLL) scheme is applied for the temporal discretization. The convective term is evaluated by using a hybrid second-order upwind scheme. SIMPLE algorithm is employed to treat the pressure and velocity coupling.

4.1.1 Governing equations

The governing Navier-Stokes equations solved for the incompressible flow can be written as:

$$\nabla \cdot \bar{u} = 0, \quad (4.1)$$

$$\frac{\partial \bar{u}}{\partial t} + \bar{u} \cdot \nabla \bar{u} = -\frac{1}{\rho} \nabla \bar{p} + \nu \nabla^2 \bar{u} + \frac{1}{\rho \nabla \tau}, \quad (4.2)$$

where ∇ is the Hamiltonian operator; u is the velocity vector; t is the time; p is the pressure; ρ is the density of water; ν is the kinematic viscosity of the water; The last term of Equation (4.2) is the Reynolds stress tensor $\tau = -\rho(\overline{u'u'})$, where u' denotes the fluctuating velocity. The Reynolds stress tensor is an additional term that represents the effects of turbulence.

4.1.2 IDDES approach

The IDDES model is chosen for simulations of flows over a multi-column floating platform as a turbulent flow modelling approach. The IDDES is a hybrid model which combines DDES and WMLES. The DDES length scale is implemented to eliminate the modelled-stress depletion in the original DES approach, while WMLES is applied to achieve more accurate prediction of the mean velocity in the boundary-layer. In this approach, the turbulent stress is written as:

$$-\rho(\overline{u'u'}) = 2u_t \bar{S} - \frac{2}{3} \rho k I, \quad (4.3)$$

where S is the mean strain rate tensor; u_t is the turbulent eddy viscosity; k is the turbulent kinetic energy; I is the Kronecker delta.

The turbulent eddy viscosity is obtained by solving a transport equation for a transport variable $\tilde{\nu}$ in the S-A turbulence formulation (Spalart and Allmaras, 1994).

4.1.3 Computational domain

For all of the simulations, a $9B_L \times 6B_L \times 3B_T$ sized computational domain was used in the present simulations (where B_L is the overall width of the structure and B_T is the draft of the structure). Zou *et al.* (2008) previously used a $32L \times 20L \times 3L$ (about $7.1B_L \times 4.4B_L \times 3L$) domain. The computational domains were $6B_L \times 4.5B_L \times 2.8B_T$ and $5B_L \times 4B_L \times 2.2B_T$ in the

studies by Lee *et al.* (2014). Tan *et al.* (2013) performed a $27B_L \times 18B_L \times 6.5B_T$ domain and Liu *et al.* (2015) used a $11B_L \times 6B_L \times 3B_T$ domain. Koop *et al.* (2016), however, chose a $10B_L \times 6B_T$ cylindrical domain for simulating flow with their numerical models. In our earlier study (Liang *et al.*, 2016), a computational domain size of $9.5B_L \times 6.3B_L \times 3B_T$ was employed. Compared with aforementioned computational domain sizes, a $9B_L \times 6B_L \times 3B_T$ domain (see Figure 4.1) was considered to be sufficiently large to eliminate both the far field effects from the boundaries and the three-dimensional effects from a spanwise cross flow direction.

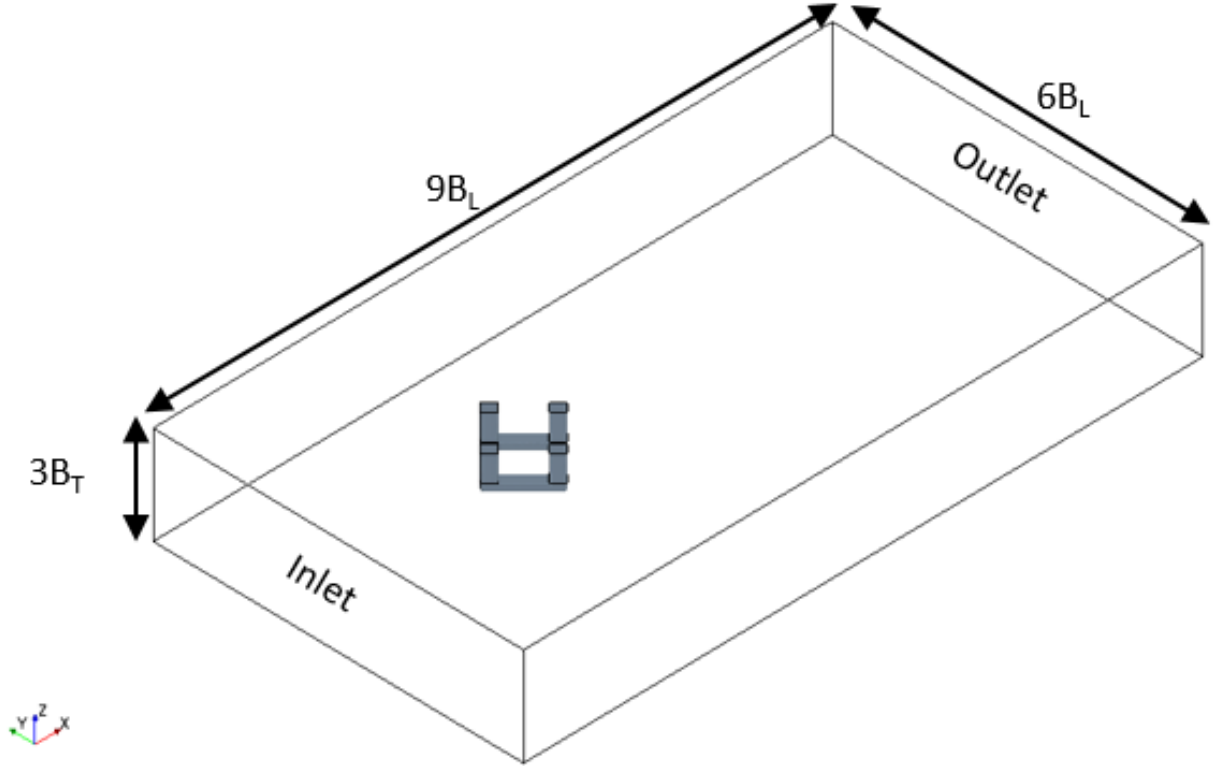


Figure 4.1 Computational domain.

The computational domain was modelled with a three-dimensional mesh of elements. A polyhedral mesh (CD-adapco, 2014) was used in this study. The overall element mesh domain is illustrated at a mid-depth horizontal layer in Figure 4.2. In the present study, a near wall refinement method named “Prism Layer Mesher (CD-adapco, 2014)” was adopted. The “Prism Layer Mesher” model (as shown in Figure 4.3) is used with a core volume mesh to generate orthogonal prismatic cells next to wall surfaces. This layer of cells is necessary to improve the accuracy of the flow solution (CD-adapco, 2014). The y^+ values were smaller than 1 in all simulations to improve the performance of the boundary layer simulation. Another five regional refinements (see Table 4.1, the base sized defined in the present study is set as the width of the

column) were added in the domain in order to refine both the near wake and the far wake regions (see Figure 4.4).

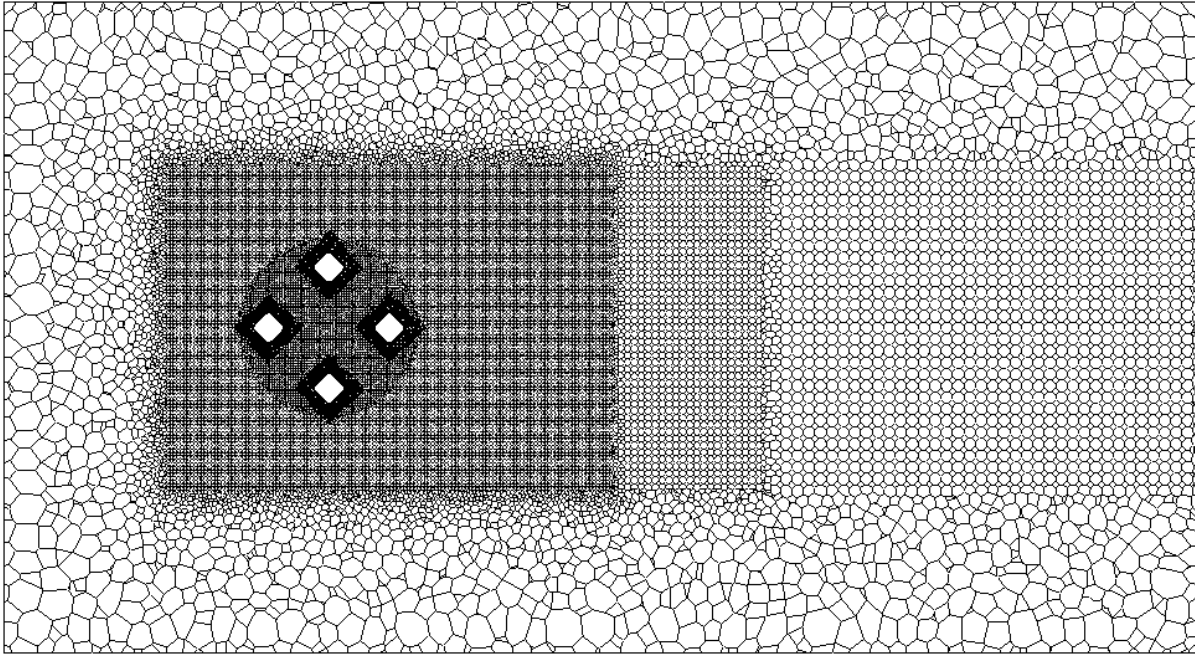


Figure 4.2 Visualization of the mesh at the middle draft level of the DDS (XY plane at the middle draft of the DDS).

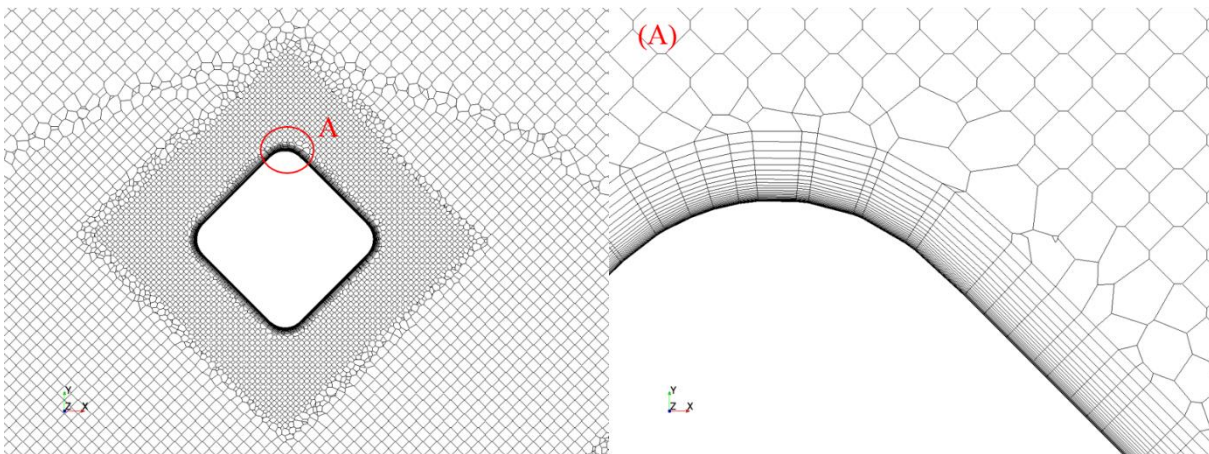


Figure 4.3 Mesh around the column at the middle draft level of the DDS (XY plane at the middle draft of the DDS) showing the “Prims Layer Mesher”.

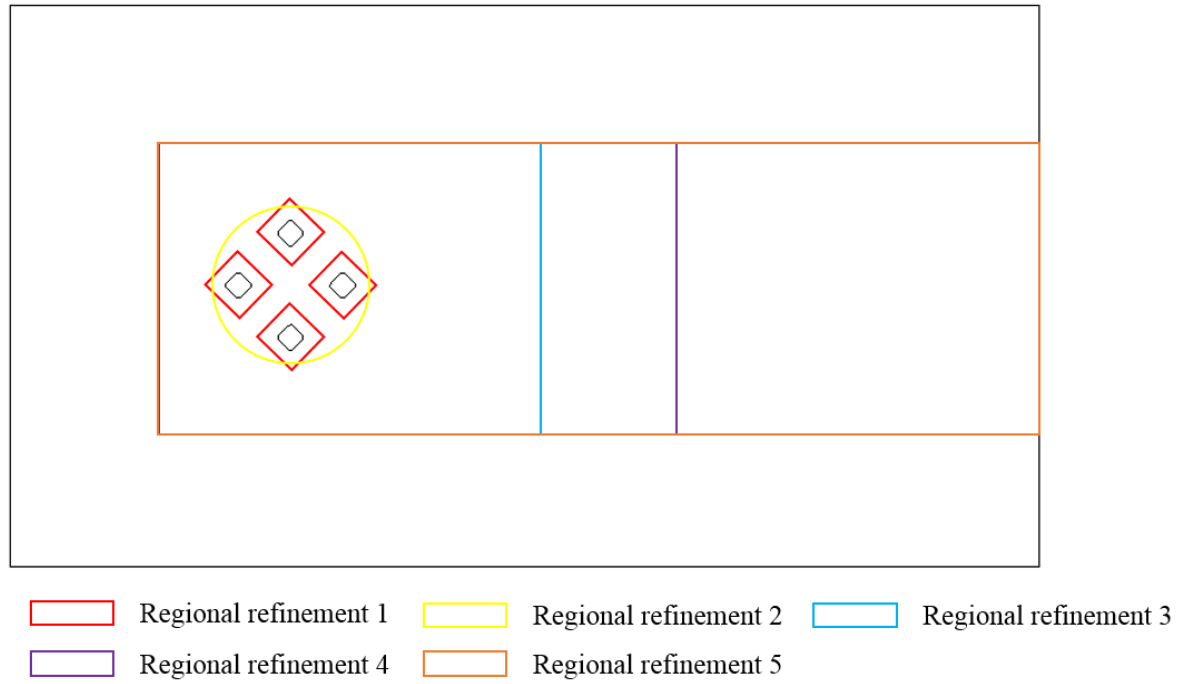


Figure 4.4 The outlines of five regional refinements.

Table 4.1 The regional refinement level

Regional refinement	Percentage of base size
1	4%
2	10%
3	15%
4	30%
5	50%

The boundary conditions are kept same in all the simulations. At the inlet, a uniform and constant flow velocity is specified directly for all sensitivity studies. Along the outlet boundary, the pressure is prescribed to be equal to zero. The velocity at the boundary is extrapolated from the interior using reconstruction gradients (CD-adapco, 2014). For the body surface of the DDS, a no-slip boundary condition is specified in terms of the tangential velocity which is explicitly set to be zero and the pressure at the boundary is extrapolated from the adjacent cells using reconstruction gradients (CD-adapco, 2014). It is noted that the Froude number is quite small ($Fr < 0.2$, $Fr = U/\sqrt{gD}$, where U is the current velocity, g is the acceleration of gravity and D is the projected width of the column) in all simulations of the present investigation. As observed in the physical model tests, the free surface effects were rather limited and can be ignored. Therefore, only the submerged geometry is considered, and the geometry of the structure above

the waterline will not affect the simulation results. However, the gravity centre, the mass of the structure and the moment of inertia are still using the values from the entire structure design. Thus, the free surface boundary is prescribed as being a symmetry boundary.

4.2 Sensitivity Study

To verify reliability and accuracy of the numerical model, a mesh sensitivity study and a time step study were carried out. These studies were aimed to obtain a computationally efficient process providing meaningful numerical results independent of mesh and time step variations.

The sensitivity studies, based on the effects of mesh refinement and time step variations, provided results for the mean drag force coefficient (\bar{C}_D), the root-mean-square lift force coefficient (C_{Lrms}), and the Strouhal number (St).

A grid convergence method (Celik *et al.*, 2008) is further performed in this section offering an uncertainty analysis into the performance of the mesh.

4.2.1 Sensitivity studies for the DDS model

Table 4.2 Numerical set-up information.

Case	Elements (million)	Base size (%)	Non-dimensional time step ($\Delta t U/L$)
DDS_M1	0.15	400	0.008
DDS_M2	0.56	200	0.008
DDS_M3	0.94	160	0.008
DDS_M4	3.43	100	0.008
DDS_M5	6.86	75	0.008
DDS_T1	3.43	100	0.016
DDS_T2	3.43	100	0.004

This section demonstrates the sensitivity studies undertaken for the DDS model. Details of the mesh and time step settings are presented in Table 4.2 for a stationary DDS under 45° flow incidence. The Reynolds number set for the mesh sensitivity study was 1.1×10^6 , which is the highest Reynolds number in all the simulations undertaken for the DDS model. The results for all cases were obtained by averaging after more than fifteen vortex shedding cycles.

Firstly, five tests at $Re = 7.6 \times 10^4$ were carried out with six different mesh densities especially in the near wake region of the structure. The DDS_M1 case is presented as being a relatively coarse mesh in the test. In this model, the computational domain consists of 0.15 million elements. Further cases ranged from 0.56 million to 6.86 million elements (see Table 4.2). All cases initially used the same non-dimensional time step of 0.008. The convergence lines are further illustrated in Figure 4.5, Figure 4.6 and Figure 4.7 which show the results for the relevant convergence trends.

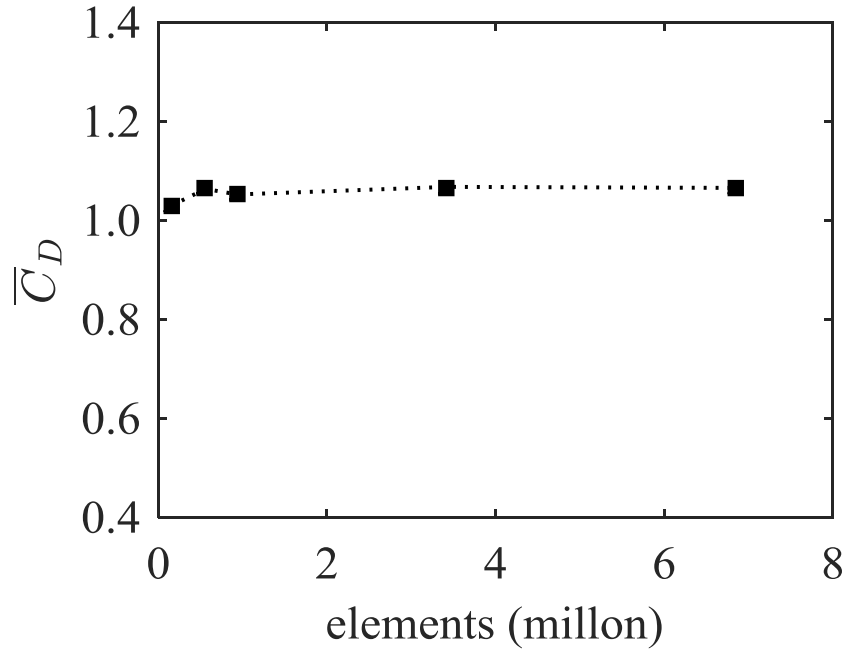


Figure 4.5 Convergence line for the mean drag force coefficient (\bar{C}_D) for the DDS model.

It is noted that in Figure 4.6, the root-mean-square lift force coefficient was first increased then started to drop. This is due to the rough resolution of the mesh cannot catch majority of the vortices. Thus, the lift force on the structure for a very rough resolution is smaller than the relatively fine resolution.

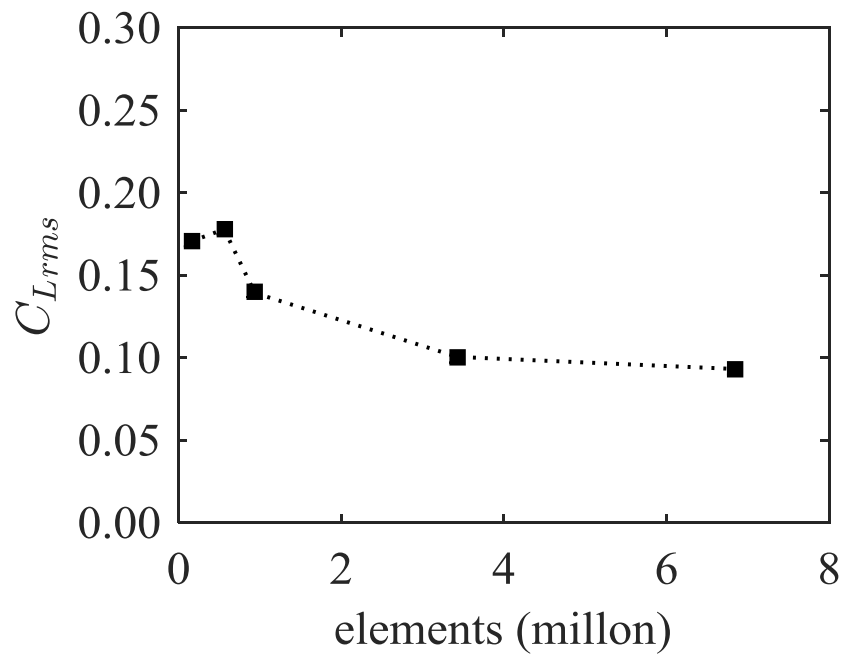


Figure 4.6 Convergence line for the root-mean-square lift force coefficient (C_{Lrms}) for the DDS model.

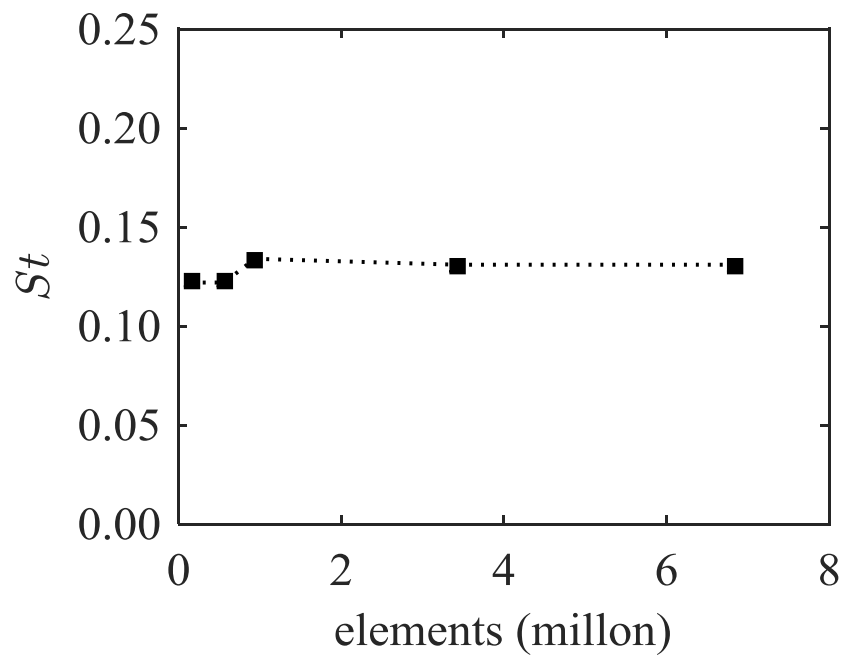


Figure 4.7 Convergence line for the Strouhal number (St) for the DDS model.

Table 4.3 Calculations of discretization error (Celik *et al.*, 2008) for the DDS model; the grid convergence index (*GCI*) represents the numerical uncertainty.

	$\overline{C_D}$	C_{Lrms}	St
$N_1, N_2, N_3(\text{million})$	6.86, 3.43, 0.94	6.86, 3.43, 0.94	6.86, 3.43, 0.94
r_{21}	1.333	1.333	1.333
r_{32}	1.6	1.6	1.6
\emptyset_1	1.066	0.093	0.131
\emptyset_2	1.068	0.101	0.131
\emptyset_3	1.053	0.139	0.134
p	4.561	2.71	NaN
GCI_{normal}^{32}	0.23%	18.31%	NaN
GCI_{fine}^{21}	0.09%	9.13%	NaN

In order to have a thorough sensitivity study, the numerical discretization errors (also be known as the grid convergence index) have been calculated based on the cases DDS_M3, DDS_M4 and DDS_M5 (which correspond to N_3, N_2, N_1 in Table 4.3). Following the guideline proposed by Celik *et al.* (2008), where N_3, N_2, N_1 represent the total number of grids from a course grid refinement level to a relatively fine grid refinement; r is the grid refinement factor, where $r = h_{coarse}/h_{fine}$ and h is the grid size; \emptyset is the calculation results for different grid refinements; p is the apparent order; GCI is the grid convergence index which shows the level of numerical uncertainty. The definitions for each parameter are presented below:

The grid size h for three-dimensional calculations,

$$h = \left[\frac{1}{N} \sum_{i=1}^N (\Delta V_i) \right]^{1/3}, \quad (4.4)$$

where ΔV_i is the volume and N is the total number of cells used for the computations.

The apparent order p of the method can be calculated using the expression,

$$p = \frac{1}{\ln(r_{21})} |\ln|\varepsilon_{32}/\varepsilon_{21}| + q(p)|, \quad (4.5)$$

$$q(p) = \ln \left(\frac{r_{21}^p - s}{r_{32}^p - s} \right), \quad (4.6)$$

$$s = l \cdot \text{sgn}(\varepsilon_{32}/\varepsilon_{21}), \quad (4.7)$$

$$\varepsilon_{32} = \phi_3 - \phi_2, \quad (4.8)$$

$$\varepsilon_{21} = \phi_2 - \phi_1, \quad (4.9)$$

The approximate relative error,

$$e_a^{21} = \left| \frac{\phi_1 - \phi_2}{\phi_1} \right|, \quad (4.10)$$

$$e_a^{32} = \left| \frac{\phi_2 - \phi_3}{\phi_2} \right|, \quad (4.11)$$

and the fine-grid convergence index,

$$GCI_{fine}^{21} = \frac{1.25e_a^{21}}{r_{21}^p - 1}, \quad (4.12)$$

$$GCI_{normal}^{32} = \frac{1.25e_a^{32}}{r_{32}^p - 1}, \quad (4.13)$$

As can be seen in Table 4.3, the GCI for C_{Lrms} is higher than that for the other two variables. However, there is a large reduction in the GCI for the successively finer grid refinement, where the GCI_{fine}^{21} is relatively low compared to the GCI_{normal}^{32} , indicating that the dependence of the numerical simulation on the mesh has been reduced. Moreover, the relative variation of C_{Lrms} between DDS_M4 and DDS_M5 is 8.6% (see Table 4.4). It has a significant reduction compared with the relative variation between DDS_M3 and DDS_M5 (which is 37.6%, see Table 4.4). Thus, the mesh convergence (grid independent) can be said to have been nearly achieved.

Table 4.4 The mesh refinement tests.

Case	Elements (million)	\bar{C}_D	Relative variation (%)	C_{Lrms}	Relative variation (%)	St	Relative variation (%)
DDS_M1	0.15	1.030		0.171		0.122	
DDS_M2	0.56	1.064	3.195	0.178	3.933	0.122	0
DDS_M3	0.94	1.053	1.040	0.139	28.060	0.134	8.955
DDS_M4*	3.43	1.068	1.404	0.101	37.620	0.131	2.290
DDS_M5	6.86	1.066	0.190	0.093	8.600	0.131	0

Additionally, the St in Table 4.3 may indicate that the “exact” solution has been attained. In Figure 4.7, it is graphically shown that the St has converged at around the value of 0.131. Therefore, the numerical uncertainty of the obtained Strouhal number is prescribed as NaN (i.e. Not a Number) in Table 4.3.

As shown in Table 4.3 and Table 4.4 as well as plotted in Figure 4.5, Figure 4.6 and Figure 4.7, the results of the detailed mesh sensitivity study show that the DDS_M4 mesh setting is fine enough to obtain confident results within an acceptable computation time.

Table 4.5 The time step sensitivity study.

Case	Non-dimensional time step ($\Delta t U/L$)	\bar{C}_D	Relative variation (%)	St	Relative variation (%)
DDS_T1	0.016	1.020		0.148	
DDS_M4*	0.008	1.068	4.706	0.131	12.977
DDS_T2	0.004	1.068	0	0.131	0

It is noted that the non-dimensional time step value was chosen as 0.008 (non-dimensional time step = $\Delta t U/L$, where Δt is the time step, U is the inlet velocity and L is the width of the DDS column) for all cases based on mesh sensitivity tests. The constant non-dimensional time step size will result in varying courant (CFL) numbers as the grid is refined. A major benefit of employing the IDDES approach is that a large portion of the flow should be resolved with the large eddy simulation (LES), however this requires rather strict control on CFL number limits. In the present study, the CFL numbers for the majority of the overall flow region are less than 1. Only in some tiny flow areas, the CFL numbers are found to be between 1 to 2. Therefore, the time step is considered to be fine enough for the current simulations' requirements. Additionally, a brief time step study has been carried out. As shown in Table 4.5, DDS_M4 case was considered to be fine enough for a suitable time step. Thus, case DDS_M4 was chosen for the further validation of the numerical model against the experimental data for the DDS model.

4.2.2 Sensitivity studies for the four columns model

Table 4.6 Mesh sensitivity study for the four columns model.

Case	Elements (million)	\bar{C}_D	Relative variation (%)	C_{Lrms}	Relative variation (%)	St	Relative variation (%)
FC_M1	0.02	0.931		0.105		0.127	
FC_M2	0.13	1.052	11.502	0.111	5.405	0.139	8.633
FC_M3	0.95	1.065	1.221	0.078	42.308	0.139	0
FC_M4*	3.50	1.068	0.281	0.066	18.182	0.150	7.333
FC_M5	8.18	1.100	2.909	0.065	1.538	0.145	3.448

Table 4.7 Calculations of discretization error (Celik *et al.*, 2008) for the four columns model; the grid convergence index (GCI) represents the numerical uncertainty.

	\bar{C}_D	C_{Lrms}	St
N_1, N_2, N_3 (million)	8.18, 3.50, 0.95	8.18, 3.50, 0.95	8.18, 3.50, 0.95
r_{21}	1.333	1.333	1.333
r_{32}	1.6	1.6	1.6
\emptyset_1	1.100	0.065	0.145
\emptyset_2	1.068	0.066	0.150
\emptyset_3	1.065	0.078	0.139
p	22.56	4.92	1.92
GCI_{normal}^{32}	0.00%	2.50%	6.25%
GCI_{fine}^{21}	0.01%	0.62%	5.85%

A basic four columns model was also tested in the circulating water channel. However, due to the configuration of the model being changed, a new mesh sensitivity study also needs to be conducted. With the same methods that were employed in the above section, the convergence lines (see Figure 4.8, Figure 4.9 and Figure 4.10) and the calculations of the discretization error (as shown in Table 4.7) were performed with the results given below. The results are obtained by averaging over more than fifteen vortex shedding cycles of the whole structure. Similar as Figure 4.6, in Figure 4.9, the root-mean-square lift force coefficient was first increased then started to drop. This is due to the rough resolution of the mesh cannot catch majority of the vortices. Thus, the lift force on the structure for a very rough resolution is smaller than the relatively fine resolution.

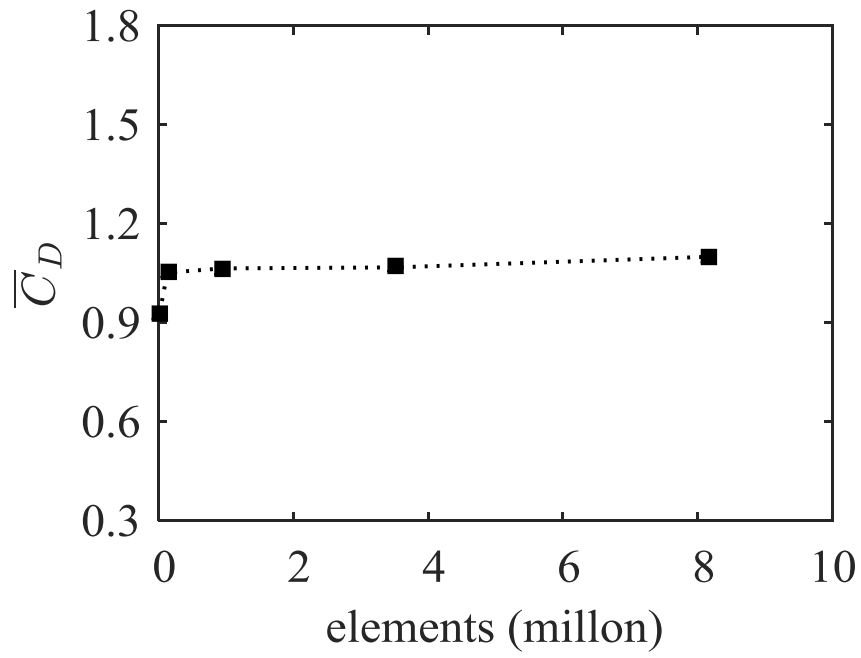


Figure 4.8 Convergence line for the mean drag force coefficient (\bar{C}_D) for the four columns model.

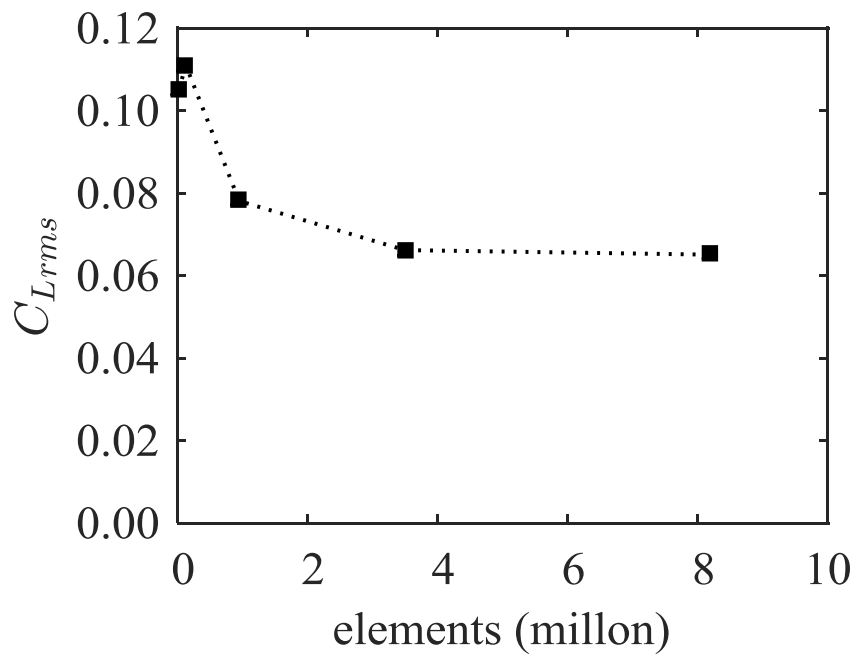


Figure 4.9 Convergence line for the root-mean-square lift force coefficient (C_{Lrms}) for the four columns model.

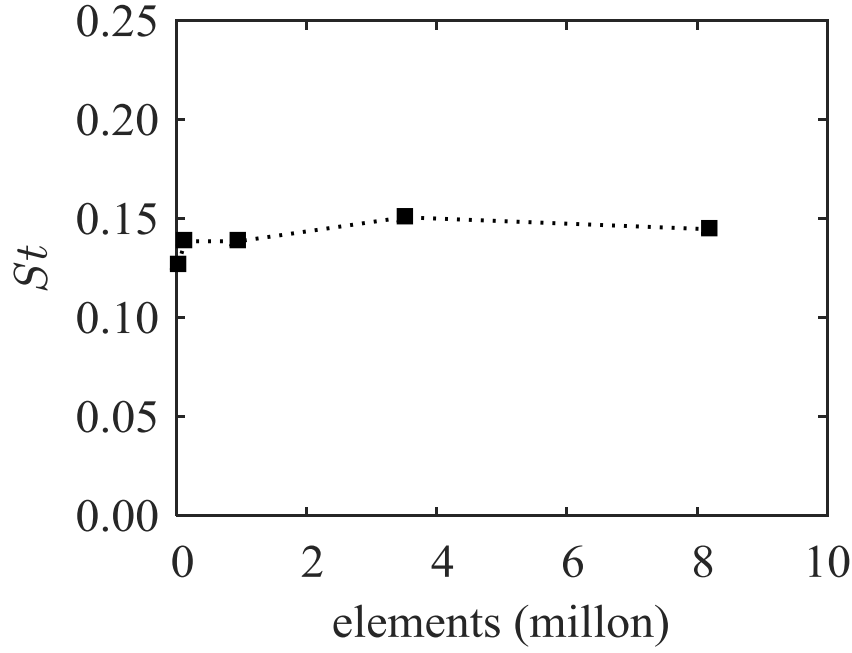


Figure 4.10 Convergence line for the Strouhal number (St) for the four columns model.

As shown in Table 4.7, the numerical uncertainty (GCI) is small for all three variables (\bar{C}_D , C_{Lrms} and St). It is noted that the discretization error of St is higher than for the other two variables. However, the relative variation of St between FC_M4 and FC_M5 is 3.4% (see Table 4.6) which is considered to be relatively small. Thus, the FC_M4 mesh refinement setting has been chosen for the further numerical simulations and for comparisons against the experimental data for the four columns model.

4.3 Model Validation

After the sensitivity studies have been carefully demonstrated and discussed in section 4.2, this section presents several validations of the present numerical model. As the numerical model validation is crucial for CFD work, the present numerical model has been validated by both the previous work and the present outcomes. There are two parts in this section: 4.3.1 Validation against MARIN experiments and 4.3.2 Validation against the present model tests. All the results listed below are obtained by averaging over more than fifteen vortex shedding cycles (15 to 25 cycles) of the whole structure.

4.3.1 Validation against MARIN experiments

Table 4.8 The main characteristics of the MARIN DDS.

	Prototype (m)	Model (m)
Distance between centre columns (S)	58.7	0.838
Column width (L)	14.0	0.200
Immersed column height above the pontoon (H)	35.0	0.500
Pontoon height (P)	10.5	0.150

In this section, the present numerical model has been validated by the previous results. The experimental data available from MARIN (Waals *et al.*, 2007) has been chosen as the pilot reference for validating the present numerical model. The main characteristics of the MARIN model are shown in Table 4.8. The scale ratio λ for this particular model is 1:70 (the flow velocity is set as 0.17 m/s which is the same as that in the experiment undertaken by Waals *et al.* (2007)). The resulting \bar{C}_D obtained from the present numerical calculation and the MARIN experimental measurements are presented in Table 4.9.

Table 4.9 Comparison of \bar{C}_D from the present numerical calculation and the MARIN experimental measurements.

Case	\bar{C}_D	Relative variation (%)
Present numerical model	1.127	8.78
MARIN test (Waals <i>et al.</i> , 2007)	1.036	

Compared with the experimental data, the results from the present numerical model show good agreement with a relative variation of 8.78%. Therefore, the developed numerical model can be used with some confidence in future numerical simulations.

4.3.2 Validation against the present model tests

It is noted that the validation work of one MARIN's mean drag test at 8.78% cannot instil confidence to do all simulations. Thus, the present numerical model has also been validated by the present outcomes from the experiments carried out as part of the current research work.

Firstly, comparisons of the results from the present numerical model and the experimental measurements for the stationary model case are presented in Table 4.10 and Table 4.11.

Table 4.10 Comparison of the results from the present numerical calculations and experimental measurements for the stationary DDS model at 45° incidence.

<i>Re</i> (10⁴)	\bar{C}_D (num.)	\bar{C}_D (exp.)	Relative variation (%)	C_{Lrms} (num.)	C_{Lrms} (exp.)	Relative variation (%)	<i>St</i> (num.)	<i>St</i> (exp.)	Relative variation (%)
3.7	1.054	0.932	13.1	0.070	0.078	10.3	0.132	0.123	7.3
4.3	1.043	0.940	11.0	0.072	0.078	7.7	0.139	0.122	13.9
5.2	1.047	0.953	9.9	0.071	0.076	6.6	0.142	0.124	14.5
6.0	1.051	0.974	7.9	0.078	0.082	4.9	0.139	0.126	10.3

As can be seen from Table 4.10, a good agreement has been shown from the comparisons of \bar{C}_D , C_{Lrms} and St for the stationary DDS model between the present experimental and numerical investigations. All of the relative variations between the numerical predictions and the experimental data are around 10%. Thus, the present numerical model predicts well comparing with the experimental results for the stationary DDS model.

Table 4.11 Comparison of the results from the present numerical calculations and experimental measurements for the four columns configuration model at 45° incidence.

<i>Re</i> (10⁴)	\bar{C}_D (num.)	\bar{C}_D (exp.)	Relative variation (%)	C_{Lrms} (num.)	C_{Lrms} (exp.)	Relative variation (%)	<i>St</i> (num.)	<i>St</i> (exp.)	Relative variation (%)
3.7	1.083	0.948	14.2	0.062	0.053	17.0	0.156	0.137	13.9
4.3	1.075	0.961	11.9	0.066	0.055	20.0	0.152	0.139	9.4
5.2	1.077	0.962	12.0	0.066	0.051	29.4	0.150	0.139	7.9
6.0	1.068	0.990	7.9	0.066	0.053	24.5	0.151	0.141	7.1

When the present numerical model was used to simulate the four columns configuration model, the relative variations were slightly increased comparing with the predictions of the DDS model (see Table 4.11), especially for C_{Lrms} . It is noted that the sharp edges at the free end of the column significantly affect the difference between the numerical predictions and the experimental results. The four columns configuration model in the numerical simulations has ideal sharp edges. However, in the experiment, the sharp edge may slightly varied. Thus, the tiny vortices shedding from the free end of the columns may affect the numerical predictions,

especially for the results of the lift force. However, it can be concluded that the numerical predictions show a reasonably good agreement when compared with the experimental data for the stationary four columns configuration model.

In general, for the two stationary models presented above (see Table 4.10 and Table 4.11), the maximum discrepancy for \bar{C}_D between the numerical simulations and the experimental results is 14.2% (observed at $Re = 3.7 \times 10^4$, for the four columns configuration). The maximum discrepancy for C_{Lrms} is 29.4% (observed at $Re = 5.2 \times 10^4$, for the four columns configuration). The discrepancy in C_{Lrms} for the majority of cases is less than 20%. Also the maximum difference for St is 14.5% (observed at $Re = 5.2 \times 10^4$, for the DDS model). It is also noted that these numerical simulations were carried out based on a high performance computer (HPC) platform with 64 cores and these simulations can take more than 100 hours to simulate around fifteen vortex shedding cycles. Considering the time efficiency issues, the relative variations can be accepted. Therefore, the developed numerical model can be used with confidence in future numerical simulations for a stationary structure.

It is noted that the above validation work has only referred to the stationary structure tests. When the flow-induced motions are coupled into the numerical model, the present numerical model needs to be validated against the VIM experimental data as well to provide confidence in motion coupled simulations. However, in the previous publications, the model characteristics are not presented in detail, especially for the mooring system arrangement and the appendages' design. Since these details of the model are very important in determining the natural frequencies of the structure, direct comparison may result in misleading conclusions without the detailed information of the mooring system design from previous publications. For this consideration, the present numerical model is validated by present model tests conducted the towing tank. The results are obtained by averaging over more than ten cycles of the VIM oscillation period. Although the sample size is relatively small, the reliability and sensitivity of the relatively small data set on the results have been discussed by Zhang *et al.* (2014). The comparison in 4.3.1 Validation against MARIN experiments is also used as a supplementary validation to provide more confidence for the present numerical model.

As mentioned above, further comparisons of \bar{C}_D , C_{Lrms} and A_y/L with the present experimental and numerical investigations for VIM are provided in Table 4.12 showing good agreements, hence providing another means of validating the numerical model developed in this study. Most of the relative variations are less than 10%, especially for the predictions of \bar{C}_D . However, it is

noted that at $Ur = 3.9$, the numerical results have a relatively large discrepancy when compared with the experimental data. The detailed discussions are presented in Chapter 5.

Table 4.12 Comparison of the results from the present numerical calculations and experimental measurements for 45° incidence.

Ur	\bar{C}_D (num.)	\bar{C}_D (exp.)	Relative variation (%)	C_{Lrms} (num.)	C_{Lrms} (exp.)	Relative variation (%)	A_y/L (num.)	A_y/L (exp.)	Relative variation (%)
3.9	2.210	2.399	7.9	0.931	0.751	23.9	0.236	0.166	41.9
6.6	2.619	2.614	0.2	0.540	0.497	8.5	0.760	0.742	2.5
8.9	2.292	2.429	5.7	0.190	0.230	17.3	0.378	0.398	5.0
12.1	2.099	2.154	2.6	0.194	0.177	9.8	0.345	0.318	8.5

Additionally, when the motions have been coupled into the simulation, the simulation time has been extended significantly. It takes about 200 to 300 hours to simulation ten cycles of the VIM oscillation period on the HPC platform with 64 cores. Considering the efficiency issues, the relative variations can be accepted. Therefore, the developed numerical model can be used with confidence in future VIM simulations.

4.4 Summary

This chapter presents the numerical scheme and the overall computational settings following with the sensitivity studies. The decent validation works provide a strong confidence to further simulations. Thus, the present numerical model can be used in further studies.

Along with the experimental results, the numerical simulations can provide more details such as the overall flow patterns at different observations planes, more cases and the force distribution on different member of the structure. All the results simulated by the present numerical model are presented and discussed in Chapter 5.

Chapter 5. Results and Discussions

To reveal the fluid physics related to VIM, this chapter summarized the results and discussions based on both experimental and numerical investigations introduced in Chapter 3 and Chapter 4. Firstly, the overall VIM characteristics of a DDS are presented to generally understand the VIM mechanism. Thereby, the most striking incidence founded in the overall study is further investigated to quantify the determining factors inducing VIM excitation and reveal the insights of the vortex dynamics associated with VIM. Finally, flow over stationary multi-column structures is discussed to study the pontoons effects on the overall hydrodynamics around the structures.

5.1 Experimental and numerical study on VIM of a DDS

The motion response of a typical moored DDS under four current velocities for each of the two headings were investigated using the present numerical model and their results are further compared with the measurements conducted in the towing tank. The motion measurements for more than ten cycles of the VIM oscillation period are collected in the present study. Additionally, the correlation among the vortex shedding patterns, the fluctuation forces on the structure, and the VIM trajectory are demonstrated in this section (Liang *et al.*, 2017).

5.1.1 Motion characteristics

Figure 5.1, which compares the results from the numerical simulation with those from the model tests, presents the non-dimensional characteristic amplitude (A_x/L , A_y/L , where Ur is defined based on $T_{0transverse}$) for motions in both the in-line and the transverse directions under flow incidences of 0° and 45° . The non-dimensional amplitude is defined as $\sqrt{2} \times \sigma\left(\frac{y(t)}{L}\right)$ (where σ is the standard deviation of the time series $y(t)/L$, and $y(t)$ represents the time series of in-line, transverse and yaw motions. For yaw motions, the non-dimensional amplitude is defined as $\sqrt{2} \times \sigma(y(t))$). As can be seen in Figure 5.1, the 45° incidence cases showed larger VIM in magnitude in both the in-line and the transverse directions. Moreover, the largest A_y/L for both incidences occurred at the same range around $Ur = 6.5$. The “lock-in” region for 0° incidence happens in the range of $6.0 \leq Ur \leq 9.5$, while for 45° incidence, the “lock-in” region occurs between $5.0 \leq Ur \leq 9.0$. It is also to be noted that the motion in the in-line direction for both incidences keeps increasing with increasing Ur . In this context, the present numerical model

predicts the motions in both the transverse and the in-line directions well. At low Ur values, the numerical model predicts a larger response than the experimental measurements in the transverse direction. When the towing speed for Ur is extremely low (0.062 m/s for 0° incidence at $Ur = 3.9$) in the towing tank test, it is likely that the “friction” of the whole physical facilities tends to affect the experimental measurements, especially the air bearing system. However, at high Ur , such effect become insignificant, especially in the “lock-in” region where the numerical predictions agree well with the experimental data.

Figure 5.2 and Figure 5.3 present the results of the motion in the transverse direction for 0° and 45° flow incidences in the frequency domain. It is clearly seen that the motion responses very much concentrate around the natural transverse frequency ($f_{0transverse}$) in the “lock-in” region. Moreover, as can be seen in Figure 5.4 and Figure 5.5 both incidences show that in the “lock-in” region, the structure’s response frequency (f_y) is approximately the same as the vortex shedding frequency (f_s) (also seen in Figure 5.6 and Figure 5.7).

It is further observed in both experiments and numerical simulations that, for 0° incidence, in the “post lock-in” region f_s increases and becomes larger than f_y . This phenomenon was also observed by Waals *et al.* (2007) and termed as galloping. Galloping is different from VIM. It describes a low frequency response and is not self-limiting. When Galloping happens, f_s is much larger than the structural response frequency (Waals *et al.*, 2007). The transverse motion tends to increase with increasing Ur as can be observed in Figure 5.2 and Figure 5.4. In the “post lock-in” region, the peak f_y is still around $f_{0transverse}$. Additionally, a high f_y appeared with increasing Ur (see Figure 5.2). However, in the vortex shedding frequency domain, at $Ur = 15.7$, there are two nearly equal weight peak transverse forces occurring at two vortex shedding frequencies (as shown in Figure 5.8b). In addition, it is clear that f_s is three times as the peak f_y at $Ur = 20.2$ in the experimental measurements (see Figure 5.2 and Figure 5.4). Thus, the motion response in the “post lock-in” region is an oscillation phenomenon which combines VIM and the galloping phenomena. In this situation, A_x/L keeps increasing in the “post lock-in” region.

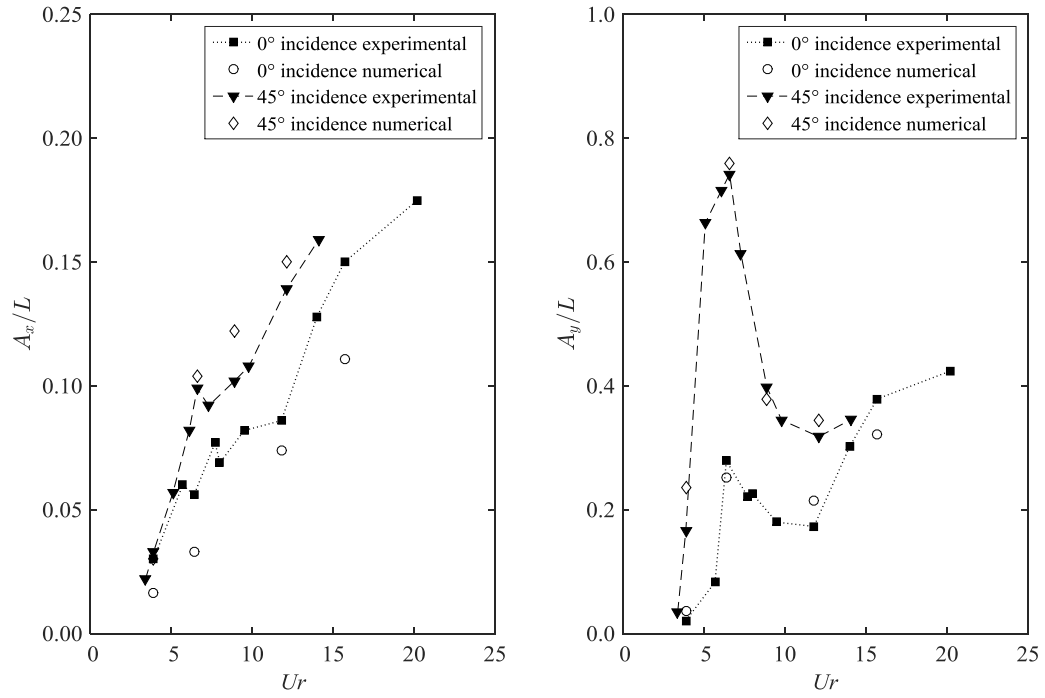


Figure 5.1 Non-dimensional in-line and transverse characteristics amplitudes (A_x/L , A_y/L), the U_r is defined based on $T_{0transverse}$).

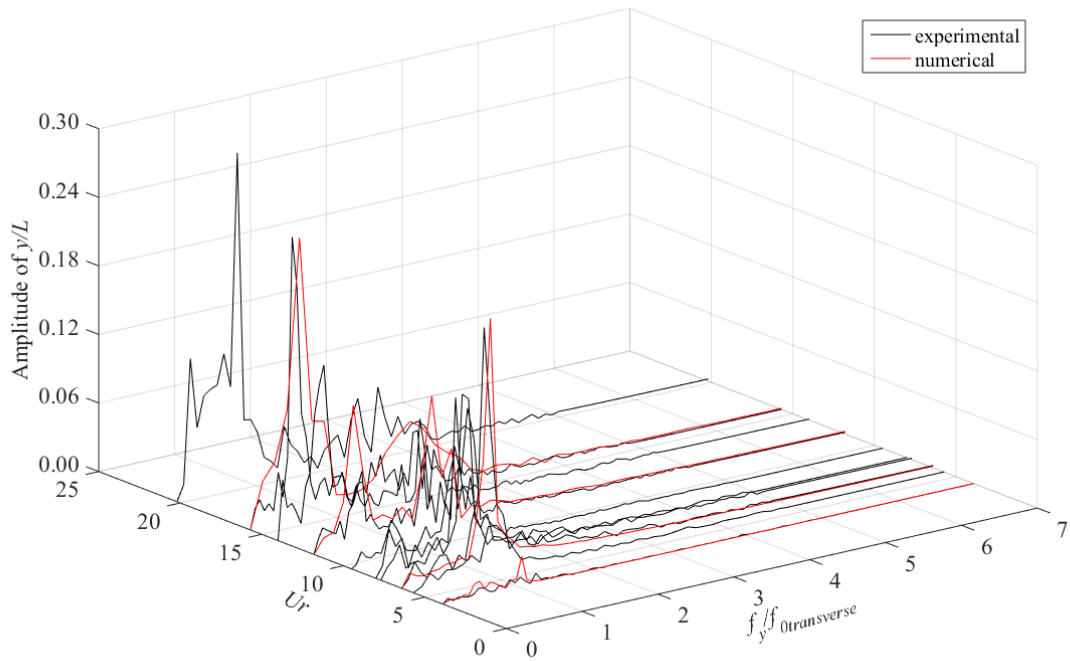


Figure 5.2 FFT of the motions in the transverse direction as a function of U_r and f_y for 0° incidence (the U_r is defined based on $T_{0transverse}$).

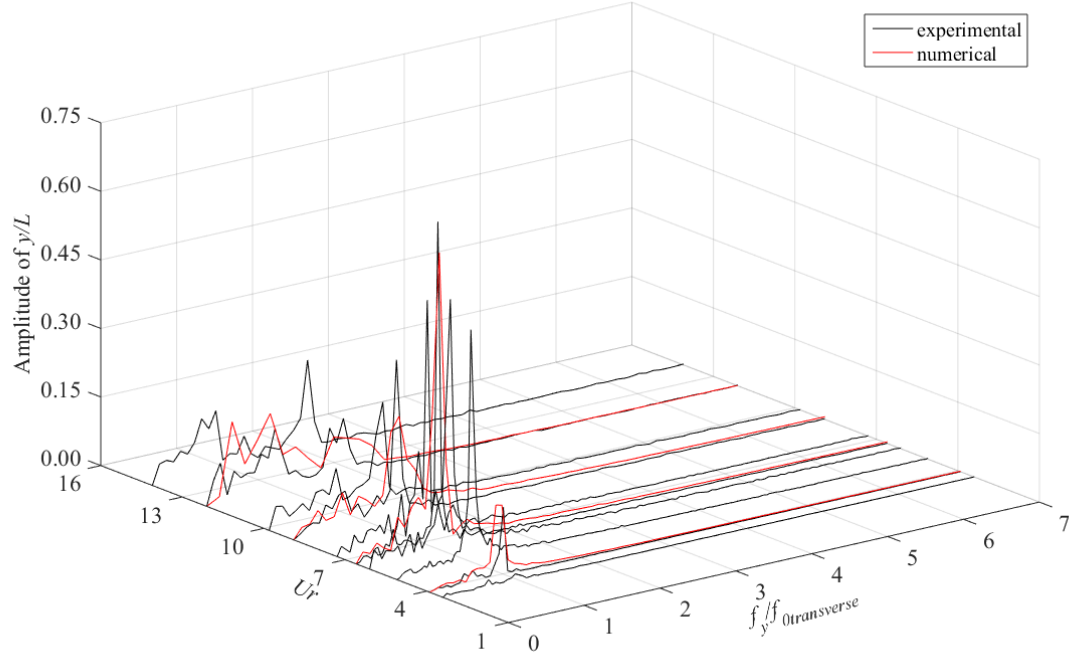


Figure 5.3 FFT of the motions in the transverse direction as a function of U_r and f_y for 45° incidence (the U_r is defined based on $T_{0transverse}$).

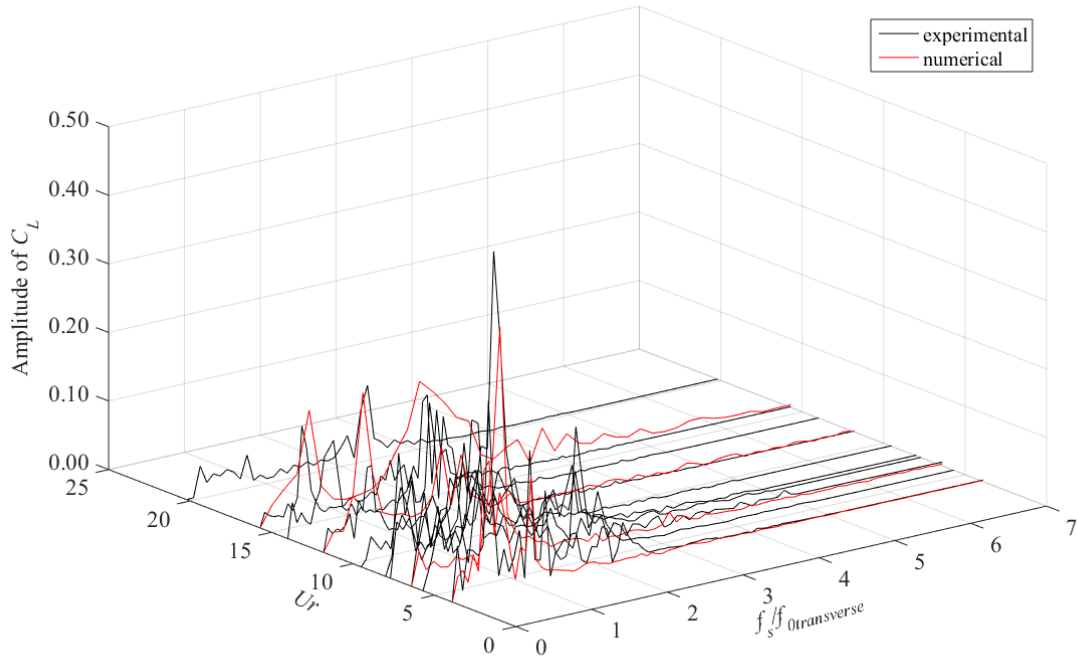


Figure 5.4 FFT of lift force coefficient as a function of U_r and f_s for 0° incidence (the U_r is defined based on $T_{0transverse}$).

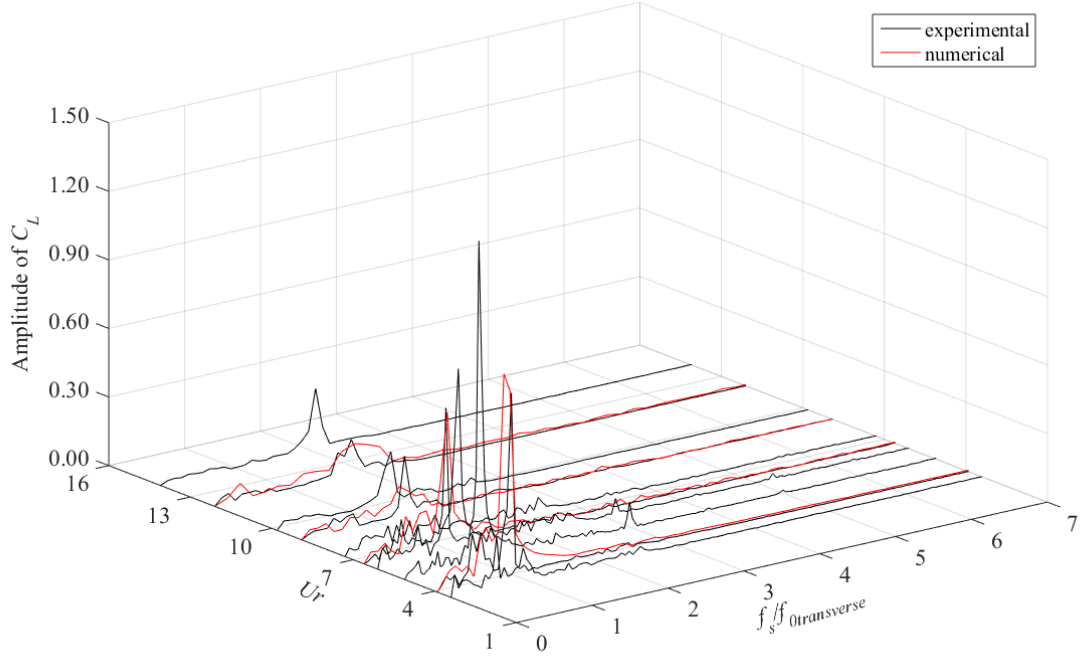


Figure 5.5 FFT of lift force coefficient as a function of Ur and f_s for 45° incidence (the Ur is defined based on $T_{0transverse}$).

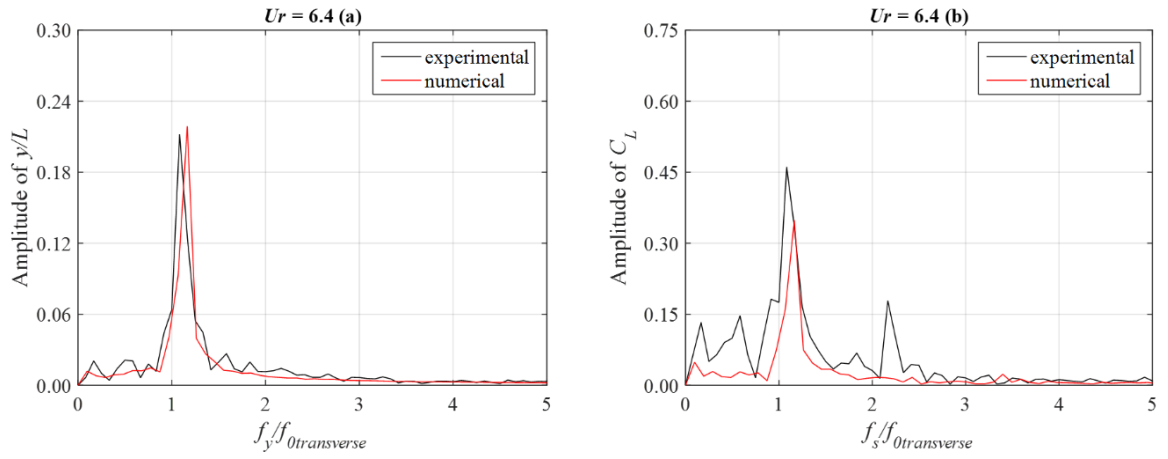


Figure 5.6 FFT of the transverse motions and the lift force coefficients at $Ur = 6.4$ for 0° incidence, (a) transverse motion (y/L); (b) lift force coefficient (C_L).

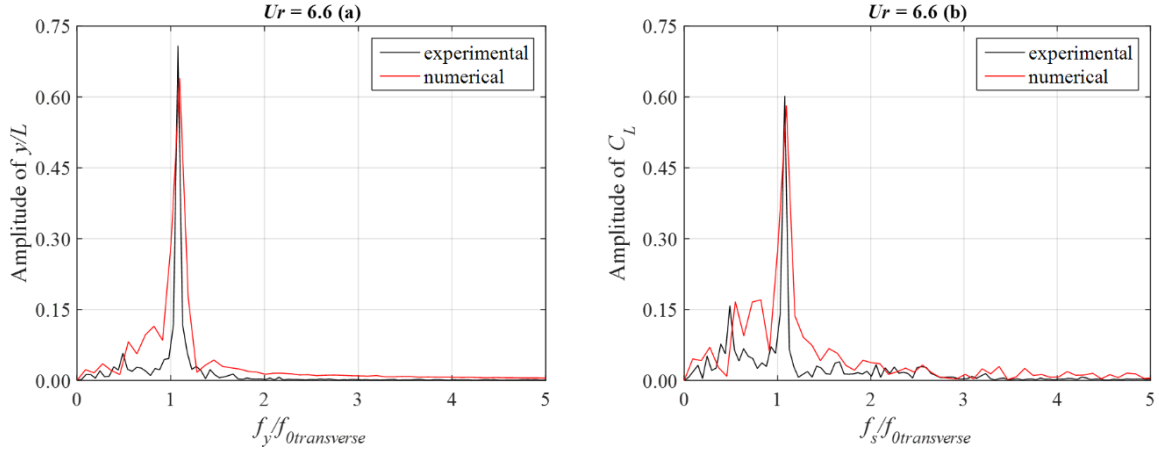


Figure 5.7 FFT of the transverse motions and the lift force coefficients at $Ur = 6.6$ for 45° incidence, (a) transverse motion (y/L); (b) lift force coefficient (C_L).

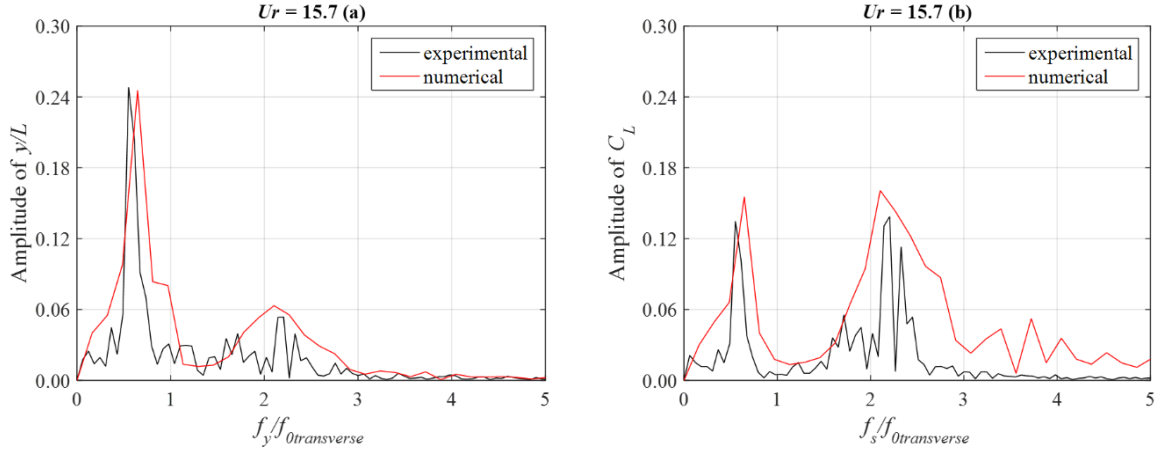


Figure 5.8 FFT of the transverse motions and the lift force coefficients at $Ur = 15.7$ for 0° incidence, (a) transverse motion (y/L); (b) lift force coefficient (C_L).

It is noted that the transverse motions are somewhat sinusoidal with near constant amplitude as would be expected at “lock-in”. However, in the “pre lock-in” and “post lock-in” region, the time history of the non-dimensional transverse amplitude shows considerable variability. Thus, a new variable called the significant value of transverse peaks ($H_{1/3}/L$) is introduced in the present study in order to examine the irregular characteristics of the transverse motions.

$$H_{1/3}/L = \frac{1}{\bar{f}_N} \sum_{m=1}^{\bar{f}_N} H_m/L, \quad (5.1)$$

where N is the number of the oscillations and L is the columns' width, the largest H_m has $m = 1$ and the lowest H_m is for $m = N$, H_m is the individual oscillation height which is defined as:

$$H_m = H_{peak} - H_{bottom}, \quad (5.2)$$

where H_{peak} and H_{bottom} are the points when $\frac{dy}{dt} = 0$ within one oscillation period.

Figure 5.9 presents $H_{1/3}/L$ as a function of Ur . It shows that, in the “pre lock-in” and “post lock-in” region, the present numerical model predicts the characteristic of the transverse motions well when compared with the experimental results. As can be seen in Figure 5.1 and Figure 5.9, the trend of $H_{1/3}/L$ is similar as A_y/L . It is noted that the value of $H_{1/3}/L$ is nearly double as A_y/L , which is due to A_y/L is defined as the standard deviation value of the oscillation amplitude. In addition, $H_{1/3}/L$ increases significantly from the “pre lock-in” region to the “lock-in” region. In the “post lock-in” region, $H_{1/3}/L$ shows a slightly difference comparing with A_y/L for 0 degree incidence. It does not increase rapidly as A_y/L in the “post lock-in” region. However, the value of $H_{1/3}/L$ at $Ur = 20.2$ is still larger than the peak value of $H_{1/3}/L$ in the “lock-in” region.

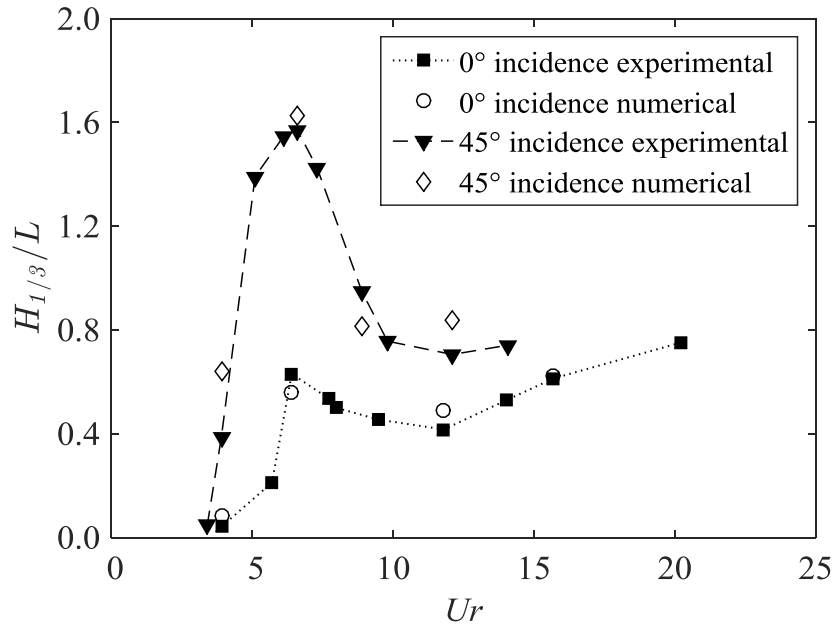


Figure 5.9 Significant values of the transverse peaks ($H_{1/3}/L$). The Ur is defined based on $T_{0transverse}$.

In addition, another variable called maximum characteristic amplitude is introduced to show the oscillation characteristics. The maximum characteristic amplitude (H_{max}/L) is defined as:

$$H_{max}/L = \frac{\max(Y(t)) - \min(Y(t))}{L}, \quad (5.3)$$

where, $y(t)$ represents the time series and L is the column width.

In Figure 5.10, the numerical predictions also show a good agreement compared with the experimental data.

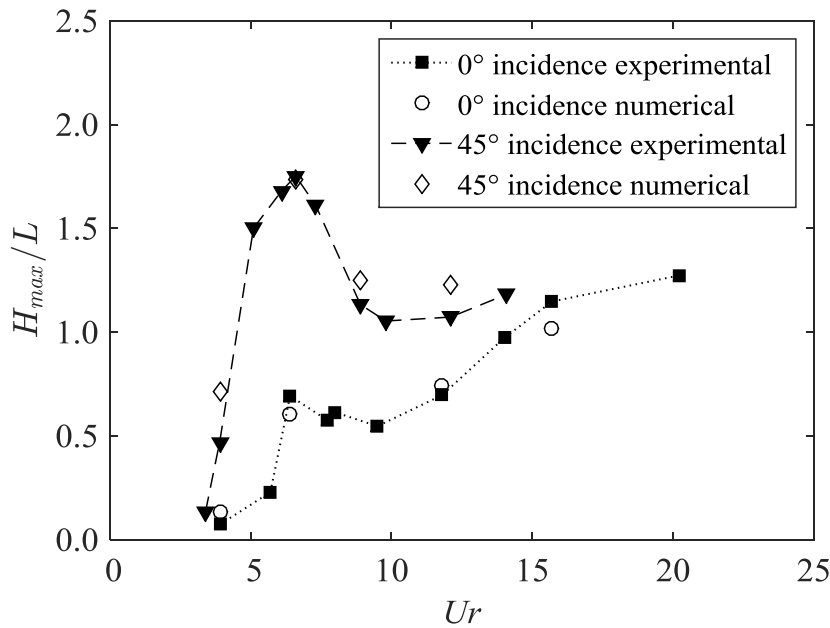


Figure 5.10 Maximum characteristic amplitude (H_{max}/L) of the transverse motion (the Ur is defined based on $T_{0transverse}$).

Figure 5.10 presents the maximum transverse motion response. Comparing with Figure 5.1, if H_{max}/L and A_y/L are the same, then the transverse motion behaviour would be a sinusoidal motion (the motion trajectory will be further discussed in section 5.1.4). The larger the difference shown in the two figures, the more variations in the transverse response amplitude are presented (Waals *et al.*, 2007). It is noted that H_{max}/L is closer to the trend of A_y/L compared to $H_{1/3}/L$.

Figure 5.11 presents the non-dimensional yaw amplitude. Figure 5.12 and Figure 5.13 present the yaw motions in the frequency domain as a function of Ur . In the current study, it is observed that the in-line, transverse and yaw natural frequencies are relatively close to each other. It is indeed true that sway and yaw motions would be significantly coupled if their natural periods are so close. The peak values of the transverse motion for all current incidences are observed in the range of $5 \leq Ur \leq 8$, and the synchronization for the yaw motions are presented in a range of $6 \leq Ur \leq 10$ similar to the transverse response, due to the natural periods of the transverse and yaw motions being close to each other. Gonçalves *et al.* (2012) pointed out that the largest yaw amplitudes occurred at $Ur \cong 8$ in which the reduced velocity was re-calculated using the yaw natural period. Thus, the coupling effect may increase the yaw motion but not critical.

The non-dimensional amplitude for the 0° incidence yaw motion shows the same trend as A_y/L . However, for 45° incidence, the yaw motion response is different from the transverse motion response. In the “lock-in” region, the non-dimensional yaw amplitudes at 0° incidence are larger than those at 45° incidence. For both flow incidences, the numerical method predicts the motion response trend well comparing with the experimental results. It is noted that in the numerical simulations, the mooring lines are idealised springs’ arrangement which are exactly symmetrical. However, in the experiments, slight differences can be observed in the forces on each side of the mooring lines possibly owing to the mooring lines being not exactly the same and the effects of spring bending due to the gravity on springs in the experimental set-up. The slight differences on the mooring lines cause the structure to have a small attack angle with the current flow during VIM. Especially for 0° incidence, the small attack angle makes the columns at the balance position not exactly perpendicular to the current leading to a slight variation in the hydrodynamic moment measurements. This may contribute to the discrepancies between the numerical predictions and the experimental data for the yaw motion.

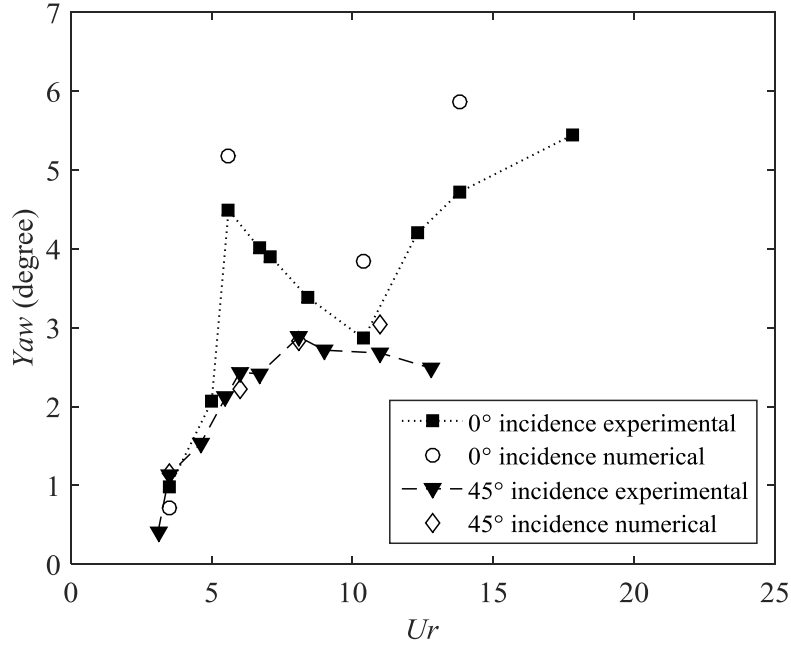


Figure 5.11 Non-dimensional yaw characteristics amplitude (the Ur is defined based on $T_{\theta_{yaw}}$).

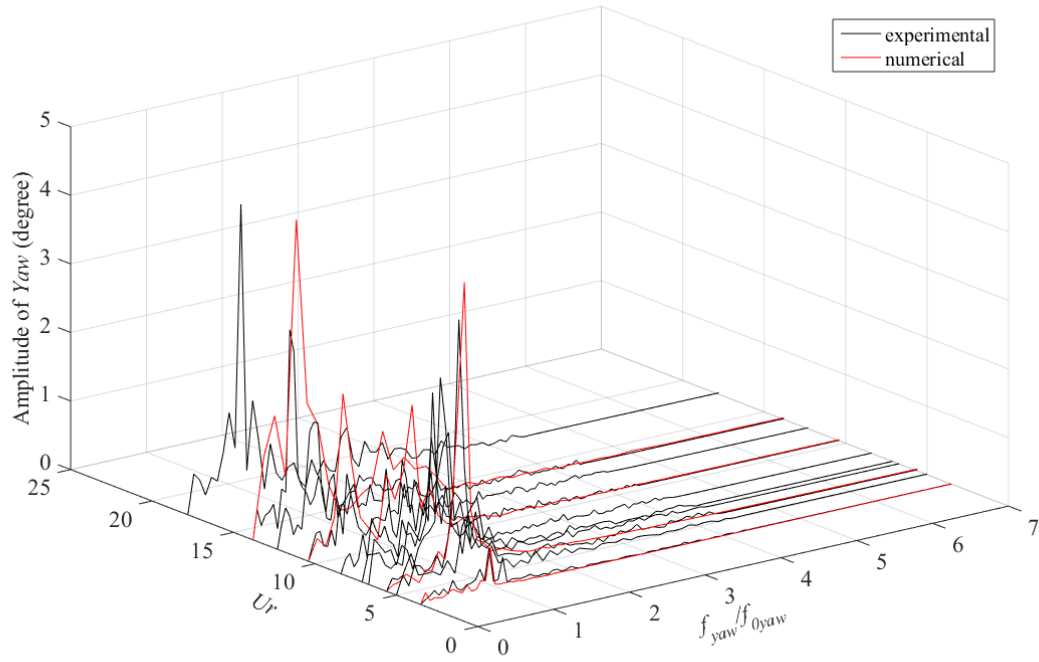


Figure 5.12 FFT of the yaw motion as a function of Ur and f_{yaw} for 0° incidence (the Ur is defined based on $T_{\theta_{yaw}}$).

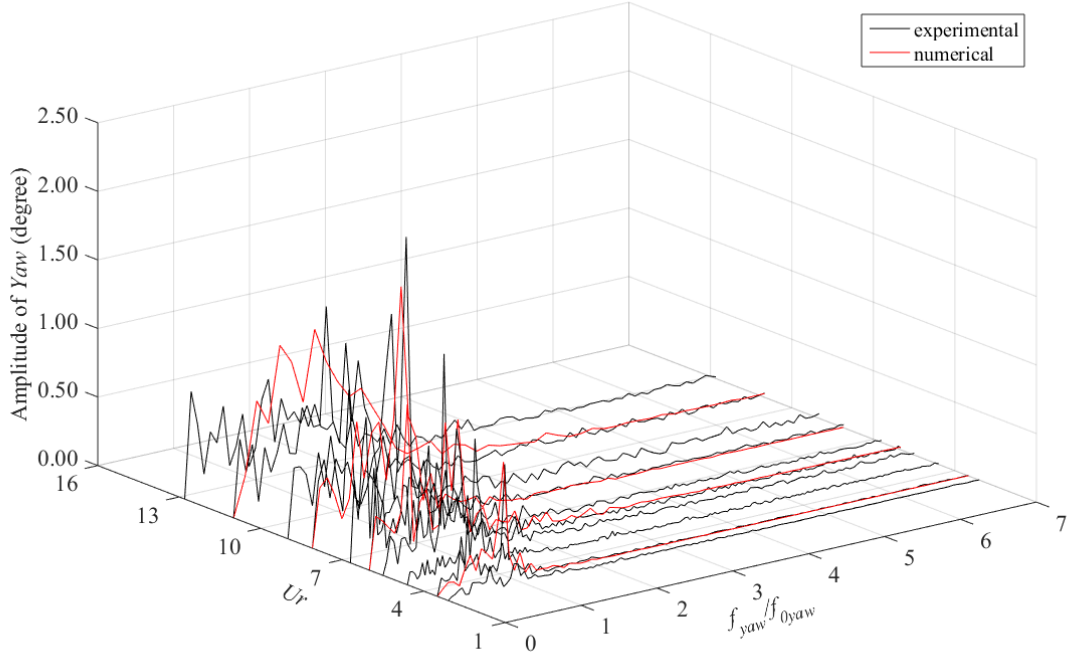


Figure 5.13 FFT of the yaw motion as a function of Ur and f_{yaw} for 45° incidence (the Ur is defined based on T_{0yaw}).

5.1.2 Force analysis

The fluid forces on the structure are calculated by the equation given by Sarpkaya (2004) as:

$$m\ddot{X}(t) + C\dot{X}(t) + K_x X(t) = F_x(t), \quad (5.4)$$

$$m\ddot{Y}(t) + C\dot{Y}(t) + K_y Y(t) = F_y(t), \quad (5.5)$$

where m is the platform mass; C is the structural damping coefficient; K_x and K_y are the linear spring constant in the in-line and transverse directions; $F_x(t)$ and $F_y(t)$ represent the in-line and transverse hydrodynamic forces acting on the structures.

As the structural damping coefficient is very small and can be disregarded, the hydrodynamic forces which include added mass and hydrodynamic damping forces due to fluid are placed on the right side of the equations. Thus, the Equation (5.4) and (5.5) can be written as:

$$m\ddot{X}(t) + K_x X(t) = F_x(t), \quad (5.6)$$

$$m\ddot{Y}(t) + K_y Y(t) = F_y(t), \quad (5.7)$$

In the present study, the total hydrodynamic forces in the experiments were measured indirectly by using the equations given by Sarpkaya (2004). However, the total hydrodynamic forces of the numerical predictions are obtained directly from the CFD simulations.

The drag coefficients for both 0° and 45° flow incidences are shown in Figure 5.14. For 0° incidence, the numerical results show a large discrepancy to experimental measurements at low Ur . This is possibly due to the extremely low towing speed (0.062 m/s for reduced velocity at $Ur = 3.9$) in the experiment where the mechanical friction in the system set-up affects the force measurements especially at the very low towing speed. In addition, the mooring lines can have the most striking effects on the results. To investigate this further, the mooring line forces have been examined in both the experiment measurement and the numerical simulation. As shown in Table 5.1, the numerical predictions show that the forces on the mooring lines are symmetrical along the in-line direction. However, in the experiments, slight differences can be observed in the forces on each sides of the mooring lines possibly owing to the mooring lines being not exactly same and the effects of spring bending by the gravity in the experimental set-up. The differences of the mooring force between the upstream mooring lines (Mooring line 1 and Mooring line 2) are smaller than the downstream mooring lines (Mooring line 3 and Mooring line 4). The asymmetrical forces in the mooring lines make the motions of the structure asymmetrical. Especially for 0° incidences cases, the asymmetrical forces in the mooring lines make the structure to have a small attack angle with the current flow. This rotational offset is the main contributor to the differences between numerical predictions and experimental data. When the Ur increases, the offset of the platform relative to the in-line direction also increases leading to the forces on the downstream mooring line decreasing. Consequently, the effect of the force difference in the downstream mooring lines is weakened with increasing Ur . Therefore, the numerical results agree well with experimental measurements for high Ur for 0° incidence.

As shown in Figure 5.14, \bar{C}_D increases when “lock-in” occurs. This is because the fluctuations of the force on the structure were excited by resonance. As can be seen in Figure 5.14, \bar{C}_D at 45° incidence is higher than that at 0° incidence. Similar observation was also reported by Sumer and Fredsøe (1997) for flow past a sharp-corner square cylinder.

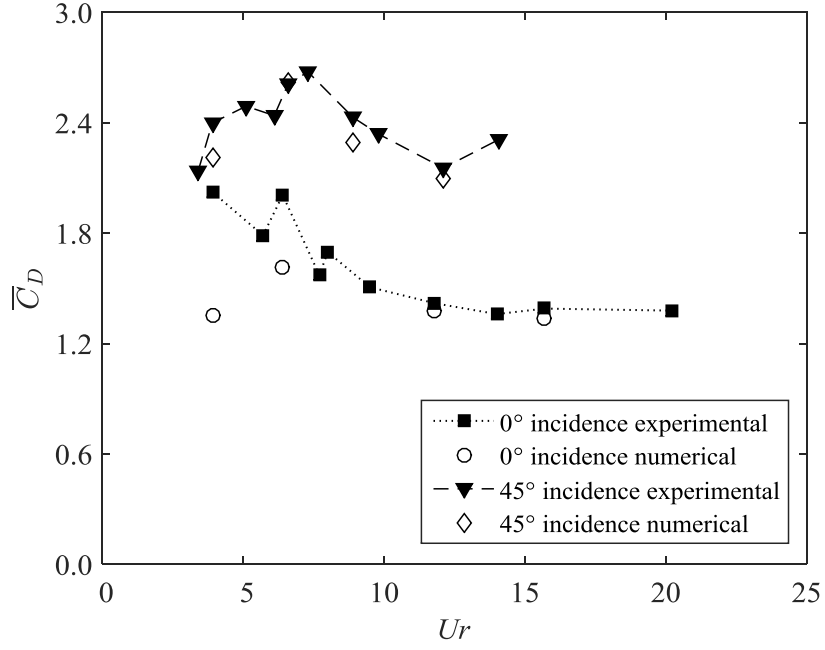


Figure 5.14 Mean drag coefficient (\bar{C}_D), where A is the projected area at 0° incidence.

Table 5.1 Comparison of the mooring line mean forces for 0° incidence at $Ur = 3.9, 6.4$ (The mooring lines arrangement is shown in Figure 3.3).

Mean mooring force	Mooring line 1 (N)	Mooring line 2 (N)	Mooring line 3 (N)	Mooring line 4 (N)
$Ur = 3.9$ numerical	7.365	7.375	6.425	6.415
$Ur = 3.9$ experimental	7.489	7.745	6.445	5.896
$Ur = 6.4$ numerical	8.481	8.405	5.523	5.601
$Ur = 6.4$ experimental	8.617	8.934	5.417	4.859

5.1.3 Vortex shedding characteristics

To have a general visual appreciation of the vortex shedding pattern, the vorticity magnitude contours obtained from the numerical simulations for “pre lock-in”, “lock-in” and “post lock-in” regions are plotted in Figure 5.15.

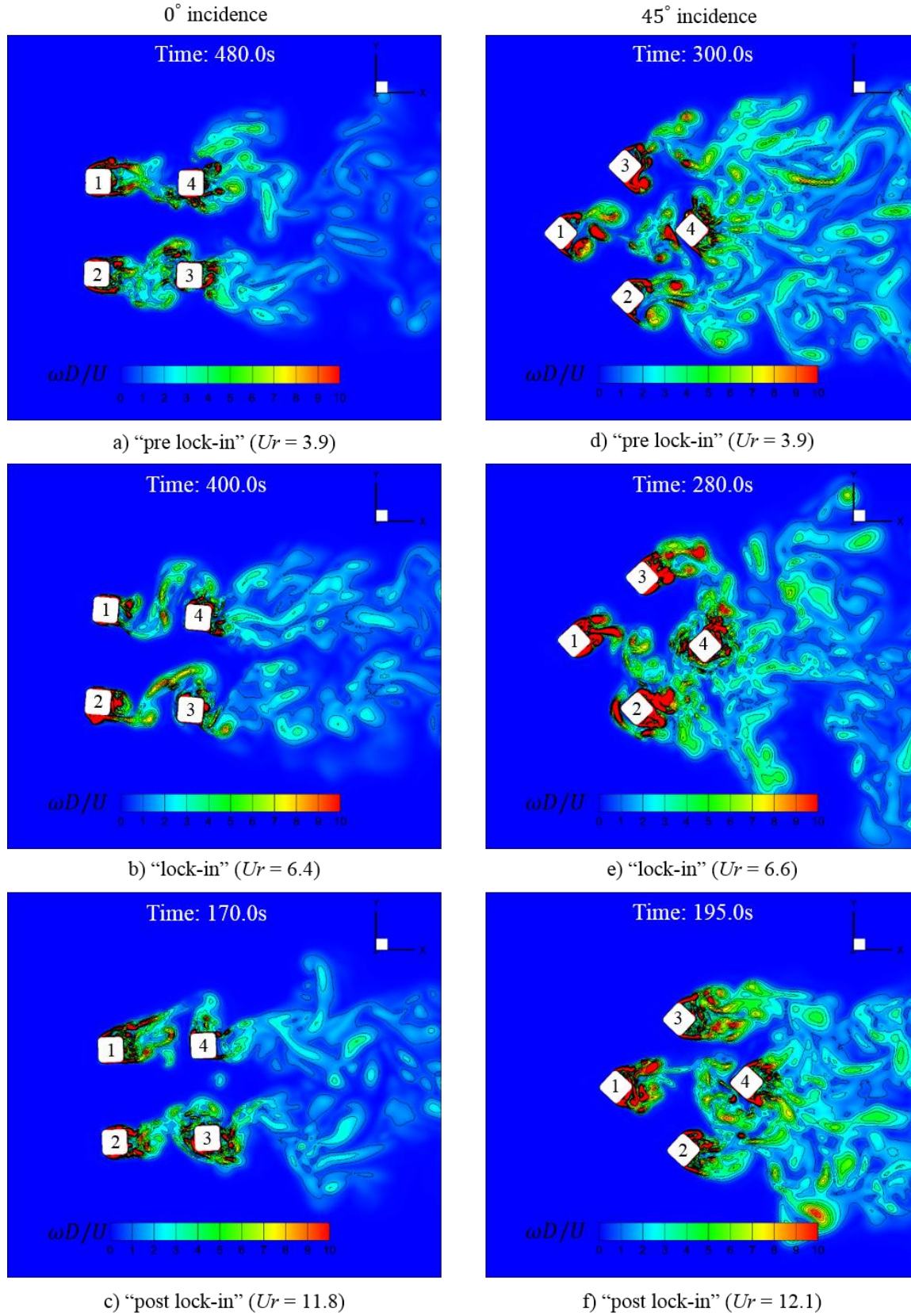


Figure 5.15 Non-dimensional vorticity magnitude ($\omega D/U$) contours of the DDS model for “pre lock-in”, “lock-in” and “post lock-in” regions for 0° and 45° incidence, XY plane at middle draft location of the DDS.

Figure 5.15 presents the three-dimensional vorticity magnitude ($\omega D/U$, where $\omega = \sqrt{(\omega_x^2 + \omega_y^2 + \omega_z^2)}$). As can be seen, under 45° incidence, in the “pre lock-in” region, the vortices that form and then detach from column 1 can only impinge directly on column 3 located downstream. However, in the “lock-in” region, it can be clearly seen that the vortices detached from column 1 directly act on column 2. As the vortex shedding frequency at this reduced velocity closes to the natural frequency of the structure, the vortices acting on the structure become synchronised with the model oscillation. This is the reason that causes “lock-in” to occur. In the “post lock-in” region, the vortices detached from column 1 strongly act on column 3 again, and the vortex shedding frequency starts to be away from the natural frequency of the structures resulting in the decreased structure motion.

At 0° incidence, the phenomena of VIM are similar to that at 45° incidence. Since the column leading surfaces are vertically faced to the current, the vortices that are detached from the upstream columns are not as significant as those in the 45° incidence cases. However, it can still be clearly seen that in the “lock-in” region, the vortices detached from the upstream columns directly act on the downstream columns.

5.1.4 Correlation of vortex shedding, force and VIM

The flow patterns at the peak transverse motion point may reveal the key factor which induced the VIM. The vortex shedding patterns, at the time instances close to the transverse motion peak value occurrence within one oscillation period, are shown in Figure 5.16, Figure 5.17, Figure 5.18 and Figure 5.19. Additionally, sub-picture (B) presents the vortex shedding process between the two peak point and sub-picture (D) presents the vortex shedding process after the peak point C (see Figure 5.16, Figure 5.17, Figure 5.18 and Figure 5.19), in order to show the continuous vortex shedding process within one VIM oscillation period.

Figure 5.16 presents the time history of the transverse motions, the lift force coefficient the vorticity contours and the motion trajectory under 0° incidence at $Ur = 3.9$ (“pre lock-in”). The sub-pictures A, B, C and D show the vorticity contours within one complete vortex shedding period. As can be seen in Figure 5.16, the vortices shed from the upstream columns directly impinge on the front faces of the downstream columns. The downstream columns correspondingly break or degrade the vortices being shed from the upstream columns. Unlike the vortices shed from the upstream columns, only relatively small vortices can be seen in the

wake region of the downstream columns. Thus, the vortices are broken into small elements with weak vortices by the downstream columns. As the small vortices are asymmetrical, generated by breaking the vortices shed from the upstream columns, the corresponding lift force are fluctuating asymmetrically as well. The time histories of the transverse motions and the lift forces show the same trend in Figure 5.16.

Similar to Figure 5.16, Figure 5.17 presents the time history of the transverse motions, the lift force coefficients, the vorticity contours and the motion trajectory under 0° incidence at the higher reduced velocity of $Ur = 6.4$ (“lock-in”). With the increase of Ur , in the “lock-in” region, the vortices shed from the upstream columns act on the downstream columns as if vortices being “shed” of a significant nature from the downstream column itself. The vortices are nearly symmetrically generated in the downstream area of the platform and the vortex street can be clearly seen in the vorticity contours in Figure 5.17. This makes both the C_L variations and the time history of the transverse motions to become more symmetrical. Because the vortex shedding frequency is close to the overall structure’s natural frequency in the transverse direction, the structure’s motion trajectory in the transverse direction is nearly same as the vortex shedding trajectory. Hence, the motions of the downstream columns do not break apart the vortices shed from the upstream columns. The vortices formed upstream are acting together with the downstream formed vortices thus to enhance the motions of the structure. Moreover, as the vortices shed from the upstream columns are not effectively broken by the downstream columns, the whole wake region of the structure is significantly enhanced. Similarly, the non-dimensional force fluctuations and corresponding motions are induced by the enhanced wake region. This can be clearly seen in Figure 5.17. It is to be noted that the trends of the lift force coefficient and the transverse motions are nearly the same indicating that when the lift force reaches to a peak value, the transverse motion also approaches a peak value.

In the “post lock-in” region, as shown in Figure 5.18, the downstream columns break the vortices shed from the upstream columns. Due to the vortex shedding frequency increasing more rapidly than the structure’s motion frequency (this can be seen by comparing Figure 5.2 and Figure 5.4), the vortices shed from the upstream columns are broken by the lateral motion of the downstream columns. However, as the current speed increases, the strength of the vortices is stronger than in the “pre lock-in” region. Although the vortices shed from the upstream columns are seen broken by the downstream columns, “strong vortices” can still be found in the downstream area of the platform. However, the vortex street is not clearly seen as the case in the “lock-in” region. The vortices show a disordered structure in the downstream

area. The time history of the lift force coefficient similarly becomes irregular and has less correlation with the time history of the transverse motions. The transverse motion still however has a general trend similarity to the lift force coefficient.

When the flow incidence changes to 45° , the attack angle of the columns makes the transverse motions more pronounced than that for the 0° incidence condition. With the attack angle of 45° , the columns are not vertically faced to the current. When the vortices shed from the upstream column hit on the downstream column leading faces and edge, the vortices explode and spread far more on the transverse direction compared with 0° incidence. Because three columns are on the downstream area at 45° incidence, the vortex street is more complicated compared with the vortex street at 0° incidence. Figure 5.19 presents the time histories of the lift force coefficient, the motions, the vorticity contours and the motion trajectory at 45° incidence. It is seen that the trends of the time history of C_L and the transverse motions fluctuations are nearly the same. Good correlation between the lift force and the transverse motions is also observed.

The motion trajectories are also plotted in Figure 5.16, Figure 5.17, Figure 5.18 and Figure 5.19. According to the 0° incidence results, there are no eight-shaped trajectories appeared. However, at 45° incidence, the eight-shaped trajectory can be found in the “lock-in” region as those typically presented for a single cylindrical structure.

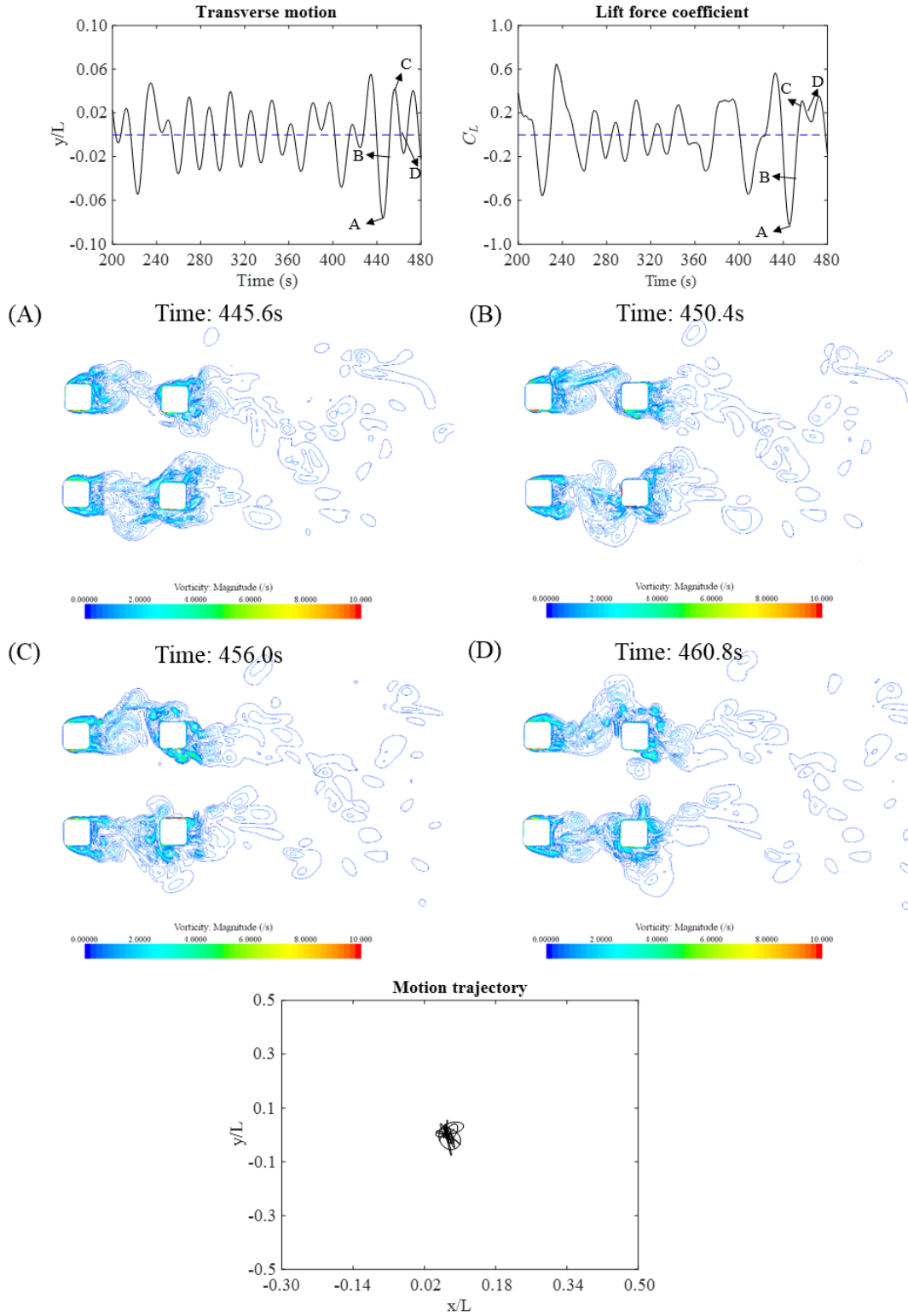


Figure 5.16 Time history of the motion in the transverse direction (y/L), lift force coefficient (C_L) for 0° incidence at $Ur = 3.9$ (pre lock-in), the vorticity contours in the XY plane at middle draft of the DDS (A and C refer to the point close to the transverse motion peak value within one oscillation period, B is the vortex shedding process between A and C, D is the vortex shedding process after C, corresponded simulation time are shown in the figure), and the motion trajectory in the XY plane.

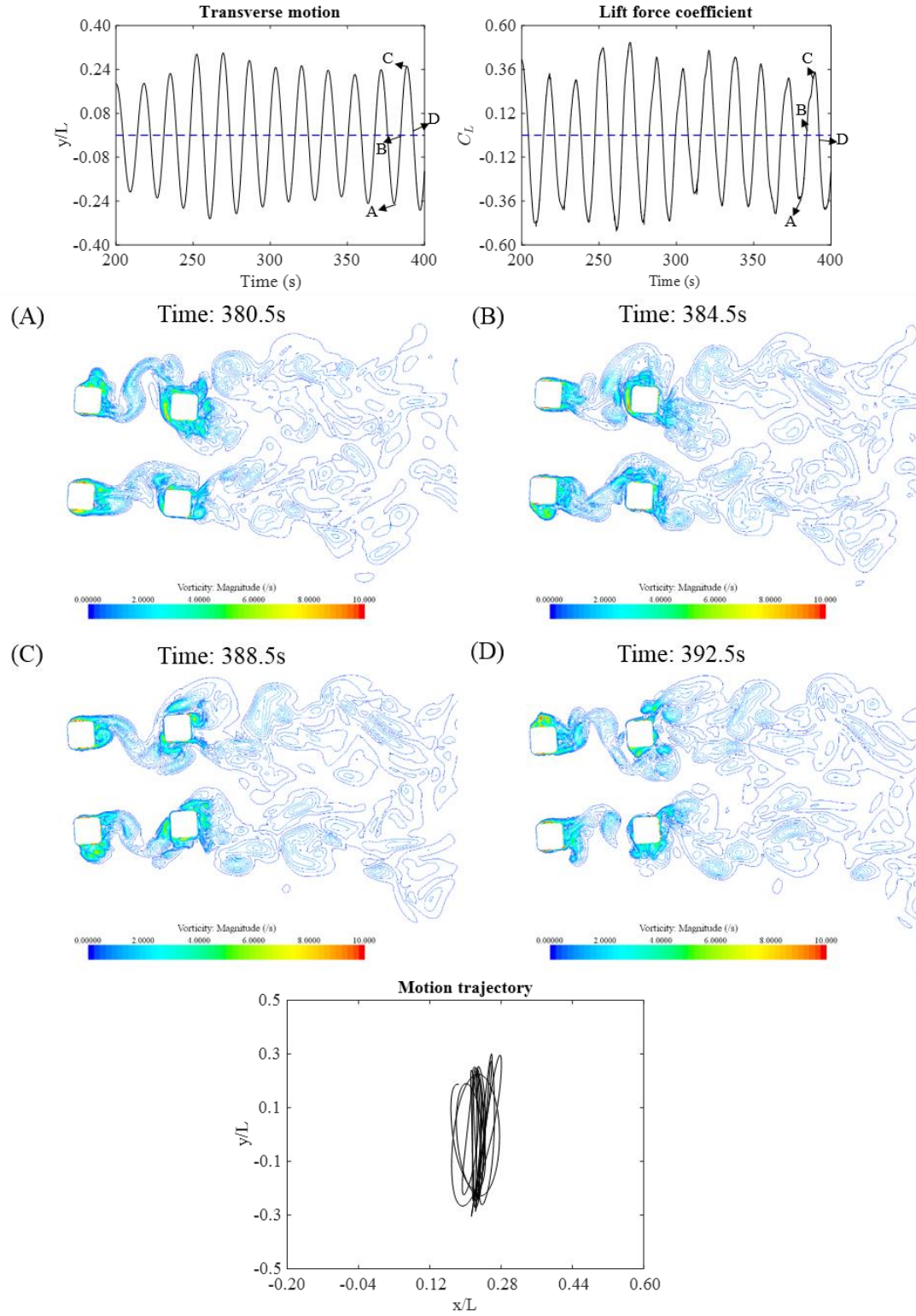


Figure 5.17 Time history of the motion in the transverse direction (y/L), lift force coefficient (C_L) for 0° incidence at $Ur = 6.4$ (lock-in), the vorticity contours in the XY plane at middle draft of the DDS (A and C refer to the point close to the transverse motion peak value within one oscillation period, B is the vortex shedding process between A and C, D is the vortex shedding process after C, corresponded simulation time are shown in the figure), and the motion trajectory in the XY plane.

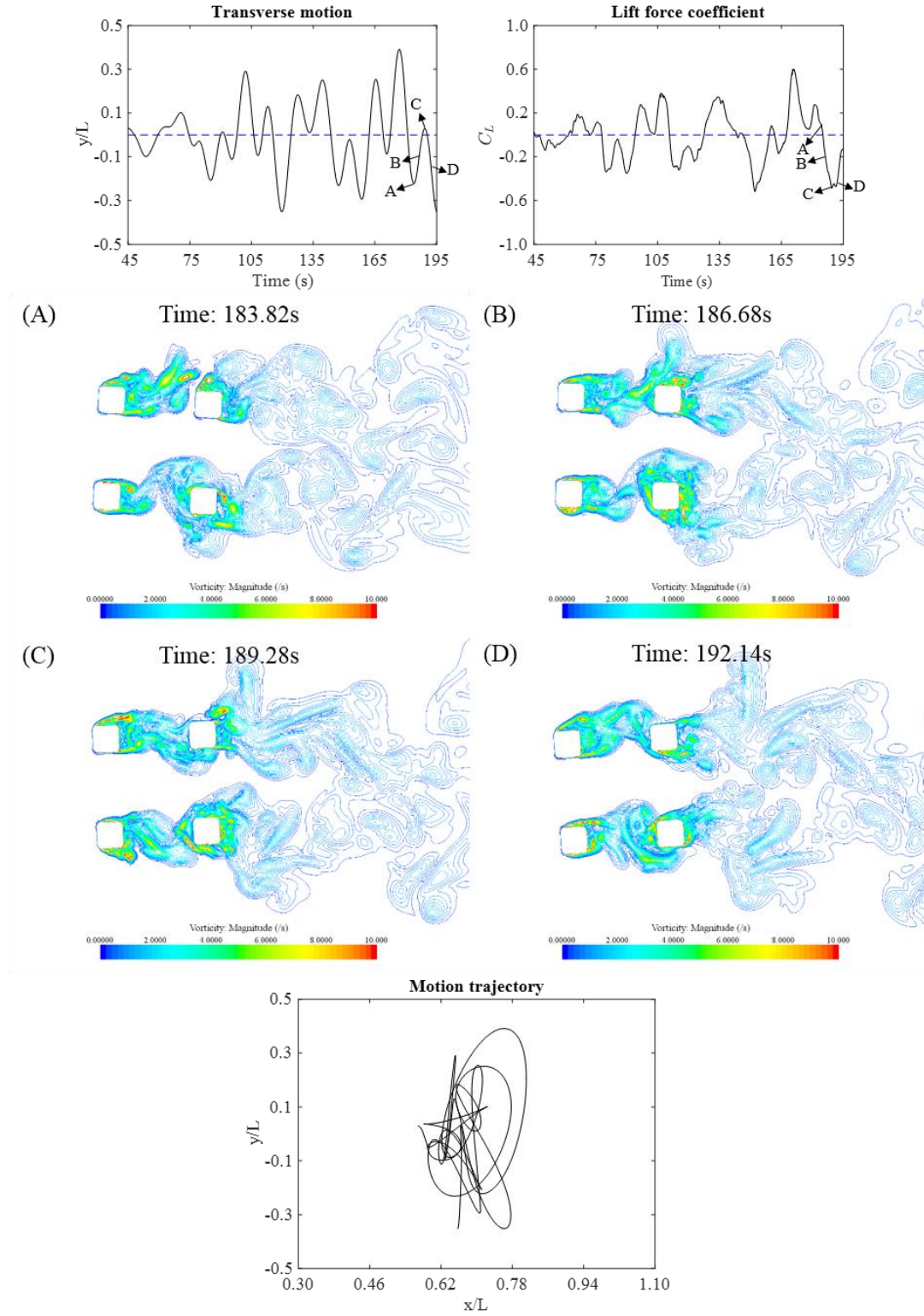


Figure 5.18 Time history of the motion in the transverse direction (y/L), lift force coefficient (C_L) for 0° incidence at $Ur = 11.8$ (post lock-in), the vorticity contours in the XY plane at middle draft of the DDS (A and C refer to the point close to the transverse motion peak value within one oscillation period, B is the vortex shedding process between A and C, D is the vortex shedding process after C, corresponded simulation time are shown in the figure), and the motion trajectory in the XY plane.

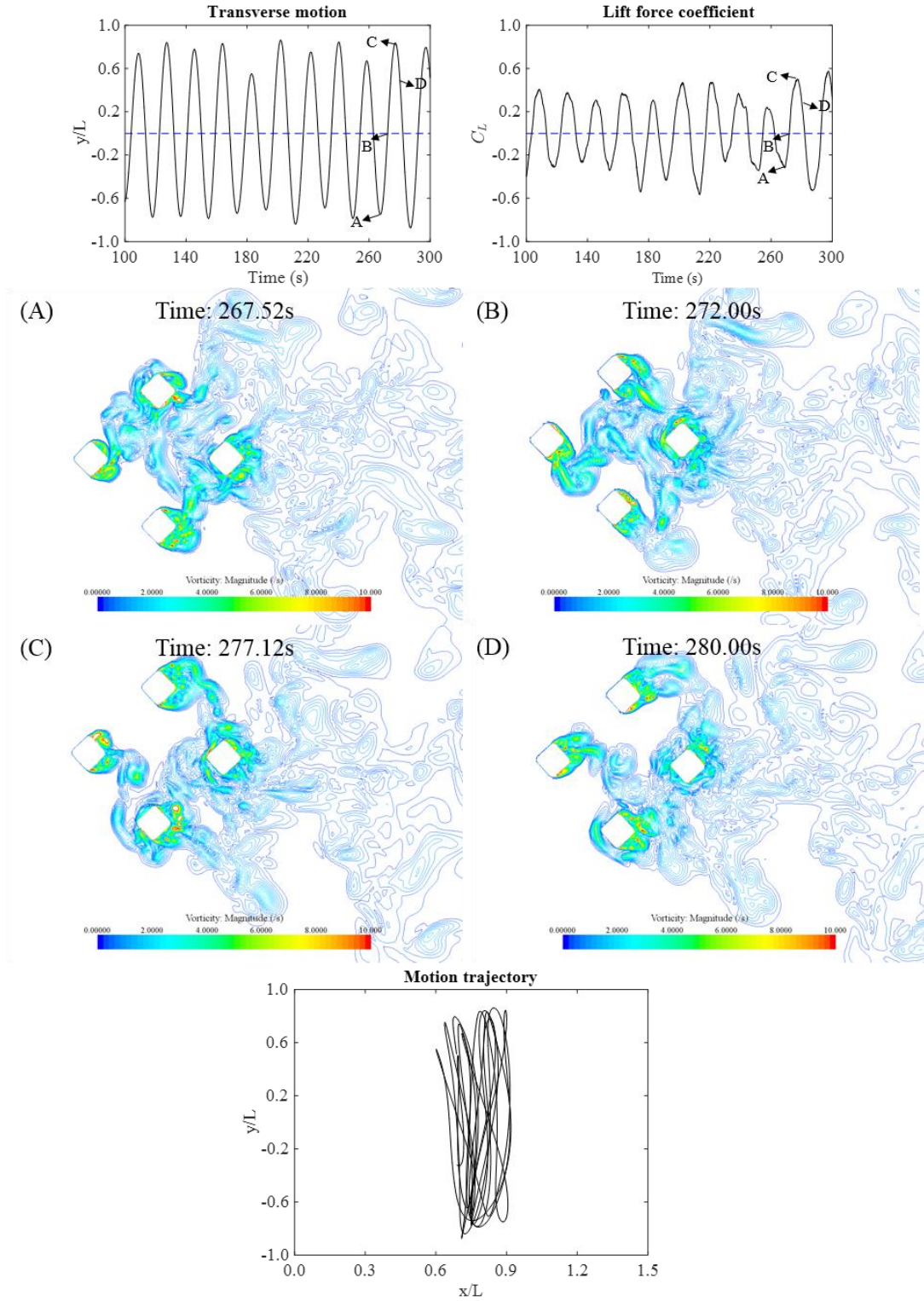


Figure 5.19 Time history of the motion in the transverse direction (y/L), lift force coefficient (C_L) for 45° incidence at $Ur = 6.6$ (lock-in), the vorticity contours in the XY plane at middle draft of the DDS (A and C refer to the point close to the transverse motion peak value within one oscillation period, B is the vortex shedding process between A and C, D is the vortex shedding process after C, corresponded simulation time are shown in the figure), and the motion trajectory in the XY plane.

5.2 Interaction of vortex shedding processes at 45° angle of incidence

As confirmed in both the field measurements and the model tests (Waals *et al.*, 2007; Rijken and Leverette, 2008; Magee *et al.*, 2011; Gonçalves *et al.*, 2012; Ma *et al.*, 2013; Lee *et al.*, 2014; Koop *et al.*, 2016), as well as the present study, for square-section shaped multi-column structures, the most severe transverse motion occurred at 45 degree incidence. As Koop *et al.* (2016) noted, the scale effects of a DDS in a 45 degree flow are less than that in a 0 degree flow. This indicates that the Reynolds number does not have a significant effect on the model predictions at 45 degree incidence. Aiming to investigate the VIM of a DDS at a realistic field condition with the real engineering applications, the flow over a VIM model of a DDS at 45 degree incidence have been numerically investigated after the rigorous validation against the experimental data. The hydrodynamic loads on different members of the structure, including four columns and pontoons, are compared in order to quantify the determining factors which induced VIM excitation. Moreover, the flow patterns are further examined to reveal the insights of the vortex dynamics associated with VIM.

In addition, a hysteresis phenomenon was observed between the force and motion domains - the peak lift force occurs slightly earlier than the peak transverse motion. Due to this phenomenon, one more numerical simulation case is further conducted to examine the mechanism of the hysteresis phenomenon.

In this section, the numerical simulations of the flow over a three-degree-of-freedom deep-draft semi-submersible model with different Reynolds numbers from 3.6×10^4 to 1.1×10^5 are carried out to investigate the overall hydrodynamics of the structure. Results for all cases are obtained by averaging after more than ten vortex shedding cycles. Although the sample size is relatively small, the reliability and sensitivity of the relatively small data set on the results have been discussed by Zhang *et al.* (2014). The current numerical predictions are subsequently validated by the motion and force measurements obtained from the corresponding experiments undertaken in a towing tank (as discussed in section 4.3). The characteristics of vortex shedding processes and their interactions due to multiple cylindrical columns are also discussed (Liang and Tao, 2017).

5.2.1 Motion characteristics

Figure 5.20, Figure 5.21 and Figure 5.22 present the non-dimensional transverse, in-line and yaw motion amplitudes obtained from the numerical simulations and the experimental measurements. In each case, the numerical predictions show a good agreement with the experimental results. However, at low Ur values, the numerical simulation predicts a slightly larger transverse response than the experimental data. An analysis of the error will be given in the following section together with the added mass analysis. From the non-dimensional transverse characteristic amplitude shown in Figure 5.20, the “lock-in” phenomenon can be clearly seen occurring in a reduced velocity range from 5 to 9. The transverse motion increased rapidly from the “pre lock-in” region to the “lock-in” region, and then sharply declined from the “lock-in” region to the following “post lock-in” region. The peak point for the transverse motion occurred at $Ur = 6.6$.

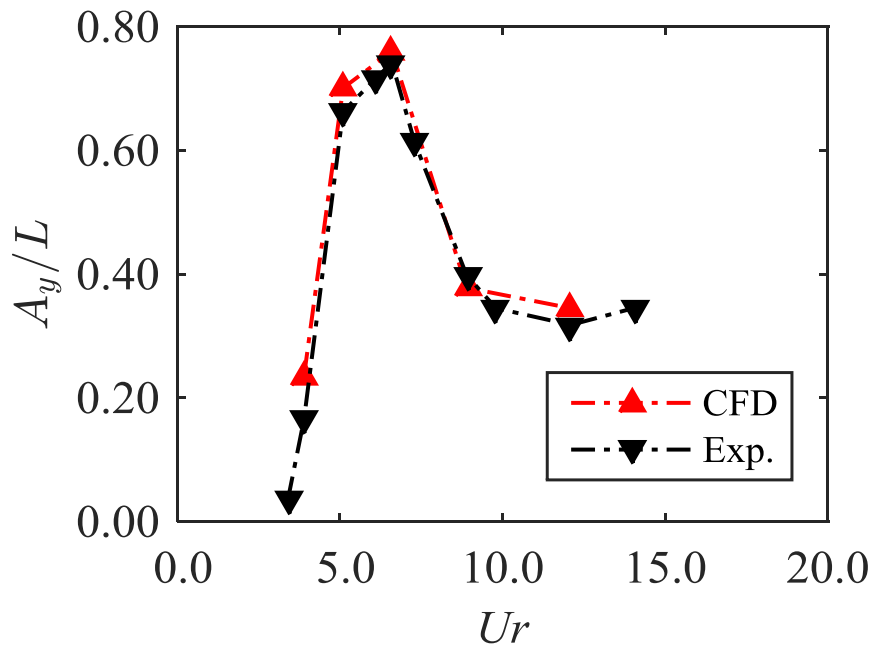


Figure 5.20 Non-dimensional transverse characteristic amplitudes (A_y/L), the Ur is defined based on the natural period of the transverse motion.

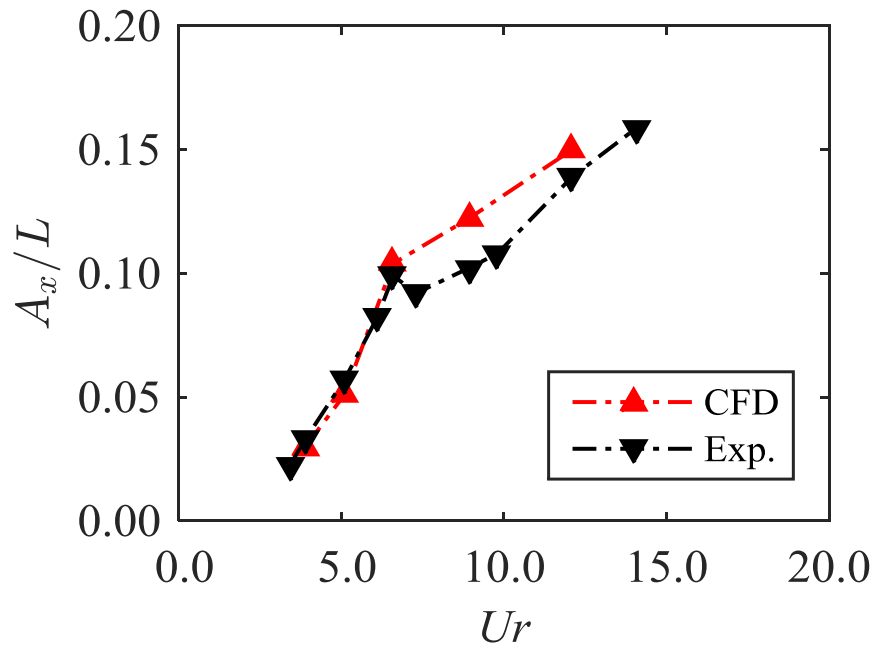


Figure 5.21 Non-dimensional in-line characteristic amplitudes (A_x/L), the U_r is defined based on the natural period of the transverse motion.

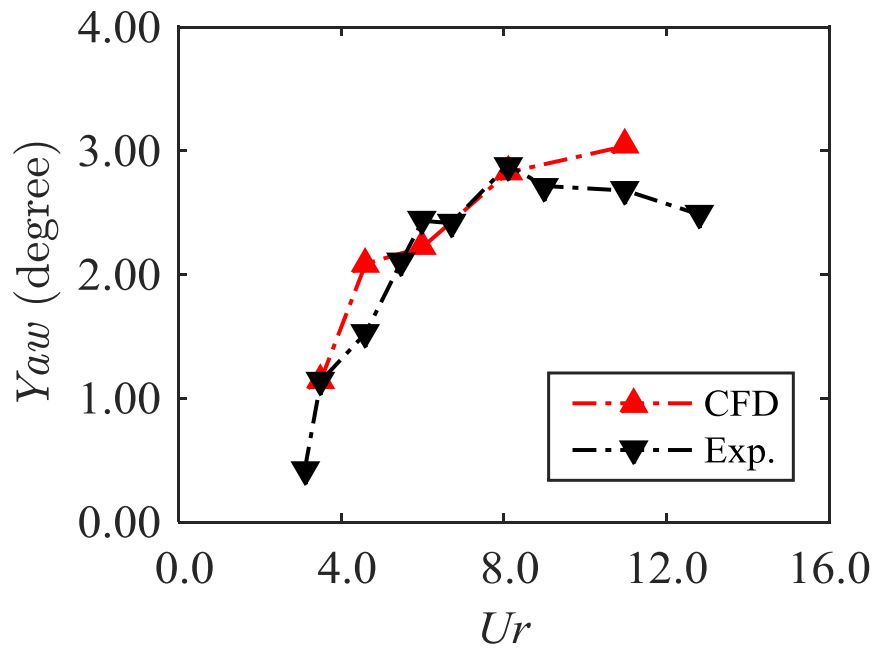


Figure 5.22 Non-dimensional yaw characteristic amplitudes, the U_r is defined based on the natural period of the yaw motion.

5.2.2 Drag and lift force analysis

In order to study the fluctuation forces responsible for VIM, the lift and drag forces and the related coefficients are further analysed. Figure 5.23 and Figure 5.24 show the mean drag force coefficient (\bar{C}_D) and the root-mean-square lift force coefficient (C_{Lrms}) respectively as a function of the reduced velocity (Ur) for both numerical and experimental results.

The numerical method predicts well compared with the experimental measurements. However, as can be seen in Figure 5.24, there is a discrepancy between the numerical predictions and the experimental data at low reduced velocity levels for the root-mean-square lift force coefficient, similar to the trend observed in the non-dimensional transverse characteristic amplitudes in Figure 5.20.

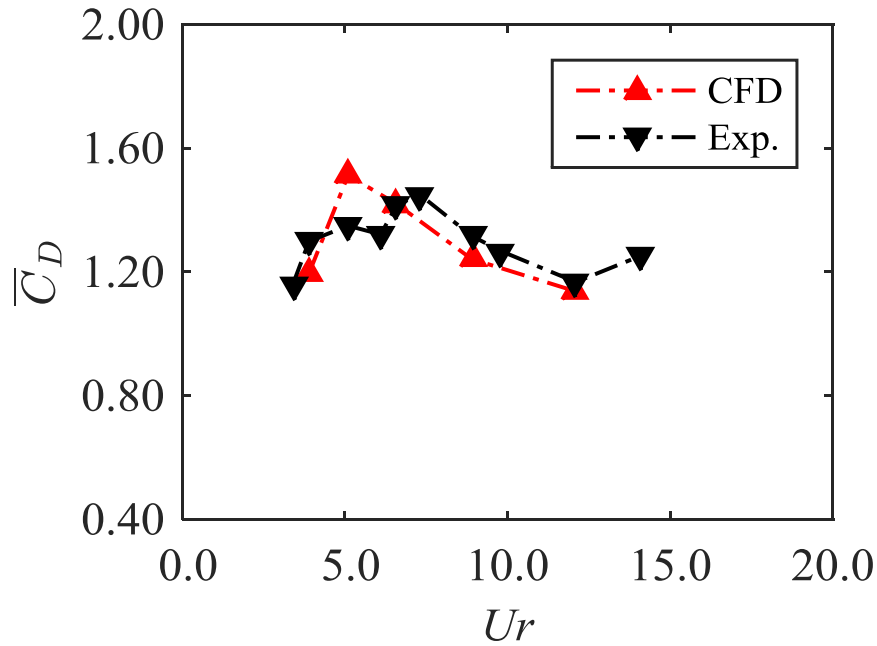


Figure 5.23 Mean drag coefficient (\bar{C}_D) from the numerical and experimental results on the VIM model, the Ur is defined based on the natural period of the transverse motion.

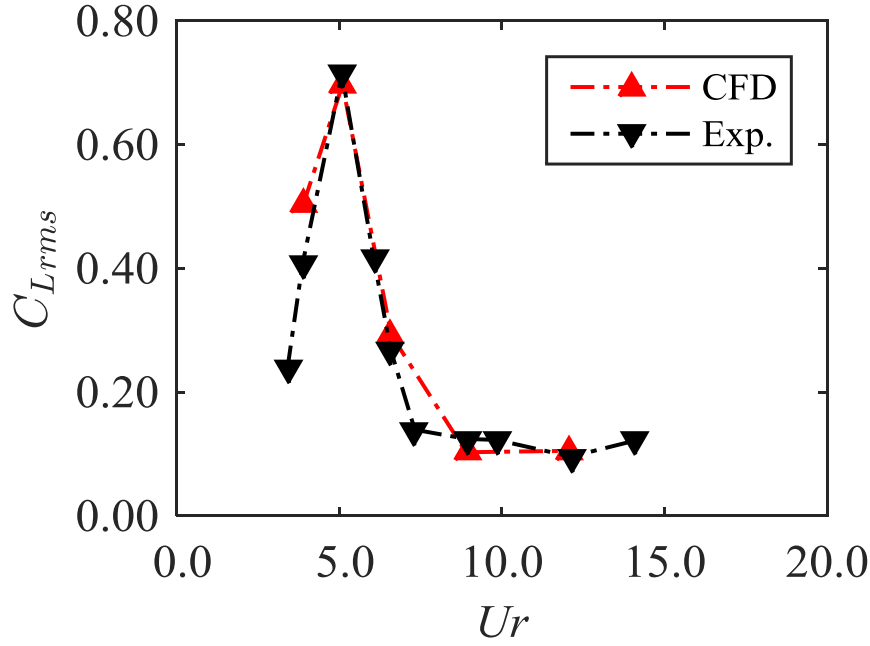


Figure 5.24 Root-mean-square lift coefficient (C_{Lrms}) from the numerical and experimental results on the VIM model, the Ur is defined based on the natural period of the transverse motion.

To further examine the differences, a virtual variable so-called added mass coefficient (C_a) has been introduced to compare the differences between the numerical predictions and the experimental measurements. Similar to the discussions made by Sarpkaya (2004) in their vortex-induced vibrations study, Zhang *et al.* (2014) introduced this variable into a Spar VIM investigation. In their work, the added mass coefficient (C_a) is estimated by the equations proposed by Vikestad *et al.* (2000) as follows:

$$C_a = \frac{m_a}{\rho\Delta}, \quad (5.8)$$

$$C_a = -\frac{2}{nT\rho\Delta(\sqrt{2}rms(\dot{y}))^2} \int_t^{t+nT} F_y \ddot{y} dt, \quad (5.9)$$

where n is an integer number of oscillation periods, nT is the time length, ρ is the fresh water density, Δ is the displacement of the structure, F_y is the cross-flow component of the total hydrodynamic force on the structure and y is the transverse displacement of the motion.

Figure 5.25 shows the comparison of the added mass coefficients (C_a) obtained from the numerical calculations and the experiments. The numerical prediction shows a decreasing trend similar to that reported in an earlier study by Zhang *et al.* (2014). This trend is also the same as

the results from the studies conducted by Sarpkaya (2004). However, the added mass coefficient (C_a) obtained from the experimental measurements at low reduced velocity range are significantly different to those from the present numerical predictions. A distinct feature shown in Figure 5.25 is that the added mass coefficient from experiments is much smaller at very low Ur and tends to increase initially and then decrease rapidly with the increases of the reduced velocity. The apparent discrepancy between the numerical and experimental results at low reduced velocities is likely to be caused by the experimental measurements. There are a few possibilities that could cause the error. Firstly, the towing speed during the experiment is extremely low for an equivalent low reduced velocity (for example, 0.073 m/s for reduced velocity at $Ur = 3.4$), and the whole system mechanical friction may affect the experimental measurements at such a low towing speed; secondly, the influence of the mooring line settings may also affect the experimental measurements, because the theoretically linear springs set in numerical simulations are ideal springs and the mooring lines in the experimental set-up may not be arranged as symmetrically as in the numerical simulations. Due to these factors, the numerical results may be more reliable and accurate than the experimental data in the low reduced velocity range.

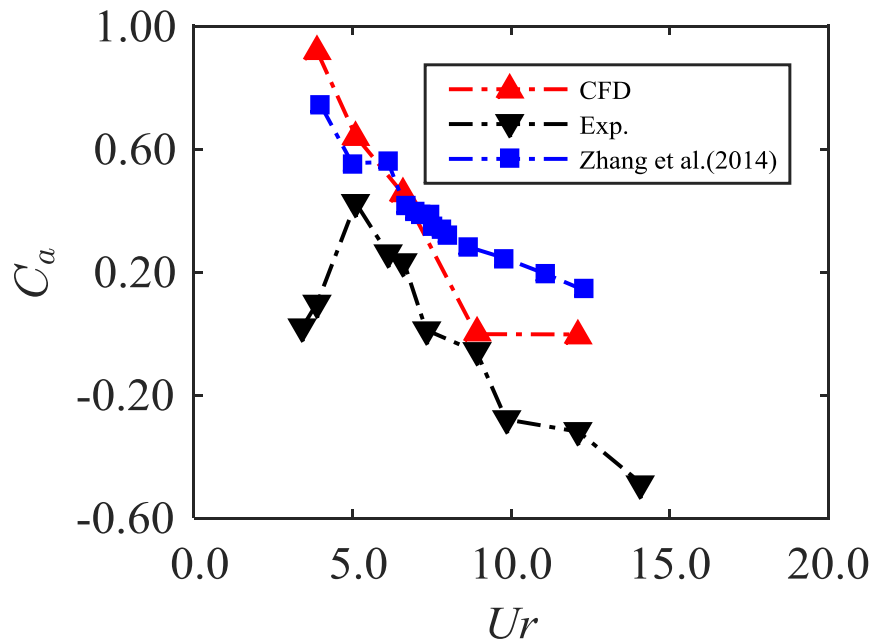


Figure 5.25 Added mass coefficient (C_a) of the VIM model from the numerical predictions and the experiments, the Ur is defined based on the natural period of the transverse motion. (*To better compare the general trend with present results, the results from Zhang *et al.* (2014) is scaled 20% from their original data).

Similar to the motion observation, the “lock-in” phenomenon can also be seen in Figure 5.23 and Figure 5.24. However, it is noted that the “lock-in” phenomenon in the force domain is seen to occur slightly earlier than in the transverse motion domain, as also observed by Gonçalves *et al.* (2012) in their experiments. The peak point for the drag and lift force coefficients in the present study are at $Ur = 5.1$ while the peak point for the transverse motion is at $Ur = 6.6$.

Both the transverse motion time histories and the lift force coefficient time histories are transferred from the time domain to the frequency domain by using the Fast Fourier transform (FFT) in order to study the “lock-in” phenomenon. The frequency domain results are shown in Figure 5.26 to Figure 5.30, inclusive the “pre lock-in”, “lock-in” and “post lock-in” regions. The transverse motion frequency and vortex shedding frequency are both close to the transverse natural frequency in still water at the “pre lock-in” and “lock-in” regions. The oscillation and vortex shedding frequency are shown increasing with the increase in reduced velocity. When the “post lock-in” started, the oscillation frequency and vortex shedding frequency started to be further away from the transverse motion natural frequency as can be seen in Figure 5.29. For the highest reduced velocity case at $Ur = 12.1$, Figure 5.30 shows multiple peak frequencies appearing in the frequency domain.

As can be seen in Figure 5.26 to Figure 5.29, the agreement between the numerical predictions and the experimental measurements for both transverse motions and the lift force coefficients are reasonably well. It is seen in Figure 5.30, however, at “ $Ur = 12.1$ ”, the agreement is less well especially the magnitudes of motion and force coefficient though the dominant frequencies were still predicted accurately. It is noted that, at such a high reduced velocity ($Ur = 12.1$) way beyond the “lock-in” region (approx. $Ur = 6.6$), the magnitudes of the transverse motion and lift force coefficient are much smaller, thus, the relatively larger discrepancies appeared in Figure 5.30.

Compared to Figure 5.28 with $Ur = 6.6$, Figure 5.27 shows that the oscillation frequency and vortex shedding frequency are closer to the transverse natural frequency at $Ur = 5.1$, where the values of the peak drag and lift force coefficients appear. Furthermore, the added mass may also contribute to the earlier peak drag and lift force occurrence. Since the added mass keeps decreasing with the reduced velocity increasing, the force domain and the motion domain may have a hysteresis phenomenon which requires further studies.

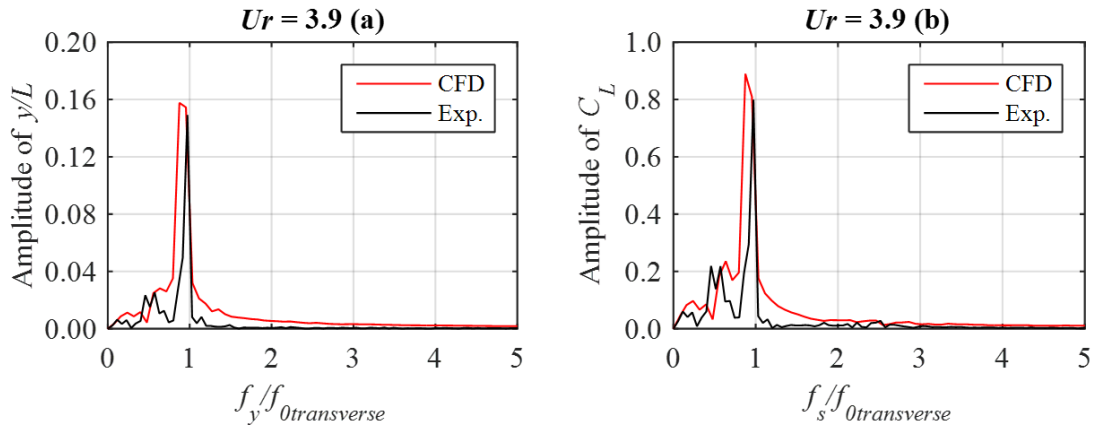


Figure 5.26 FFT of the transverse motions and the lift force coefficients at $Ur = 3.9$, (a) transverse motion; (b) lift force coefficient.

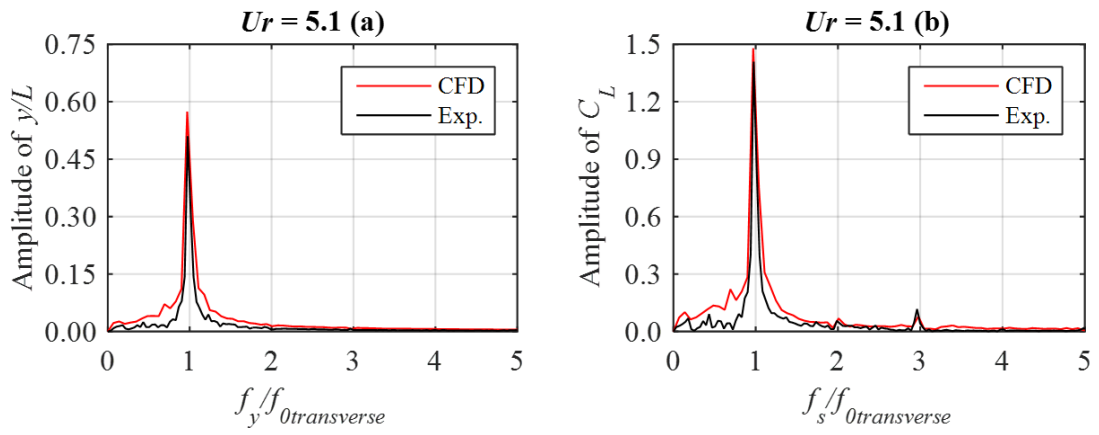


Figure 5.27 FFT of the transverse motions and the lift force coefficients at $Ur = 5.1$, (a) transverse motion; (b) lift force coefficient.

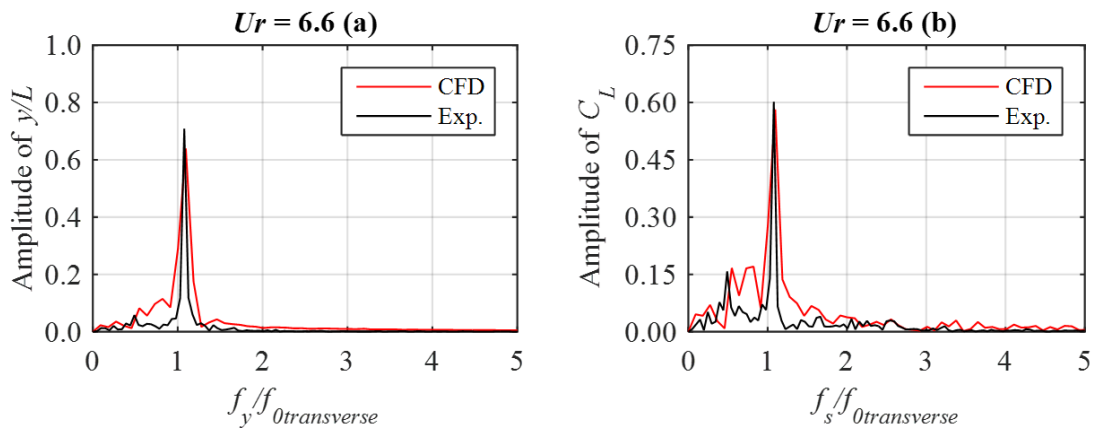


Figure 5.28 FFT of the transverse motions and the lift force coefficients at $Ur = 6.6$, (a) transverse motion; (b) lift force coefficient.

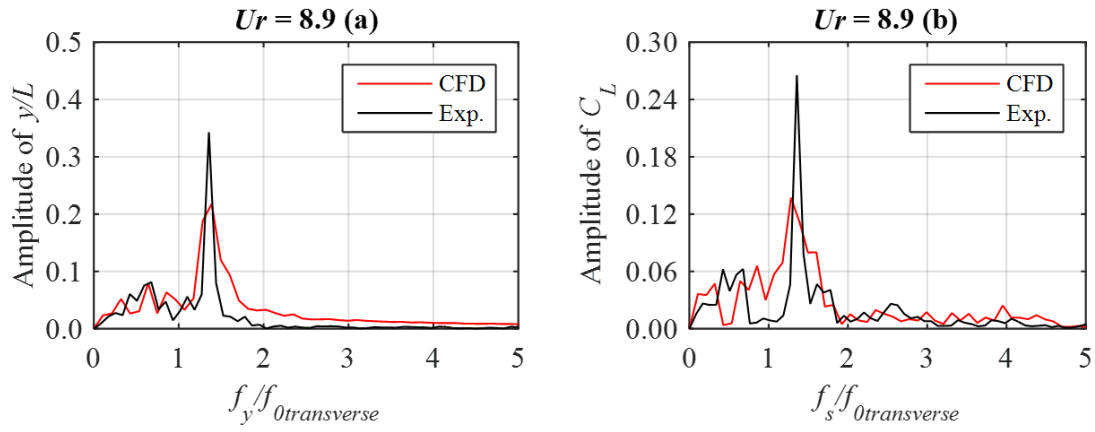


Figure 5.29 FFT of the transverse motions and the lift force coefficients at $Ur = 8.9$, (a) transverse motion; (b) lift force coefficient.

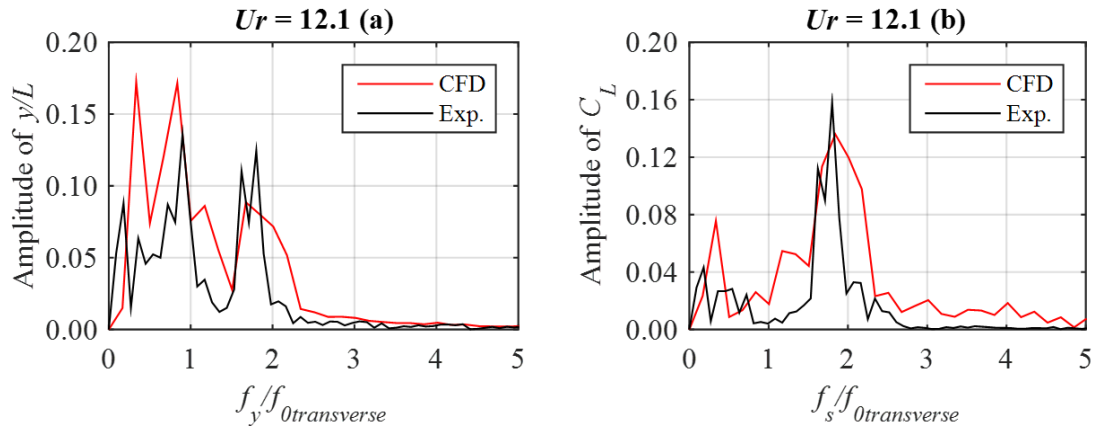


Figure 5.30 FFT of the transverse motions and the lift force coefficients at $Ur = 12.1$, (a) transverse motion; (b) lift force coefficient.

To examine the complex fluid mechanisms on the structure and the corresponding motion driven parts of the structure, the drag and lift force coefficients on different structure members of the DDS are further calculated and analysed. The definition of the individual members are shown in Figure 5.31.

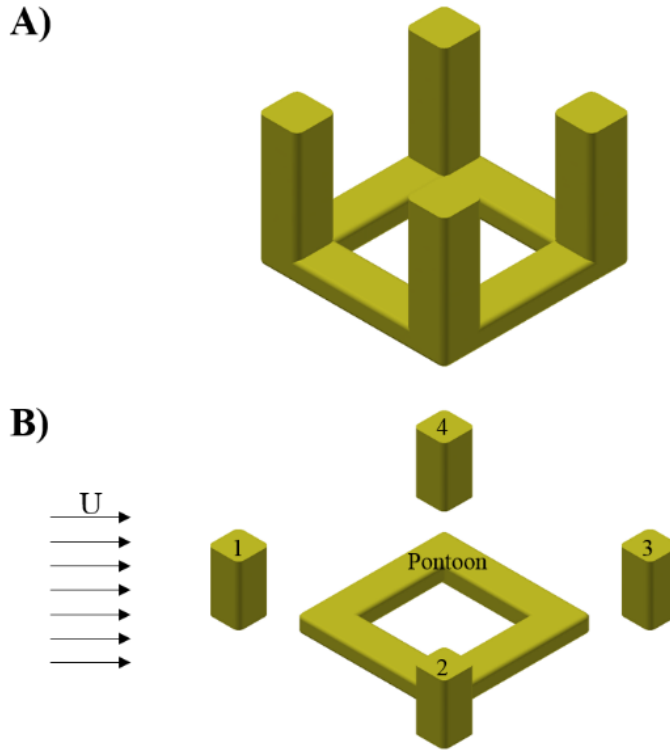


Figure 5.31 The DDS model (A is the entire model and B is the decomposed model which show the definition of the individual members).

The drag and lift force coefficients are changed when the reduced velocity increases (Figure 5.32 and Figure 5.33). The mean drag coefficient (\bar{C}_D) on the upstream column (column 1), the portside column (column 2) and the starboard side column (column 4) are significantly increased in the “lock-in” region. The drag coefficients on the pontoons increase slightly compared to the three aforementioned columns. However, the drag force coefficient on the downstream column (column 3) is decreasing while coefficients for the other members experiencing increasing trends and only recovers when “post lock-in” phase starts. The drag force coefficient on the downstream column is also much smaller than that for other members of the structure. On the other hand, the lift force coefficient (C_{Lrms}) on the downstream column, the portside and starboard side columns, and on the pontoons, are all significantly increased in the “lock-in” region. At this time, the leading upstream column shows a different trend. The lift force coefficient on the upstream column is seen to decrease while an increasing trend is observed for the other components, and conversely starts to recover as the other components begin to decrease. This is due to the wake region changing behind each of the columns. Further details will be discussed in section 5.2.3.

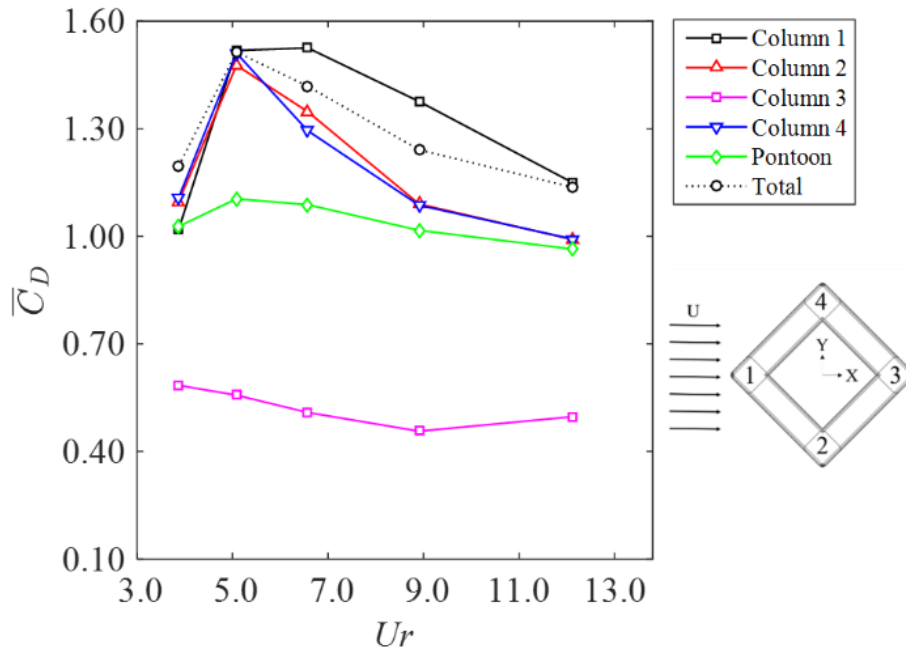


Figure 5.32 Mean drag coefficients (\bar{C}_D) on each member of the DDS from the VIM model.

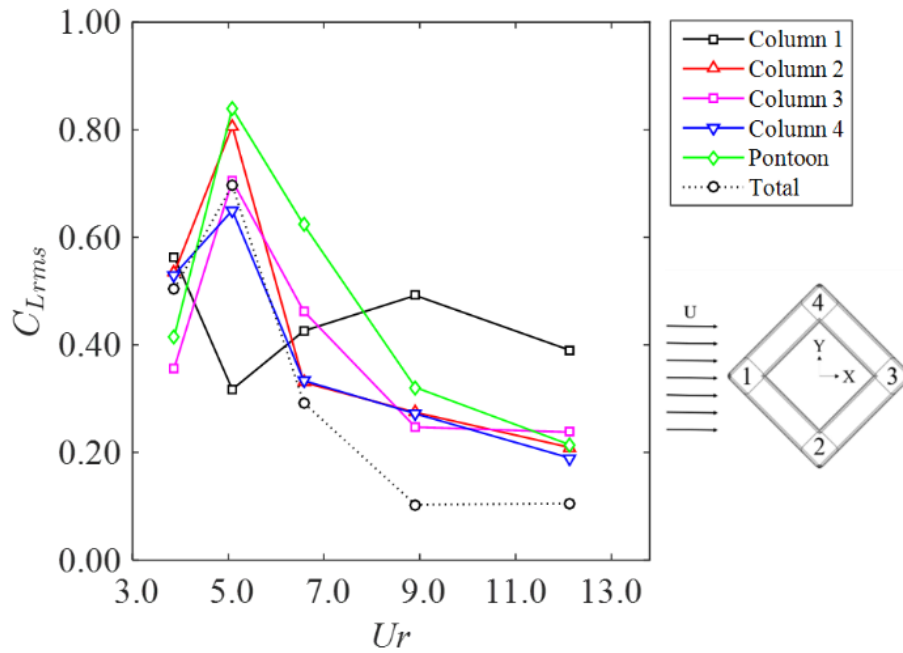


Figure 5.33 Root-mean-square lift coefficients (C_{Lrms}) on each member of the DDS from the VIM model.

The drag and lift forces on the structure are nearly symmetric except the lift force coefficient distribution at $Ur = 5.1$. Due to the results being based on the motion-coupled simulations, the rigid body motion also needs to be included in the analysis. With this aim, the work done by

each member of the structure during the stabilized VIM time is calculated and the results are presented in Figure 5.34. The work done is calculated using the following equations:

$$W = F \cdot S, \quad (5.10)$$

where F is the total drag and lift force of the structure and S is the displacement of the structure motion.

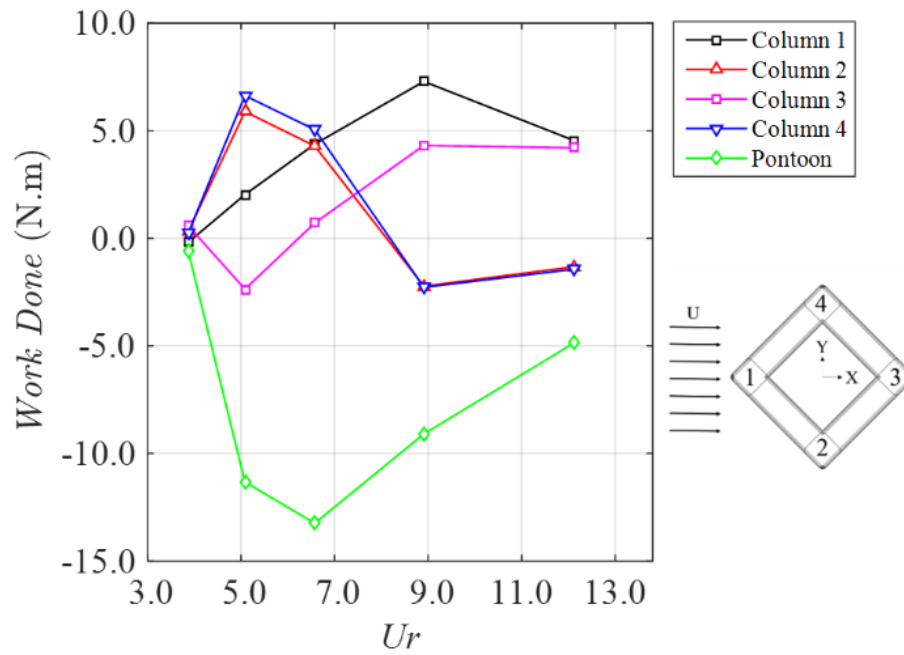


Figure 5.34 Work done by each member of the DDS on VIM model.

In Figure 5.34, the symmetrical characteristics can be clearly identified, and the following features can be observed:

- 1) The pontoon reduces the VIM response throughout the reduced velocity range. Thus, adding on the pontoons into the overall structure is a good design for restraining VIM responses.
- 2) The vortex shedding processes due to the three upstream columns are primarily responsible for the VIM responses. Further, the vortex shedding processes due to the portside and starboard side columns are the primary contributors to the VIM responses in the “lock-in” region and tend to resist the VIM responses in the “post lock-in” region.

3) The downstream column shows a different trend compared to the portside and starboard side columns; the work done by the downstream column drops initially and then recovers.

5.2.3 Flow pattern

With the aim to reveal the force dynamic behaviours on the structure, the time histories of the lift force coefficients corresponding with the flow patterns on a stationary DDS at $Re = 4.3 \times 10^4$ are firstly presented in Figure 5.35, Figure 5.36 and Figure 5.37 to compare with the flow patterns during VIM in order to show the differences.

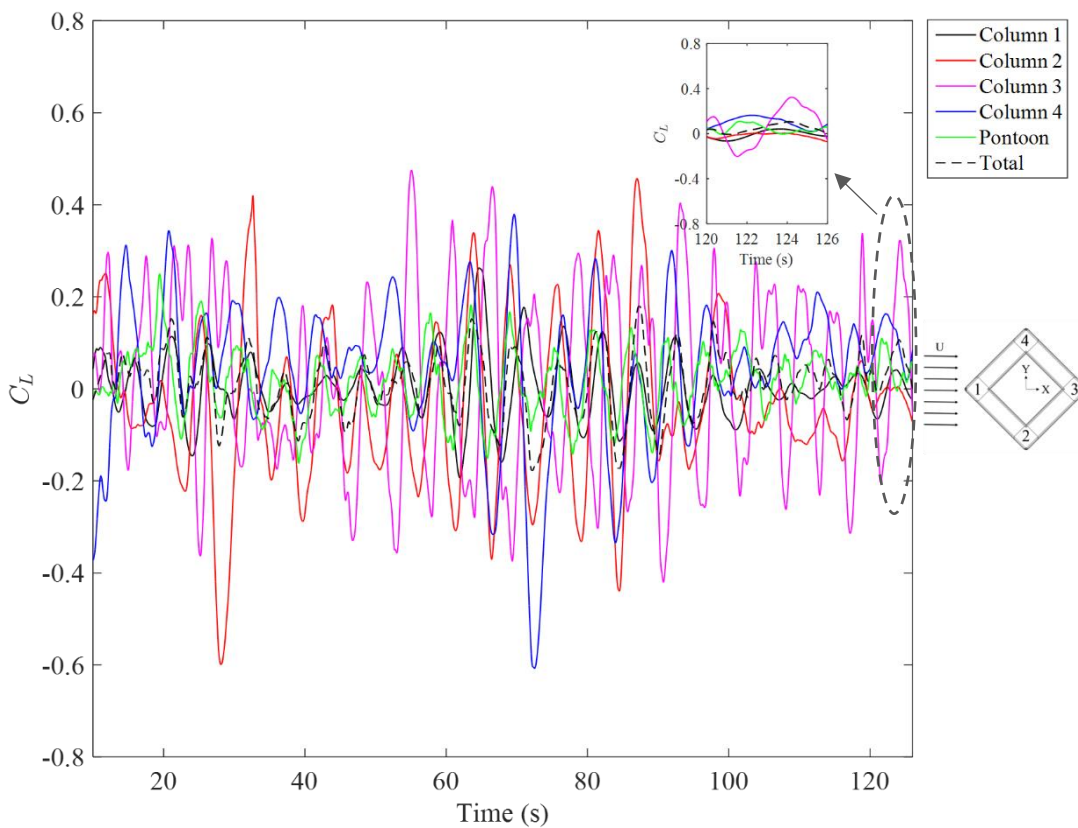


Figure 5.35 Lift force coefficient time history on different members of the stationary DDS at $Re = 4.3 \times 10^4$, including locally zoomed in the last 6s.

As can be seen in Figure 5.35, for a stationary model, the time history of the lift force coefficient on column 3 shows a phase delay phenomenon which indicates the lift force oscillating period on column 3 always delayed compared with other structure members. The maximum values of the lift coefficient on column 3 are almost corresponded to the minimum values of other

structure members at the time instantaneous of the lift force coefficient, especially at the last 6s which is locally zoomed in Figure 5.35, and vice versa.

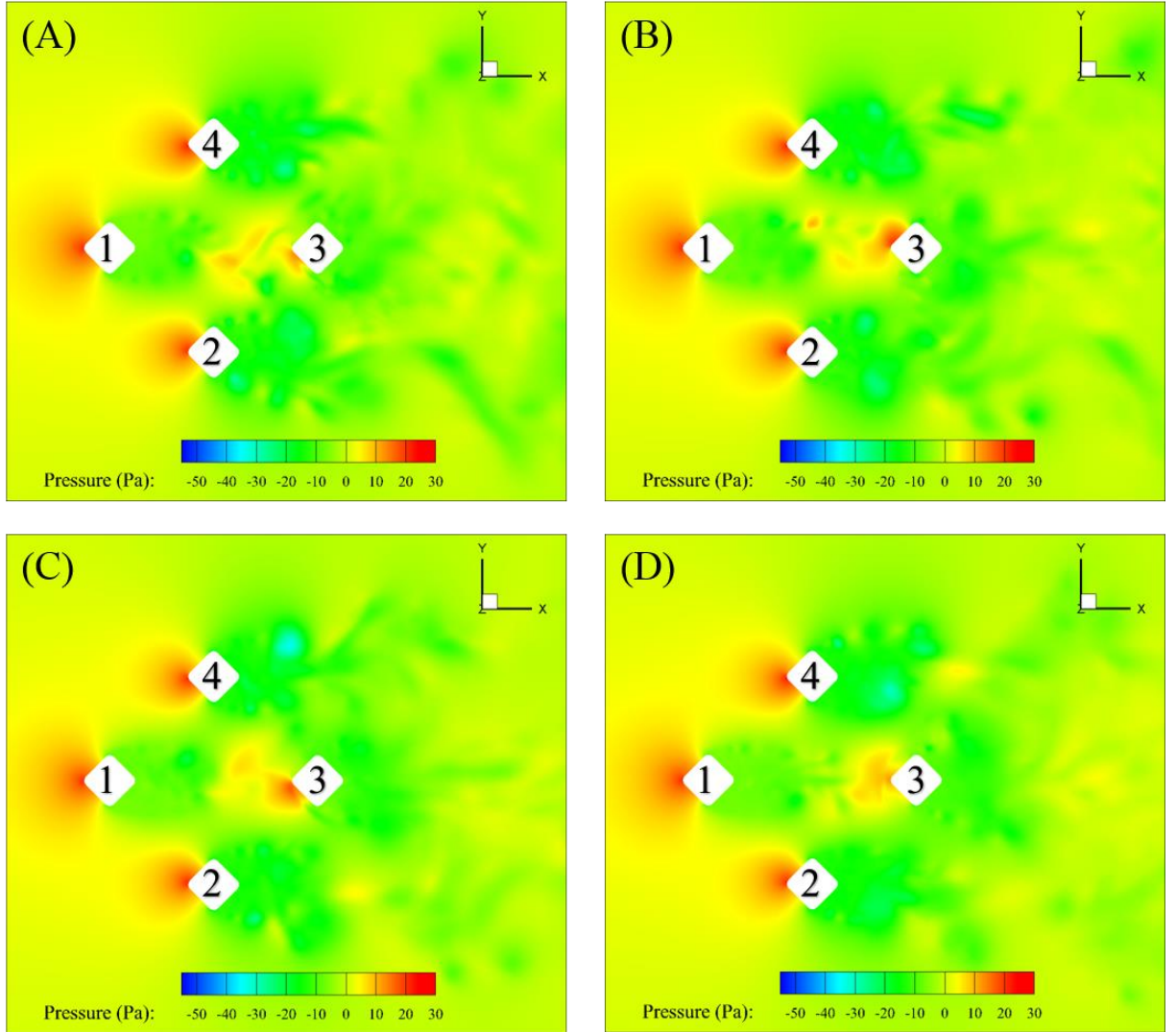


Figure 5.36 A time series of the pressure distribution around the DDS at middle draft showing the instantaneous flow fields around the stationary DDS at $Re = 4.3 \times 10^4$ corresponding to the lift force coefficient time history (A: 120.6 s; B: 122.4 s; C: 124.2 s; D: 126.0 s).

From the pressure contours (Figure 5.36), it can be clearly observed that there is a relatively stationary high pressure zone in front of column 1, 2 and 4. However, the high pressure zone in front of the downstream column 3 keeps changing along with the vortex shedding processes. The fluctuations of the pressure in front of column 3 are primarily induced by the impingement of the upstream generated vortices, and these fluctuations of the pressures cause the downstream column 3 to have lower \bar{C}_D values compared with other three upstream columns. The pressure fluctuations in front of column 3 are mainly resulted in the interaction between the vortices shed

from the upstream column 1 and the shear layers separated from the downstream column 3, which can be clearly seen in Figure 5.37. Similar observations were also noted by Ljungkrona *et al.* (1991), Chen and Chiou (1997) and Liu and Chen (2002). The higher C_{Lrms} of column 3 are primarily due to the vortices shed from the three upstream columns affect the wake region of column 3, as can be seen in Figure 5.37.

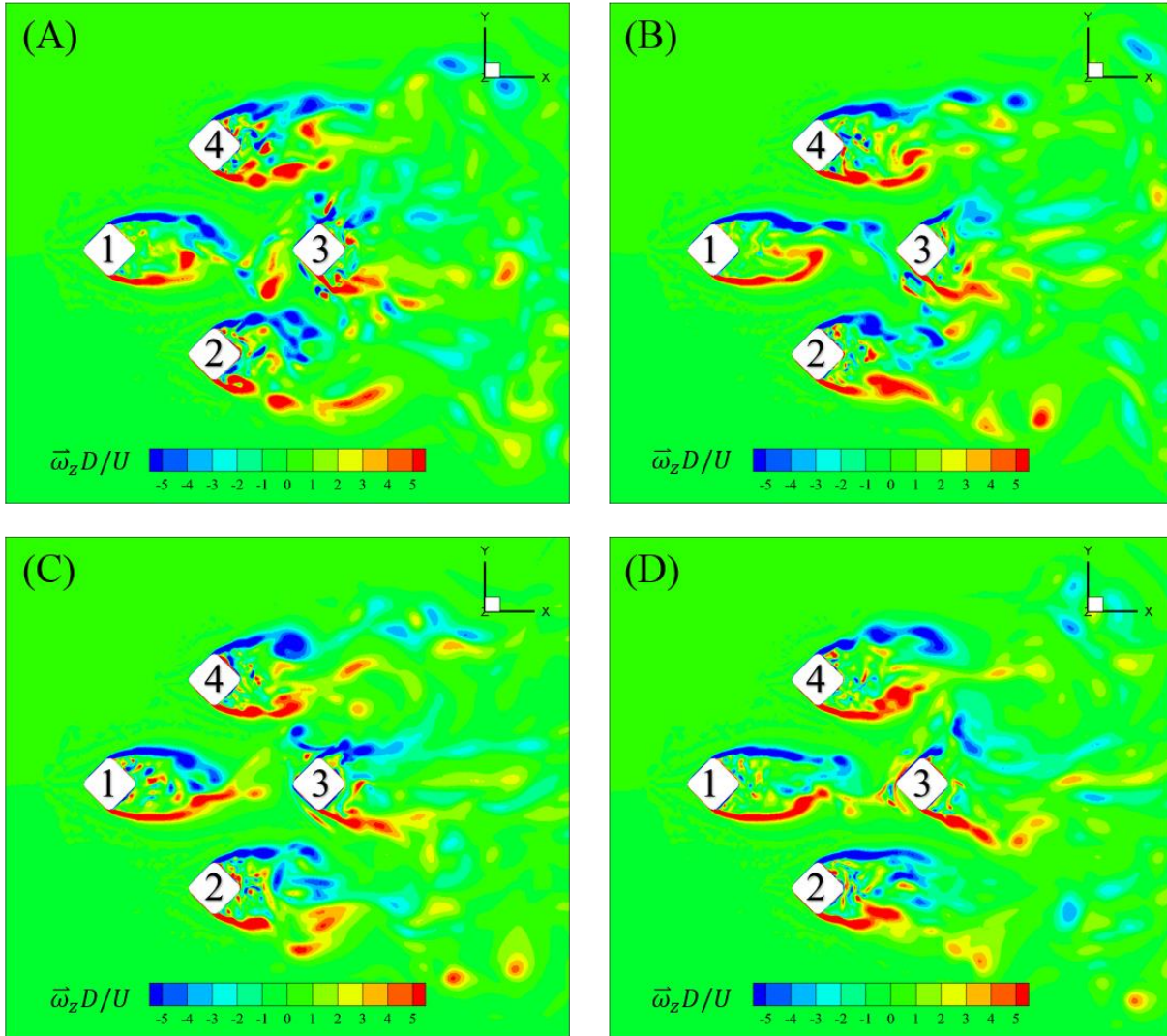


Figure 5.37 A time series of non-dimensional spanwise vorticity ($\vec{\omega}_z D/U$) contours around the DDS at the middle draft level showing the instantaneous flow fields around the stationary DDS at $Re = 4.3 \times 10^4$ corresponding to the lift force coefficient time history (A: 120.6 s; B: 122.4 s; C: 124.2 s; D: 126.0 s).

In addition, the *non-dimensional spanwise vorticity* (the definition is shown below) is used to prescribe the vortices in the horizontal plane (see Figure 5.37).

$$\text{non-dimensional spanwise vorticity} = \vec{\omega}_z D/U, \quad (5.11)$$

where $\vec{\omega}_z$ is the z component of the vorticity, D is the projected length of the column and U is the current speed.

Figure 5.37 also shows that the vortex shedding patterns due to each column are very different. It is seen that very slim vortices are shed from the corners of column 1. However, the vortices shed from the two side columns, i.e., column 2 and column 4 appear to be not as slim as the ones of column 1, and even shorter vortices shed from the corners of downstream column 3 are clearly visible. Moreover, column 2 and column 4 shed the large vortices symmetrically, where column 2 shed the vortices on its portside corner and column 4 shed on its starboard side corner. This symmetrical vortex shedding pattern contributes to the symmetrical values of \bar{C}_L for column 2 and column 4 which will be discussed in detail in section 5.3.4 Drag and lift force on each member.

When the DDS started to have a motion in the horizontal plane, the fluctuations of the lift forces on each member of the DDS is altered significantly. As can be seen in Figure 5.38, the presence of the hysteresis phenomenon for a stationary DDS (see Figure 5.35) is disappeared. The fluctuations of the lift force on each member are more severe as VIM progresses. At the “pre lock-in” region, the lift forces on each member already started to amplify. The largest fluctuation of the lift forces on each member of the DDS is observed in the “lock-in” region. However, when VIM developed into the “post lock-in” region, the fluctuations of the lift forces start to decrease and the value of C_L is closed to a stationary DDS case at $Ur = 12.1$. In addition, at the reduced velocity which has the largest value for \bar{C}_D and C_{Lrms} , where $Ur = 5.1$, the lift forces on all the members of the DDS start to be synchronised (see Figure 5.38, $Ur = 5.1$). This will be further explained through the analysis of the vortex shedding processes during VIM.

In order to have a general visual appreciation of the vortex shedding patterns during VIM, the vorticity contours are plotted from Figure 5.40 to Figure 5.49. Another non-dimensional variable (*non-dimensional vorticity*) is used to describe the vorticity in the current study.

$$\text{non-dimensional vorticity} = \omega D/U, \quad (5.12)$$

$$\omega = \sqrt{(\omega_x^2 + \omega_y^2 + \omega_z^2)}, \quad (5.13)$$

where ω is the vorticity magnitude, ω_x is the x component of the vorticity, ω_y is the y component of the vorticity, ω_z is the z component of the vorticity D is the projected length of the column and U is the current speed.

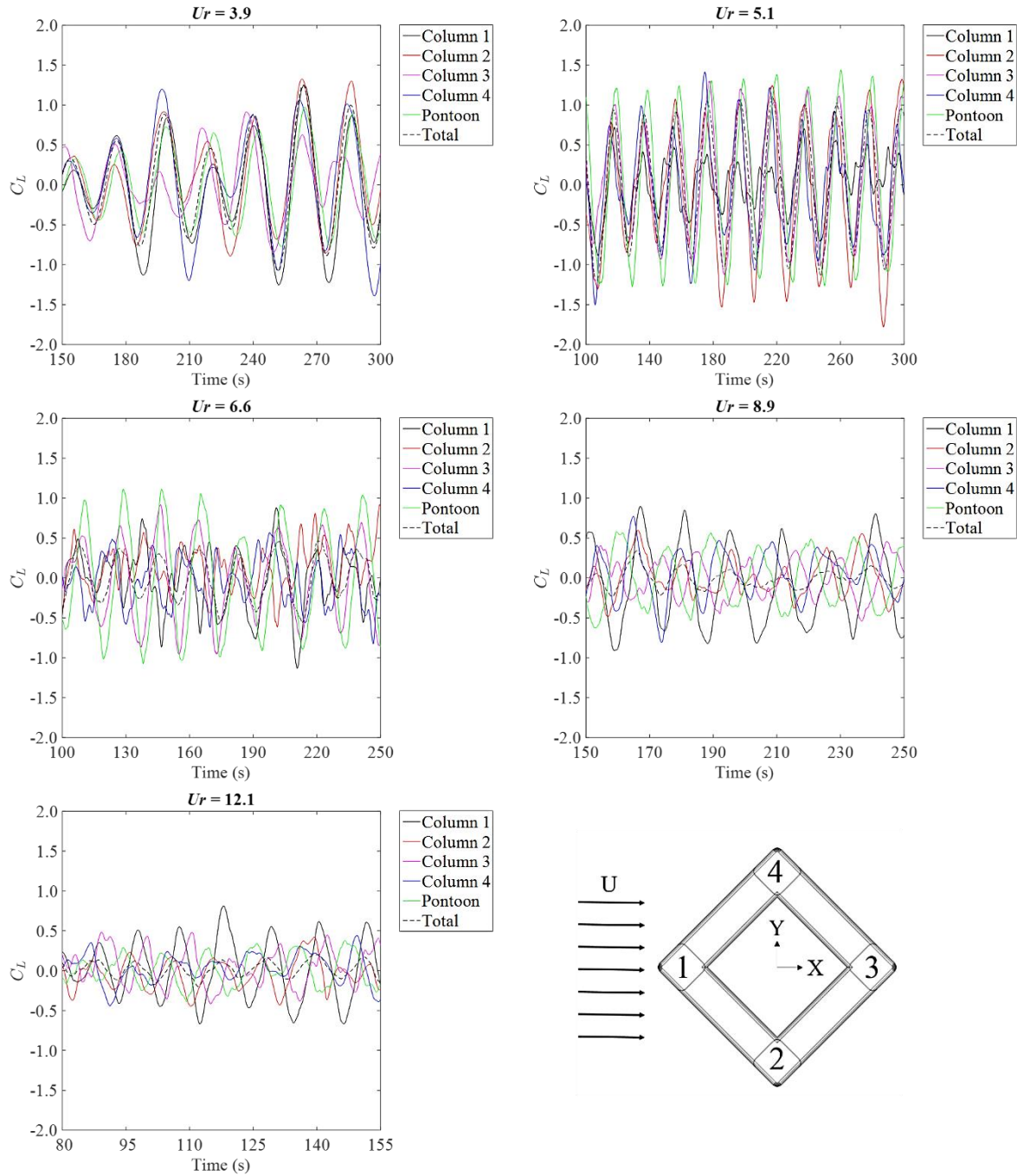


Figure 5.38 Lift force coefficient time history on different members of the DDS during VIM at $Ur = 3.9, 5.1, 6.6, 8.9$ and 12.1 .

For convenience in describing the vortex development processes, four regions are defined around the column, named as NW (Northwest), NE (Northeast), SW (Southwest) and SE

(Southeast) (see Figure 5.39). The vortices shed from each side of the column are denoted in chronological order of genesis (e.g., A1, A2 ...) from the upper side of column 1, see Table 5.2.

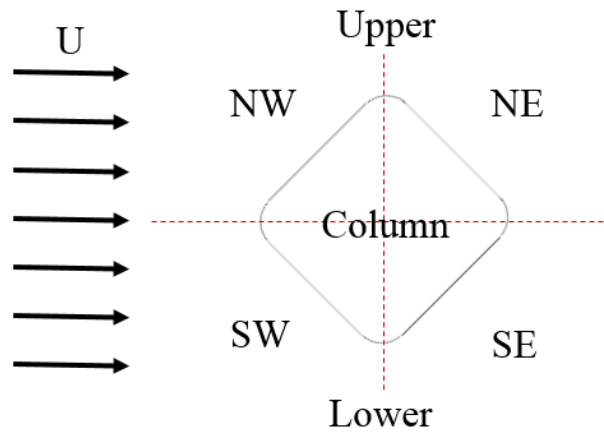


Figure 5.39 Definition of the regions around an individual column.

Table 5.2 The chronological order of vortices genesis for each column.

Column	Shear layer	Vortex street
1	Upper	A1, A2 ...
	Lower	B1, B2 ...
2	Upper	C1, C2 ...
	Lower	D1, D2 ...
3	Upper	E1, E2 ...
	Lower	F1, F2 ...
4	Upper	G1, G2 ...
	Lower	H1, H2 ...

Figure 5.40 presents the non-dimensional spanwise vorticity ($\vec{\omega}_z D/U$) contours at $Ur = 3.9$. As can be seen, the vortices shed from the upstream column (column 1) directly impinge on the downstream column (column 3) and then join into the downstream column's weak region. The vortex street can be clearly found behind the upstream column where the "2S" type shedding ("P" means a vortex pair and "S" means a single vortex. The definition of the vortex shedding patterns, e.g. "2S", "2P", "P + S", "P", etc., are made by Williamson and Roshko (1988)) occurs. Additionally, the vortices shed from the portside and starboard side columns (column 2 and 4) also impinge on the downstream column, which are red circled in Figure 5.41(B). These vortex patterns are not visible in the spanwise vorticity contour (Figure 5.40) indicating that there are three-dimensional effects on the flow characteristics especially on the side columns' wake

region and the flow region in front of the downstream column. With the increase of the Ur , in the “lock-in” region, the flow patterns are changed. When $Ur = 5.1$, the structure oscillation frequency is close to the natural frequency of the structure in still water. As the result of the resonance developing, the motion starts to amplify and the flow patterns are changed significantly. Vortex streets only appear on the opposite of the transverse direction (see Figure 5.42 and Figure 5.43). The vortices shed from the upstream column (column 1) where the “P + S” type shedding occurred periodically and symmetrically impinge on the portside and starboard side (column 2 and 4). Respectively, the vortices generated by the upstream column impinge on the NW face of the portside column (column 2) and the SW face of the starboard side column (column 4). Only one strong vortex will form on the opposite side to the transverse direction behind portside and starboard side columns (see “D1, H1, G1” in Figure 5.42). The vortices shed from the side columns impinge on the downstream column (column 3). As a result, there is no clear vortex street behind the downstream column. Small vortices in piece can be seen in the downstream of column 3. In addition, the motion trajectory shows a figure “8” shape under $Ur = 5.1$.

With a further slight increase of the Ur , in contrast to that the transverse motion keeps amplifying, the lift force coefficient starts to decrease (see Figure 5.20 and Figure 5.24). This hysteresis phenomenon can be explained by Figure 5.44. As the transverse motion is amplified, after impinging on the starboard side column (column 4), the vortices that are shed from the upstream column (column 1) move back to impinge on the portside column (column 2). This can be seen by following the trajectory of the vortices “B1”. Additionally, the vortices like “B1” affect the vortices detached from the upper side of column 2 and lower side of column 4. As can be seen in Figure 5.44(B) (red circled), two different clockwise vortices are mixed together on the SE face of the starboard side column. The interaction of the vortices with opposite vorticity leads to decrease of the lift force on the structure. This is one of the reasons that makes the lift force coefficient on the structures drops while the transverse motion increases. By comparing the differences between Figure 5.42 and Figure 5.44, there is another factor which may contribute to the hysteresis phenomenon. In Figure 5.44, it is seen that strong vortices are detached from both portside and starboard side at same time. While in Figure 5.42, only one strong vortex will form on the opposite side to the transverse velocity direction behind portside and starboard side columns. The differences of the flow characteristics shown in Figure 5.42 and Figure 5.44 lead to the peak point in the force domain occurs slightly earlier than that in the transverse motion domain.

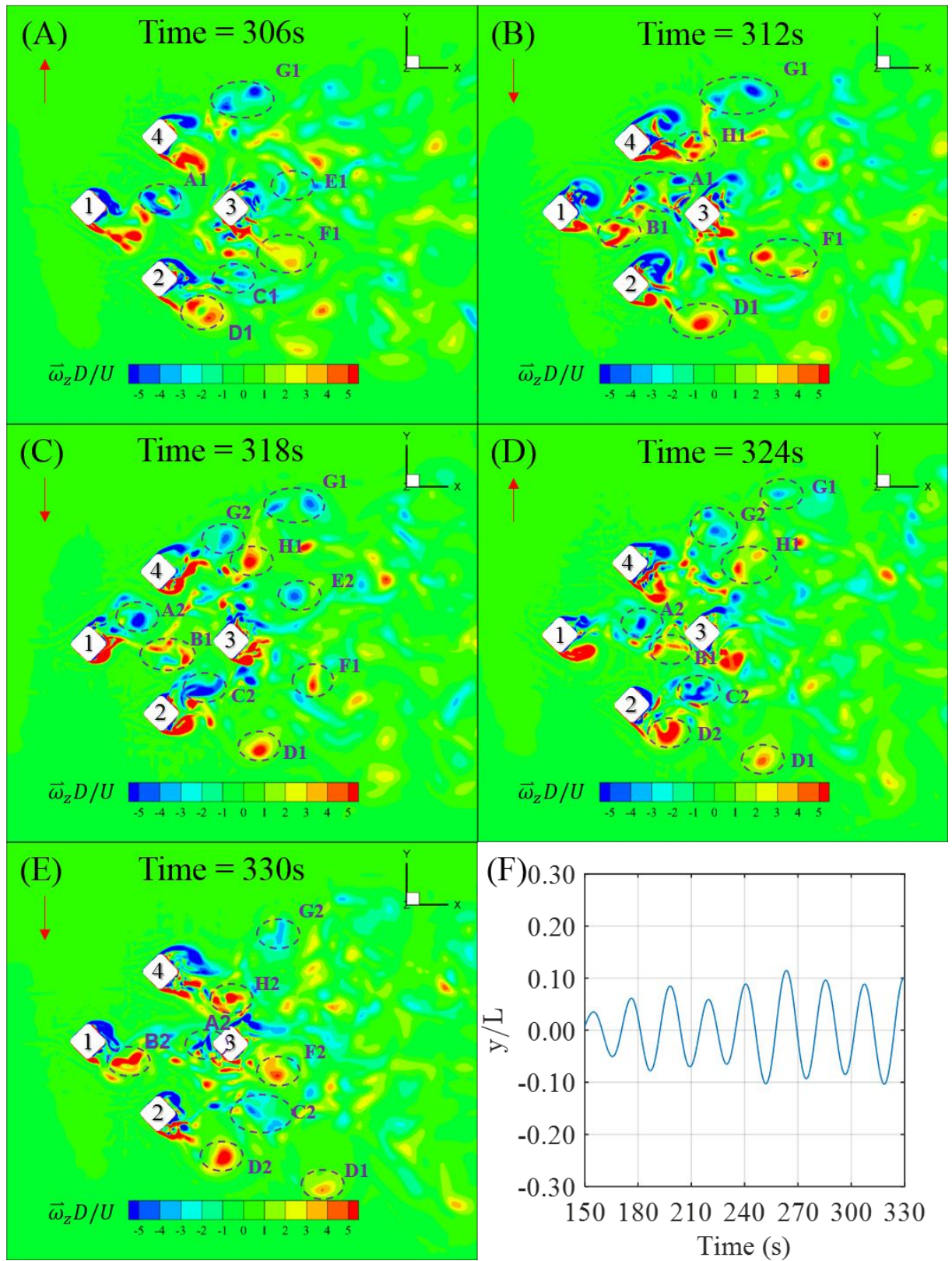


Figure 5.40 A time series of the non-dimensional spanwise vorticity ($\bar{\omega}_z D/U$) contours around the DDS at middle draft showing the instantaneous flow fields around the DDS at $Ur = 3.9$ (A, B, C, D, E) and the non-dimensional transverse motion (y/L) time history (F); the red arrow is the DDS transverse velocity direction.

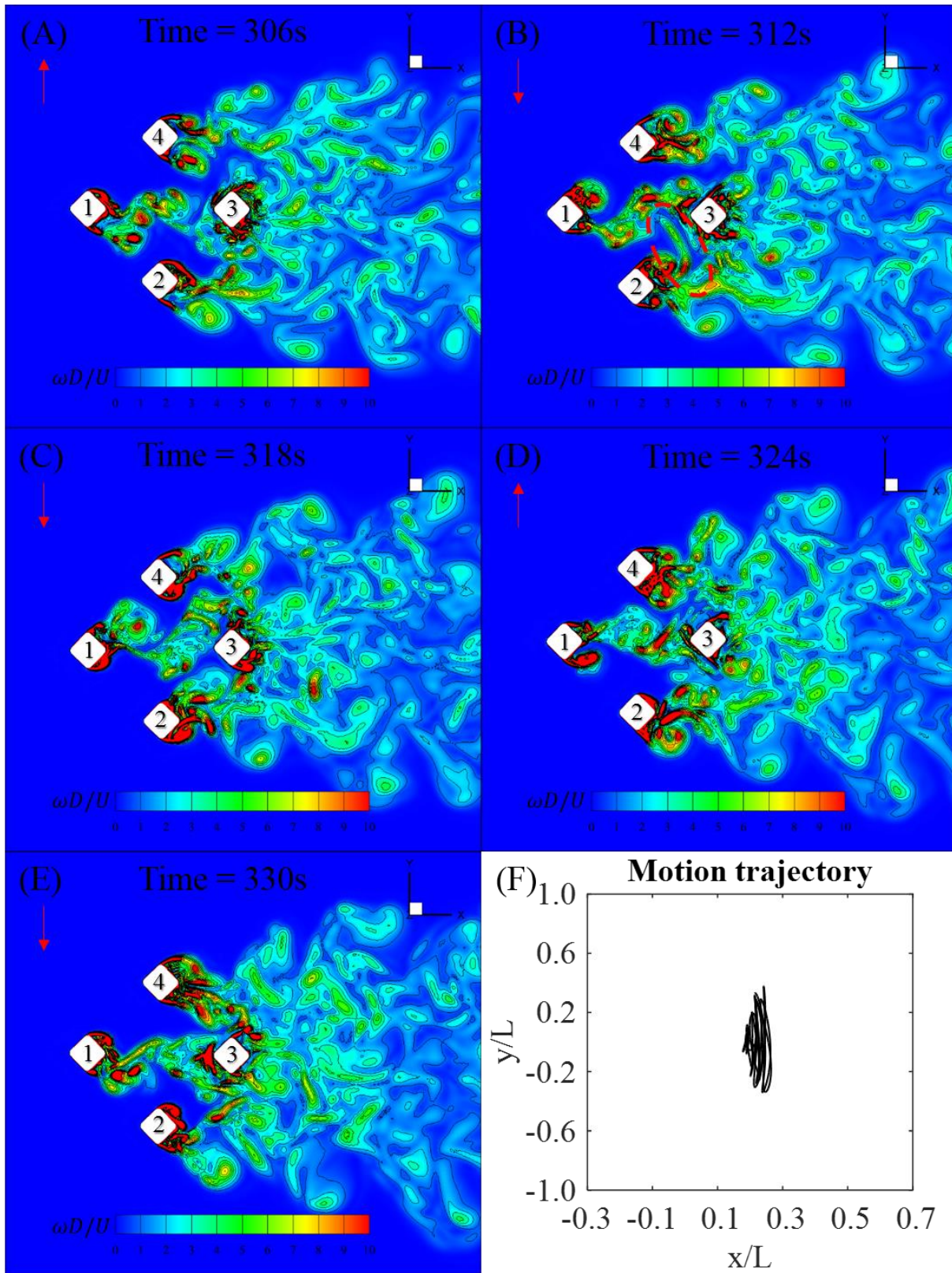


Figure 5.41 A time series of the non-dimensional vorticity ($\omega D/U$) contours around the DDS at middle draft showing the instantaneous flow fields around the DDS at $Ur = 3.9$ (A, B, C, D, E) and the non-dimensional motion trajectory (F); the red arrow is the DDS transverse velocity direction.

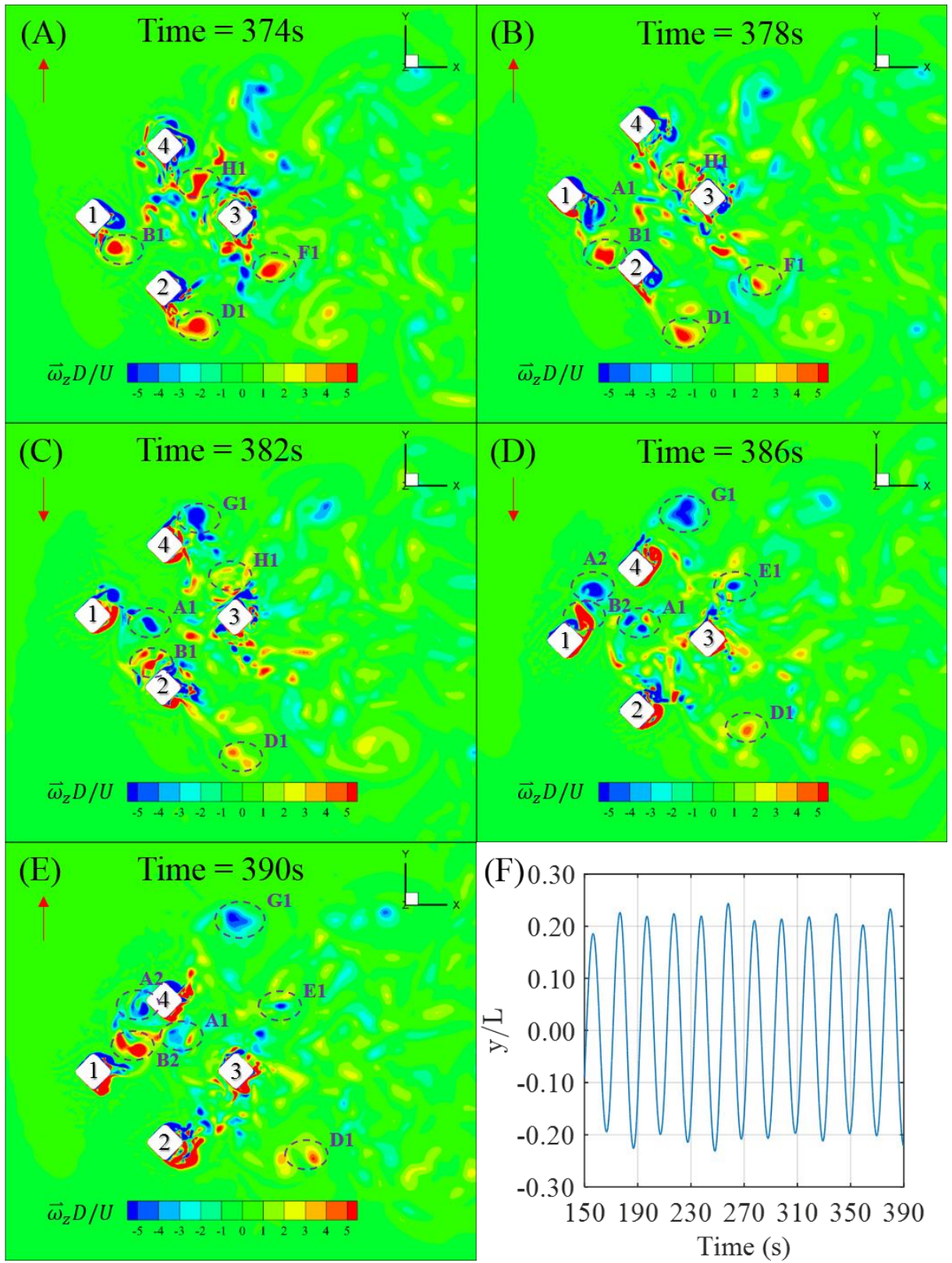


Figure 5.42 A time series of the non-dimensional spanwise vorticity ($\bar{\omega}_z D/U$) contours around the DDS at middle draft showing the instantaneous flow fields around the DDS at $Ur = 5.1$ (A, B, C, D, E) and the non-dimensional transverse motion (y/L) time history(F); the red arrow is the DDS transverse velocity direction.

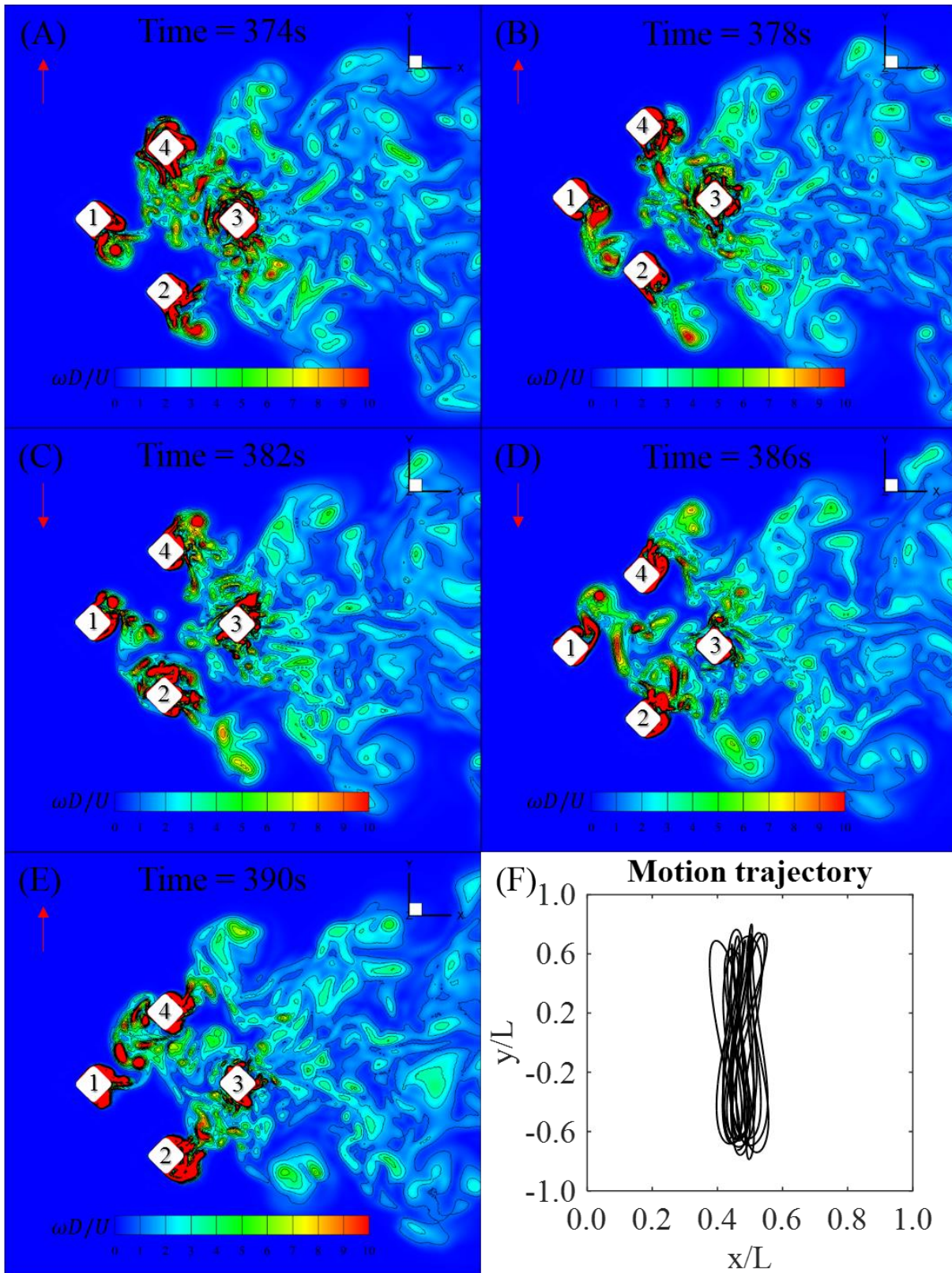


Figure 5.43 A time series of the non-dimensional vorticity ($\omega D/U$) contours around the DDS at middle draft showing the instantaneous flow fields around the DDS at $Ur = 5.1$ (A, B, C, D, E) and the non-dimensional motion trajectory (F); the red arrow is the DDS transverse velocity direction.

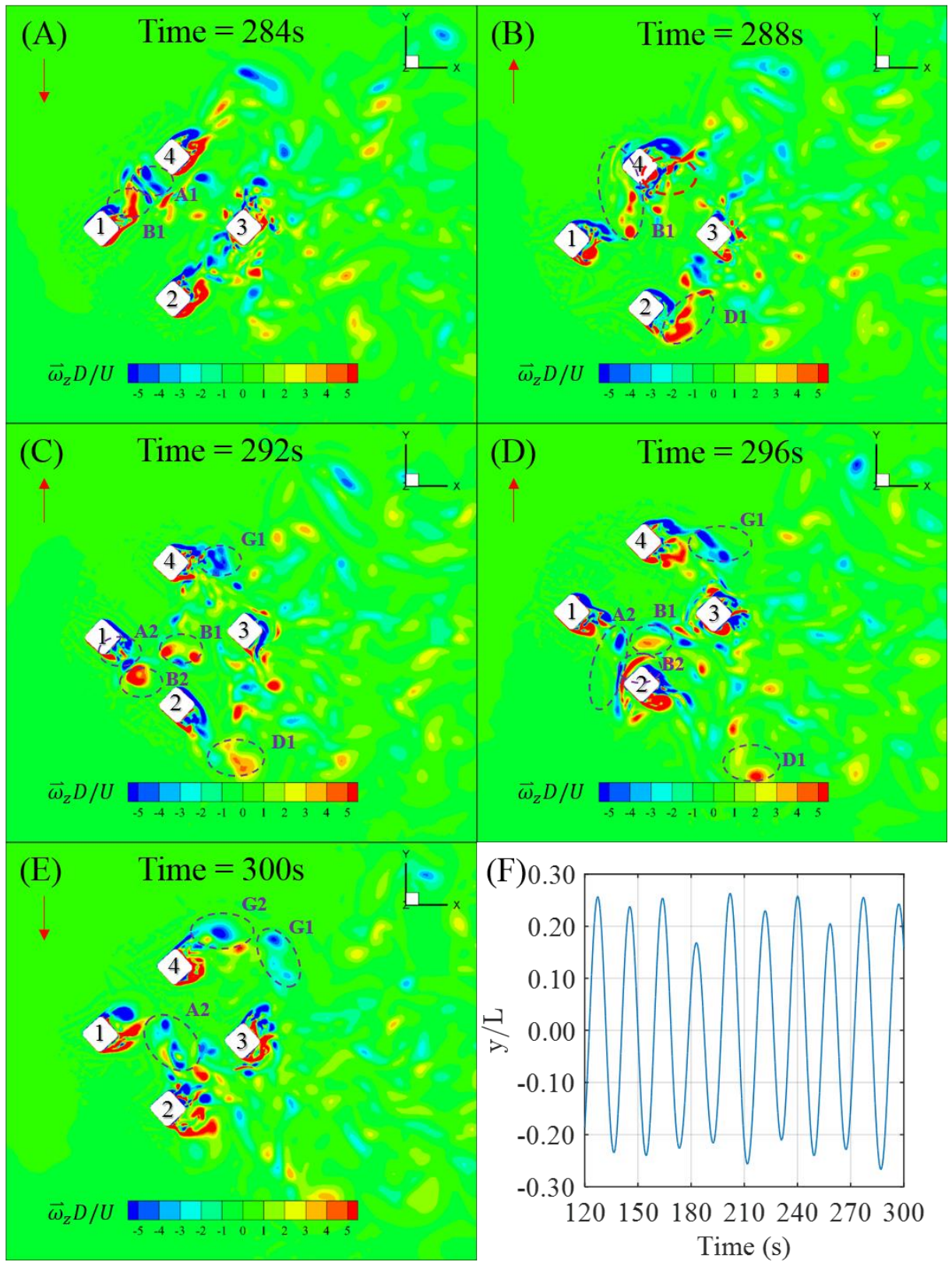


Figure 5.44 A time series of the non-dimensional spanwise vorticity ($\bar{\omega}_z D/U$) contours around the DDS at middle draft showing the instantaneous flow fields around the DDS at $Ur = 6.6$ (A, B, C, D, E) and the non-dimensional transverse motion (y/L) time history (F); the red arrow is the DDS transverse velocity direction.

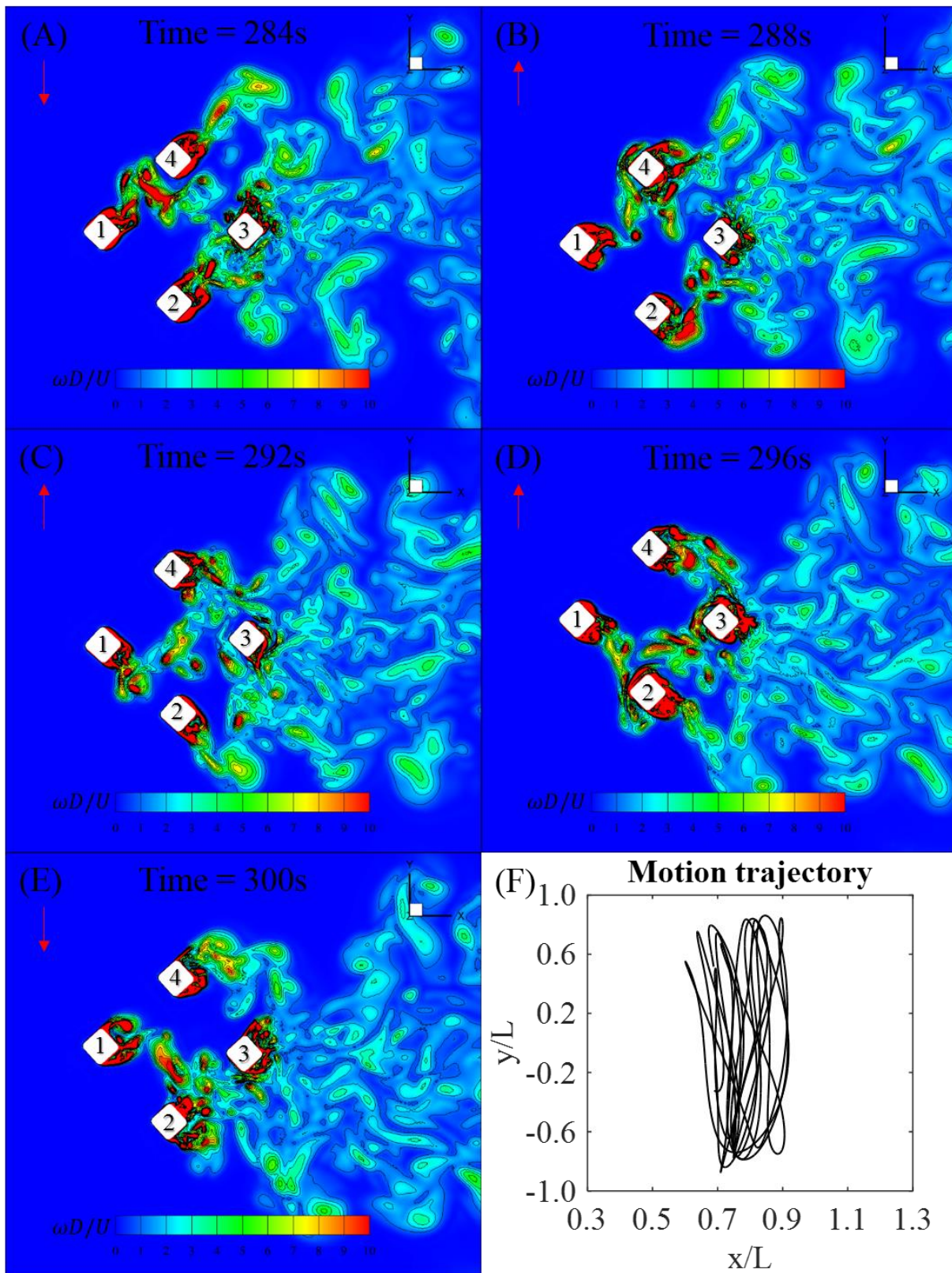


Figure 5.45 A time series of the non-dimensional vorticity ($\omega D/U$) contours around the DDS at middle draft showing the instantaneous flow fields around the DDS at $Ur = 6.6$ (A, B, C, D, E) and the non-dimensional motion trajectory (F); the red arrow is the DDS transverse velocity direction.

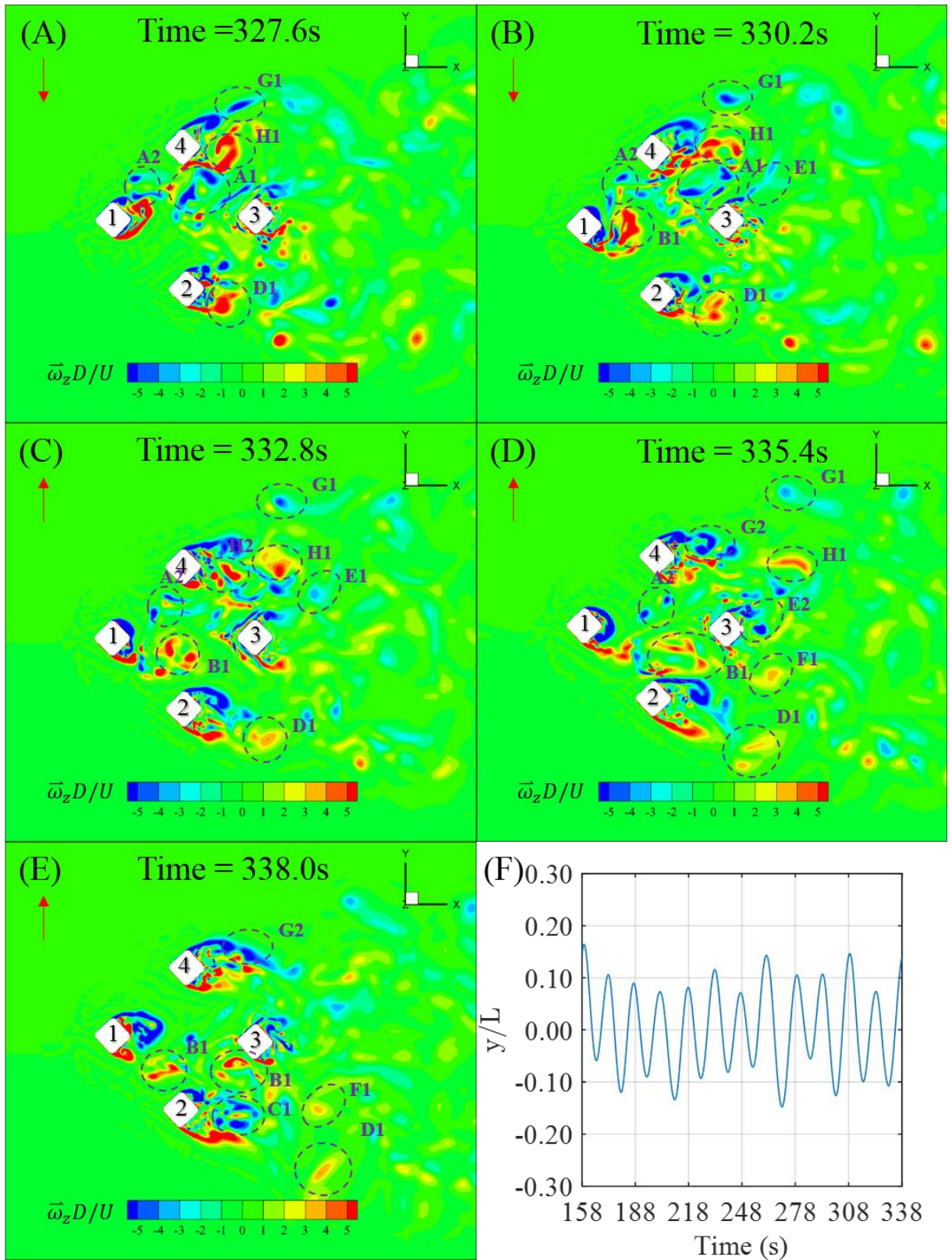


Figure 5.46 A time series of the non-dimensional spanwise vorticity ($\bar{\omega}_z D/U$) contours around the DDS at middle draft showing the instantaneous flow fields around the DDS at $Ur = 8.9$ (A, B, C, D, E) and the non-dimensional transverse motion (y/L) time history (F); the red arrow is the DDS transverse velocity direction.

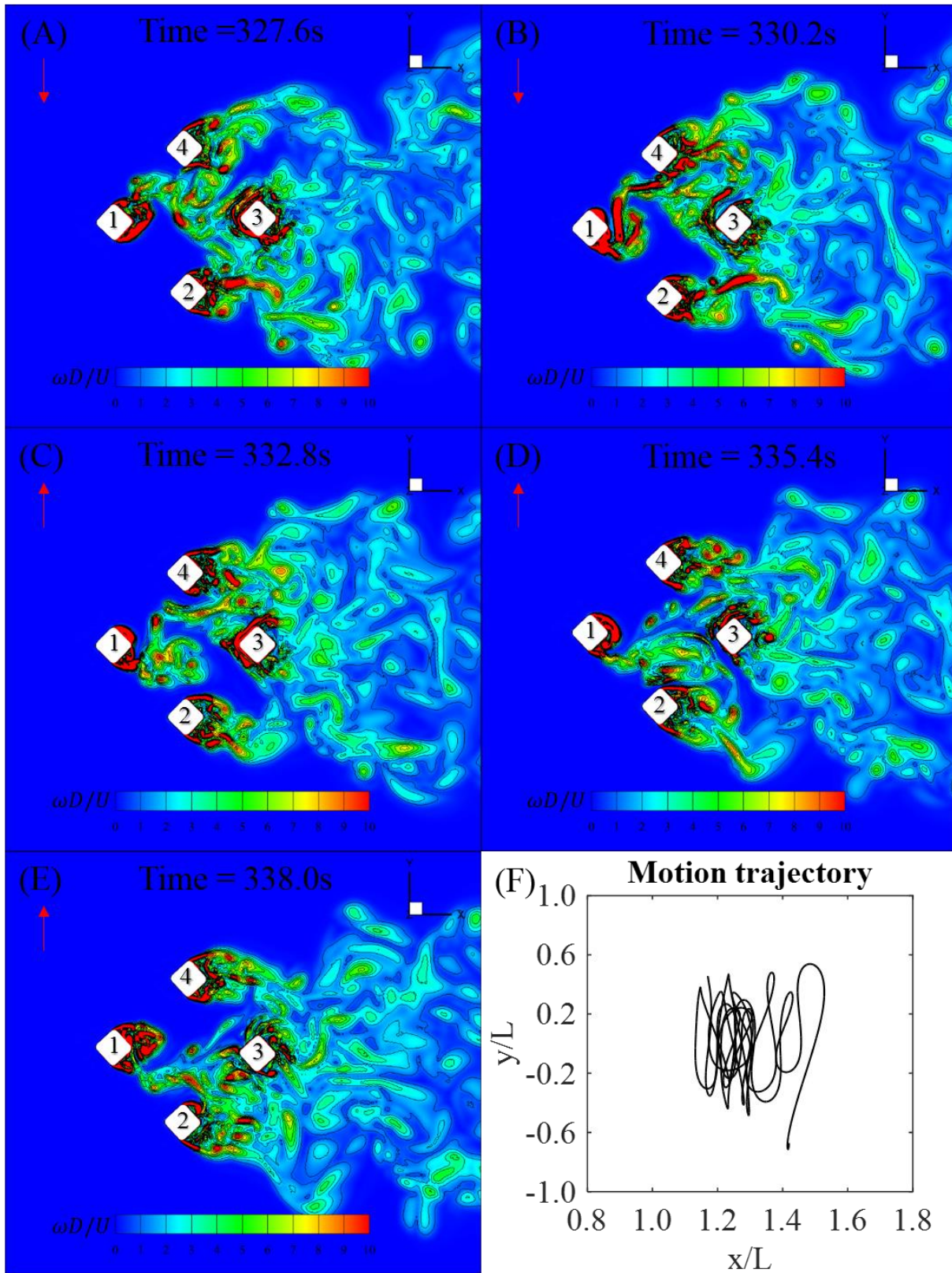


Figure 5.47 A time series of the non-dimensional vorticity ($\omega D/U$) contours around the DDS at middle draft showing the instantaneous flow fields around the DDS at $Ur = 8.9$ (A, B, C, D, E) and the non-dimensional motion trajectory (F); the red arrow is the DDS transverse velocity direction.

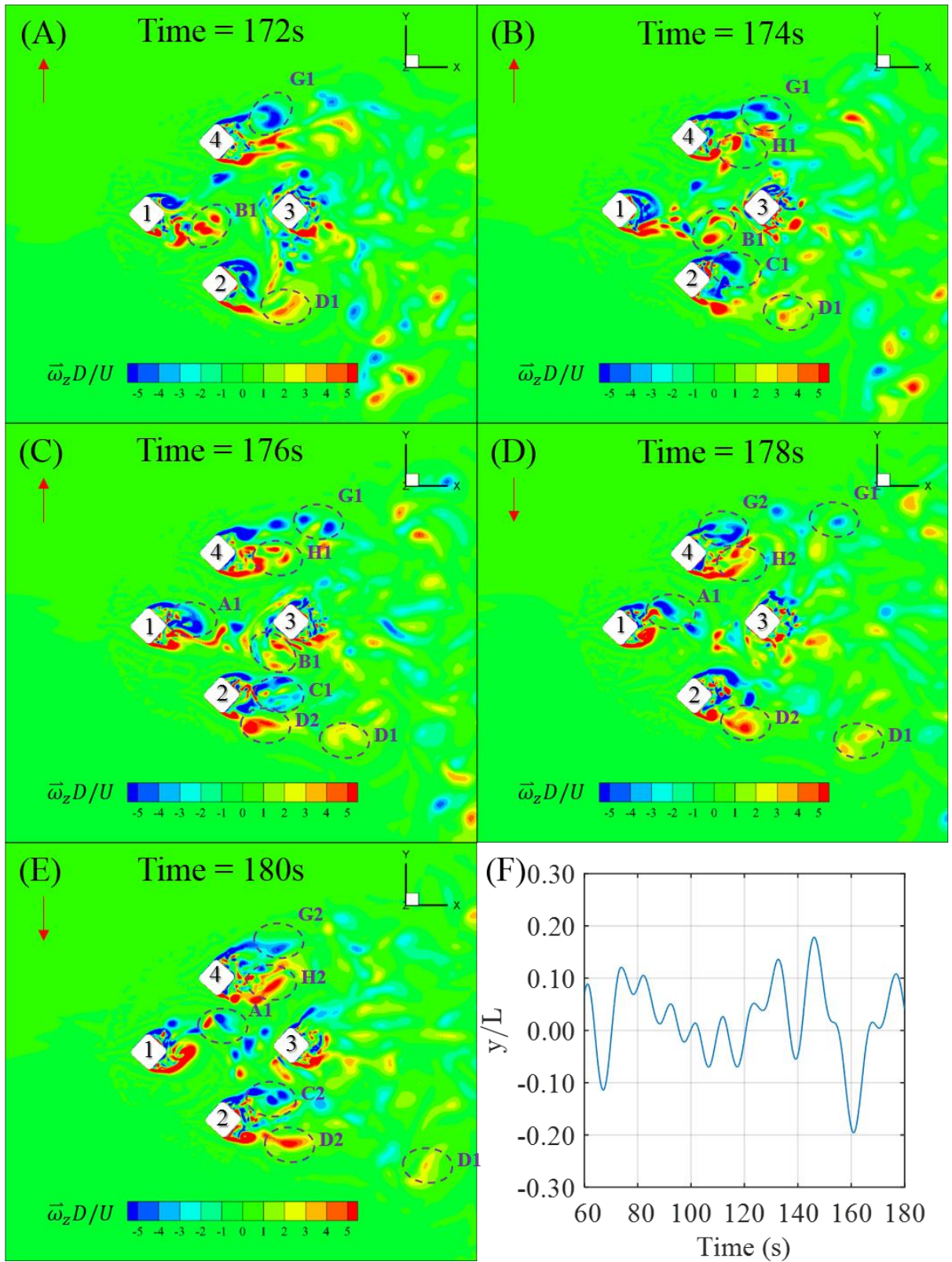


Figure 5.48 A time series of the non-dimensional spanwise vorticity ($\bar{\omega}_z D/U$) contours around the DDS at middle draft showing the instantaneous flow fields around the DDS at $Ur = 12.1$ (A, B, C, D, E) and the non-dimensional transverse motion (y/L) time history (F); the red arrow is the DDS transverse velocity direction.

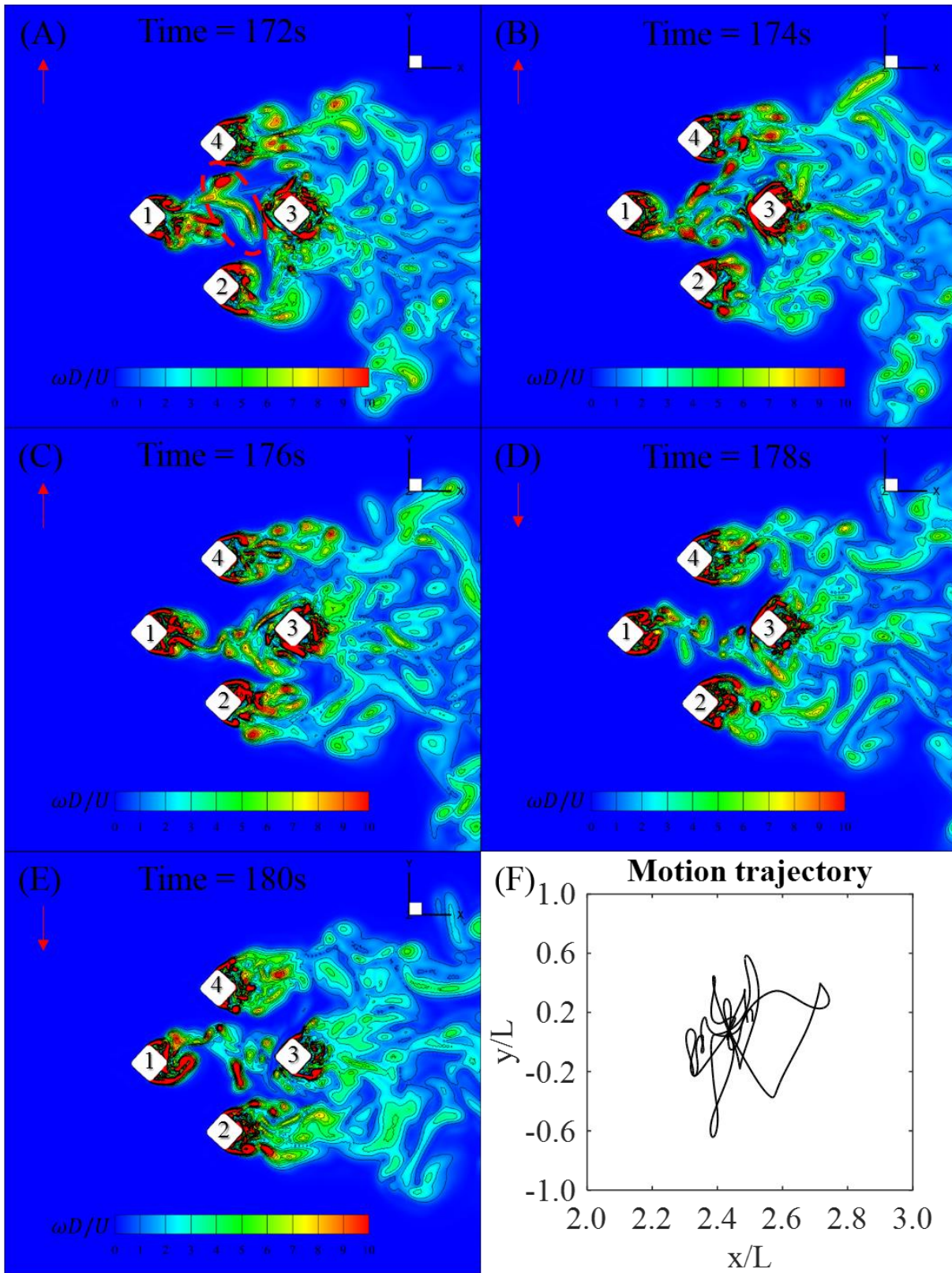


Figure 5.49 A time series of the non-dimensional vorticity ($\omega D/U$) contours around the DDS at middle draft showing the instantaneous flow fields around the DDS at $Ur = 12.1$ (A, B, C, D, E) and the non-dimensional motion trajectory (F); the red arrow is the DDS transverse velocity direction.

When the reduced velocity reaches the “post lock-in” region, the vortices shed from the upstream column (column 1) no longer impinge on the incidence flow faces of the portside and starboard side columns (column 2 and 4). Instead, the vortices are seen to join the weak region of the portside and starboard side (see Figure 5.46 to Figure 5.49). The vortex street behind column 1, 2 and 4 can be clearly seen. In addition, it can be seen in Figure 5.49(A) that parts of these vortices (red circled) do act on the incidence flow face of the downstream column (column 3). As the vortices shed from the upstream column do not impinge on the portside and starboard side columns, the lift force coefficient and the transverse motion decrease and then remain a stable value in the measurement range of the “post lock-in” region in the present study.

5.3 Interaction of vortex shedding processes on the flow around four columns with and without pontoons connected

It is revealed that the pontoons play an important role to resist the VIM in the above section. Thus, this section is aimed to investigate the pontoons effects on the overall hydrodynamics around a stationary four columns structure.

Two different model conditions (columns both with and without pontoons connected) under 45 degree flow incidence were investigated using the established numerical models and their results are further compared against the corresponding experimental data.

5.3.1 Flow characteristics in the horizontal plane

In order to reveal some further insights of the fluid physics due to the flow interactions by multiple columns and pontoons arrangements, a general visual appreciation of the vortex shedding patterns (e.g. the time-averaged velocity contours and the vorticity contours) at $Re = 4.3 \times 10^4$ from both the experimental results and the numerical simulations are plotted and discussed in this section.

The velocity profiles around column 3 in the wake region in a horizontal XY plane (at the middle draft) from both the experimental and numerical results were compared first, followed by the contours that are plotted in Figure 5.50 and Figure 5.51 (where $U_{mean} = \sqrt{\bar{U}_i^2 + \bar{U}_j^2}$, U_i is the streamwise flow velocity, U_j is the transverse flow velocity). The velocities were sampled over the horizontal cross section coinciding with XY plane (i, j plane) to have directly quantifiable comparisons between the experimental data and the numerical predictions (shown in Figure

5.52 and Figure 5.53). Typical, a characteristic U-shaped velocity profiles are observed in Figure 5.53. The numerical results show a good trend agreement when compared with the experimental results, especially for capturing the recirculation flows in the wake region. The numerical simulations give similar velocity values to those from the experimental results. It is noted that, in the present work, the PIV measurements have collected the flow data from a quite wide area (about 0.6 m² measurement area) compared with the studies made by other researchers (Ünal and Atlar, 2010; Wang *et al.*, 2013). There are larger discrepancies observed at the sides of column 3. As these larger discrepancies regions were in the areas that are closed to the edge of the camera screen, the resolution of the PIV image in these regions was often not as good as in the more central part of the camera lens. In general, the numerical simulations predict well when compared with the experimental results.

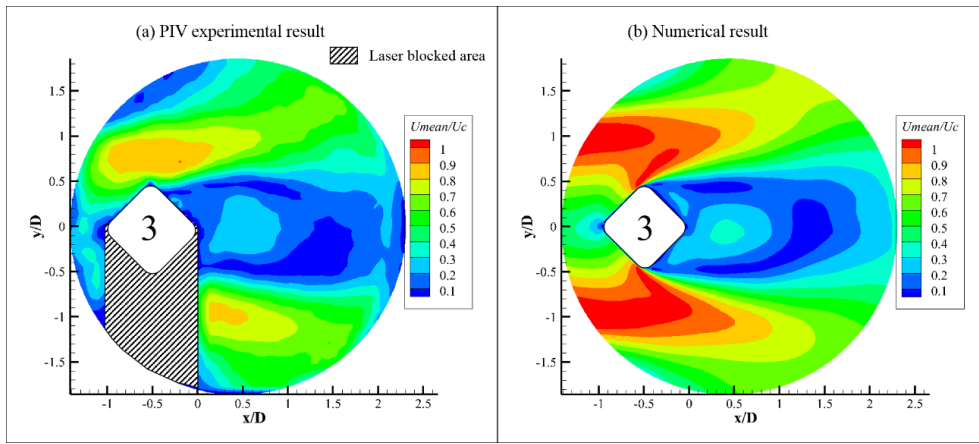


Figure 5.50 Time-averaged velocity distribution after column 3 at the middle draft level of the four columns configuration in *XY* plane.

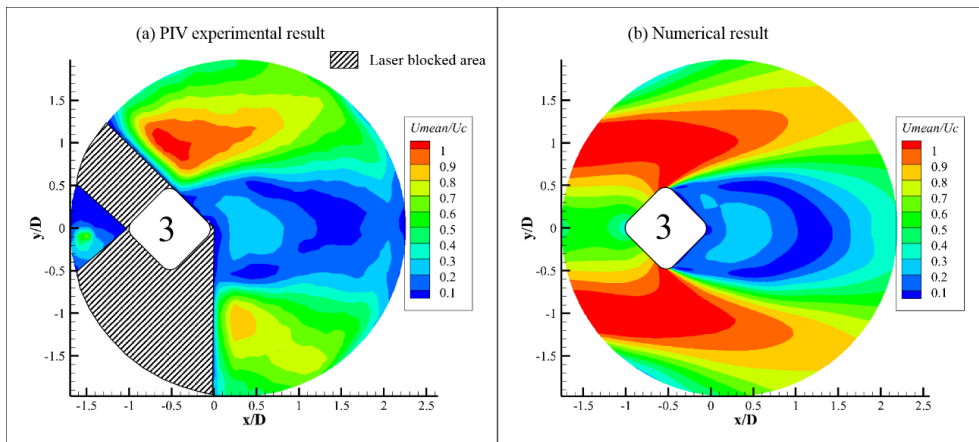


Figure 5.51 Time-averaged velocity distribution after column 3 at the middle draft level of the four columns with pontoons connected configuration in *XY* plane.

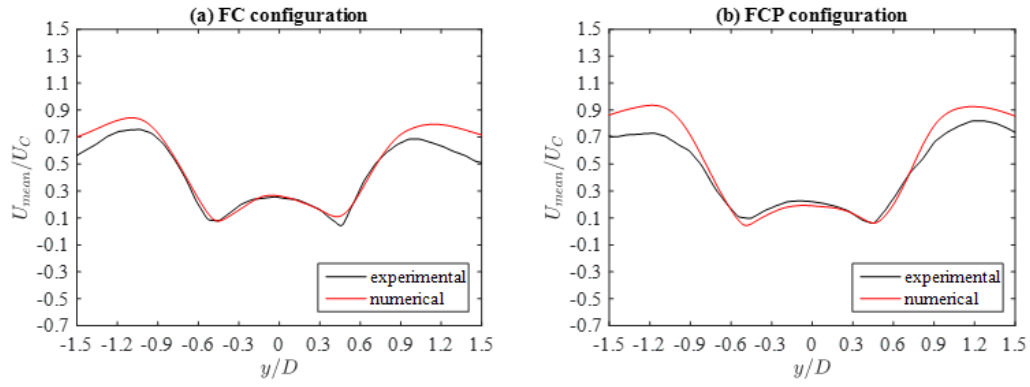


Figure 5.52 Time-averaged flow properties of the U_{mean}/U_C in XY plane (middle draft level of the structure) for column 3, at $x/D = 0.75$ $Re = 4.3 \times 10^4$, “FC” is the four columns configuration and “FCP” is the four columns with pontoons connected configuration.

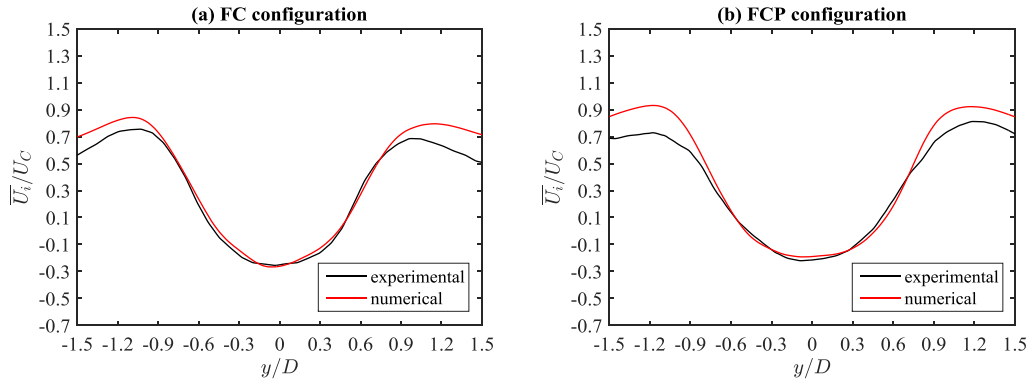


Figure 5.53 Time-averaged flow properties of the \overline{U}_i/U_C (velocity component i) in XY plane (middle draft level of the structure) for column 3 at $x/D = 0.75$, $Re = 4.3 \times 10^4$. “FC” is the four columns configuration and “FCP” is the four columns with pontoons connected configuration.

It is noted that the experimental results are quite limited due to a limitation of the PIV measuring range. In order to have a more in-depth study of the flow characteristics, the numerical results serve as a good complementary study in the present work. The time-averaged streamwise velocity components (velocity component i) after each column are determined as shown in Figure 5.54. By adding on the pontoons into the structure, the minimum values of the streamwise velocities after each column are seen to be slightly raised. It is noted that each column has some individual differences. For column 1, adding the pontoons increases the recirculating region’s streamwise velocity, but it decreases the velocity distribution trend at the sides of the column. Unlike the upstream column 1, the downstream column 3 shows a different trend of the velocity at the two sides of the column: The four columns with pontoons connected configuration has a larger streamwise velocity than the four columns configuration has. At the

recirculation region, the velocity trend turns out to be flatter for the four columns with pontoons connected configuration. For the two side columns (column 2 and 4), as can be seen in Figure 5.54, their streamwise velocity distributions are symmetric.

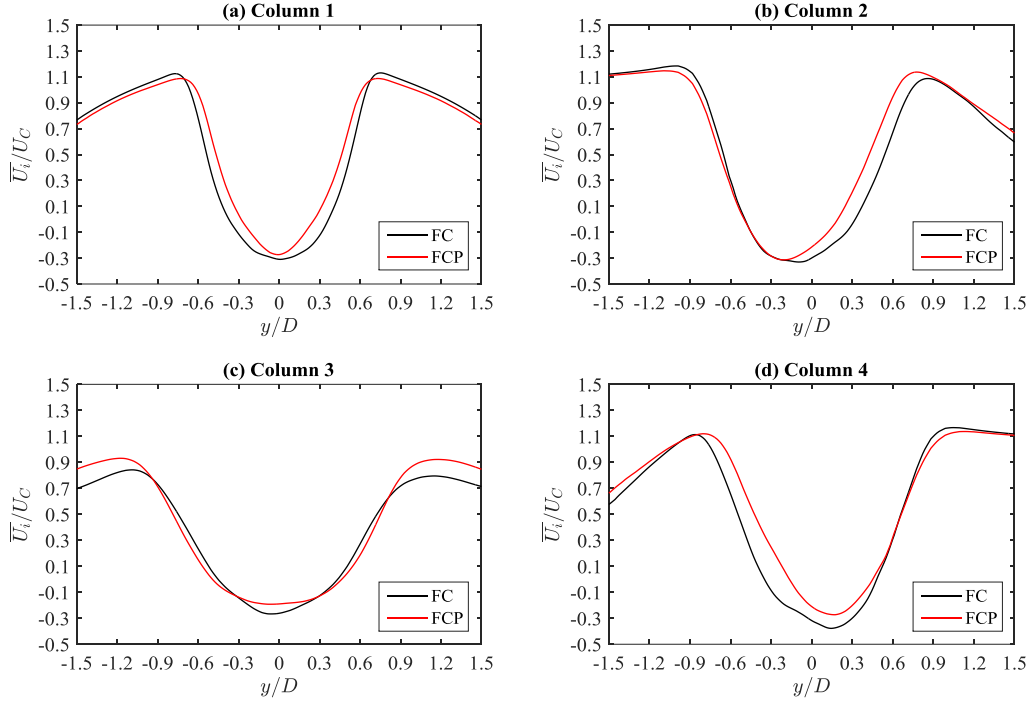


Figure 5.54 Numerical predicted time-averaged flow properties of the \bar{U}_i/U_C (velocity component i) in XY plane (middle draft level of the structure) for each column at $x/D = 0.75$, $Re = 4.3 \times 10^4$. “FC” is the four columns configuration and “FCP” is the four columns with pontoons connected configuration.

The instantaneous non-dimensional vorticity ($\bar{\omega}_z D/U$) contours obtained from the experiments within one vortex shedding period for column 3 of both configurations are shown in Figure 5.55 and Figure 5.56 respectively. As can be seen in these figures, due to the effects of the vortices that have been shed from the three upstream columns, the wake region after column 3 is full of fragmentized vortices. The vortices shed from column 3 quickly break into pieces and mix with the vortices that have been shed from the two side columns (column 2 and 4) after they have been separated from the column. It is noted that, by adding on the pontoons, the vortex street that is trailing from column 3 becomes clearer and that the vortices shed from column 3 break up relatively slowly when compared with the pure four columns configuration. Strong vortices can be found flowing afterward from column 3 in the four columns with pontoons connected configuration.

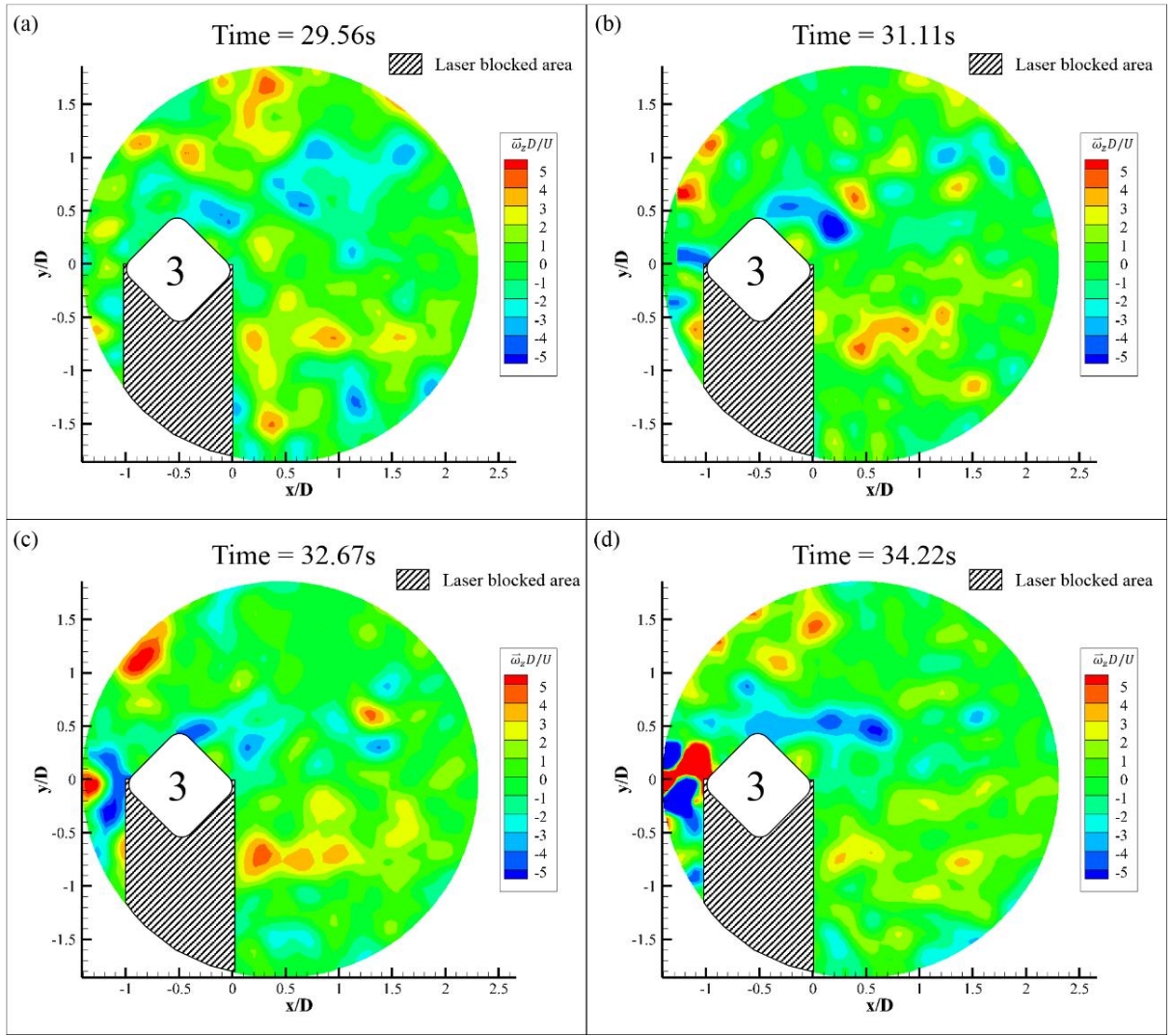


Figure 5.55 Instantaneous flow fields around column 3 for the four columns configuration at XY plane (middle draft level of the structure), where $\bar{\omega}_z D/U$ is the non-dimensional spanwise vorticity.

In order to have a more general understanding of the overall flow patterns, the vorticity contours obtained from the numerical simulations for the two different configurations are shown in Figure 5.57 and Figure 5.58. For convenience in describing the vortex development processes, the vortices that are shed from each side of the column are denoted in Table 5.2, similar as the definition in Interaction of vortex shedding processes on the flow around four columns with and without pontoons connected section.

As shown in Figure 5.57, for the four columns configuration, the vortices that are shed from each side of the individual column break into pieces easily after being separated from the

columns. There are a large number of small vortices near the reverse side of the columns in the downstream weak area, especially for column 1.

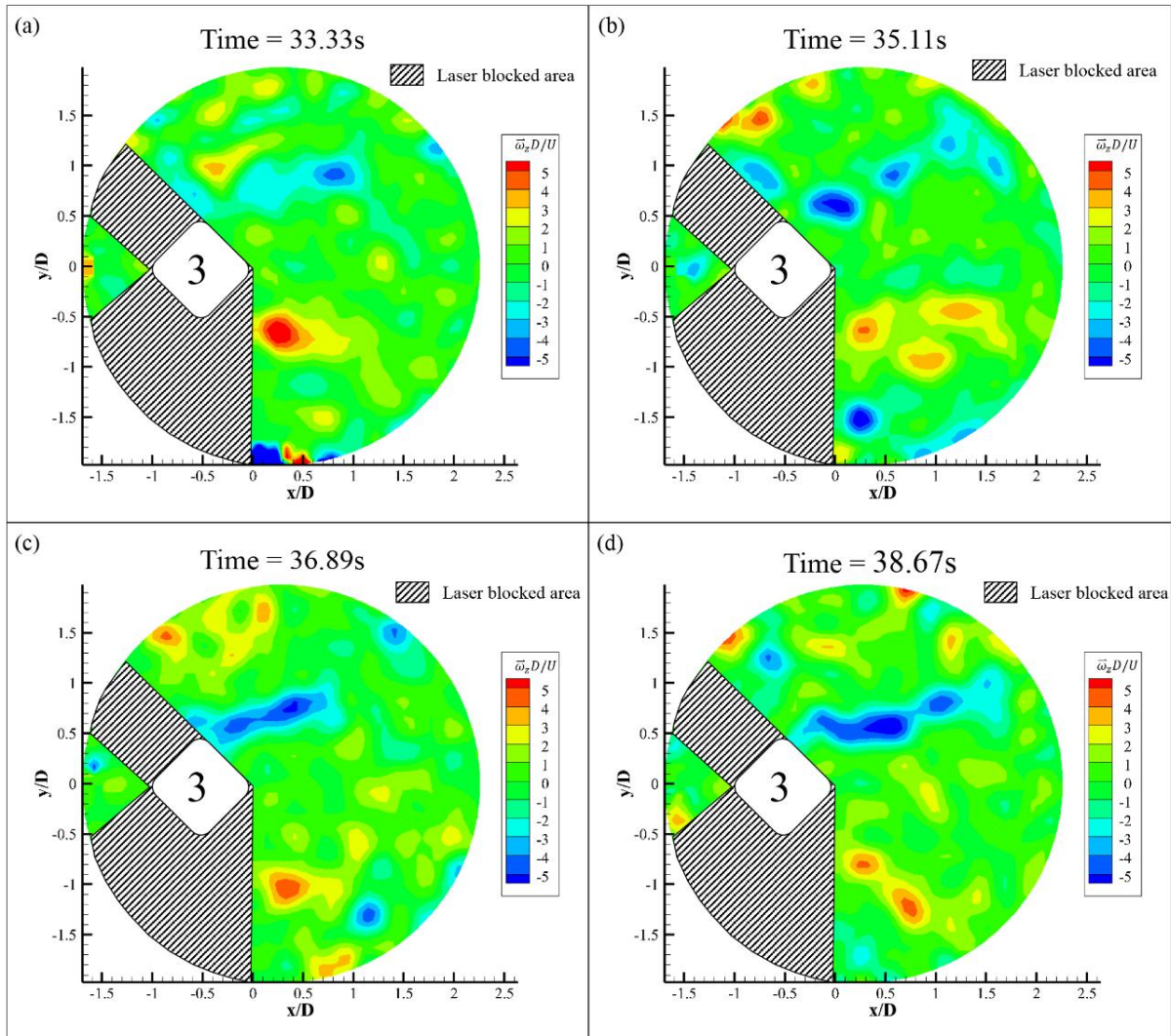


Figure 5.56 Instantaneous flow fields around column 3 for the four columns with pontoons connected configuration at XY plane (middle draft level of the structure), where $\vec{\omega}_z D/U$ is the non-dimensional spanwise vorticity.

The vortices that are shed from the upstream column (column 1) directly impinge on the downstream column (column 3). After impinging on the downstream column, the vortices (see B1 in Figure 5.57(c)) break into two parts and then joined in to the wake region of the other three columns (see two B1' in Figure 5.57(d)). Additionally, the vortices that have been shed from the inner sides of the portside and the starboard side columns (column 2 and 4) break into pieces rapidly after shedding from the inner corner of the related column (see C1, H1 in Figure 5.57). However, the vortices that are shed from the outer sides of the portside and the starboard side columns can remain for a relatively long time compared with the inner side shed vortices

(see D1, D2, G1, G2 in Figure 5.57). The downstream column 3 shows a rather different phenomenon. The vortices (see E1, F1 in Figure 5.57) that are shed from column 3 can remain in one position for an indeterminate time and then break into two parts. A portion of the vortices join in to the wake region of the whole structure. Another part of the vortices moves back to impinge on column 3 (see two F1' in Figure 5.57(d)). In general, the whole flow region around the four columns model are fully occupied with fragmentized vortices the same as was observed in the experiments (as shown in Figure 5.55).

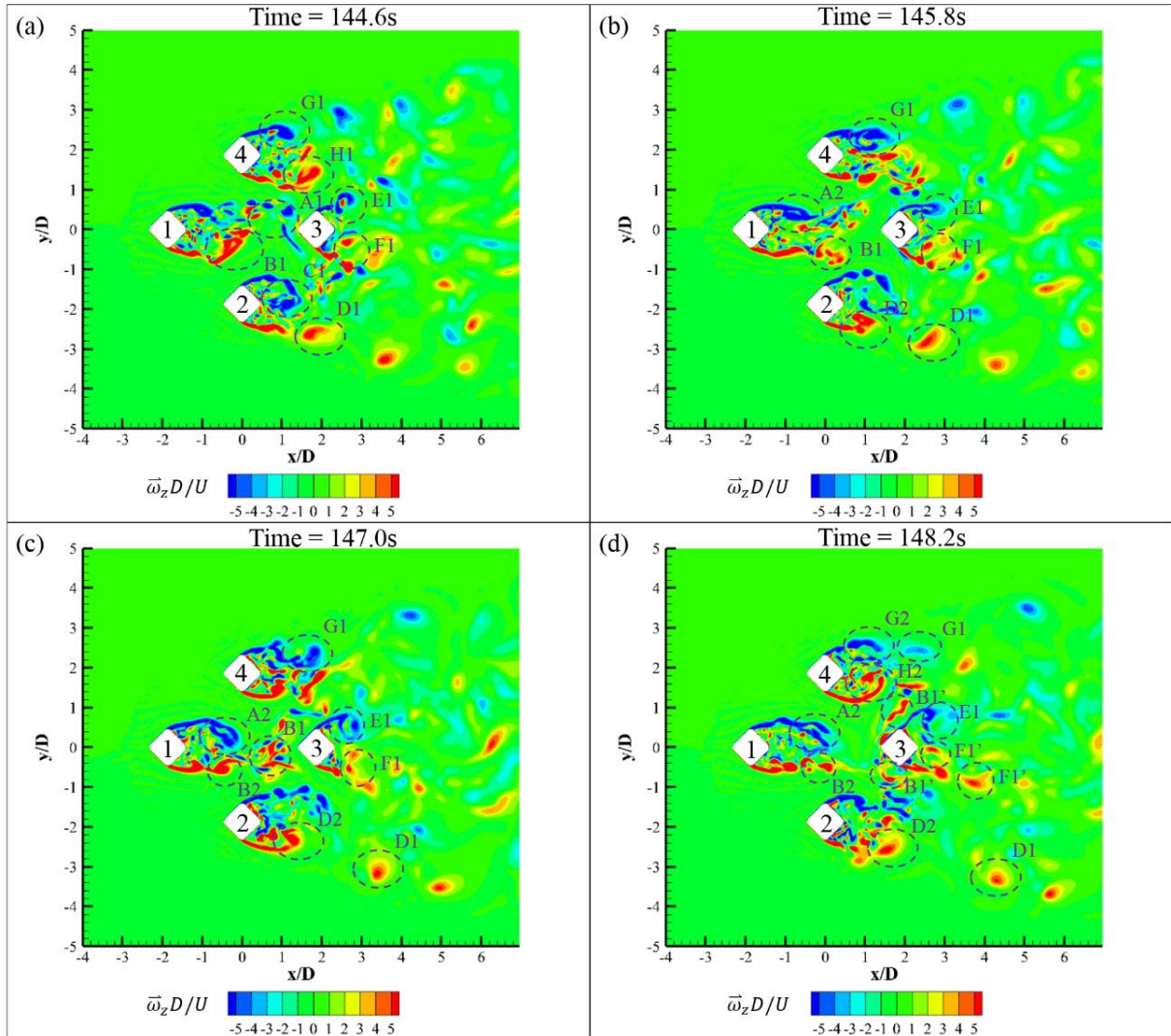


Figure 5.57 A time series of the non-dimensional spanwise vorticity ($\bar{\omega}_z D/U$) contours around the four columns configuration model at the middle draft level showing the instantaneous flow fields in XY plane at $Re = 4.3 \times 10^4$.

By adding the pontoons to the structure, the flow characteristics were appreciably altered. As shown in Figure 5.58, when compared with the four columns configuration, the vortices that

are shed from each column become more structured and clearly defined. Very slim vortices are shed from the corners of column 1 and then they directly impinge on column 3. Strong vortices are observed from both the portside and starboard side columns (column 2 and 4), in particular from the outer corners of the two side columns. It is noted that the vortices (see H1 and C2 in Figure 5.58) that are shed from the inner sides of the side columns can break into two pieces (see H1' and C2' in Figure 5.58). Unlike the four columns configuration model, with the pontoons connected, the vortices that are shed from the downstream column (column 3) are seen to quickly disappear after they separate from the corner of column 3 (see E1, E2, F1 and F2 in Figure 5.58). Thus, adding on the pontoons into the structure can structure the vortices be more stable when compared with the pure four columns configuration.

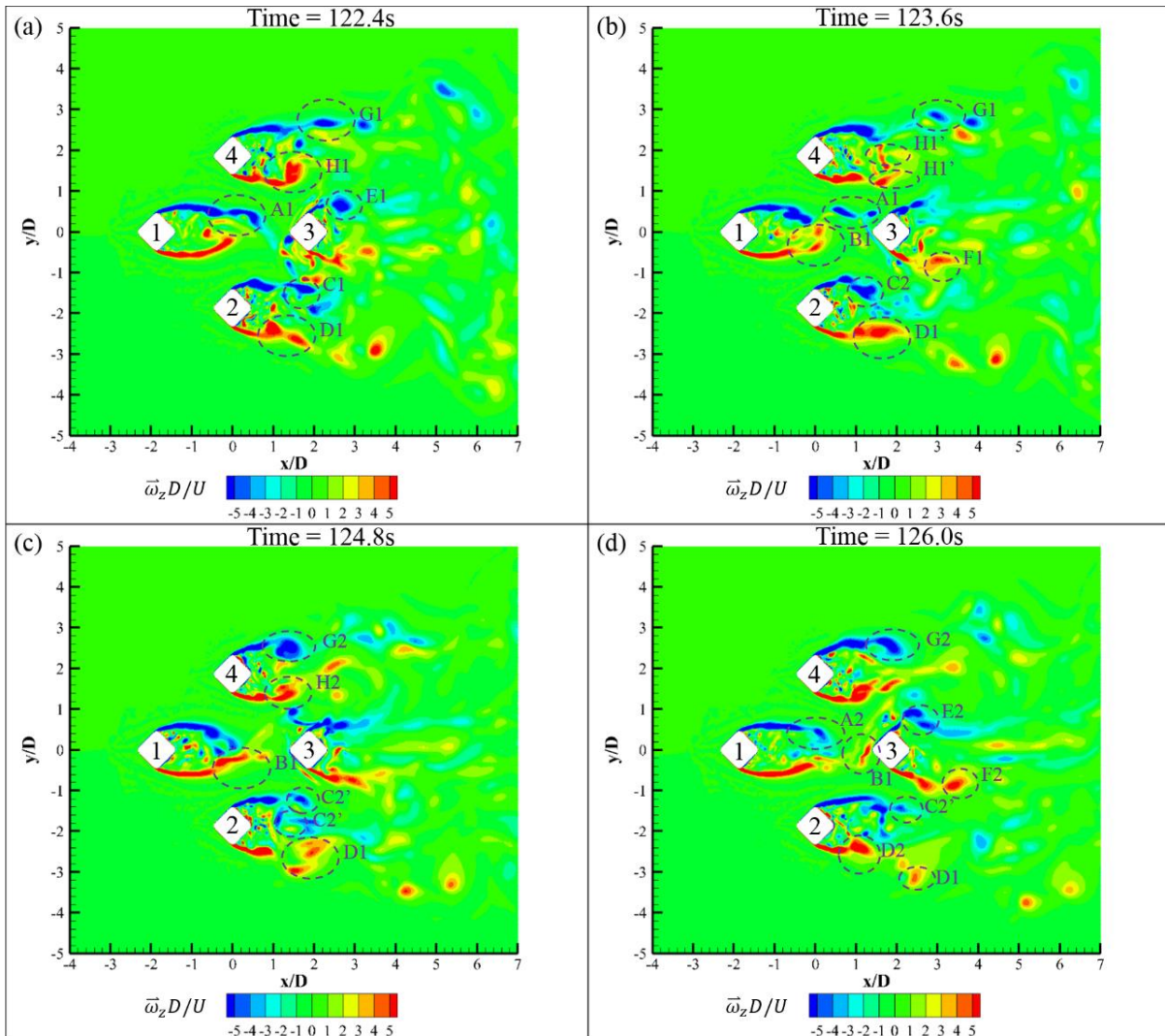


Figure 5.58 A time series of the non-dimensional spanwise vorticity ($\bar{\omega}_z D/U$) contours around the four columns with pontoons connected configuration model at the middle draft level showing the instantaneous flow fields in XY plane at $Re = 4.3 \times 10^4$.

5.3.2 Flow characteristics in the vertical plane

It is noted that the vortices that are shed from the free end of each column make the main contribution to the changes in the hydrodynamics between the two configurations. Thus, further study the flow characteristics in vertical plane is warranted.

Vertical velocity components (velocity component k) are sampled over several vertical cross sections coinciding with XZ plane (i, k plane) in order to investigate the differences of the downstream velocity distribution at several certain offset distances ($x/D = 0.25$, $x/D = 0.75$ and $x/D = 1.5$) after each column. Herein, the pontoons' effects can be directly observed in Figure 5.59, Figure 5.60 and Figure 5.61.

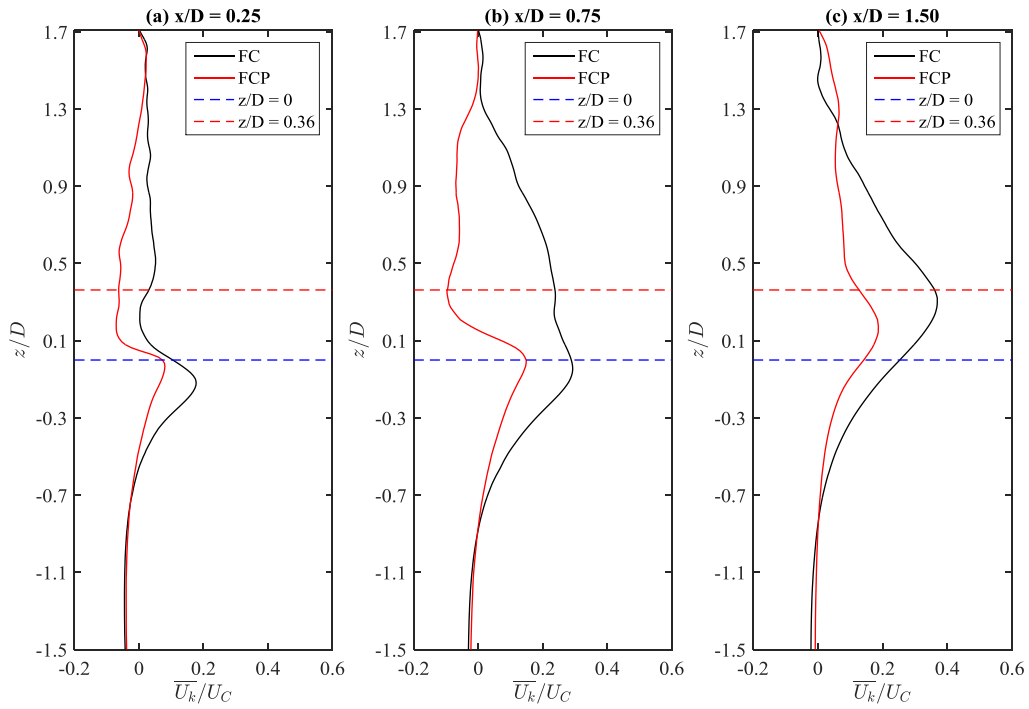


Figure 5.59 Numerically predicted time-averaged flow properties of the \overline{U}_k/U_C (velocity component k) in XZ plane for column 1 with certain distances ($x/D = 0.25$, $x/D = 0.75$ and $x/D = 1.5$) at $y/D = 0$ (the central line of column), $Re = 4.3 \times 10^4$. “FC” is the four columns configuration and “FCP” is the four columns with pontoons connected configuration. “ $z/D = 0$ ” is the bottom of the column and “ $z/D = 0.36$ ” is the pontoon upper face level.

According to Figure 5.59, by adding the pontoons in the structure, the vertical velocity distributions alter significantly for the upstream column 1. There is a reduction of the velocity

component k between two configurations. With pontoons connected, the vertical velocity decreases rapidly over the bottom level at the downstream positions of $x/D = 0.25$ and $x/D = 0.75$ behind column 1. Additionally, the four columns with pontoons connected configuration is observed to have a stronger recirculation phenomenon when compared with the four columns configuration. The four columns configuration has a smooth velocity change at points along the vertical direction at the position slightly far from column 1 ($x/D = 0.75$ and $x/D = 1.50$). The same as for column 1, the side column, column 2, also has an obvious recirculation phenomenon for the four columns with pontoons connected configuration (see Figure 5.60 at $x/D = 0.25$). With adding on the pontoons, the vertical velocities decrease as well. However, this time, the differences of vertical velocity distributions are not as significant as in the case of column 1. As can be seen in Figure 5.61, for the downstream column 3, the differences between two configurations are smaller than those for the three upstream column. The four columns with pontoons connected configuration has a very smooth vertical velocity distribution after column 3 at the position of $x/D = 0.75$ and $x/D = 1.50$.

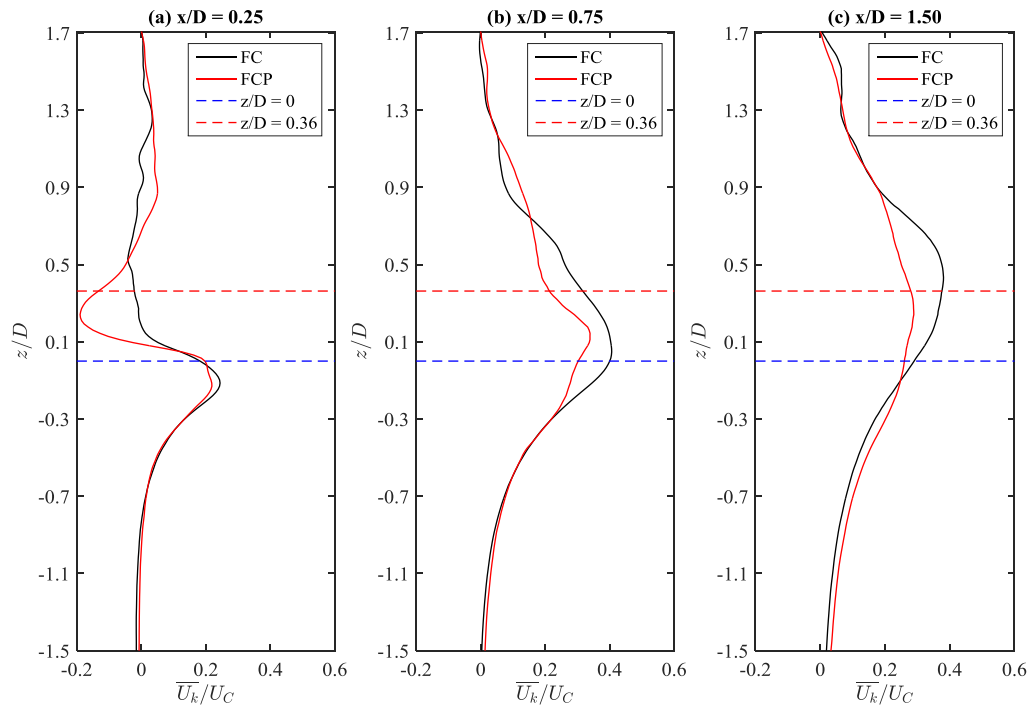


Figure 5.60 Numerically predicted time-averaged flow properties of the \overline{U}_k/U_C (velocity component k) in XZ plane for column 2 with certain distances ($x/D = 0.25$, $x/D = 0.75$ and $x/D = 1.5$) at $y/D = 0$ (the central line of column), $Re = 4.3 \times 10^4$. “FC” is the four columns configuration and “FCP” is the four columns with pontoons connected configuration. “ $z/D = 0$ ” is the bottom of the column and “ $z/D = 0.36$ ” is the pontoon upper face level.

It is noted that the four columns configuration still has the bulge between the bottom level and the pontoon upper face level. In addition, the vertical velocities of the four columns with pontoons connected configuration are larger than the vertical velocities of the four columns configuration for most part of the vertical region.

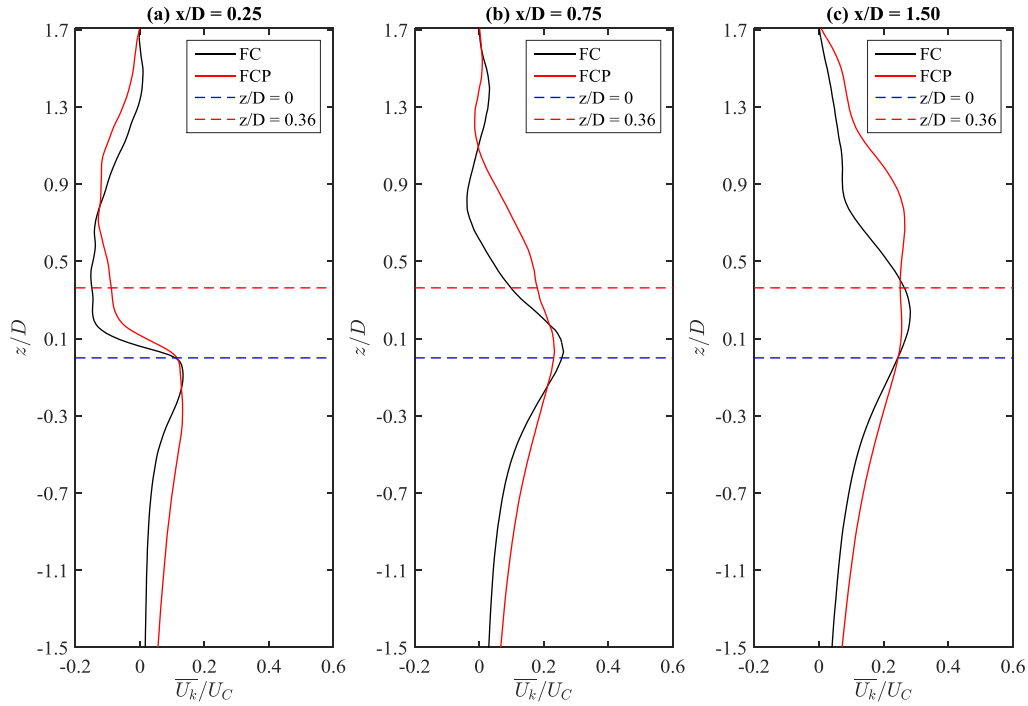


Figure 5.61 Numerically predicted time-averaged flow properties of the \overline{U}_k/U_C (velocity component k) in XZ plane for column 3 with certain distances ($x/D=0.25$, $x/D=0.75$ and $x/D=1.5$) at $y/D=0$ (the central line of column), $Re=4.3 \times 10^4$. “FC” is the four columns configuration and “FCP” is the four columns with pontoons connected configuration. “ $z/D=0$ ” is the bottom of the column and “ $z/D=0.36$ ” is the pontoon upper face level.

In addition, the flow patterns observed in the vertical cross sections are discussed in detail to study the free end effects on the hydrodynamics.

For the four columns configuration, the vertical wake region after column 1 is quite similar to that developing in the horizontal wake region. The wake region is fully occupied with fragmentized vortices, which can be clearly seen in Figure 5.62. Unlike column 1, column 3 has a clearer organised and tidy wake region, where only one obvious strong vortices can be seen (see Figure 5.62). In addition, only a small portion of the vortices which shed from the free end of column 1 can join into the column 3 free end shear layer, these vortices are red

circled in Figure 5.62(a) and Figure 5.62(b). Parts of the vortices that have been shed from the free end of column 1 appear to recirculate to impinge back on column 1. Majority of the vortices shed from column 1 impinge on the incidence flow face of column 3, which are red circled in Figure 5.62(c) and Figure 5.62(d). When looking at the side column (column 2, see Figure 5.63), this column shows a quite similar flow pattern as a single finite column does (Sumner, 2013), and this is as expected because there is no blocked structure behind this column.

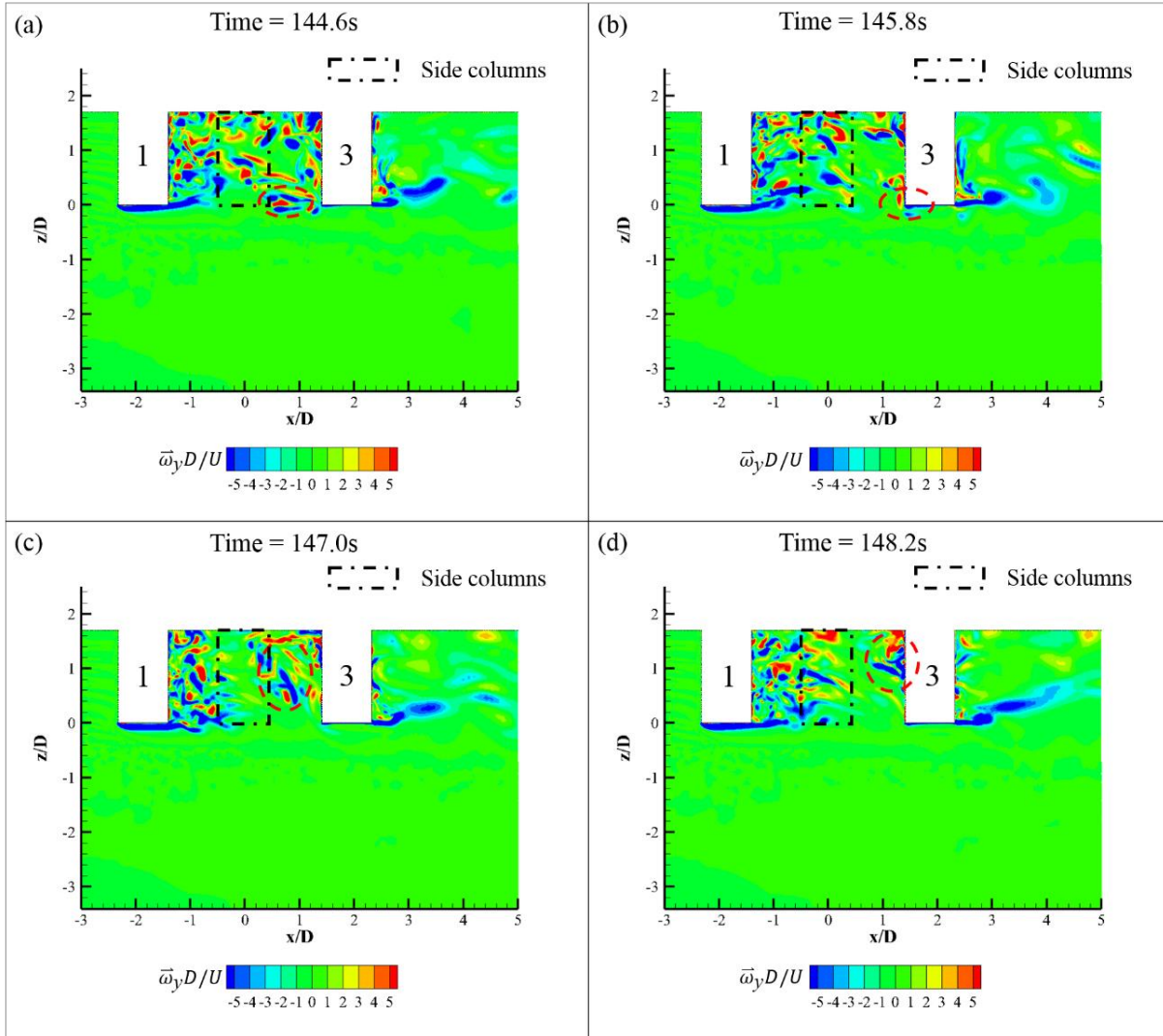


Figure 5.62 A time series of the non-dimensional transverse vorticity ($\bar{\omega}_y D/U$) contours around the four columns configuration model at the central line of column 1 and 3 showing the instantaneous flow fields in XZ plane at $Re = 4.3 \times 10^4$.

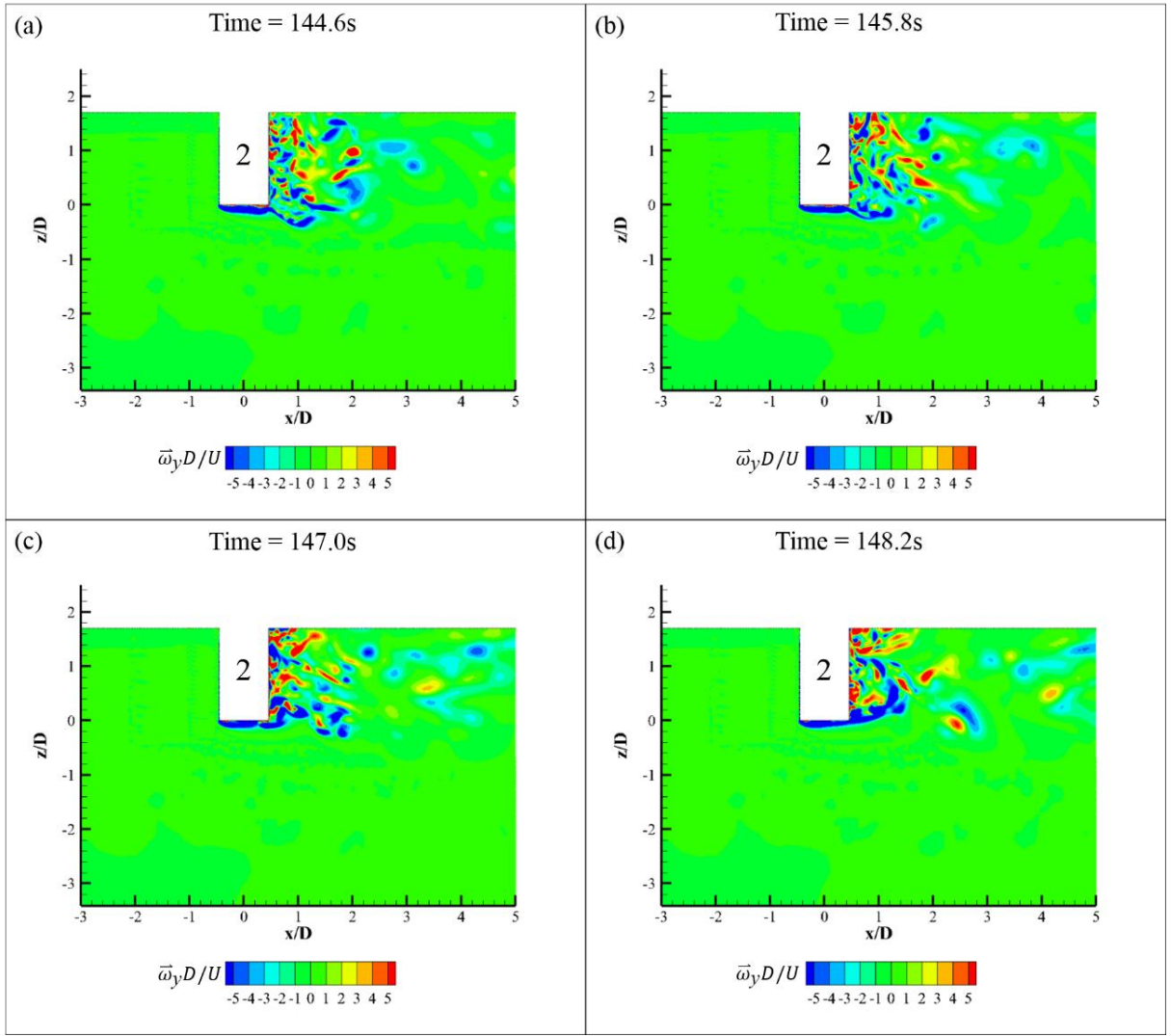


Figure 5.63 A time series of the non-dimensional transverse vorticity ($\bar{\omega}_y D/U$) contours around the four columns configuration model at the central line of column 2 showing the instantaneous flow fields in XZ plane at $Re = 4.3 \times 10^4$.

With the pontoons added into the whole structure, the vertical flow patterns from each column change significantly. For column 1, the vortices that are shed from the free end become slimmer when compared with the corresponding vortices from the four columns configuration. Additionally, the amount of the fragmentized vortices behind column 1 was reduced after adding the pontoons. Unlike the four columns configuration, the majority of the vortices that have been shed from the free end of column 1 join with the vortices being shed from the free end of column 3 (see red circled part in Figure 5.64(c) and Figure 5.64(d)). This vortex mixing behaviour makes the vortices behind column 3 to be shorter than in the four columns configuration vortices. When it comes to the side columns (e.g. column 2), by connecting the pontoons between the columns, the vortex shedding behaviour at the free end completely

changes. As shown in Figure 5.65, two vortices are shed from the separate edges of the free end. One of the vortices quickly mixes with the vortices being shed from the side of the column. The other vortices tend to keep at a certain vertical level for a time and then join into the wake region that is generated by the vortices being shed from the sides of the column.

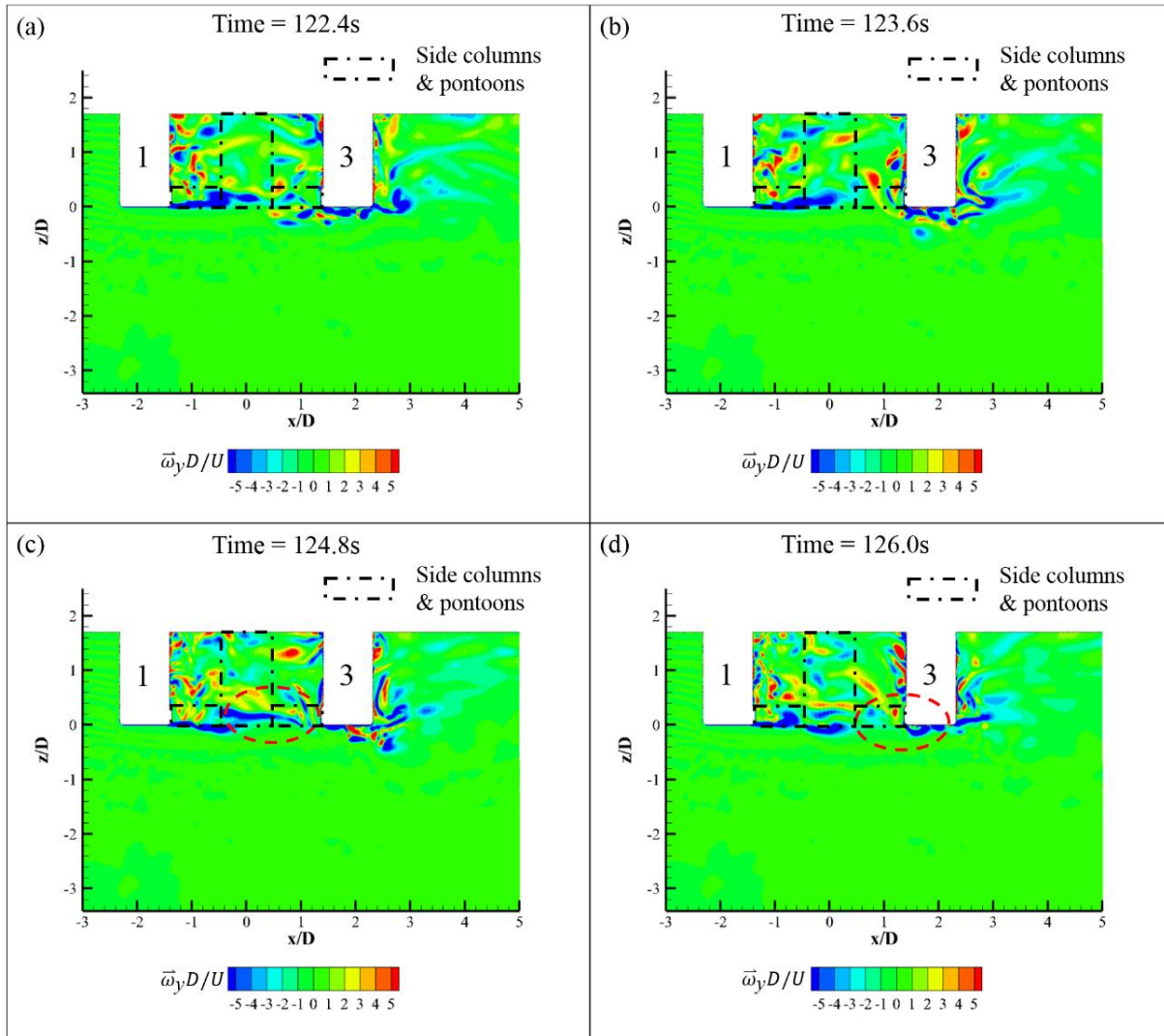


Figure 5.64 A time series of the non-dimensional transverse vorticity ($\bar{\omega}_y D/U$) contours around the four columns with pontoons connected configuration model at the central line of column 1 and 3 showing the instantaneous flow fields in XZ plane at $Re = 4.3 \times 10^4$.

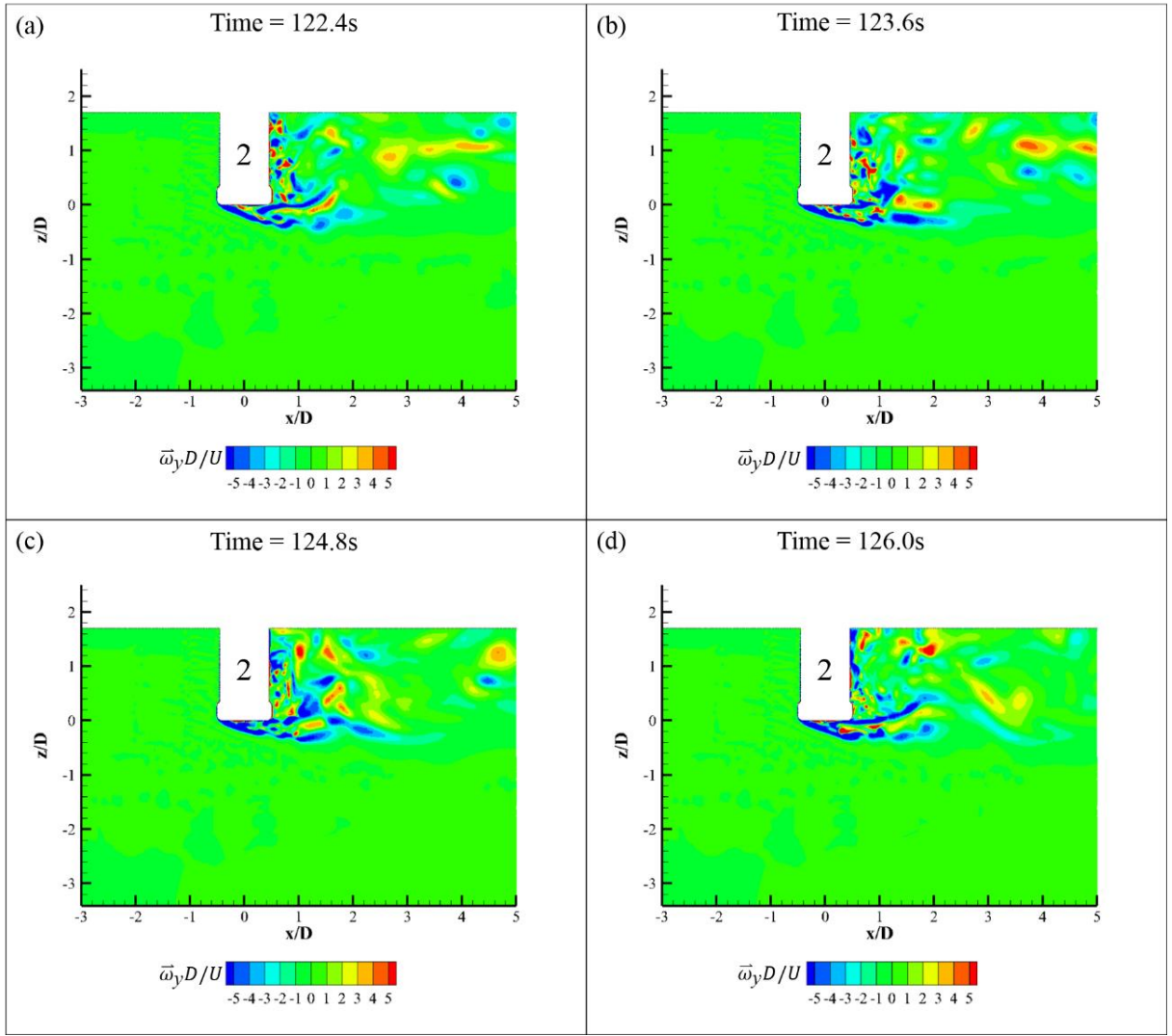


Figure 5.65 A time series of the non-dimensional transverse vorticity ($\bar{\omega}_y D/U$) contours around the four columns with pontoons connected configuration model at the central line of column 2 showing the instantaneous flow fields in XZ plane at $Re = 4.3 \times 10^4$.

5.3.3 Overall drag and lift forces

The overall drag and lift forces on the structures are presented as the non-dimensional coefficients C_D , C_L and St . Details of the results from both the experimental and the numerical results are shown in this section.

Table 5.3 The resulting non-dimensional coefficients \bar{C}_D , C_{Lrms} and St for the four columns configuration (“num.” represents “numerical”; “exp.” represents “experimental”).

Re	\bar{C}_D (num.)	\bar{C}_D (exp.)	C_{Lrms} (num.)	C_{Lrms} (exp.)	St (num.)	St (exp.)
3.7×10^4	1.083	0.948	0.062	0.053	0.156	0.137
4.3×10^4	1.075	0.961	0.066	0.055	0.152	0.139
5.2×10^4	1.077	0.962	0.066	0.051	0.150	0.139
6.0×10^4	1.068	0.990	0.066	0.053	0.151	0.141

Table 5.4 The resulting non-dimensional coefficients \bar{C}_D , C_{Lrms} and St for the four columns with pontoons connected configuration (“num.” represents “numerical”; “exp.” represents “experimental”).

Re	\bar{C}_D (num.)	\bar{C}_D (exp.)	C_{Lrms} (num.)	C_{Lrms} (exp.)	St (num.)	St (exp.)
3.7×10^4	1.054	0.932	0.070	0.078	0.132	0.123
4.3×10^4	1.043	0.940	0.072	0.078	0.139	0.122
5.2×10^4	1.047	0.953	0.071	0.076	0.142	0.124
6.0×10^4	1.051	0.974	0.078	0.082	0.139	0.126

As can be seen in Table 5.3 and Table 5.4, the overall hydrodynamics remain relatively stable in the examined Reynolds number range. Comparisons between the results from the numerical simulations and the experimental data of the differences of \bar{C}_D , C_{Lrms} as well as St values between two model conditions (that are columns with/without pontoons) are plotted in Figure 5.66, Figure 5.67 and Figure 5.68. Observations are given in a discussion as presented in the following text.

In order to illustrate any level of uncertainty in the experimental measurements, the error bars are shown in each figure. For \bar{C}_D , the maximum discrepancy between the numerical simulations and the experimental results is 14% (observed at $Re = 3.7 \times 10^4$, for the four columns configuration).

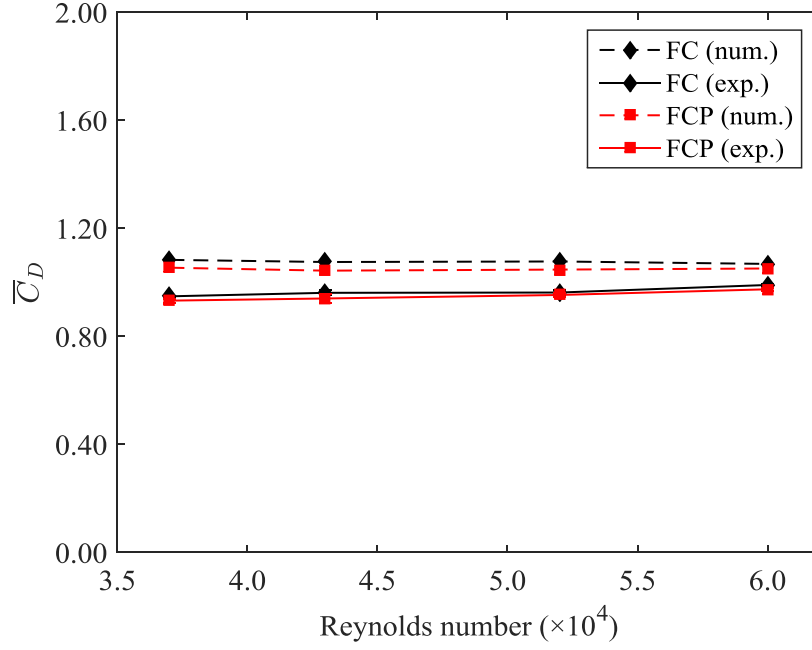


Figure 5.66 Mean drag coefficient (\bar{C}_D) from the numerical (num.) and experimental (exp.) results for the four columns configuration (FC) and the four columns with pontoons connected configuration (FCP).

The maximum discrepancy for C_{Lrms} is 34% (observed at $Re = 5.2 \times 10^4$, for the four columns configuration). Additionally, the discrepancy in C_{Lrms} for the majority of cases is less than 20%. The maximum difference for St is 18% (observed at $Re = 5.2 \times 10^4$, for the four columns with pontoons connected configuration). Thus, it can be concluded that the numerical predictions show a reasonably agreement when compared with the experimental data in the present study. As Figure 5.66 and Figure 5.68 show, both variables (\bar{C}_D and St) decrease by the adding the pontoons especially for St . On the contrary, adding the pontoons can increase the lift force coefficient on the structure (as shown in Figure 5.67). However, the increment of C_{Lrms} predicted by the numerical model is slightly smaller than the increment measured by the experiments.

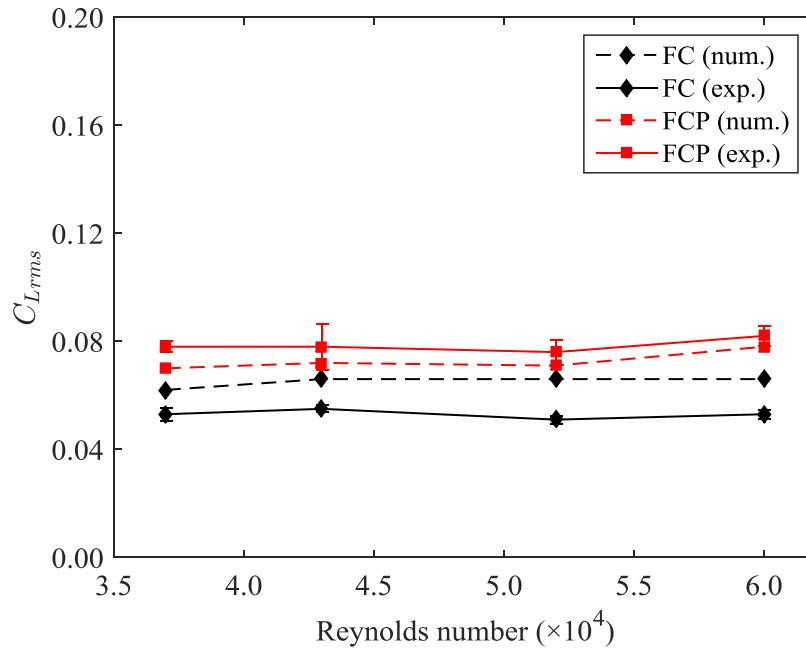


Figure 5.67 Root-mean-square lift coefficient (C_{Lrms}) from the numerical (num.) and experimental (exp.) results for the four columns configuration (FC) and the four columns with pontoons connected configuration (FCP).

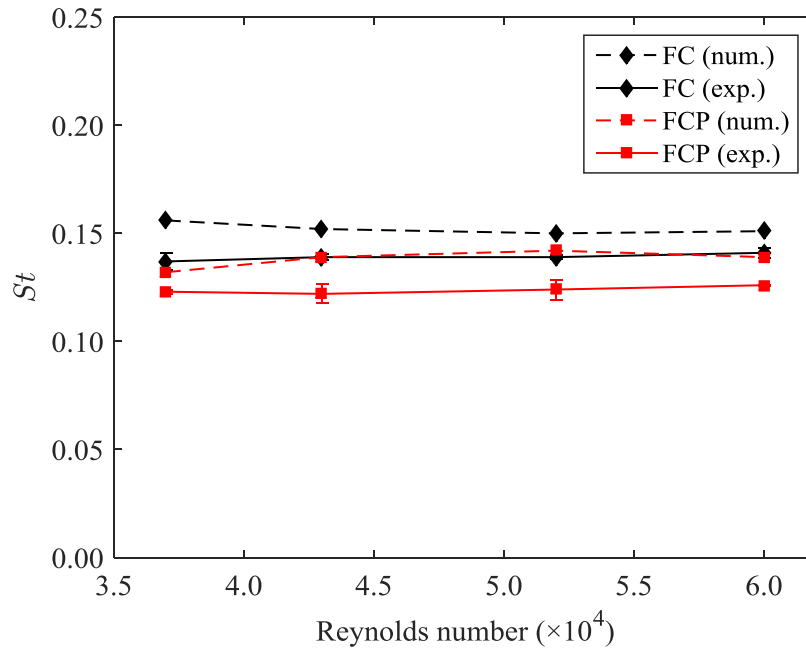


Figure 5.68 Strouhal number (St) from the numerical (num.) and experimental (exp.) results for the four columns configuration (FC) and the four columns with pontoons connected configuration (FCP).

5.3.4 Drag and lift force on each member

In order to examine the complex fluid mechanisms on the structure and to improve the understanding of interactions between each of the columns of the structures, the hydrodynamic force coefficients on each individual column in each of the two configurations are further calculated and the results are presented in Figure 5.69, Figure 5.70 and Figure 5.71.

The mean drag force coefficient (see Figure 5.69) on each column remains stable within the current Reynolds number range and is similar to the trend of the overall \bar{C}_D . The two side columns (column 2 and 4) experience the largest \bar{C}_D of all the columns. The upstream column (column 1) experiences a slightly smaller \bar{C}_D than the \bar{C}_D of the two side columns but is still far beyond the \bar{C}_D of the downstream column (column 3). The drag force coefficient on the downstream column (column 3) decreases slightly when the pontoons were added into the whole structure, while the drag force coefficient on the portside and starboard side columns (column 2 and 4) increases. When looking at the C_{Lrms} , the upstream column has the smallest value among all four columns and for both configurations. As the portside and starboard side columns (column 2 and 4) are symmetrically exposed to the flow, the fluctuating lift forces on them are symmetric (as shown in Figure 5.70 and Figure 5.71). However, there is a significant increment for the C_{Lrms} on the two side columns between the two configurations owing to the pontoons. The upstream column was also observed to experience a large increment as shown in Figure 5.70, by adding on the pontoons. It is noted that the downstream column experiences the largest fluctuating lift force coefficient than other columns. Although the root-mean-square lift force coefficients on the downstream column fluctuate considerably, the coefficient remains at a stable level within current Reynolds number range. It is also revealed that the lift force coefficient on the three upstream columns (column 1, 2, and 4) will increase by adding on the pontoons into the structure. And the increment finally reflects in the C_{Lrms} of the overall structure.

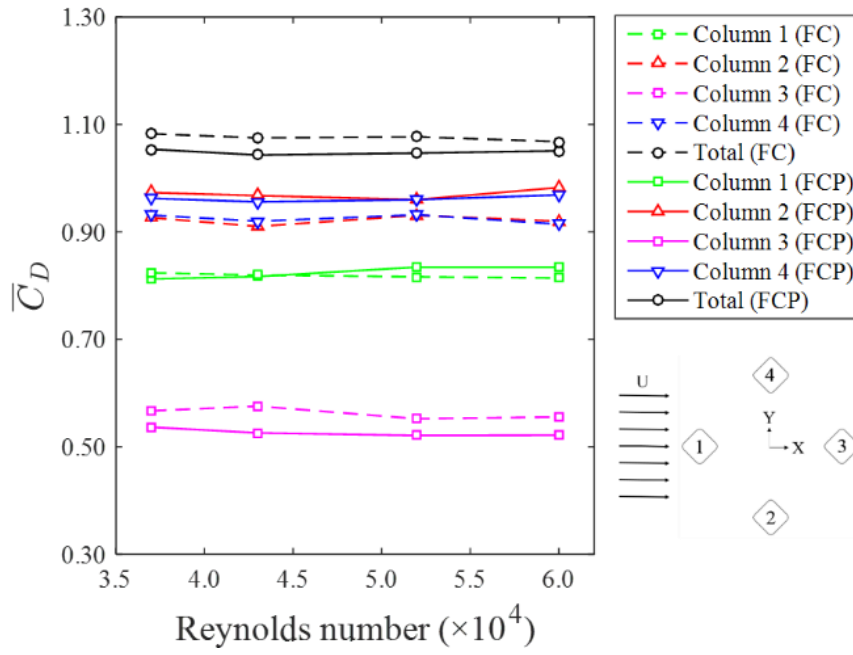


Figure 5.69 Mean drag coefficients (\bar{C}_D) on each member of the models (FC represents the four columns configuration; FCP represents the four columns with pontoons connected configuration).

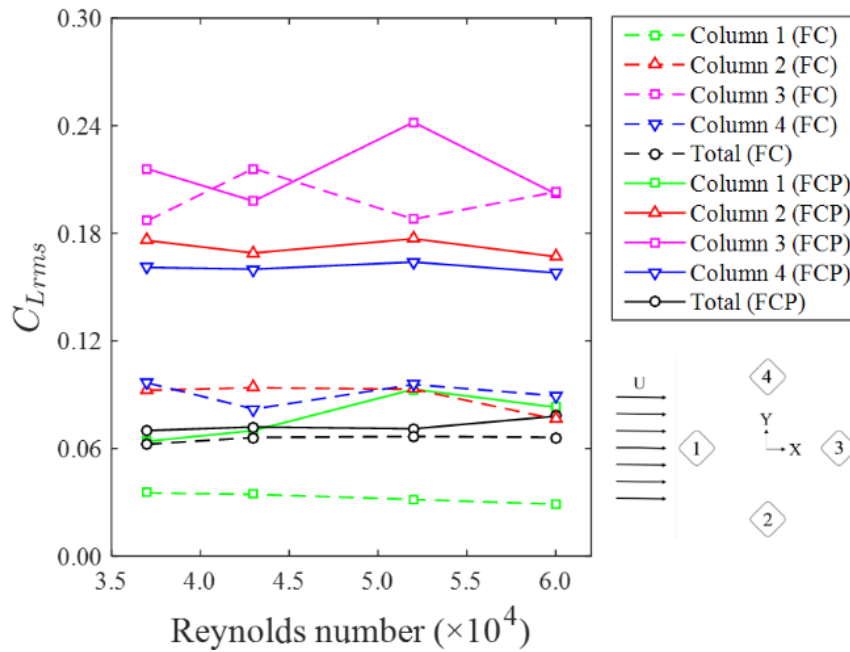


Figure 5.70 Root-mean-square lift coefficients (C_{Lrms}) on each member of the models (FC represents the four columns configuration; FCP represents the four columns with pontoons connected configuration).

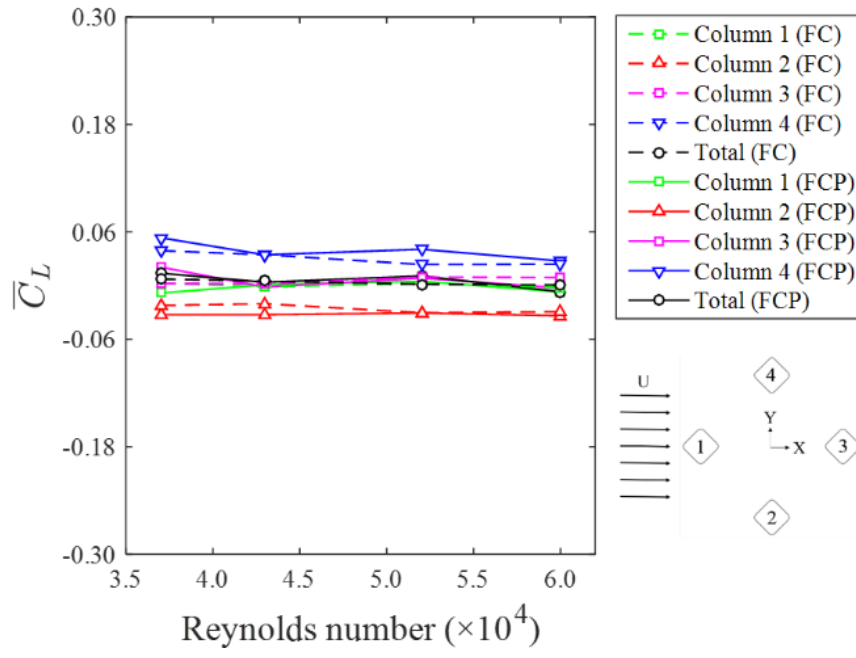


Figure 5.71 Mean lift coefficient (\bar{C}_L) on each member of the models (FC represents the four columns configuration; FCP represents the four columns with pontoons connected configuration).

Chapter 6. Conclusions and Future Works

6.1 Conclusions

The strength of the present study is in developing both experimental and numerical study focusing on various aspects of the VIM of a DDS as well as the overall hydrodynamics of a multi-column structures. While model tests conducted in towing tank and circulating water channel served as a reliable benchmark for validating the numerical model, it also provided comprehensive measurements on the flow characteristics around the structures, motion responses and associated forces acting on the structure. Numerical simulation on the other hand, provided substantial details on the vortex shedding characteristics under different current incidence angles and wide range of current strength which further adds to the in-depth analysis of the correlations between the vortex shedding flow characteristics and motion induced.

The principal contributions and conclusions of the present research are summarised below:

1. For two flow incidences investigated in the towing tank, VIM behaviour of the DDS in the horizontal XY plane occurs in a range of $4.0 \leq Ur \leq 11.0$, with peaks around $6.0 \leq Ur \leq 7.0$ corresponding to “lock-in”. When $Ur \geq 15.0$, a high vortex shedding frequency appeared (galloping) is observed. In the “post lock-in” region, the motion response may be dominated by both VIM and galloping. Both in-line and transverse motions under 45° incidence are larger than that in the 0° incidence condition with yaw motions showing opposite responses.
2. Good correlation has been demonstrated among the vortex shedding patterns, the fluctuation forces on the structure, and the VIM trajectory in the present work. The “lock-in” phenomenon was found to have the most striking effect on the vortex shedding processes, the force and the VIM trajectories. During the “lock-in”, the vortices shed from the upstream columns of the DDS act on the downstream columns as if vortices being “shed” of a significant nature from the downstream column itself.
3. Analysis of the drag and lift force coefficients on and the work done by different members of the DDS revealed that the vortex shedding processes due to the portside and starboard side columns are the primary contributors to the VIM responses in the “lock-in” region while the vortex shedding processes due to the pontoons are acting to restrain the VIM responses.

4. The present numerical study confirmed the hysteresis phenomenon - the peak lift force occurs slightly earlier than the peak transverse motion. By examining the flow patterns at the time instantaneous near the peak response, it is revealed that the hysteresis phenomenon between the force and motion is mainly due to the vortices shed from the upstream column move back to impinge on one of the side columns after impinging on the other side column and the symmetrical strong vortices which shed from the side columns.

5. By examining the flow patterns at the time instantaneous from both the experimental and the numerical results, it is revealed that adding the pontoons into the structure can serve to organise and structure the vortices that are shed from the columns well and make the overall wake region tidy and more clearly defined. The pontoons connected between each column block the vortices shed from the free end of the column, especially pushing the recirculation region further away from the free end of each column. Difference in the wake region indicate that adding on the pontoons to a basic multi-column structure makes the vortex street tends to be more tidy and structured. Hence, the vortex shedding period and lift force are increased.

6. The analyses of the hydrodynamic force coefficients on the structures revealed that adding the pontoons onto the structure had a large effect on the fluctuation force coefficients, especially for the portside and starboard side columns. However, the influence on the drag force coefficient is not as significant as that on the lift force coefficient.

6.2 Suggestions for future work

Although the present study has cover most aspects for the interactions of vortex shedding processes on the flow around multi-column structures, fluctuation forces on the structure, and the VIM trajectory, certain limitations are also apparent. There are still some aspects requiring further research and study.

1. It is worth noting that the differences of the mooring line settings between the experiments and numerical simulations may affect the forces on the structures. In order to improve the accuracy of the numerical simulations, a further study considering the gravity force on and the material characteristics of the mooring lines is needed to examine their effects in the numerical model properly.

2. This study mostly focuses on the flow with 45 degree incidence around the DDS, more incidences should be considered and examined in order to obtain a more generalized understanding on VIM of a multi-column structures.
3. The wave effects, the damping effects from the risers and the Reynolds number effects should be further considered to have a more generalised understanding on VIM in the real world. More investigations are required to examine such aspects in field measurements.
4. The flow characteristics around the stationary structures in the vertical plane should be further measured to provide the flow patterns around the free end in detail.
5. With the limitation of PIV measuring area, this study only focusses on the flow region around the most downstream column in the physical experiments. The flow region around the overall structure is expected to be recorded in future to provide more details about the flow characteristics between the columns.

Appendix A

Test matrix and results for the towing tank experiment

Incidence (°)	Towing Speed (m/s)	Ur	A_x/L	A_y/L	Yaw	\bar{C}_D	C_{Lrms}
0	0.062	3.9	0.030	0.021	0.979	2.024	0.062
0	0.089	5.7	0.060	0.083	2.063	1.788	0.372
0	0.100	6.4	0.056	0.279	4.492	2.007	0.579
0	0.120	7.7	0.077	0.222	4.009	1.572	0.313
0	0.126	8.0	0.069	0.226	3.900	1.697	0.341
0	0.150	9.5	0.082	0.180	3.389	1.506	0.171
0	0.185	11.8	0.086	0.173	2.862	1.419	0.209
0	0.220	14.0	0.128	0.302	4.198	1.360	0.261
0	0.247	15.7	0.150	0.379	4.721	1.390	0.226
0	0.318	20.2	0.175	0.424	5.443	1.379	0.124
45	0.073	3.4	0.022	0.035	0.418	1.159	0.237
45	0.083	3.9	0.033	0.166	1.141	1.299	0.407
45	0.109	5.1	0.057	0.663	1.527	1.349	0.715
45	0.130	6.1	0.082	0.716	2.119	1.321	0.416
45	0.141	6.6	0.099	0.742	2.435	1.416	0.269
45	0.157	7.3	0.092	0.613	2.416	1.450	0.139
45	0.191	8.9	0.102	0.398	2.885	1.316	0.124
45	0.211	9.8	0.108	0.345	2.716	1.267	0.123
45	0.260	12.1	0.139	0.318	2.679	1.167	0.096
45	0.302	14.1	0.159	0.346	2.486	1.252	0.122

Numerical predictions for the towing tank test

Incidence (°)	Current Speed (m/s)	Ur	A_x/L	A_y/L	Yaw	\bar{C}_D	C_{Lrms}
0	0.062	3.9	0.016	0.037	0.706	1.356	0.280
0	0.100	6.4	0.033	0.251	5.183	1.613	0.396
0	0.185	11.8	0.074	0.214	3.835	1.377	0.223
0	0.247	15.7	0.111	0.322	5.873	1.338	0.265
45	0.083	3.9	0.030	0.236	1.148	1.196	0.504
45	0.109	5.1	0.051	0.701	2.087	1.512	0.697
45	0.141	6.6	0.104	0.760	2.222	1.419	0.292
45	0.191	8.9	0.122	0.378	2.826	1.241	0.103
45	0.260	12.1	0.150	0.345	3.040	1.139	0.105

Appendix B

Test matrix and results for the circulating water channel experiment

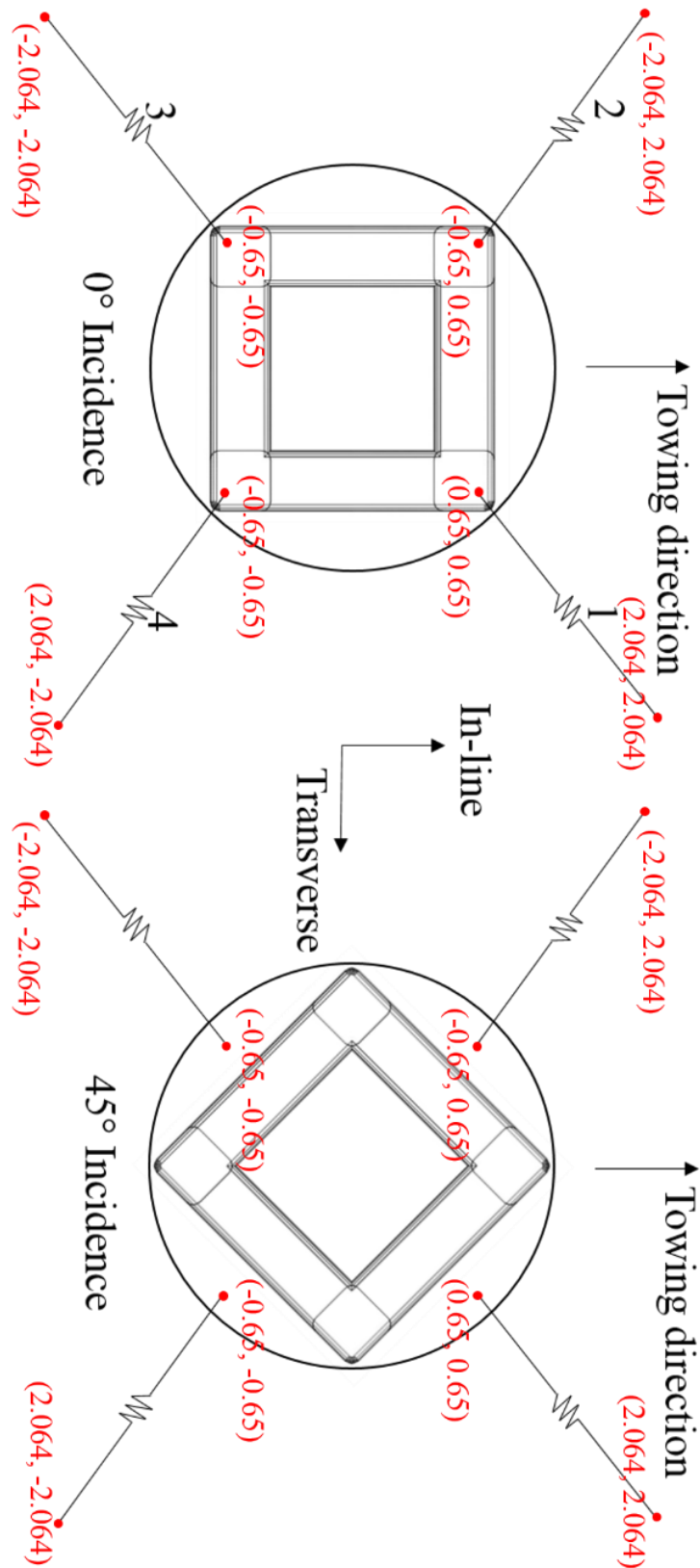
Configuration	Current Speed (m/s)	Re	\bar{C}_D	C_{Lrms}	St
Four columns	0.17	37000	0.946	0.051	0.133
Four columns	0.17	37000	0.949	0.055	0.141
Four columns	0.20	43000	0.970	0.056	0.141
Four columns	0.20	43000	0.951	0.055	0.137
Four columns	0.24	52000	0.971	0.052	0.140
Four columns	0.24	52000	0.952	0.049	0.139
Four columns	0.28	60000	0.995	0.051	0.143
Four columns	0.28	60000	0.984	0.055	0.139
Four columns with pontoons	0.17	37000	0.940	0.080	0.122
Four columns with pontoons	0.17	37000	0.925	0.076	0.124
Four columns with pontoons	0.20	43000	0.952	0.087	0.125
Four columns with pontoons	0.20	43000	0.925	0.077	0.118
Four columns with pontoons	0.20	43000	0.942	0.071	0.124
Four columns with pontoons	0.24	52000	0.949	0.071	0.119
Four columns with pontoons	0.24	52000	0.961	0.078	0.128
Four columns with pontoons	0.24	52000	0.949	0.078	0.124
Four columns with pontoons	0.28	60000	0.980	0.086	0.126
Four columns with pontoons	0.28	60000	0.967	0.079	0.126

Numerical predictions for the circulating water channel test

Configuration	Current Speed (m/s)	Re	\bar{C}_D	C_{Lrms}	St
Four columns	0.17	37000	1.083	0.062	0.156
Four columns	0.20	43000	1.075	0.066	0.152
Four columns	0.24	52000	1.077	0.066	0.150
Four columns	0.28	60000	1.068	0.066	0.151
Four columns with pontoons	0.17	37000	1.054	0.070	0.132
Four columns with pontoons	0.20	43000	1.043	0.072	0.139
Four columns with pontoons	0.24	52000	1.047	0.071	0.142
Four columns with pontoons	0.28	60000	1.051	0.078	0.139

Appendix C

Anchor and failed point position (Unit: m). (0, 0) is the gravity centre of the DDS.



References

- Antony, A., Vinayan, V., Halkyard, J., Kim, S.-J., Holmes, S. and Spornjak, D. (2015) 'A CFD Based Analysis of the Vortex Induced Motion of Deep-Draft Semisubmersibles', *The Twenty-fifth International Offshore and Polar Engineering Conference*. International Society of Offshore and Polar Engineers.
- Antony, A., Vinayan, V., Madhavan, S., Parambath, A., Halkyard, J., Sterenborg, J., Holmes, S., Spornjak, D., Kim, S.J. and Head, W. (2016) 'VIM Model Test of Deep Draft Semisubmersibles Including Effects of Damping', *Offshore Technology Conference*. Offshore Technology Conference.
- Bearman, P.W. (1969) 'On vortex shedding from a circular cylinder in the critical Reynolds number regime', *Journal of Fluid Mechanics*, 37(03), pp. 577-585.
- Bearman, P.W., Graham, J.M.R., Obasaju, E.D. and Drossopoulos, G.M. (1984) 'The influence of corner radius on the forces experienced by cylindrical bluff bodies in oscillatory flow', *Applied Ocean Research*, 6(2), pp. 83-89.
- Bindingsbo, A.U. and Bjørset, A. (2002) 'Deep draft semi submersible', *ASME 2002 21st International Conference on Offshore Mechanics and Arctic Engineering*. American Society of Mechanical Engineers, pp. 651-659.
- Bishop, R.E.D. and Hassan, A.Y. (1964a) 'The lift and drag forces on a circular cylinder in a flowing fluid', *Proceedings of the Royal Society of London. Series A. Mathematical and Physical Sciences*, 277(1368), pp. 32-50.
- Bishop, R.E.D. and Hassan, A.Y. (1964b) 'The Lift and Drag Forces on a Circular Cylinder Oscillating in a Flowing Fluid', *Proceedings of the Royal Society of London. Series A. Mathematical and Physical Sciences*, 277(1368), pp. 51-75.
- Blazek, J. (2015) *Computational fluid dynamics: principles and applications*. Butterworth-Heinemann.

- Breuer, M. (1998) 'Numerical and modeling influences on large eddy simulations for the flow past a circular cylinder', *International Journal of Heat and Fluid Flow*, 19(5), pp. 512-521.
- Cantwell, B. and Coles, D. (1983) 'An experimental study of entrainment and transport in the turbulent near wake of a circular cylinder', *Journal of Fluid Mechanics*, 136, pp. 321-374.
- CD-adapco (2014) *User Guide*. Star-CCM+ Version 9.04.
- Celik, I.B., Ghia, U. and Roache, P.J. (2008) 'Procedure for estimation and reporting of uncertainty due to discretization in CFD applications', *Journal of Fluids Engineering-Transactions of the ASME*, 130(7).
- Chen, J.M. and Chiou, C.-C. (1997) 'Flow past a blunt flat plate subjected to the disturbance of incident vortex street', *Journal of wind engineering and industrial aerodynamics*, 66(3), pp. 179-196.
- Christopher, N.M. and Chad, S. (2012) *2012 WORLDWIDE SURVEY of SPAR, DDCV, and MinDOC VESSELS*. Offshore Magazine & WoodGroup Mustang.
- Christopher, N.M., Chad, S., Albaugh, E.K. and Jones, C. (2012) *2012 DEEPWATER SOLUTIONS & RECORDS FOR CONCEPT SELECTION*. Offshore Magazine & WoodGroup Mustang.
- Delany, N.K. and Sorensen, N.E. (1953) *Low-speed drag of cylinders of various shapes*. National Advisory Committee for Aeronautics.
- Dennis, S.C.R. and Chang, G.-Z. (1970) 'Numerical solutions for steady flow past a circular cylinder at Reynolds numbers up to 100', *Journal of Fluid Mechanics*, 42(03), pp. 471-489.
- Dong, S. and Karniadakis, G.E. (2005) 'DNS of flow past a stationary and oscillating cylinder at $Re = 10\,000$ ', *Journal of Fluids and structures*, 20(4), pp. 519-531.

- Finn, L.D., Maher, J.V. and Gupta, H. (2003) 'The cell spar and vortex induced vibrations', *Offshore Technology Conference, OTC*.
- Fontoura, D.V.R., Tsukada, R.I. and Shiguemoto, D.A. (2015) 'Numerical Simulation of a Submersible Buoy Using a Wake Oscillator Model Calibrated for VIM', *ASME 2015 34th International Conference on Ocean, Offshore and Arctic Engineering*. American Society of Mechanical Engineers, pp. V002T08A009-V002T08A009.
- Fujarra, A.L.C., Rosetti, G.F., de Wilde, J. and Gonçalves, R.T. (2012) 'State-of-art on vortex-induced motion: a comprehensive survey after more than one decade of experimental investigation', *ASME 2012 31st International Conference on Ocean, Offshore and Arctic Engineering*. American Society of Mechanical Engineers, pp. 561-582.
- Gonçalves, R.T., Freire, C.M., Rosetti, G.F., Franzini, G.R., Fujarra, A.L.C. and Meneghini, J.R. (2011) *ASME 2011 30th International Conference on Ocean, Offshore and Arctic Engineering*. American Society of Mechanical Engineers.
- Gonçalves, R.T., Fujarra, A.L.C., Rosetti, G.F., Kogishi, A.M. and Koop, A. (2015) 'Effects of Column Designs on the VIM Response of Deep-Draft Semi-Submersible Platforms', *The Twenty-fifth International Offshore and Polar Engineering Conference*. International Society of Offshore and Polar Engineers.
- Gonçalves, R.T., Fujarra, A.L.C., Rosetti, G.F., Nishimoto, K., Cueva, M. and Siqueira, E.F.N. (2009) *ASME 2009 28th International Conference on Ocean, Offshore and Arctic Engineering*. American Society of Mechanical Engineers.
- Gonçalves, R.T., Rosetti, G.F., Fujarra, A.L.C. and Oliveira, A.C. (2012) 'Experimental study on vortex-induced motions of a semi-submersible platform with four square columns, Part I: Effects of current incidence angle and hull appendages', *Ocean Engineering*, 54, pp. 150-169.
- Gonçalves, R.T., Rosetti, G.F., Fujarra, A.L.C. and Oliveira, A.C. (2013) 'Experimental study on vortex-induced motions of a semi-submersible platform with four square columns, Part II: Effects of surface waves, external damping and draft condition', *Ocean Engineering*, 62, pp. 10-24.

- Grove, A.S., Shair, F.H. and Petersen, E.E. (1964) 'An experimental investigation of the steady separated flow past a circular cylinder', *Journal of Fluid Mechanics*, 19(01), pp. 60-80.
- Halkyard, J., Srinivas, S., Holmes, S., Constantinides, Y., Oakley, O.H. and Thiagarajan, K. (2005) 'Benchmarking of truss spar vortex induced motions derived from CFD with experiments', *ASME 2005 24th International Conference on Offshore Mechanics and Arctic Engineering*. American Society of Mechanical Engineers, pp. 895-902.
- Holmes, S. (2008) 'Predicting spar VIM using CFD', *ASME 2008 27th International Conference on Offshore Mechanics and Arctic Engineering*. American Society of Mechanical Engineers, pp. 895-900.
- Hong, Y., Choi, Y., Lee, J. and Kim, Y. (2008) 'Vortex-induced motion of a deep-draft semi-submersible in current and waves', *The Eighteenth International Offshore and Polar Engineering Conference*. International Society of Offshore and Polar Engineers.
- Inoue, O., Mori, M. and Hatakeyama, N. (2006) 'Aeolian tones radiated from flow past two square cylinders in tandem', *Physics of Fluids*, 18(4), p. 046101.
- Irani, M. and Finn, L. (2004) 'Model testing for vortex induced motions of spar platforms', *ASME 2004 23rd International Conference on Offshore Mechanics and Arctic Engineering*. American Society of Mechanical Engineers, pp. 605-610.
- Irani, M., Jennings, T., Geyer, J. and Krueger, E. (2015) 'Some Aspects of Vortex Induced Motions of a Multi-Column Floater', *ASME 2015 34th International Conference on Ocean, Offshore and Arctic Engineering*. American Society of Mechanical Engineers, pp. V002T08A036-V002T08A036.
- Irani, M., Perryman, S., Brewer, J. and McNeill, S. (2008) 'Vortex Induced Motions of the Horn Mountain Truss Spar', *ASME 2008 27th International Conference on Offshore Mechanics and Arctic Engineering*. American Society of Mechanical Engineers, pp. 967-973.
- Khalifa, A., Weaver, D. and Ziada, S. (2012) 'A single flexible tube in a rigid array as a model for fluidelastic instability in tube bundles', *Journal of Fluids and Structures*, 34, pp. 14-32.

- Kim, S.J., Spornjak, D., Holmes, S., Vinayan, V. and Antony, A. (2015) 'Vortex-induced motion of floating structures: CFD sensitivity considerations of turbulence model and mesh refinement', *ASME 2015 34th International Conference on Ocean, Offshore and Arctic Engineering*. American Society of Mechanical Engineers, pp. V002T08A057-V002T08A057.
- Kiya, M., Tamura, H. and Arie, M. (1980) 'Vortex shedding from a circular cylinder in moderate-Reynolds-number shear flow', *Journal of Fluid Mechanics*, 101(04), pp. 721-735.
- Kokkinis, T., Sandström, R.E., Jones, H.T., Thompson, H.M. and Greiner, W.L. (2004) 'Development of a Stepped Line Tensioning Solution for Mitigating VIM Effects in Loop Eddy Currents for the Genesis Spar', *ASME 2004 23rd International Conference on Offshore Mechanics and Arctic Engineering*. American Society of Mechanical Engineers, pp. 995-1004.
- Koop, A., Rijken, O., Vaz, G., Maximiano, A. and Rosetti, G. (2016) 'CFD Investigation on Scale and Damping Effects for Vortex Induced Motions of a Semi-Submersible Floater', *Offshore Technology Conference*. Offshore Technology Conference.
- Lam, K. and Fang, X. (1995) 'The effect of interference of four equispaced cylinders in cross flow on pressure and force coefficients', *Journal of Fluids and Structures*, 9(2), pp. 195-214.
- Lam, K., Gong, W.Q. and So, R.M.C. (2008) 'Numerical simulation of cross-flow around four cylinders in an in-line square configuration', *Journal of Fluids and Structures*, 24(1), pp. 34-57.
- Lam, K., Li, J.Y., Chan, K.T. and So, R.M.C. (2003a) 'Flow pattern and velocity field distribution of cross-flow around four cylinders in a square configuration at a low Reynolds number', *Journal of Fluids and Structures*, 17(5), pp. 665-679.
- Lam, K., Li, J.Y. and So, R.M.C. (2003b) 'Force coefficients and Strouhal numbers of four cylinders in cross flow', *Journal of Fluids and Structures*, 18(3), pp. 305-324.

- Lam, K. and Lo, S.C. (1992) 'A visualization study of cross-flow around four cylinders in a square configuration', *Journal of Fluids and Structures*, 6(1), pp. 109-131.
- Lam, K. and Zou, L. (2010) 'Three-dimensional numerical simulations of cross-flow around four cylinders in an in-line square configuration', *Journal of Fluids and Structures*, 26(3), pp. 482-502.
- Lee, S.-K., Chien, H.-P. and Gu, H. (2014) 'CFD Study of Deep Draft SemiSubmersible VIM', *Offshore Technology Conference-Asia*. Offshore Technology Conference.
- Lefevre, C., Constantinides, Y., Kim, J.W., Henneke, M., Gordon, R., Jang, H. and Wu, G. (2013) 'Guidelines for CFD Simulations of Spar VIM', *ASME 2013 32nd International Conference on Ocean, Offshore and Arctic Engineering*. American Society of Mechanical Engineers, pp. V007T08A019-V007T08A019.
- Liang, Y. and Tao, L. (2017) 'Interaction of vortex shedding processes on flow over a deep-draft semi-submersible', *Ocean Engineering*, 141, pp. 427-449.
- Liang, Y., Tao, L., Xiao, L. and Liu, M. (2016) 'Experimental and Numerical Study on Flow Past Four Rectangular Columns in Diamond Configuration', *ASME 2016 35th International Conference on Ocean, Offshore and Arctic Engineering*. American Society of Mechanical Engineers, pp. V001T01A044-V001T01A044.
- Liang, Y., Tao, L., Xiao, L. and Liu, M. (2017) 'Experimental and numerical study on vortex-induced motions of a deep-draft semi-submersible', *Applied Ocean Research*, 67, pp. 169-187.
- Liu, C.-H. and Chen, J.M. (2002) 'Observations of hysteresis in flow around two square cylinders in a tandem arrangement', *Journal of Wind Engineering and Industrial Aerodynamics*, 90(9), pp. 1019-1050.
- Liu, M., Xiao, L., Liang, Y. and Tao, L. (2017a) 'Experimental and numerical studies of the pontoon effect on vortex-induced motions of deep-draft semi-submersibles', *Journal of Fluids and Structures*, 72, pp. 59-79.

- Liu, M., Xiao, L., Lu, H. and Xiao, X. (2017b) 'Experimental study on vortex-induced motions of a semi-submersible with square columns and pontoons at different draft conditions and current incidences', *International Journal of Naval Architecture and Ocean Engineering*, 9(3), pp. 326-338.
- Liu, M., Xiao, L., Lyu, H. and Tao, L. (2015) 'Numerical Analysis of Pontoon Effect on Flow-Induced Forces of the Deep Draft Semisubmersible in a Cross-Flow', *ASME 2015 34th International Conference on Ocean, Offshore and Arctic Engineering*. American Society of Mechanical Engineers, pp. V001T01A030-V001T01A030.
- Ljungkrona, L., Norberg, C.H. and Sunden, B. (1991) 'Free-stream turbulence and tube spacing effects on surface pressure fluctuations for two tubes in an in-line arrangement', *Journal of Fluids and Structures*, 5(6), pp. 701-727.
- Ma, W., Wu, G., Thompson, H., Prislun, I. and Maraju, S. (2013) 'Vortex induced motions of a column stabilized floater', *Proceedings of the DOT International Conference*. pp. 22-24.
- Magee, A., Sablok, A. and Gebara, J. (2003) 'Mooring design for directional spar hull VIV', *Offshore Technology Conference*. Offshore Technology Conference.
- Magee, A., Sheikh, R., Guan, K.Y.H., Choo, J.T.H., Malik, A.M.A., Ghani, M.P.A. and Abyn, H. (2011) 'Model tests for VIM of multi-column floating platforms', *ASME 2011 30th International Conference on Ocean, Offshore and Arctic Engineering*. American Society of Mechanical Engineers, pp. 127-136.
- Manning, M. (2016) *Offshore oil production in deepwater and ultra-deepwater is increasing*. Available at: <https://www.eia.gov/todayinenergy/detail.php?id=28552> (Accessed: 19th July).
- Maribus (2014) *World ocean review: living with the oceans 3 Marine Resources - Opportunities and Risks*.
- National Academies of Sciences, E. and Medicine (2016) *Strengthening the Safety Culture of the Offshore Oil and Gas Industry*. Transportation Research Board.

- Norberg, C. (1987) 'Effects of Reynolds number and a low-intensity freestream turbulence on the flow around a circular cylinder', *Dept. of Appl. Thermodynamics and Fluid Mech., Chalmers Univ. of Tech., Gothenburg, Sweden, Publ.*, (87/2).
- Norberg, C. (1994) 'An experimental investigation of the flow around a circular cylinder: influence of aspect ratio', *Journal of Fluid Mechanics*, 258, pp. 287-316.
- Norberg, C. (2003) 'Fluctuating lift on a circular cylinder: review and new measurements', *Journal of Fluids and Structures*, 17(1), pp. 57-96.
- Oakley, O.H., Constantinides, Y., Navarro, C. and Holmes, S. (2005) 'Modeling vortex induced motions of spars in uniform and stratified flows', *ASME 2005 24th International Conference on Offshore Mechanics and Arctic Engineering*. American Society of Mechanical Engineers, pp. 885-894.
- Ong, L. and Wallace, J. (1996) 'The velocity field of the turbulent very near wake of a circular cylinder', *Experiments in fluids*, 20(6), pp. 441-453.
- Perryman, S., Gebara, J., Botros, F. and Yu, A. (2005) 'Holstein truss spar and top tensioned riser system design challenges and innovations', *Offshore Technology Conference*. Offshore Technology Conference.
- Pratt, J.A., Priest, T. and Castaneda, C.J. (1997) *Offshore pioneers: Brown & Root and the history of offshore oil and gas*. Gulf Professional Publishing.
- Rijken, O. and Leverette, S. (2008) 'Experimental Study into Vortex Induced Motion Response of Semi Submersibles with Square Columns', *ASME 2008 27th International Conference on Offshore Mechanics and Arctic Engineering*. American Society of Mechanical Engineers, pp. 263-276.
- Rijken, O. and Leverette, S. (2009) 'Field measurements of vortex induced motions of a deep draft semisubmersible', *ASME 2009 28th International Conference on Ocean, Offshore and Arctic Engineering*. American Society of Mechanical Engineers, pp. 739-746.
- Rijken, O., Leverette, S. and Davies, K. (2004) *Proceedings of the 16th Deep Offshore Technology Conference and Exhibition. New Orleans, Louisiana, USA*.

- Rijken, O., Schuurmans, S. and Leverette, S. (2011) 'Experimental investigations into the influences of SCRs and appurtenances on DeepDraft Semisubmersible Vortex Induced Motion response', *ASME 2011 30th International Conference on Ocean, Offshore and Arctic Engineering*. American Society of Mechanical Engineers, pp. 269-279.
- Sarpkaya, T. (2004) 'A critical review of the intrinsic nature of vortex-induced vibrations', *Journal of Fluids and Structures*, 19(4), pp. 389-447.
- Sayers, A.T. (1988) 'Flow interference between four equispaced cylinders when subjected to a cross flow', *Journal of Wind Engineering and Industrial Aerodynamics*, 31(1), pp. 9-28.
- Sayers, A.T. (1990) 'Vortex shedding from groups of three and four equispaced cylinders situated in a cross flow', *Journal of Wind Engineering and Industrial Aerodynamics*, 34(2), pp. 213-221.
- Schewe, G. (1983) 'On the force fluctuations acting on a circular cylinder in crossflow from subcritical up to transcritical Reynolds numbers', *Journal of Fluid Mechanics*, 133, pp. 265-285.
- Shur, M.L., Spalart, P.R., Strelets, M.K. and Travin, A.K. (2008) 'A hybrid RANS-LES approach with delayed-DES and wall-modelled LES capabilities', *International Journal of Heat and Fluid Flow*, 29(6), pp. 1638-1649.
- Smith, D.W., Thompson, H.M., Kokkinis, T. and Greiner, W.L. (2004a) 'Hindcasting VIM-Induced Mooring Fatigue for the Genesis Spar', *ASME 2004 23rd International Conference on Offshore Mechanics and Arctic Engineering*. American Society of Mechanical Engineers, pp. 1005-1014.
- Smith, D.W., Thompson, H.M., Kokkinis, T. and Greiner, W.L. (2004b) *Proceedings of the Conference on Offshore Mechanics and Arctic Engineering*, OMAE2004-51547, Vancouver, Canada.
- Son, J.S. and Hanratty, T.J. (1969) 'Velocity gradients at the wall for flow around a cylinder at Reynolds numbers from 5×10^3 to 10^5 ', *Journal of Fluid Mechanics*, 35(02), pp. 353-368.

- Spalart, P.R. and Allmaras, S.R. (1994) 'A one equation turbulence model for aerodynamic flows', *RECHERCHE AEROSPATIALE-FRENCH EDITION*-, pp. 5-5.
- Spalart, P.R., Deck, S., Shur, M.L., Squires, K.D., Strelets, M.K. and Travin, A. (2006) 'A new version of detached-eddy simulation, resistant to ambiguous grid densities', *Theoretical and Computational Fluid Dynamics*, 20(3), pp. 181-195.
- Spalart, P.R., Jou, W.H., Strelets, M. and Allmaras, S.R. (1997) 'Comments on the feasibility of LES for wings, and on a hybrid RANS/LES approach', *Advances in DNS/LES*, 1, pp. 4-8.
- Sumer, B.M. and Fredsøe, J. (1997) *Hydrodynamics around cylindrical structures*. World Scientific.
- Sumner, D. (2013) 'Flow above the free end of a surface-mounted finite-height circular cylinder: a review', *Journal of Fluids and Structures*, 43, pp. 41-63.
- Sumner, D., Price, S.J. and Paidoussis, M.P. (2000) 'Flow-pattern identification for two staggered circular cylinders in cross-flow', *Journal of Fluid Mechanics*, 411, pp. 263-303.
- Surry, D. (1972) 'Some effects of intense turbulence on the aerodynamics of a circular cylinder at subcritical Reynolds number', *Journal of Fluid Mechanics*, 52(03), pp. 543-563.
- Szechenyi, E. (1975) 'Supercritical Reynolds number simulation for two-dimensional flow over circular cylinders', *Journal of Fluid Mechanics*, 70(03), pp. 529-542.
- Tahar, A. and Finn, L. (2011) 'Vortex Induced Motion (VIM) Performance of the Multi Column Floater (MCF)–Drilling and Production Unit', *ASME 2011 30th International Conference on Ocean, Offshore and Arctic Engineering*. American Society of Mechanical Engineers, pp. 755-763.
- Tamura, T. and Miyagi, T. (1999) 'The effect of turbulence on aerodynamic forces on a square cylinder with various corner shapes', *Journal of Wind Engineering and Industrial Aerodynamics*, 83(1), pp. 135-145.

- Tamura, T., Miyagi, T. and Kitagishi, T. (1998) 'Numerical prediction of unsteady pressures on a square cylinder with various corner shapes', *Journal of Wind Engineering and Industrial Aerodynamics*, 74, pp. 531-542.
- Tan, J.H.C., Magee, A., Kim, J.W., Teng, Y.J. and Zukni, N.A. (2013) 'CFD Simulation for Vortex Induced Motions of a Multi-Column Floating Platform', *ASME 2013 32nd International Conference on Ocean, Offshore and Arctic Engineering*. American Society of Mechanical Engineers, pp. V007T08A066-V007T08A066.
- Tan, J.H.C., Teng, Y.J., Magee, A., Ly, B.T.H. and Aramanadka, S.B. (2014) 'Vortex Induced Motion of TLP With Consideration of Appurtenances', *ASME 2014 33rd International Conference on Ocean, Offshore and Arctic Engineering*. American Society of Mechanical Engineers, pp. V002T08A025-V002T08A025.
- Thiagarajan, K.P., Constantinides, Y. and Finn, L. (2005) 'CFD analysis of vortex-induced motions of bare and straked cylinders in currents', *ASME 2005 24th International Conference on Offshore Mechanics and Arctic Engineering*. American Society of Mechanical Engineers, pp. 903-908.
- Thom, A. (1933) 'The flow past circular cylinders at low speeds', *Proceedings of the Royal Society of London. Series A, Containing Papers of a Mathematical and Physical Character*, pp. 651-669.
- Thompson, M., Hourigan, K. and Sheridan, J. (1996) 'Three-dimensional instabilities in the wake of a circular cylinder', *Experimental Thermal and Fluid Science*, 12(2), pp. 190-196.
- Tian, X., Ong, M.C., Yang, J. and Myrhaug, D. (2013) 'Unsteady RANS simulations of flow around rectangular cylinders with different aspect ratios', *Ocean Engineering*, 58, pp. 208-216.
- Tutar, M. and Holdo, A.E. (2000) 'Large eddy simulation of a smooth circular cylinder oscillating normal to a uniform flow', *Journal of Fluids Engineering*, 122(4), pp. 694-702.

- Ünal, U.O. and Atlar, M. (2010) 'An experimental investigation into the effect of vortex generators on the near-wake flow of a circular cylinder', *Experiments in Fluids*, 48(6), pp. 1059-1079.
- Upton., M.A., Gawlikowski., G. and Roffer., M.A. (2017) *ROFFS™ Gulf of Mexico Early Season Preview 2017 – GULF OF MEXICO CONDITIONS LOOKING GOOD*. Available at: <https://www.roffs.com/2017/04/roffs-gulf-mexico-early-season-preview-2017-gulf-mexico-conditions-looking-good/>.
- van Dijk, R., Magee, A., van Perryman, S. and van Gebara, J. (2003a) 'Model test experience on vortex induced vibrations of truss spars', *Offshore Technology Conference*. Offshore Technology Conference.
- van Dijk, R.R.T., Voogt, A., Fourchy, P. and Mirza, S. (2003b) 'The effect of mooring system and sheared currents on vortex induced motions of truss spars', *ASME 2003 22nd International Conference on Offshore Mechanics and Arctic Engineering*. American Society of Mechanical Engineers, pp. 285-292.
- Vikestad, K., Vandiver, J.K. and Larsen, C.M. (2000) 'Added mass and oscillation frequency for a circular cylinder subjected to vortex-induced vibrations and external disturbance', *Journal of Fluids and Structures*, 14(7), pp. 1071-1088.
- Vinayan, V., Antony, A., Halkyard, J., Kim, S.-J., Holmes, S. and Spornjak, D. (2015) 'Vortex-Induced Motion of Deep-Draft Semisubmersibles: A CFD-Based Parametric Study', *ASME 2015 34th International Conference on Ocean, Offshore and Arctic Engineering*. American Society of Mechanical Engineers, pp. V002T08A003-V002T08A003.
- Waals, O.J., Phadke, A.C. and Bultema, S. (2007) 'Flow Induced Motions on Multi Column Floaters', *ASME 2007 26th International Conference on Offshore Mechanics and Arctic Engineering*. American Society of Mechanical Engineers, pp. 669-678.
- Wang, X.K., Gong, K., Liu, H., Zhang, J.X. and Tan, S.K. (2013) 'Flow around four cylinders arranged in a square configuration', *Journal of Fluids and Structures*, 43, pp. 179-199.

- Wang, Y., Yang, J., Peng, T. and Li, X. (2009) 'Model test study on vortex-induced motions of a floating cylinder', *ASME 2009 28th International Conference on Ocean, Offshore and Arctic Engineering*. American Society of Mechanical Engineers, pp. 293-301.
- Williamson, C.H.K. (1988) 'Defining a universal and continuous Strouhal–Reynolds number relationship for the laminar vortex shedding of a circular cylinder', *Physics of Fluids (1958-1988)*, 31(10), pp. 2742-2744.
- Williamson, C.H.K. (1996) 'Vortex dynamics in the cylinder wake', *Annual review of fluid mechanics*, 28(1), pp. 477-539.
- Williamson, C.H.K. and Roshko, A. (1988) 'Vortex formation in the wake of an oscillating cylinder', *Journal of fluids and structures*, 2(4), pp. 355-381.
- Xu, Q., Kim, J., Bhaumik, T., O’Sullivan, J. and Ermon, J. (2012) *ASME 2012 31st International Conference on Ocean, Offshore and Arctic Engineering*. American Society of Mechanical Engineers.
- Yung, T., Sandström, R.E., Slocum, S.T., Ding, Z.J. and Lokken, R.T. (2004) 'Advancement of spar VIV prediction', *Offshore Technology Conference*. Offshore Technology Conference.
- Zhang, H., Yang, J., Xiao, L. and Lu, H. (2014) 'Study on added mass coefficient and oscillation frequency for a Truss Spar subjected to Vortex-Induced Motions', *Ships and Offshore Structures*, 9(1), pp. 54-63.
- Zhao, J., Leontini, J.S., Jacono, D.L. and Sheridan, J. (2014) 'Fluid–structure interaction of a square cylinder at different angles of attack', *Journal of Fluid Mechanics*, 747, pp. 688-721.
- Zhao, M. and Cheng, L. (2012) 'Numerical simulation of vortex-induced vibration of four circular cylinders in a square configuration', *Journal of Fluids and Structures*, 31, pp. 125-140.

Zou, L., Lin, Y.-f. and Lam, K. (2008) 'Large-eddy simulation of flow around cylinder arrays at a subcritical Reynolds number', *Journal of Hydrodynamics, Ser. B*, 20(4), pp. 403-413.

